



**The Influence of Hull Form on the Slamming Behaviour of Large
High-Speed Catamarans**

by

Jalal Rafie Shahraki

National Centre for Maritime Engineering and Hydrodynamics (NCMEH)

Australian Maritime College

Submitted for fulfilment of PhD Candidature

Supervisors:

Professor Giles Thomas

Dr Irene Penesis

Professor Michael Davis

Dr Walid Amin

January 2014

Declaration of originality

This thesis contains no material that has been accepted for a degree or diploma by the University of Tasmania or any other institution, and to the best of my knowledge and belief no material previously published or written by another person except where due acknowledgement is made in the text of the thesis.

Jalal Rafie Shahraki

January 2014

Originally Blank

Statement of Authority of Access

This thesis is not to be made available for loan or copying for two years following the date this statement was signed. Following that time the thesis may be made available for loan and limited photocopying in accordance with the Copyright Act 1968.

Jalal Rafie Shahraki January 2014

Originally Blank

Abstract

Wave-piercing catamarans are used extensively for both defence and commercial sea transportation because of their many advantages. Issues such as the impact of the bow into the water when operating in large waves, better known as wetdeck slamming, can affect their mission capability and cause structural damage. However, the design criteria for this type of craft are not yet sufficiently accurate.

Based on an exploratory study, wave-piercing catamarans such as the vessels built by INCAT Tasmania often have a centrebow that provides reserve buoyancy under the wetdeck to reduce heave and pitch motions and avoid deck diving in following seas. Over time, for INCAT large catamarans, hull parameters such as tunnel clearance, centrebow length and centrebow volume have decreased as the vessels have grown in length.

To evaluate the effect of various bow forms on motions and slamming loads, an adjustable hydroelastic segmented model was designed and constructed as part of the collaboration between AMC, UTAS and INCAT. This segmented model is a scaled model of a 112m INCAT wave-piercing catamaran and has two transverse cuts and a separate centrebow. The centrebow was equipped with two six degree of freedom force/torque transducer to measure slam forces both in vertical and horizontal directions. The model shell was built from a sandwich panel of carbon-fibre layers and Divinycell foam core. Lessons learnt from an existing hydroelastic catamaran model were taken into consideration to design and construct this model.

Three centrebow volumes (lengths) were designed and tested in head seas in the AMC towing tank for 2.76 m regular wave heights and 20 knots speed. The results showed a significant variation in slam loads when comparing the three centrebow lengths, with the highest loads found on the longest centrebow, caused by larger water volume constrained between the centrebow and demihulls. The slams in shorter centrebows occurred further forward and at more inclined angles. Results also showed that the longer centrebows have higher pitch motions in slamming conditions due to higher vertical forces on the centrebow. It could be concluded that in the tested condition, the shorter centrebow performed better overall in waves.

Also a study with Smoothed Particle Hydrodynamics (SPH) was conducted investigating slamming especially for enclosed sections. Various vessel bow sections were dropped into water to replicate slamming. The simulations included single-phase, two-dimensional and three-dimensional modelling of two simple wedges, a wedge with two side-plates and a fully INCAT catamaran bow section comparing with experimental drop tests results. It is concluded that SPH is capable of simulating monohull sections slamming successfully. However, simulation results of enclosed sections did not match well with the experiments, most likely due to inclusion of air under the section which will be the subject for future research.

Originally Blank

Acknowledgments

I would like to thank my friends and colleagues at the Australian Maritime College at the University of Tasmania, INCAT Tasmania and Revolution Design for the help and encouragement they have provided during the course of this project. I am particularly grateful to:

- Professor Giles Thomas for providing the best guidance both technically and spiritually over the course of this project
- Professor Michael Davis, Dr Irene Penesis and Dr Walid Amin for providing support and supervision through the project.
- Stuart Friezer and Gary Davidson of Revolution Design in providing technical data from INCAT catamarans.
- Australian Maritime College's towing tank staff who helped me conducting my experiments.
- Alejandro J.C. Crespo from University of Vigo (Spain) for providing valuable help for my slamming simulations.
- My partner Elaheh, she has been a wonderful support for me especially in the final stages of candidature. I give her big thanks for her patience.

This was a collaborative project between the Australian Maritime College, University of Tasmania and INCAT Tasmania. The project was supported by the Federal Government through the Australian Research Council's linkage funding scheme.

Table of Contents

Declaration of originality	I
Abstract.....	V
Acknowledgments.....	VII
Table of Contents.....	IX
Table of Figures	XIII
Publications Relevant to the Thesis	XXVII
1. Introduction.....	1
1.1. Full-scale measurements	4
1.2. Slamming model experiments.....	6
1.2.1. Scaling laws	6
1.2.2. Drop tests	7
1.2.3. Towing tank model tests	10
1.2.4. Experimental methods summary	14
1.3. Computational methods and slamming	15
1.3.1. Analytical solutions for slamming	15
1.3.2. Numerical solutions for 2-D water entry problem	16
1.3.3. Numerical 3-D ship slamming problem.....	18
1.4. Thesis arrangement	19
2. Wave-piercing catamarans hull form and slamming: an exploratory study.....	23
2.1. High tunnel clearance approach to catamaran design	23
2.2. INCAT approach to catamaran design.....	24
2.2.1. Tunnel clearance	26
2.2.2. Centrebow	27
2.2.3. Reserve buoyancy	29
2.2.4. Centrebow length	30
2.2.5. Centrebow unprotected area.....	31
2.3. Summary	33

3.	Hydroelastic segmented model development.....	35
3.1.	Hydroelastic segmented catamaran model (HSM01)	35
3.2.	The new HSM design objectives	38
3.3.	New hull forms for application to the HSM02 model.....	39
3.3.1.	Variation of centrebow length.....	40
3.3.2.	Various tunnel clearance	43
3.3.3.	Adjustable flat wetdeck design	45
3.4.	Flexural rigidity and vibratory response of the model	47
3.4.1.	Strain gauges and VBM calibration	48
3.5.	Centrebow load measuring system	50
3.5.1.	Feasibility study of installing 6DOF Force transducers.....	52
3.5.2.	Load measuring system final configuration	53
3.5.3.	Extracting centrebow loads from the 6DOF Force transducers	55
3.6.	Slam pressure measurement and instrumentation	56
4.	Hydroelastic model commissioning tests and calibration	59
4.1.	Modal structural frequency tests	59
4.2.	Strain gauges and VBM calibration	62
4.3.	Centrebow load calibration	64
4.3.1.	Individual 6DOF force transducer calibration check	65
4.3.2.	Calibration check for centrebow load measuring system.....	66
4.4.	Summary	72
5.	Effect of centrebow length on motions and loads: experimental process, results and discussion	73
5.1.	Experimental Procedure.....	73
5.1.1.	Facility	73
5.1.2.	Model setup.....	74
5.1.3.	Instrumentation and data acquisition	75
5.2.	Test conditions	78
5.3.	Results and discussion	79
5.3.1.	Motions	79

5.3.2.	Centrebow loads.....	83
5.3.3.	Vertical centrebow force results.....	85
5.3.4.	Vertical slam load magnitudes	92
5.3.5.	Horizontal centrebow forces	99
5.3.6.	Slam force direction	103
5.3.7.	Slam locations	104
5.3.8.	Vertical Bending Moments (VBM)s.....	107
5.3.9.	Wetdeck archway pressure results	115
5.3.10.	Further investigations into the centrebow force signals (a hypothesis)	117
5.4.	Summary	120
6.	Numerical modelling of slamming using Smoothed Particle Hydrodynamics (SPH)	123
6.1.	The SPH model	124
6.1.1.	Basic formulations	124
6.1.2.	Time stepping.....	130
6.1.3.	Boundary conditions	131
6.1.4.	Modelling of floating bodies.....	133
6.1.5.	Dual-SPHysics code and efficiency	134
6.2.	Implementation of SPH model for drop tests.....	135
6.2.1.	Drop test experiments	135
6.2.2.	SPH model configuration, boundaries and domain setup	137
6.2.3.	Speed of sound.....	138
6.2.4.	Particle density independency study	139
6.2.5.	Damping in the fluid: spatial filter and artificial viscosity.....	140
6.2.6.	Visualisation of results.....	144
6.2.7.	Drop kinematics	145
6.2.8.	Wall pressures	148
6.2.9.	Summary of configuration and parameter selection	149
6.3.	Drop tests results and comparison with experimental data	150
6.3.1.	25 degree wedge.....	150

6.3.2.	15 degree wedge.....	152
6.3.3.	25 degrees wedge with side plates	156
6.3.4.	INCAT wave-piercing catamaran with centrebow (Incat1).....	160
6.3.5.	Effect of hull form on slamming of arched sections	165
6.4.	Three-dimensional modelling of drop geometries	166
6.5.	Summary	169
7.	Conclusions.....	171
7.1.	Results of the research methodologies.....	171
7.1.1.	Exploratory study into existing large high-speed catamarans.....	171
7.1.2.	Hydroelastic model design, construction and experiments	172
7.1.3.	Slam modelling with smoothed particle hydrodynamics (SPH)	174
7.2.	Implication of the research.....	175
7.3.	Recommendations for future research	176
	References:.....	178
	Appendices.....	187
	Appendix 1: Specifications of ATI MINI45 Force transducer	187
	Appendix 2: Feasibility study of using two 6DOF Force transducers	189
	Appendix 3: Pressure measurement instruments	195
	(a) ENDEVCO Piezoresistive pressure transducer model 8510C-50	195
	(b) ENDEVCO DC Amplifier model 136.....	197
	Appendix 4: Acceleration measurement instruments	199
	(a) B&K 4370 accelerometer specifications	199
	(b) Conditioning Amplifier 2626 to amplify the B&K accelerometer signal	201

Table of Figures

Figure 1.1: Typical conventional catamaran body sections	1
Figure 1.2: Ocean Lala, the catamaran ferry losing the bow structure from severe wetdeck slamming in Taiwan waters. The waves have damaged the front car ramp, cross deck structure, front bulkhead and gate. The lower right: the vessel before damage occurred (http://www.chinapost.com.tw , http://www.gov.cn/english/2009-07/16/content_1366854.htm)	2
Figure 1.3: Condor Express, INCAT Hull042, an 86m car-passenger wave piercing catamaran (Barry Quince). The centrebow can be seen between the two demihulls.....	3
Figure 1.4: The drop test rig of Whelan in University of Tasmania [12, 33]. Catamaran sections with centrebows were free dropped into water tank	9
Figure 1.5: Profile and plan (starboard side only) view of 2.5m catamaran HSM [52].....	14
Figure 1.6: Schematic of isolation of the centrebow piece from the demihulls. Slam forces have been isolated and measured [52].	14
Figure 1.7: Three stages in slamming of wave-piercing catamaran with centrebow. (a) Bottom slamming; (b)centrebow keel slamming; (c) severe arch top slamming	16
Figure 2.1: Trinidad and Tobago 41m Water Taxi built by Austal Ships. The Z-shape demihull bow and high tunnel height is of some important features of these catamarans (www.Austal.com).	23
Figure 2.2: INCAT large catamarans demihull bow shapes. (a) conventional demihull bow (INCAT K-class); (b) sharp elliptical demihull bow (waterline below the tip – 78 m WPC); (c) semi-oval surface-piercing bow (waterline above the tip – 112 m WPC); (www.incat.com.au).	24
Figure 2.3: Typical bow profiles of WPCs and conventional catamarans. Narrow water-plane area of demihulls, low tunnel clearance and centrebow are the main characteristics of INCAT large WPCs. 24	
Figure 2.4: Natchan Rera, INCAT 112 m wave-piercing catamaran (www.INCAT.com.au) showing the fine entry demihull bows and the centrebow	25
Figure 2.5: Tunnel clearance of some of INCAT catamarans and DNV recommendations. INCAT catamarans have lower tunnel clearance.....	26
Figure 2.6: Evolution of the centrebow volume in INCAT wave piercing catamarans.....	28
Figure 2.7: Tunnel clearance ratio (TCR) and centrebow volume ratio (CBVR) for INCAT wave-piercing catamarans versus demihull length.	28
Figure 2.8: INCAT 112m wave-piercing catamaran; the forward demihull volume, centrebow volume, unprotected area and the centrebow length definitions are illustrated.	29
Figure 2.9: Reserve buoyancy indicators of INCAT wave-piercing catamarans versus demihull length.	30
Figure 2.10: INCAT wave-piercing catamarans centrebow length ratio versus demihull length.	31

Figure 2.11: (a) INCAT 112m WPC; (b) INCAT 78m WPC (www.incat.com.au); (c) AMD1800, the 95 m WPC. The unprotected centrebow area in 78m vessel is much larger than the 112m WPC. In the 95 m WPC the jaw is moved a long way aft (http://www.amd.com.au/designs/amd1800.php).....	32
Figure 2.12: INCAT wave-piercing catamarans unprotected centrebow area	32
Figure 3.1: The first AMC-UTas segmented catamaran model HSM01 with its main components and elastic links.....	35
Figure 3.2: HSM01 transverse beam and cross-deck system. Two aluminium transverse beams connected to demihull backbone beams hold the demihulls together in mid segment. Aft wetdeck is attached to another cantilever beam extended from mid segment	37
Figure 3.3: Aft wetdeck in HSM01 is attached to a cantilever beam extended from mid segment. In case of wave loading on the aft wetdeck, the VBMs are transferred to both sides of the mid segment.....	38
Figure 3.4: Centrebow length ratio (CLR) of INCAT large wave-piercing catamarans and this ratio variation tested in model scale	40
Figure 3.5: The creation of three centrebow lengths by adding and cutting out 150 mm pieces from the model parent centrebow truncation. The hatched area shows the parent centrebow volume	41
Figure 3.6: The transverse truncation section of the long, parent and short Centrebows	41
Figure 3.7: The definition of centrebow clearance area and blocked area shown for a catamaran bow section	42
Figure 3.8: Three centrebow length segments under construction. The short centrebow achieved by cutting 150mm from centrebow aft and a separate segment was built to form the long centrebow	42
Figure 3.9: Tunnel clearance ratio of INCAT WPCs and the HSM02. The 112 m WPC is the parent hull configuration. The tunnel clearance is illustrated in the bottom left corner figure.....	43
Figure 3.10: High tunnel height centrebow body plan (right), compared to parent hull bow form (left)	44
Figure 3.11: Low tunnel height bow body plan (right), compared to parent hull centrebow (left)	44
Figure 3.12: Schematic port side cross section of the carbon wetdeck box and its attachment to the demihull. The aluminium reinforcing plates with three premade 3 mm holes for height adjustment are shown in the bottom right of the figure.....	46
Figure 3.13: The location of wetdeck box and the arrangement of the reinforcing plates along the hull. The wetdeck box can move up and down the plates to change tunnel height.....	46
Figure 3.14: HSM02 mid segment wetdeck and demihulls assembly configuration.....	46
Figure 3.15: The three degree of freedom model of HSM02 to obtain the first modal frequency and the dimensions of the elastic links	47
Figure 3.16: Fabricated HSM02 elastic link configuration.....	47
Figure 3.17: Backbone beams and the transverse frames arrangement in HSM02.....	48
Figure 3.18: The HSM02 assembly of backbone beams and transverse frames under construction. Epoxy glue was used to connects various parts together	48

Figure 3.19: The sagging and hogging VBMs are measured in two segment cuts of the HSM01	49
Figure 3.20: (a) Locating strain gauges on both sides of a bar to measure strains by change of grid resistance; (b) metal wire strain gauge (www.ni.com/white-paper/3642/en)	49
Figure 3.21: The strain gauges on the link and the Wheatstone half-bridge circuit.....	50
Figure 3.22: The centrebow isolation technique. The cuts are made so the slam loads can be captured by the centrebow segment alone	50
Figure 3.23: ATI MINI45 Force transducer and its load axes. The Z-axis will be used for vertical slam force measurements. Tool side is attached to the tool (centrebow) and mount side is attached to the support	51
Figure 3.24: The proposed configuration of centrebow load measuring system where two aluminium transverse beams location the centrebow and the 6DOF force transducers.....	52
Figure 3.25: The side edge displacement of centrebow by loading asymmetrically on the archways close to centrebow truncation	53
Figure 3.26: The connection of transverse T-bars and the demihull via a carbon-fibre deck and transverse frames inside the demihulls. Aluminium cradles were designed to rigidly attach the T-bars to the deck (note that the demihull shell has been removed in this rendering)	54
Figure 3.27: Centrebow segment transverse beam arrangement and 6DOF sensors. A stiffened carbon-fibre sandwich deck provides the base support for the beams	55
Figure 3.28: Centrebow free body diagram. Two 6DOF Force transducers measure the slam force...	55
Figure 3.29: Pressure transducer casing arrangement on the centrebow starboard. The fittings are arranged in a longitudinal manner along the top of the arch with three transverse locations close to parent centrebow truncation.....	58
Figure 3.30: The centrebow with pressure transducer casings installed after construction	58
Figure 4.1: The elastic links from the top view. The cross section and the gap size determine the stiffness of the link.....	59
Figure 4.2: The impact test setup for measuring modal frequency. The centrebow tip was impacted and the accelerations were measured along the hull	60
Figure 4.3: A sample time series of impact test accelerations of the model in the water. The whipping oscillations start after the impact and continue while getting damped slowly	61
Figure 4.4: An impact test sample FFT analysis of the accelerations on the model. The analysis shows 14.72 Hz as the fundamental mode whipping frequency and 1.685 Hz as the rigid body motion response of the model inside the water	61
Figure 4.5: The position of the model and the supports location during loading for bending moment calibration	62
(a) Loading the model for Forward cut VBM calibration in Position 2.....	62
(b) Loading the model from transom to calibrate VBM in Position 3	62

Figure 4.6: The model was set up on the wet dock edges of the towing tank and loaded with a hook and string.....	62
Figure 4.7: Elastic link strain gauge calibration graph. The calibration factor is taken as the average slope of the graph for different positions before and after tests.....	63
Figure 4.8: Some of the load combinations applied on individual 6DOF Force transducers. An especial rig including a rigid base and an end plate were designed for this purpose.....	65
Figure 4.9: Results of calibration check for the individual forward and aft 6DOF force transducers ..	66
Figure 4.10: The centrebow loads calibration setup. The model was set upside down and loaded in angles to evaluate the accuracy of the load measuring system	67
Figure 4.11: Centrebow load application points locations measured from the aft sensor (distances are in millimetres).....	67
Figure 4.12: The centrebow loads calibration setup. The model was set upside down and loaded in angles to evaluate the accuracy of the load measuring system	68
Figure 4.13: Measured vertical applied load and the measured vertical loads (F_z) in vertical loading setup	68
Figure 4.14: Applied load and the measured forces in HSM01 performed by Matsubara (thesis, page 80) [51]. The first row shows the applied and measured vertical forces 1.956 m from transom, versus the 1:1 line. The left is for the aft transverse beam (FTB) and the right is for the forward beam gauges. The second row graphs show the insufficient forces predicted by each transverse beam (CBS stands for centrebow segment).....	69
Figure 4.15: Applied load location and the measured location from the aft 6DOF force transducer. The trend line slope shows less than 0.5% error in predicting locations	70
Figure 4.16: Applied load location and the measured location from the aft centrebow transverse beam (FTB) in HSM01 performed by Matsubara (thesis, page 83) [51]. The results before applying correction could predict the forces up to 80 mm astern the actual location.....	70
Figure 4.17: Measured vertical loads versus applied vertical loads (F_z) in different loading angle setup. The vertical setup and higher angles setups show less than 1.5% error in measuring the applied loads; for small application angles the relative error could be around 5%	71
Figure 4.18: Measured horizontal load versus applied Horizontal force (F_x) in different inclination setups. The larger the angle, the more accurate is the load measurement.....	71
Figure 5.1: The towing tank carriage and the HSM02 on the water	73
Figure 5.2: The set up for Bifalar swing test to estimate the model pitch radius of gyration	74
Figure 5.3 The static resistance wave probe which was located 5 m from the wave generator.....	75
Figure 5.4: The wave probe signal conditioner.....	75
Figure 5.5: The arrangement of the posts connecting the model to the carriage. The forward tow post tows the model and the aft post is located on a longitudinal slider. The motions of the model are calculated from the relative vertical motion at the two posts.....	76

Figure 5.6: Crossbow IMU440 inertia system to measure pitch motions and linear accelerations	78
Figure 5.7: Sample heave and pitch raw data (run 45, $H_w=60$ mm, $H_w=60$ mm, speed=1.53 m/s, wave frequency=0.75).....	79
Figure 5.8: Non-dimensional heave response for various centrebow lengths in HSM02 ($H_w=60$ mm, speed=1.53 m/s).....	80
Figure 5.9: Non-dimensional heave response with respect to Centrebow Length Ratio and Centrebow Volume Ratio in different encounter wave frequencies ($H_w=60$ mm, speed=1.53 m/s).....	81
Figure 5.10: Non-dimensional pitch response for the three centrebow lengths in HSM02 ($H_w=60$ mm, speed=1.53 m/s).....	81
Figure 5.11: The non-dimensional pitch results versus the Centrebow Length Ratio and Centrebow Volume Ratio of the three centrebows in different encounter wave frequencies ($H_w=60$ mm, speed=1.53 m/s).....	82
Figure 5.12: The centrebow forces and moments on force transducers. The centrebow force is calculated as the addition of the two sensors' readings	83
Figure 5.13: The centrebow F_z in run 45, (a) the raw forces and the filtered 3db low pass 500 Hz cut-off frequency; (b) the graph zoomed to show one single slam spike ($H_w=60$ mm, speed=1.53 m/s, $\omega_e^*=4.136$).....	84
Figure 5.14: Change in magnitude picked up in various 3db low pass cut-off filtering frequencies ($H_w=60$ mm, speed=1.53 m/s, $\omega_e^*=4.136$). 500 Hz was chosen to be the best filtering frequency. The sampling frequency is 5 kHz, thus 2500 Hz means no filtering	84
Figure 5.15: (a) Recorded centrebow vertical forces (F_z) from the run 45 ($H_w=60$ mm, speed=1.53 m/s, $\omega_e^*=4.136$); (b) close up of the graph (positive is upward force). The sharp peaks from slamming and the more frequent oscillations from the whipping are clearly seen.....	85
Figure 5.16: Spectral analysis of the centrebow forces in run 45 ($H_w=60$ mm, speed=1.53 m/s, $\omega_e^*=4.136$)	86
Figure 5.17: Still sequences of snapshots from one encounter frequency of HSM02 with the parent centrebow in run 45 ($H_w=60$ mm, speed=1.53 m/s, $\omega_e^*=4.136$).....	87
Figure 5.18: Free body diagram of the centrebow and the acceleration. F_z is the reaction of the 6DOF sensors and F_{ex} is the external forces acting on the centrebow.	88
Figure 5.19: The centrebow and slam force for run 45. Including the inertia removes the whipping oscillations from the centrebow measured forces ($H_w=60$ mm, speed=1.53 m/s, $\omega_e^*=4.136$).....	89
Figure 5.20: Sample time series of centrebow forces and motions from run 45 ($H_w=60$ mm, speed=1.53 m/s, $\omega_e^*=4.136$).	90
Figure 5.21: Sample time series of centrebow forces and motions from run 38 on a short wave ($H_w=60$ mm, speed=1.53 m/s, $\omega_e^*=5.37$).....	91
Figure 5.22: Sample time series of centrebow forces and motions from run 44 on a relatively long wave ($H_w=60$ mm, speed=1.53 m/s, $\omega_e^*=3.39$)	92

Figure 5.23: Sample time series of the parent centrebow slam forces (F_s) in various encounter wave frequencies. The slam forces are greatest in mid-range frequencies ($H_w=60$ mm, speed=1.53 m/s)...	93
Figure 5.24: Vertical centrebow slam forces for three centrebow lengths in HSM02 ($H_w=60$ mm, speed=1.53m/s, positive shows upward slam forces and the bars show the 95% confidence intervals)	95
Figure 5.25: Non-dimensional vertical centrebow slam forces ($F_s^* = F_{spg}H_w\sqrt{2/3}$) for three centrebow lengths in HSM02.....	96
Figure 5.26: The slamming upwash water exits the centrebow in open jaw, but becomes restricted under the archway behind the jawline.....	96
Figure 5.27: The time histories of slam force and pitch response of the three centrebows. The time axis is shifted for better visual comparison ($H_w=60$ mm, speed=1.53 m/s, $\omega_e^*=4.136$)	97
Figure 5.28: The pitch motion and slam forces of the three centrebows for the peak slamming condition ($H_w=60$ mm, speed=1.53 m/s, $\omega_e^*=4.53$).....	97
Figure 5.29: Sample time series from run 60 with the short centrebow. In this run, a slam slows the relative motion to prevent a slam on the next wave, but the motion then increases for the next wave encounter ($H_w=60$ mm, speed=1.53 m/s, $\omega_e^*=4.9$)	98
Figure 5.30: The non-dimensional slam forces ($F_s^* = F_{spg}H_w\sqrt{2/3}$) for the peak slamming condition as a function of the Centrebow Length Ratio (CLR) and Centrebow Volume Ratio (CBVR) of the three centrebows	99
Figure 5.31: Horizontal centrebow forces for three centrebow lengths in HSM02. Negative is the aftward direction ($H_w=60$ mm, speed=1.53 m/s, $\omega_e^*=4.13$).	100
Figure 5.32: Horizontal centrebow forces for three centrebow lengths. Positive is the aftward direction	101
Figure 5.33: Non-dimensional horizontal centrebow force ($F_x^* = F_{xpg}H_w\sqrt{2/3}$) for three centrebow lengths	101
Figure 5.34: The variation of the tunnel blockage at the centrebow truncation between the three centrebows	102
Figure 5.35: The non-dimensional horizontal force ($F_x^* = F_{xpg}H_w\sqrt{2/3}$) in slamming conditions in the three centrebows versus Centrebow Volume Ratio (CBVR) and Tunnel Blockage Factor (TBF)	102
Figure 5.36: The definition of the slam angle (direction). F_x and F_z are the average peak slam forces measured for each slam event	103
Figure 5.37: The slam angles for slamming conditions for three centrebows (speed =1.53 m/s, $H_w=60$ mm)	103
Figure 5.38: Slam directions versus Centrebow Length Ratio (CLR) and Tunnel Blockage Factor (TBF) of the three centrebows in slamming conditions.....	104

Figure 5.39: Centrebow resultant force locations for three centrebow lengths. The centrebow truncations and the aft of the jaw-line of the bow profiles are shown.	105
Figure 5.40: Trends of slam locations pitch and heave motions in the mid frequency range (slamming zone) for the parent centrebow.....	105
Figure 5.41: Schematic of the slam resultant force locations in peak slamming condition ($H_w=60$ mm, speed=1.53 m/s, $\omega_e^*=4.53$)	106
Figure 5.42: A photo of slamming for the parent centrebow configuration in the head seas ($H_w=60$ mm, speed=1.53 m/s and $\omega_e^*=4.136$). The spray pattern after the slam shows that water displaced by the centrebow passes outboard of the demihull, forward of the aftmost jaw point.....	106
Figure 5.43: The slam resultant force locations in peak slamming condition ($H_w=60$ mm, speed=1.53 m/s) as a function of Centrebow Length Ratio (CLR) and Tunnel Blockage Factor (TBF) of the centrebow	107
Figure 5.44: The hogging and sagging of the model and vertical bending moment in each segment cut. Sagging VBM is positive and hogging is negative	107
Figure 5.45: (a) Sample run recording data of aft cut vertical bending moment (VBM) for run 45 ($H_w=60$ mm, speed=1.53 m/s, $\omega_e^*=4.136$); (b) close up of the data. The more frequent oscillations are the whipping responses of the model, while the high peaks are slam induced VBMs.	108
Figure 5.46: keel plate stresses frame 24.5 of full-scale measurements on INCAT Hull042 (86 m length) [115].....	109
Figure 5.47: Amplitude spectrum of vertical bending moments of run 45 ($H_w=60$ mm, speed=1.53 m/s, $\omega_e^*=4.136$) extracted using FFT analysis	109
Figure 5.48: The histogram of slam induced VBM peak values for the forward cut during 4 runs ($H_w=60$ mm, speed=1.53 m/s, $\omega_e^*=4.53$). The mean is 38.48 Nm and standard deviation is 2.79....	110
Figure 5.49: The cumulative distribution of the VBM peak values of parent centrebow compared to the normal distribution ($H_w=60$ mm, speed=1.53 m/s, $\omega_e^*=4.53$)	111
Figure 5.50: The measured forward vertical bending moment (VBM) for the three centrebow lengths. The positive shows sagging VBM values and the negative shows hogging VBM ($H_w=60$ mm, speed=1.53 m/s).....	112
Figure 5.51: The measured aft cut VBM in the model for the three centrebow lengths. The positive shows sagging VBM values and the negative shows hogging values ($H_w=60$ mm, speed=1.53 m/s).	112
Figure 5.52: The non-dimensional forward cut (56% LOA) vertical bending moment (VBM^*) for the three centrebow lengths ($VBM^* = VBM \rho g H_w \nabla$)	113
Figure 5.53: The non-dimensional aft cut (33% LOA) vertical bending moment (VBM^*) for the three centrebow lengths ($VBM^* = VBM \rho g H_w \nabla$)	113
Figure 5.54: The vertical bending moment of the forward cut of the three centrebow lengths $VBM^* = VBM \rho g H_w \nabla$	114

Figure 5.55: The vertical bending moments of the Aft cut of the three centrebow lengths $VBM^* = VBMpgHwV$	114
Figure 5.56: The relationship between the forward cut (56% LOA) vertical bending moments and the slam locations (x) multiplied by slam forces (F_s) in peak slamming conditions.....	115
Figure 5.57: Time history of pressures at frame 72, top of the arch pressure transducer in run 45 ($\omega_e^*=4.136$).....	116
Figure 5.58: The pressure signal for one slam case in run 45. The (b) shows the peak of the (a) slam event. It shows strong effect of aliasing in finding the slam peak pressure	116
Figure 5.59: The schematic diagram of the air flow below and above the wetdeck when running in waves. An air pressure difference is generated applying a small upward force	117
Figure 5.60: Sample time series of the centrebow forces (speed=1.53 m/s, $H_w=60$ mm, $\omega_e^*=4.136$). The centrebow external force can be divided into water slam forces and air forces	118
Figure 5.61: Sample time series of pressures in the transducer at frame 72 arch top and the calculated air pressure forces in run 45 (speed=1.53 m/s, $H_w=60$ mm, $\omega_e^*=4.136$)	119
Figure 5.62: Air pressure forces under the centrebow archways (speed=1.53 m/s, $H_w=60$ mm)	119
Figure 6.1: Smoothing function W and the support domain in SPH	125
Figure 6.2: particles within support domain using of the smoothing function W for particle i . The support domain S is circular with a radius of kh and $\mathbf{rij} = \mathbf{xi} - \mathbf{xj}$	127
Figure 6.3: Dynamic boundary condition with (a) linear boundary particle arrangement and (b) staggered particle arrangement. The larger circles are support domains for particle i and j	132
Figure 6.4: Open periodic boundary condition in SPH where the support domain of particle i is extended through the other side of the open periodic boundary (from SPHysics user guide [141]) ..	133
Figure 6.5: computational diagram for CPU (left) and GPU (right) implementation of Dual-SPHysics code [154, 155]	135
Figure 6.6: Schematic outlines of the drop experiments by Whelan [33] where H is the drop height	135
(c) The 25 degree wedge with side plates	137
(d) Incat1, INCAT wave-piercing catamaran with centrebow	137
Figure 6.7: Four of the drop geometries tested by Whelan [33], used for comparison in this work...	137
Figure 6.8: Initial 2-D particle arrangement, boundary conditions and pressure field of the tank and drop section in SPH	137
Figure 6.9: Particle arrangement on the bottom right corner of the tank. The blue (larger) particles are the boundary particles and the red (smaller) ones are the fluid domain particles.	138
Figure 6.10: The approximate distance the jet flow under the 25 degree wedge has travelled in 60 milliseconds	139
Figure 6.11: Comparison of drop acceleration for the 25 degree wedge with different particle spacing with mass number=0.29 and normalised drop height (NDH)=0.85.....	140

Figure 6.12: Comparison of drop acceleration for the 25 degree wedge with different artificial viscosity values with mass number=0.29 and normalised drop height (NDH)=0.85	141
Figure 6.13: Comparison of drop acceleration for the 25 degree wedge with different artificial viscosity values with mass number=0.29 and normalised drop height (NDH)=0.85	142
Figure 6.14: Drop acceleration of 25° wedge in SPH with DP=0.005 m with Shepard filter applied every (a) 5 and (b) 30 time steps compared to experiments (mass number=0.29 and normalised drop height (NDH)=0.85).....	143
Figure 6.15: Drop acceleration of 25° wedge in SPH with DP=0.00125 m with Shepard filter applied every 30 time steps with artificial viscosity coefficient (α) of 0.01 and 0.001 compared to experiments (mass number=0.29 and normalised drop height (NDH)=0.85)	143
Figure 6.16: Comparison of 2-D SPH simulations of the 25° wedge drop section in various time steps with experiments of Whelan et al. [12, 33] (mass number=0.29 and normalised drop height (NDH)=0.85).....	144
Figure 6.17: Velocity contours of 25° wedge simulations 60 milliseconds after drop (mass number=0.29 and normalised drop height (NDH)=0.85).....	145
Figure 6.18: Immersion of 25° wedge simulations with mass number=0.29 and normalised drop height (NDH)=0.85	145
Figure 6.19: drop velocity with mass number=0.29 and normalised drop height (NDH)=0.85	146
Figure 6.20: Drop acceleration of 25° wedge with mass number=0.29 and normalised drop height (NDH)=0.85	147
Figure 6.21: Pressure contour plot of the SPH fluid domain as it moves up from the bottom boundary	147
Figure 6.23: The close up of the jet flow in spray root and the wall pressure interpolation domain .	148
Figure 6.24: Drop pressures at P1 of the 25° wedge with mass number=0.29 and normalised drop height (NDH)=0.85	148
Figure 6.25: Drop pressures at P2 of the 25° wedge with mass number=0.29 and normalised drop height (NDH)=0.85	148
Figure 6.26: Drop pressures at P3 of the 25° wedge with mass number=0.29 and normalised drop height (NDH)=0.85	149
Figure 6.27: Drop pressures at P4 of the 25° wedge with mass number=0.29 and normalised drop height (NDH)=0.85	149
Figure 6.28: drop acceleration of 25° wedge with SPH for NDH=0.8 and mass number=0.29	150
Figure 6.29: Drop velocity with SPH of 25° wedge with SPH for NDH=0.8 and mass number=0.29	150
Figure 6.30: Drop acceleration with SPH of 25° wedge for NDH=1.06 and mass number=0.29	151
Figure 6.31: Drop velocity with SPH of 25° wedge for NDH=1.06 and mass number=0.29.....	151
Figure 6.32: Drop acceleration with SPH of 25° wedge for NDH=1.2 and mass number=0.29	151

Figure 6.33: Drop velocity with SPH of 25° wedge for NDH=1.2 and mass number=0.29.....	151
Figure 6.34: Drop acceleration with SPH of 25° wedge for NDH=0.89 and mass number=0.58	152
Figure 6.35: Drop velocity with SPH of 25° wedge for NDH=0.89 and mass number=0.58.....	152
Figure 6.36: Comparison of 2–D SPH simulations of the 15° wedge drop section in various time steps (20,40 and 60 ms) with experiments of Whelan [33] (mass number=0.29 and normalised drop height (NDH)=0.89).....	153
Figure 6.37: Drop acceleration with SPH of 15° wedge for NDH=0.8 and mass number=0.29	154
Figure 6.38: Drop velocity with SPH of 15° wedge for NDH=0.8 and mass number=0.29.....	154
Figure 6.39: Drop acceleration with SPH of 15° wedge for NDH=0.89 and mass number=0.29	154
Figure 6.40: Drop velocity with SPH of 15° wedge for NDH=0.89 and mass number=0.29.....	154
Figure 6.41: Drop acceleration with SPH of 15° wedge for NDH=1.06 and mass number=0.29	155
Figure 6.42: Drop velocity with SPH of 15° wedge for NDH=1.06 and mass number=0.29.....	155
Figure 6.43: Pressure results of P1 with SPH of 15° wedge for NDH=0.89 and mass number=0.29	155
Figure 6.44: Pressure results of P2 with SPH of 15° wedge for NDH=0.89 and mass number=0.29	155
Figure 6.45: Pressure results of P3 with SPH of 15° wedge for NDH=0.89 and mass number=0.29	156
Figure 6.46: The location of pressure transducers on 15° wedge drop section.....	156
Figure 6.47: Comparison of 2–D SPH simulations of the 25° wedge with side plates drop section in various time steps (40, 60, 80 and 85 ms) with experiments of Whelan [12, 33] (mass number=0.29 and normalised drop height (NDH)=0.85).....	157
Figure 6.48: Drop acceleration with SPH of the 25° wedge with side plates section for NDH=0.85 and mass number=0.29	158
Figure 6.49: Drop velocity with SPH of the 25° wedge with side plates section for NDH=0.85 and mass number=0.29	158
Figure 6.51: Pressure results at location P1 of the 25° wedge with side plates for NDH=0.85 and mass number=0.29	159
Figure 6.52: Pressure results at location P2 of the 25° wedge with side plates for NDH=0.85 and mass number=0.29	159
Figure 6.53: Pressure results at location P3 of the 25° wedge with side plates for NDH=0.85 and mass number=0.29	159
Figure 6.54: Pressure results at location P4 of the 25° wedge with side plates for NDH=0.85 and mass number=0.29	159
Figure 6.55: Drop accelerations of Incat1 section with normalised drop height (NDH)=0.86 and mass number=0.29 by Whelan [33]	160
Figure 6.56: Comparison of 2–D SPH simulations of the Incat1 drop section in various time steps (40,60 80, 90,100 and 110 ms) with experiments of Whelan [12, 33] (mass number=0.29 and normalised drop height (NDH)=0.86).....	162
Figure 6.57: Drop acceleration with SPH of Incat1 section for NDH=0.86 and mass number=0.29 .	163

Figure 6.58: Drop velocity with SPH of Incat1 section for NDH=0.86 and mass number=0.29	163
Figure 6.59: Drop acceleration with SPH of Incat1 section for NDH=0.77 and mass number=0.29 .	163
Figure 6.60: Drop velocity with SPH of Incat1 section for NDH=0.77 and mass number=0.29	163
Figure 6.61: Incat1 drop section with pressure transducers location	164
Figure 6.62: Pressure results at location P1 of the 25° wedge with side plates for NDH=0.86 and mass number=0.29	164
Figure 6.63: Pressure results at location P2 of the 25° wedge with side plates for NDH=0.86 and mass number=0.29	164
Figure 6.64: Pressure results at location P3 of the 25° wedge with side plates for NDH=0.86 and mass number=0.29	165
Figure 6.65: Pressure results at location P4 of the 25° wedge with side plates for NDH=0.86 and mass number=0.29	165
Figure 6.67: The clearance between the 3-D drop geometry particles and the tank open periodic boundary condition. The clearance should be sufficiently larger than the smoothing length (h) of the particles	167
Figure 6.68: Three-dimensional geometry modelling in SPH for Incat1 drop geometry in a full size tank.....	167
Figure 6.69: Three-dimensional geometry modelling in SPH for Incat1 drop geometry, the tank side walls are open periodic boundary condition, and the drop section and the tank bottom are dynamic boundary condition	168
Figure 6.70: Three-dimensional SPH modelling of Incat1 drop geometry. Water particles can slide into the wall clearance and move upwards	168
Figure 6.71: Comparison of the drop acceleration results of two and three-dimensional SPH modelling of INCAT catamaran with centrebow geometry (normalised drop height (NDH)=0.86 and mass number=0.29).....	169
Figure 0.1: Deflection of the centrebow because of flexibility of the transducer where the centrebow structure is assumed rigid.....	189
Figure 0.2: Aluminium block with threaded holes as dummy transducer.	190
Figure 0.3: The configuration of the asymmetric force, the dummy sensor and holding frames on HSM01 centrebow	191
Figure 0.4: Aluminium blocks and the holding frames of the mock up centrebow load measuring system	191
Figure 0.5: Measuring the deflection of the centrebow edge under asymmetric loading with a dial gauge. The centrebow was fixed upside down on aluminium frames.	191
Figure 0.6: Asymmetric load application and measuring locations on the centrebow.....	192
Figure 0.7: Displacement of centrebow edge in asymmetric loading conditions	193

Table of Tables

Table 2.1: INCAT Catamarans Specifications.....	25
Table 3.1: Three Centrebow Length Dimensions Designed for Experiments	42
Table 3.2: The Three Designed WPC Specifications with Various Tunnel Heights	44
Table 3.3: Tunnel Clearance of Three Different Model Tunnel Clearance Ratio Configurations in HSM02.....	44
Table 3.4: Load Capacity of MINI45 Force Transducer And Its Measurement Uncertainty (95% Confidence Level, Percent Of Full-Scale Load). The Calibration Is Done by The Manufacturer	51
Table 4.1: Elastic Links vertical Bending Moment Calibration Factors in Nm/Volts.....	64
Table 4.2: The Calibration Matrix for Forward Force Transducer	64
Table 4.3: The Calibration Matrix for Aft Force Transducer	64
Table 4.4: Loading Conditions and The Location of The Application Points (W:with; W/O:without).....	67
Table 5.1: HSM02 Model Particulars	75
Table 5.2: Wave Probes Calibration Factors and the Errors Involved in Three Days of Testing.....	76
Table 5.3: Calibration Factors and Errors of LVDT Motion Sensors during Three Main Test Dates..	77
Table 5.4: DAQ Card Set Up For Recording the Sensor Signals and Each Channel's Signal Conditioning Units.....	77
Table 5.5: Towing Tank Test Conditions for testing HSM02 Model	79
Table 5.6: The T-Value Of Student's T-Distribution For 95% Confidence Interval [113].	94
Table 6.1: The Reference Speed of Sound (C0) Calculated for Coefficients of the Speed of Sound (Ccoef) for 1 m of Still Water Level	130
Table 6.2: The Simulation Parameters for Conducting Particle Density Independency Study	139
Table 6.3: The SPH Simulation Parameters for modelling slamming of various geometries	149
Table 0.1: Stiffness Values of MINI45 Force Transducer.....	189
Table 0.2: Loading Conditions and Measuring Locations on The Centrebow. The Locations Are Shown in Figure 0.6.....	192

Publications Relevant to the Thesis

Reprints of publications which are relevant to the thesis have been included in plastic folders at the end of the thesis. The publications are as follows:

- Shahraki, J. R., Penesis, I., Thomas, G., Davis, M.R., Whelan, J. “Prediction of Slamming Behaviour of Monohull and Multihull Forms using Smoothed Particle Hydrodynamics” HSMV 2011 Conference Proceedings, 25 - 27 May 2011, Naples, Italy, pp. 1-10. ISBN 978-88-906112-0-9 (2011) [Refereed Conference Paper]
- Jalal Rafie Shahraki, Giles Thomas, Irene Penesis, Walid Amin, Michael Davis, Gary Davidson “Centrebow Design For Wave-Piercing Catamarans” FAST '13, 2 -5 December 2013, Amsterdam, Netherlands, (the Doi number or ISBN was not ready at current time) [Refereed Conference Paper]

1. Introduction

Catamarans currently have a wide range of applications for sea transportation including car and passenger ferries, pleasure boats and military vessels. Due to widely spaced demihulls they offer excellent stability and a large deck area, which is used for carrying passengers, cargo or other equipment depending on their particular application. Lightweight materials, such as aluminium and composites, provide these vessels options to travel efficiently at high speeds. However, passenger comfort, vessel operability and structural strength in waves are major issues which remain to be fully understood. The structural strength of catamarans becomes more critical as the size of the vessel increases and if the vessel operates at higher speeds or in harsher environmental conditions. Therefore, it is necessary to have a clear insight into the motions and environmental loads prior to designing a large high speed catamaran.

Due to the special configuration of catamarans, environmental load cases vary from conventional monohull vessels. Waves, depending on their direction and severity, can induce very large stresses on a catamaran's structure. Among various load cases, slamming is the cause of the largest structural stress induced on catamarans [1, 2]. The relative motions between the ship and water surface in large waves may be so large that the forefoot is exposed; a substantial impact or 'slam' occurs after re-entry of the body as the hull strikes the surface. These slam impacts may cause high local pressure and damage to the vessel structure [3]. The slam events are short in duration but can create a sudden high force. The relative angle between the body surface and the fluid is very important in regard to the slam magnitude; the smaller the angle, the higher the corresponding surface pressure and vessel deceleration [4]. A typical body plan of a conventional displacement catamaran section is presented in Figure 1.1.

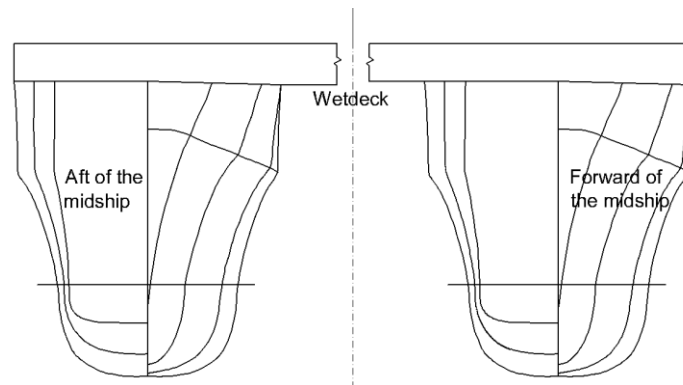


Figure 1.1: Typical conventional catamaran body sections

Slamming on ships is usually divided into bottom, bow-flare, breaking wave impact and wetdeck slamming based on its whereabouts on the structure [5]. For catamarans, bottom slamming and wetdeck slamming are of most concern. Bottom slamming, due to the narrow demihulls has less

impact in catamarans compared to wetdeck slamming. Local damage to the wetdeck structure and global damage can occur in rough seas due to severe wetdeck slamming in catamarans [2, 6]. As an example, Figure 1.2 shows the damage occurred to bow ramp and wetdeck structure of the 63m Ocean Lala in Taiwan waters in 2010 because of severe wetdeck slamming [7]. High frequency accelerations at both ends of the vessel could also cause problems for cargo lashing, machinery operations and human comfort [8]. Apart from the damage, slamming has been recognised as the primary reason for ship voluntary slowdown in adverse conditions in head seas and bow-quartering seas.



Figure 1.2: Ocean Lala, the catamaran ferry losing the bow structure from severe wetdeck slamming in Taiwan waters. The waves have damaged the front car ramp, cross deck structure, front bulkhead and gate. The lower right: the vessel before damage occurred (<http://www.chinapost.com.tw>, http://www.gov.cn/english/2009-07/16/content_1366854.htm)

Due to the nonlinearity of catamarans motions in high seas with respect to wave height and vessel speed, randomness of slamming events and the complexity of catamaran hull forms, designing catamarans to withstand slamming loads involves some uncertainties; especially for large high-speed wave-piercing catamarans where the design criteria are not yet clear or sufficiently accurate [9-11].

To avoid severe wetdeck slamming some designers tend to increase the height of the wetdeck to reduce exposure to wave impact on the wetdeck (such as Austal Ships). This could be a solution for smaller catamarans; however, it can cause practical problems, such as loading difficulties in ports for large vessels.

INCAT Tasmania is a world leader in building large high-speed Wave-Piercing Catamarans (WPC). As seen in Figure 1.3 for the 86m catamaran, the design style that INCAT has adopted is the use of centrebows and surface-piercing demihull bows, offering low wetdeck height and low drag. Narrow bow water-plane area and a low entry angle elliptical bow are the main characteristics of these special demihulls. They reduce the resistance at high speed and reduce of motions at high wave encounter

frequencies. However, due to their slender design, there can be insufficient reserve buoyancy in the bow region of the demihulls to resist large pitch motions; this has led to the introduction of centrebows. A centrebow is a volume in the vessel bow between the demihulls, protruding vertically downwards. As the vessel bow moves downwards in the waves, the centrebow acts as reserve buoyancy, reducing the motions. There are many large high speed catamarans in operation using this hull feature but little is known about the influence of the design of the centrebow.



**Figure 1.3: Condor Express, INCAT Hull042, an 86m car-passenger wave piercing catamaran (Barry Quince).
The centrebow can be seen between the two demihulls**

The University of Tasmania and the Australian Maritime College (AMC) have an ongoing record of collaboration with INCAT Tasmania and Revolution Design to investigate the performance of large high-speed catamarans. Previous work has included full scale measurements, fatigue analysis, numerical motion predictions, Finite Element analysis and model scale tests investigating the seakeeping, structural loads and slamming behaviour [6, 10-14]. The results of this collaboration have led to significant benefit for the industry partner.

It is proposed that several parameters such as tunnel height, demihull shape and centrebow shape, can affect the wetdeck slamming behaviour of large catamarans. To date these parameters have been developed based on the designers' experience or their perception of the phenomena. There has not been a systematic approach to designing for slam reduction due to a lack of information available about the effect these hull parameters have on vessel behaviour. For INCAT Tasmania, the issue of what configuration of hull form, specifically the centrebow shape and tunnel height required to improve seakeeping and reduce slam loads, has become particularly relevant. Hence, with increased knowledge of the effect of these parameters, the design of large wave-piercing catamarans could improve. This then raises an important question, what are the effects of different hull shapes (demihulls, centrebow and tunnel height) on the seakeeping and slamming behaviour of large high-speed catamarans at sea?

To answer this question, various existing hull forms of WPC's are exploratory analysed to identify the important hull parameters (variables) and their changing trends. Two methodologies are followed in this work to investigate the influence of these hull variables. The first method includes model development and experimental tests in towing tank. The second method involves numerical solution of the vessel hydrodynamics to better understand the phenomena and allow the evaluation of various designs.

Due to the importance of the slamming phenomena much work has been done to investigate this problem. Three methods have generally been used to investigate slamming: full-scale measurements, model scale experiments and computational analysis.

1.1. Full-scale measurements

Full-scale measurements are an important method for investigating slamming behaviour. Generally, in these experiments the motions of the vessel are measured using a gyro and/or accelerometers; strain gauges can be used to measure local or global structural stresses. The wave environment is usually measured using either an onboard radar system or a deployed wave buoy.

Several full-scale monohull vessel slamming experiments are reported in the literature some of which are outlined in Kapsenberg's [8] review paper on slamming. The probability of slamming, propeller emergence occurrence rates, structural stresses, Vertical Bending Moments (VBM) and slam pressure measurement were among the parameters analysed in these trials. For example, a relationship between the impact velocity and slam peak pressures was established by Ochi et al. [15]. One problem with full-scale trials has been the high uncertainties in measuring the incident waves. Methods of parallel measurements of the seaways such as using buoys and onboard radars are mostly recommended [5, 8]. The complicated instrumentation and finding the right slamming weather conditions in normal ship routes are reported as other big challenges in full-scale experiments.

Full-scale measurements of wetdeck slamming on a 30 m catamaran were undertaken by Haugen and Faltinsen [16]; accelerations, ship motions, wave conditions and hull strains were measured. The importance of the relative normal impact velocity between the wetdeck and the water surface, wetdeck angle, pitch angle and forward speed was identified. Wetdeck slamming events were characterised by large vertical accelerations with substantial vibrations in the hull girder. It was found that wetdeck slamming may occur even "when the vessel operates in sea states well below the operational limits given by the DNV rules". The vibration following a slam is called whipping and can reduce the fatigue life due to the increased cyclical loadings [3].

Full-scale experiments during the delivery voyage on an 86 m Austal high-speed catamaran were reported by Steinman, Fach and Menon in 1999 [17], with motions, wave heights and some hull strains being measured. The measured hull strain responses in slamming have shown an initial forced

impact followed by a strong backlash (excursion from the mean stress level in the opposite direction) then fluctuations with global mode structural response. Significant differences were observed between the design loads required by the classification societies and the full-scale measurements.

Full-scale tests were conducted by Roberts et.al [11] on an 81m and a 96m INCAT Wave-Piercing Catamaran (WPC) and the slam induced loads were found to be significantly larger than the global wave loads. The results of full-scale trials of an 81m INCAT wave-piercing catamaran were used by Yakimoff [18] in conjunction with a Finite Element (FE) model to investigate the fatigue life of these vessels. Whipping due to the slamming and its subsequent load strain peaks were identified to be the cause of 66% of fatigue damage in the vessel.

Thomas et al. [19] carried out full-scale strain and motion measurements on a 96m INCAT WPC to identify slam events. Slam events were characterised by structural loading, relative vertical velocity, heading angle and frequency of occurrence. The stresses in the hull structure due to slamming, were shown to be up to seven times greater than the underlying wave loads. It was also shown that the VBM from a severe asymmetric slam load could exceed the design maximum VBM from DNV rules for such vessels [2]. The difficulty with the analysis of these full-scale trial results has been the definition of the slam loads from the response of the vessels structure. The hull form is complex and it is not easy to use a straightforward formula for estimation of slam loads. Therefore, a FE model of the ship was developed to use the strain results of the full-scale tests for identifying slam loads. For this purpose, wave profiles were proposed for estimating global wave loads. An iterative process to determine a distribution for slam loads from full-scale strains in the FE model was adopted [2]. Similar measurements were conducted by Thomas et.al [6] on a 86 m INCAT wave piercing catamaran (Hull 042, Figure 1.3).

Amin et al. [14, 20, 21] completed quasi static FE analysis on a 98m INCAT hull strains in which he used a “reverse engineering” technique to estimate the slam loads. These loads then were applied to a FE model of the vessel and reasonable strain correlations were achieved. This process of deriving slam loads is difficult and can have large uncertainties due to the large range of possible load distributions.

Full-scale trials were conducted on Sea Fighter SFS-1 by Naval Surface Warfare Centre in 2007 [22] to characterise wetdeck slamming. A complex set of wave measuring systems were employed onboard including TSK radars (Doppler Effect radar correcting for ship motions), sonars and video cameras along with motion and acceleration sensors. The experiments were successful in identifying and synchronising encountered wave profiles, motions and acceleration responses in four slam cases. The results indicated that prior to all slam cases the demihull bows were out of the water. Also two consecutive high waves were necessary to cause a severe wetdeck slam. No hull strain or pressure measurements were reported in this work.

From all these full-scale sea trials and measurements, several practical and analytical issues have been identified:

- Complicated instrumentation and measurement processes are involved in acquiring data during sea trials, which makes these experiments expensive and time consuming.
- It is difficult to find the right seaway conditions for slamming to occur. The environmental factors cannot be controlled.
- The measurement of the encountered waves is difficult and has high uncertainties.
- It is difficult to collect pressure data on the hull as the owners/operators are reluctant to drill holes in the vessel's hull.
- The key difficulty is to relate the structural response of the vessel to slam loads. A complicated process using a Finite Element model can be used to obtain a load case in a "reverse engineering" process.
- It is not possible to easily investigate influence of hull form on slam behaviour.

These issues have led researchers to explore other methods to investigate slamming. Methods such as model tests or analytical/numerical calculations have been used for both load definition and response prediction.

1.2. Slamming model experiments

Model tests are widely used to predict motions and forces in marine applications. Physical models, replicating full-scale phenomena by means of dimensional analysis have provided great insight to the actual fluid or fluid/structure interactions. The main advantage in conducting scaled model tests is that the environmental conditions can be controlled and most of the required information can be captured by various instruments. Moreover, it is easier and cheaper to change the test parameters and model configurations for methodical analysis. In addition to gaining a good understanding of the phenomena, the results can be used for validating theoretical or numerical analysis.

1.2.1. Scaling laws

In the slamming problem, the use of Froude's similarity law is appropriate for model tests since the gravitational and inertia forces are the dominant forces in slamming [23]. The Froude number is v/\sqrt{Lg} where v is the velocity, g is the gravitational acceleration and L is the vessel length. This number is largely used where free surface and gravity waves are present.

The Reynolds number, vL/ν where ν is the kinematic viscosity of water, accounts for viscosity and inertia forces; however, it is not possible to achieve similarity at the same time as Froude number similarity. The flow around the model in slamming area must be turbulent to neglect Reynolds number similarity in the slam event: this is normally the case in catamaran wetdeck and centrebow slamming [1].

The oscillatory flow effects of the fluid are governed by Strouhal number fL/v where f is the frequency of flow oscillation and L is the characteristic length. Large pitch and heave motions or miniature flow oscillations around the slamming area can be investigated by similarities with this number. Thomas et al. [1] pointed out that considering the encounter wave frequency of the model and the ship, the Strouhal number similarity is satisfied.

The Weber number governs the effect of surface tension forces. This number is calculated as $\rho v^2 L / \sigma$ where σ is the surface tension and L is the characteristic length, typically the droplet diameter. The difference in surface tension forces between the model and full-scale can cause larger droplet sizes in the spray root of the model during slamming. However, since the inertia forces are significantly dominant and the sprays are not directly in touch with the structure, the Weber number effect is usually ignored in slamming model experiments [1].

Wetdeck and archway slamming in WP catamarans are associated with the formation of air pockets. Pressure and gas compressibility effects are proposed by Faltinsen [24] to be taken to account by similarity of Euler number, $p/\rho v^2$ where p is gauge pressure. This could be the case in tank sloshing problems; however, it is hard to experimentally achieve Euler similarity in slamming tests. Therefore, if the Froude number only is used, the model scale Euler number will be greater than the full-scale Euler number and this could lead to conservative full-scale loads [1].

Hydroelasticity effects are important if modelling structural loads and vibration measurements are part of the model tests. In this case, the natural modal frequency of the model and full-scale vessel are Froude scaled as $f_m = f_s \sqrt{L_m/L_s}$, where f_m and L_m are the model scale and f_s and L_s are the full-scale modal frequency and length respectively. To scale natural frequency of vibration, a different bending stiffness (k) may be used in the model. If structural stresses are to be scaled, then different materials/thicknesses may be used in model or full-scale to scale the bending stiffness [24].

There have been different techniques used for slamming model experiments. Drop tests are the most conventional with two-dimensional (2-D) vessel geometry sections dropped, either freely or by force, to the water surface and kinematics and dynamics of the event investigated. To account for three-dimensional (3-D) effects of ship slamming, full ship model tests have also been conducted in towing tanks or in wave basins

1.2.2. Drop tests

High decelerations, sharp pressure peaks and severe surface deformations make slamming a complicated and highly non-linear problem. To simplify it, drop tests have been conducted by many researchers. In these experiments, normally a simplified vessel section like a wedge or cylinder with a width is dropped freely or at constant velocity onto the water surface. The main benefit of conducting drop tests has been to provide validation data for the development of numerical methods.

Drop tests of wedges with various deadrise angles, wedges with asymmetric angles, 3-D wedges with forward speed, cylinders, cones, prisms, spheres, flat plates, parabolic panels, flying boats and realistic ship sections are all reported in the literature [15, 25-29]. Some experiments were conducted with rigid or with elastic plated sections. During drop experiments, kinematics such as accelerations, velocity and immersion of the section along with section wall pressures and surface deformations were recorded.

Wetdeck slamming phenomena was investigated through drop tests of a three beam stiffened flat plate by Haugen, Faltinsen and Aarsnes [30]. The plate was dropped onto the surface of calm water and also on to a regular wave surface with and without forward speed. The pitch angle of the plate and the drop speed was varied through the experiments. Measurements of pressures, wetted surface, acceleration, displacements and strains of the plate were conducted. It was found that the relative normal impact velocity is more important than the vertical relative velocity. Also the local hydroelasticity of plates are important in determining local pressures. Kvalsvold had modelled the flat wetdeck impact by a Timoshenko beam model and deflections and stresses of this beam was analysed based on the relative impact velocity [31]. His improved theory was validated by the experiments of Haugen, Faltinsen and Aarsnes.

Zhu and Faulkner [32] conducted three-dimensional drop tests of a SWATH-like (Small Water-plane area Twin-Hull) model to investigate the wetdeck slamming of twin hull vessels. The drop section consisted of two side plates, a flat bottom and an inclined section with deadrise angles between 0° and 20° . The worst case slam pressure occurred for 4° deadrise angles, clearly showing the effect of air entrapment under very low deadrise angle sections. The slam pressures were reported to be highly transient and the pressure peak magnitudes were less than any other previous wedge or flat plate experiments. The correlation between pressures and strains measured in the bottom showed that the wetdeck slam event is a dynamic problem and care must be given to not only pressure peaks but also their propagation under the wetdeck. The flat bottom showed highest strains on the wetdeck plating. The critical importance of wetdeck design was discussed in this work.

To simulate the slamming of catamarans, drop tests were performed by Whelan et al. [12, 33] for several bow configurations at the University of Tasmania. In this research a two-dimensional study of drop kinematics of WPC bow sections with centrebow were considered. Drop speed, pressure distribution and vertical acceleration were measured and high-speed cameras captured the surface deformation and spray roots. Two simple wedge sections, a flat wetdeck with two side plates, wedges with side plates and realistic catamaran sections with centrebows were examined. These drop tests made it possible to examine the effect of hull form change on slam pressures. The results confirmed that as the highest point in the archway between centrebow and demihulls moves vertically higher and further outboard, the further reduced is the pressure peak.



Figure 1.4: The drop test rig of Whelan in University of Tasmania [12, 33]. Catamaran sections with centrebows were free dropped into water tank

Despite the advantages of drop tests, these experiments are not capable of modelling full 3-D effects such as geometry, forward speed effects, dynamic vessel motions and global vibrations. Since there are very limited 3-D effects in these experiments, the accelerations and thus the forces acquired were found to be unrealistically high compared to full-scale results. Also, due to air entrapment, in 2-D drop tests a residual air cushion of a bubbly mixture moves under the closed section and softens the impact, whereas the ship's geometry and forward speed effects create a different situation in a three-dimensional case. It is therefore not recommended in the literature to use the pressures obtained in these tests directly for design purposes. Further, the global mode vessel hydroelasticity and vibrations are not taken into account in drop tests, even if local elasticity of the drop section surface is modelled. Therefore, full 3-D model experiments with the presence of forward speed in waves have been conducted by many authors. The following section overviews these 3-D slamming tests.

1.2.3. Towing tank model tests

Full ship model slam testing offers the opportunity to investigate slam behaviour with greater control of the environmental and operational conditions than is possible in full-scale trials. In addition the model may be more extensively instrumented and tested using more revealing techniques than a full-size vessel. These model tests are more realistic than the wedge water entry tests, since the 3-D geometry, hydroelasticity, forward speed and impact angle effects can be investigated. Among the uncertainties with these models are scaling effects and the inherent randomness of sea conditions: the scale effects are inherent to testing at model scale where similarity of important dimensionless quantities such as Reynolds and Froude numbers are difficult to maintain simultaneously. Also the environmental conditions are not controlled (inherently random) at full-scale; it is therefore not possible to fully replicate the slam conditions at model scale.

Ship model experiments involving slamming based on their objectives can be categorised into two groups: rigid models and hydroelastic models. Rigid models can be divided into full rigid models and rigid segmented models. In these models, the hydroelasticity of the ship is not modeled. Elastic models instead model the hydroelasticity of the ship, thus VBM and whipping vibratory effects could be modeled. Hydroelastic models also fall into two categories: continuous hydroelastic models and hydroelastic segmented models. All four groups are now reviewed and compared.

a. Full rigid models

These models are similar to conventional models used for seakeeping or resistance tests. A geometrically scaled model is built and tested in controlled wave and slamming conditions in a towing tank or model test basin. Forward speed and the 3-D effects of slamming are therefore accounted for. Encountered waves, vessel motions, acceleration and slam pressures are normally the measured parameters in these experiments. Finding slam occurrence rates, accelerations, slam pressures and slam kinematic characteristics are the main aims of these experiments.

There have been some slamming investigations on multihull vessels using rigid models. Zarnick et al. [34, 35] used a 1/32 scaled SWATH model in the David Taylor model test basin. Motion sensors and pressure transducers were employed and the model was tested in both regular and irregular waves. It was found that Ochi's [15] vertical velocity criteria for slam occurrence was not suitable for the slamming of these vessels; also Ochi's model for slam pressures could not be used for wetdeck slam pressures.

Tests were also conducted on a 1/15 scaled model of a high-speed 73m catamaran in the David Taylor Model Basin [36, 37]. The model was a waterjet-propelled fiberglass model complete with wetdeck and superstructure and flat plate pressure sensors were located under the wetdeck. One of the aims was to generate validation data for prediction tools such as the LAMP ship motion computation program [36]. In these model tests it was found that the maximum loads and pressures do not

necessarily occur in the forward most portion of the wetdeck. It was also noted that to properly model the wetdeck slamming pressures, it is necessary to model local structural deformation and vibrations since they will affect the peak pressures.

Although valuable information could be derived from these experiments; there are some deficiencies when investigating the influence of design parameters on slamming:

- There is no hydroelastic effect.
- There is no slam load measurement.

b. Rigid segmented models

In these models the vessel hull is divided into a number of longitudinal segments. The segments are connected together with a rigid beam to form the ship hull. Each segment is rigid and it attaches to the backbone beam via a load cell. Pressure gauges have also been used on the hull segments. These models have been used widely to validate strip theory formulations and differentiate the system of wave loads applied on the model. Because of having a strong backbone beam, these models could be built with a high number of segments and easily manufactured. The bow or stern segments could be easily swapped with new designs; also different backbone beams could be used [38].

There has been much work conducted with this type of model. For example the segmented model of Keuning et al. [39] had seven segments attached to a rigid girder via load cells. The model was equipped with a forced oscillating system to differentiate between exciting wave forces and radiated wave forces. Another example includes the container ship model reported by Kobayakawa et.al [40] which had eight segmented blocks connected to a backbone beam, equivalent to full-scale mid-ship section. Strain gauges measured strains on the internally located backbone beam measuring VBM between the segments. No severe slamming and whipping was reported from this work.

Although very valuable information could be derived from these experiments; there are some deficiencies if one needs to investigate the design parameters for slamming:

- These models do not replicate the proper hydroelastic behaviour of the full-scale vessel since they are not modelling global or local structural dynamics in slamming.
- The loading of the model structure is non-continuous and indirect because of segmentation [41].

The model is not capable of identifying hydrodynamic loading distribution, i.e. between the ordinary wave loads and the slamming forces [41].

c. continuous hydroelastic models

In order to measure wave loads and replicate the dynamic response to slamming, a hydroelastic model is required. Structural vibration modes should be correctly modelled and load measuring instruments are required.

If the model replicates the hydroelastic behaviour of the full-scale ship by its structure, it is called a hydroelastic continuous model. The weight distribution, the sectional rigidity and modal frequencies of these elastic models represent the full-scale vessel. Among the advantages of these models is that the loading is direct and continuous and there is no segmentation and problems with sealing rubbers in between segments. These models provide the possibility of obtaining much information such as VBM, shear force and torque at any cross section, stresses at the local hot spots and the local hydroelastic effects in slamming affected areas [41].

Examples include Aarsnes et.al [42] who built a monohull model using Divinycell foam and fiberglass/polyester resin. Geometrical similarity with the full-scale vessel was gained by accurately milling the foam and the stiffness was gained by laying fibre and resin inside the hull. FE model calculations were made beforehand for determination of the model shell thickness.

There are some disadvantages with this type of model;

- As the ship is thin-walled vessel, scaling the plating and stiffeners can cause practical issues.
- Repeatability and dependency of the model behaviour on material type used can be an issue [43].
- Building these models can be very expensive and time consuming [41].

d. Hydroelastic segmented models (HSM)

Hydroelastic segmented models have rigid segmented hulls and replicate the full-scale vessel fundamental modal frequencies. Full-scale flexural rigidity may also be replicated in these models. The model motions, wave induced loads and structural vibratory response of the vessel, due to severe slamming can be measured. Although less information can be gained from sectional loads compared to continuous models, there are distinct advantages with this type of model. Their construction is much simpler and new bow or stern designs could be implemented fairly easily. The model structure is robust and there is no dependency on the material used in the construction.

Among the disadvantages with HSM tests are the discontinuous and indirect loading of the model structure because of segmentation [41]. The loads between segments have to be transferred via a hinge or backbone beam. The problems with sealing the segment gaps also remain with this model type. Also local stresses in the structure are not measureable.

HSMs built so far have mainly used one of two designs; a continuous backbone beam responsible for elastic behaviour of the model or elastic hinges connecting rigid segments. The continuous backbone beams normally have varied sectional stiffness along the model to represent the correct ship stiffness. Strain gauges are installed on the beam between segments to measure the bending moments. The number of segments can be quite high without making the model too flexible: such models are described by Dessi et.al [44-46]. A 1/30 scaled model of the fast ferry MDV3000 with six segments and a 1/20 scaled patrol boat with six segment are the examples of his models. Identification of vibratory modes and the effect of forward speed on modal frequencies and damping factors are well presented in his work.

The second method uses rigid segments and connects the segments via load transducers in which the transducers themselves are acting as springs (hinges). The flexural rigidity and modal frequency of the full-scale vessel is represented via these elastic transducers. The elastic transducers can measure VBM, horizontal bending moment, vertical or horizontal shear force, axial loads or a combination of them. An example is the 1/28 model of MDV3000 fast monohull ferry by Kapsenberg and Brizzolara [47]. The model was constructed using plywood to have a stiff and lightweight hull. The model had two segments and a set of strain gauges in between to measure forces and moments. The elasticity of the model was then controlled by using different additional elastic inserts to the link. The slamming instrumentation consisted of pressure transducers and slamming panels in the forward segment. The slamming panels were scaled from the full-scale plating panels between stringers and had an accelerometer and a strain gauge to measure slamming forces and the average pressures on the panels.

Hermunstand, Aarsnes and Moan [48] designed and tested a 5m catamaran HSM which had two transverse cuts and two longitudinal cuts in which 5DOF load cells were installed to measure the model response due to wetdeck slamming. The three wetdecks were split from the demihulls via pin joints and vertical force sensors. There was a backbone beam in each demihull and they were connected with transverse beams in each segment. The three segments were then joined by 5DOF load transducers. Three elastic modes of the model were considered, vertical 2-node mode, pitch-connecting mode (the mode where demihulls rotate in pitch in opposite directions) and split mode (the demihulls rotate oppositely around their longitudinal axes). It was remarked by Ge et.al [49] that the 2-node mode in this model has the greatest influence on hydroelastic behaviour of the model in slamming.

Matsubara and Lavroff [50, 51] developed a 2.5m HSM of a 112m INCAT wave-piercing catamaran. The model has two transverse cuts, thus three rigid segments per demihull. The cuts were made at 40% and 60% of the length of the model from the transom and the segments connected via elastic links. An outline scheme of the model is presented in Figure 1.5. First modal frequency was achieved by tuning elastic links dimensions to 13.79Hz, which was close to the scaled full-scale natural frequency. There was no attempt to model any transverse modes such as lateral, pitch connecting

torsion or split mode. The model shell was built from a sandwich panel of carbon-fibre layers and Divinycell foam core. Over 2000 runs in waves have been completed with this model and its structure has shown good resilience in being exposed to harsh slamming conditions.

The centrebow was isolated from the demihulls to measure slam forces. Two transverse aluminium beams and elastic links equipped with strain gauges connected the centrebow piece to the forward segment demihull backbone beams. The schematic of the centrebow isolation technique is shown in Figure 1.6 in section view.

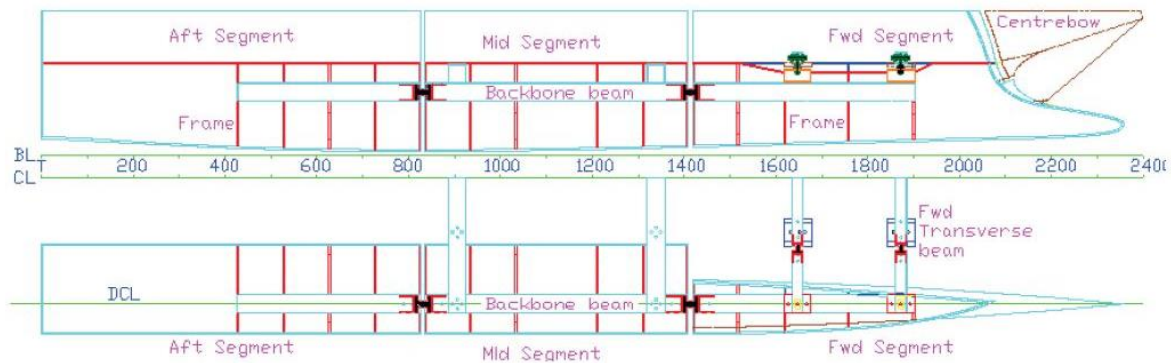


Figure 1.5: Profile and plan (starboard side only) view of 2.5m catamaran HSM [52]

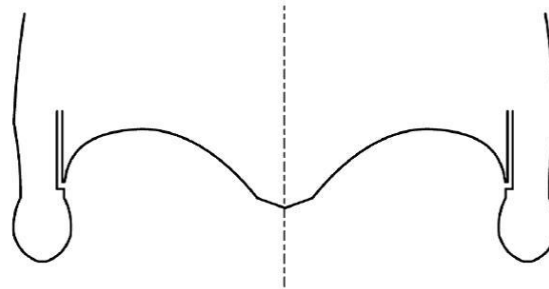


Figure 1.6: Schematic of isolation of the centrebow piece from the demihulls. Slam forces have been isolated and measured [52].

1.2.4. Experimental methods summary

Three main experimental methods of investigating slamming have been discussed. Full-scale trials, model scale drop tests and towing tank tests and the advantages and deficiencies of each method have also been discussed.

Drop tests are a useful mean for detailed pressure and flow observations on water entry sections. The main problem with the results from drop tests is the 2-D nature of these experiments give unrealistic pressure or force predictions. Therefore, application of the results of these tests and relevant theories are difficult especially in complex vessel sections such as WPC bow sections. More realistic results can be achieved through full ship model tests.

Among the ship model tests, the hydroelastic segmented model tests are more realistic, practical and useful than the other experimental techniques. The results of these experiments are useful in many

aspects such as defining slamming criteria, measuring motions, slam loads and VBM in slamming and whipping conditions.

Hydroelastic segmented model testing also offers the opportunity for investigating slam behaviour with greater control of the environmental and operational conditions than full-scale trials. In addition, the model may be more extensively instrumented using more revealing techniques than a full-size vessel. They are also more realistic than drop tests, since the geometry, hydroelasticity, forward speed and impact angle effects are properly represented and can be investigated.

1.3. Computational methods and slamming

Analytical and numerical methods in fluid dynamics primarily help to simplify, linearise, solve and predict a physical fluid phenomenon in details. Ship slamming is a relatively rapid and complex fluid-structure interaction problem for which various analytical and numerical methods have been employed to model. In this section the problem is divided into 2-D analytical and numerical solutions where each method is briefly overviewed. Finally 3-D transient methods are reviewed.

1.3.1. Analytical solutions for slamming

Analytical solutions try to find an exact (or semi-exact) solution for the simplified section impact problem. The majority of the analytical methods for predicting slamming use added mass theory which assumes that a mass of the fluid is attached to the object when it accelerates in a fluid. Von Karman [53] solved the wedge water entry problem by assuming that the added mass of the wedge is equal to mass of a cylinder with diameter of the submerged wedge beam. The details of the flow around the wedge were not considered in this work. Von Karman compared his results with seaplane landing experiments and fair agreement was achieved. Wagner [54] used potential flow and added mass theory together; he also accounted for the water upwash around the wedge surface. The pressure distribution around the wedge surface was then calculated by solving the velocity potential around accelerated section in the water. Bisplinghoff and Doherty [55] sought to analytically solve the constant speed water entry problem by the approximation of the drop section with equivalent known bodies. Hughes [56-58] presented an accurate semi-analytic method to solve the constant velocity wedge water entry problem. Satisfactory agreement with the experiments and other analytical methods were achieved.

Flat plate impacts have also been of interest from the time of the Von Karman since his wedge theory gave infinite pressure for zero deadrise angle. He recommended not using flat bottoms in seaplanes landings. Chaung [27] has used the added mass theory in combination with empirical data from drop tests to account for the trapped air underneath a flat plate or very low deadrise angle wedge. Elastic flat plate impacts were also the subject of theoretical investigations, as such those of Kvalsvold et al. [59, 60] and Faltinsen and Aarsnes [61] where the impact of hydroelastic wetdeck panels were

investigated. They used a Timoshenko beam impacting the wave surface to account for hydroelastic impacts. The strain results were compared to a set of flat plate (with stiffeners) drop experiments and reasonable agreements were found.

Korobkin [62] used potential flow theory for solving wetdeck slamming of trapped air underneath restricted wetdeck sections. He simulated a mixture of air and water piling up vertically between two vertical sidehulls to slam under the elastic wetdeck plates. His results were presented along with the experimental results of Kvalsvold et al. [59, 60, 63] and Zhu and Faulkner [32]. He concluded that having a fully bounded section should be avoided since it could lead to very high stress levels. Also solving the wetdeck slamming problem using theoretical methods is very hard due to inclusion of air.

1.3.2. Numerical solutions for 2-D water entry problem

Analytical solutions for 2-D slamming problems have proved to be complex and work only for limited conditions such as a small range of deadrise angles and are not able to appropriately handle air-inclusion effects. Therefore, Computational Fluid Dynamics (CFD) has been employed to solve this problem. CFD is a branch of fluid mechanics that uses numerical methods to solve problems that involve fluid flows. Computers are used to perform the calculations required to simulate the interaction of liquids and gases with surfaces defined by boundary conditions.

For this work focusing on wave-piercing catamaran slamming, because of the complexity of the slamming section geometry, finding the appropriate CFD method is crucial. There could be three stages of slamming in a catamaran section with a centrebow: demihull bottom slamming, centrebow keel slamming and wetdeck archway slamming as illustrated in Figure 1.7. The first two slam events disturb the surface and pile up the water from both sides toward the top of the archways. The piled up water meet at the archway top before the archway top reaches the undisturbed water datum. A large slam then occurs underneath the archway and then the mixture of water and air attempt to escape the section. Capturing all these phenomena in CFD with acceptable accuracy needs great attention and effort. The major methods used in slamming are briefly reviewed here.

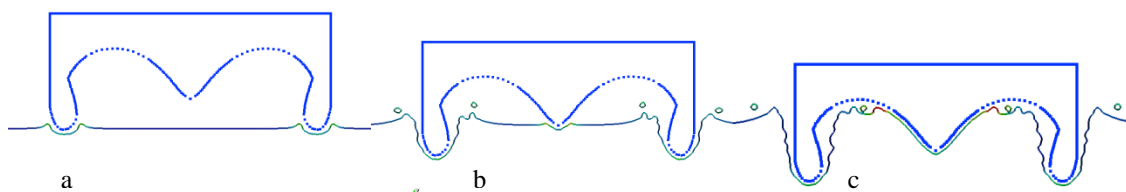


Figure 1.7: Three stages in slamming of wave-piercing catamaran with centrebow. (a) Bottom slamming; (b) centrebow keel slamming; (c) severe arch top slamming.

Numerical solutions to solve the complete boundary-value problem of Wagner [54] have been considered by several researchers such as Dobrovol'skaya [64] who used self-similar flows with conformal mapping to simulate the water entry problem of symmetric wedges at constant speed. The comparisons with analytical solutions were satisfactory. Zhao and Faltinsen [4] used boundary

element method and time matching technique to solve the Laplace equation of the constant speed wedge water entry. Their results were compared with results of Dobrovol'skaya similarity theory results. It is also shown in their work that for small deadrise angles, an asymptotic solution based on Wagner solution gives good pressure results. Xu et al. in 2008 [65] also used boundary element method for complex potential to solve the oblique water entry of asymmetric wedges. Three degree of freedom free fall of asymmetric sections to the water has also been solved by boundary element method by Xu et al. in 2010 [66] and the results have been verified by other numerical methods and some simplified experiments.

2-D Finite Difference methods to solve slamming problem were initially employed by Arai et al. in 1994 [67, 68]. A body fitted coordinate system along with the Volume Of Fluid (VOF) method to trace transient deformation of the surface was employed in his work. In the VOF method, a threshold of volume in a mesh cell is used to categorise a cell state between two phases of fluid (i.e. air and water). Fair agreement with other analytical and numerical methods and some drop tests were found.

The Finite Volume method is another CFD method which normally uses Reynolds Averaged Navier-Stokes Equations (RANSE) for simulations. There have been two main Finite Volume methods used to simulate the drop tests. One is the method of moving mesh (dynamic mesh) where the mesh of the domain around the wedge is attached to the surface of the section and moves with it. In each time step the moving mesh deforms as the section drops. When the mesh deformations become too large, the whole domain is remeshed. This procedure iterates until the section is fully dropped. The grid system is fixed to the free surface in this method. This method has been employed by authors such as Akimoto et al. [69]. Since the remeshing system is automatic and depends on section velocity and the time step, the mesh around the wedge can sometimes get too deformed and convergence problems arise. This method has also been reported to be very sensitive to setup parameters and having stability and convergence issues [70, 71]. Also large motions have been hard to capture with this method [70, 71] and this method is also high in computational costs.

The other technique for the Finite Volume method is called multi-reference frame system where the drop body is fixed to the grid and the free surface is moving toward the drop section. This method was applied by Hudson et al. [71] and various turbulence methods were used. Both air and water were simulated in this work. The pressure results were compared to the drop tests by Yeotto et al. [72] where good agreement was achieved in upright drop tests. This method requires a fine mesh in a relatively large area around the wedge section to capture the right surface deformation. Another difficulty with Finite Volume method is that spray roots are hard to capture because of the VOF definition of the free surface in which a volume fraction between zero to one of a mixture of air and water is set for identification of the free surface.

The Smoothed Particle Hydrodynamics (SPH) method has been used by various authors to solve free surface flows. SPH is a meshless Lagrangian method where the fluid domain is discretised as a number of particles [73]. This method was adapted from solar system simulations by Monaghan et al. [74-76]. These particles interact with neighbouring particles in an effective kernel diameter using continuity equations. Normally the equation of state represents a weakly compressible fluid by relating density to pressure for each particle. Among the advantages of this method are its robustness and its capability of capturing large deformations of the fluid and free surface since the particles are free to move around. Various complex free surface problems such as dam break, sloshing, drop experiments and wave run-ups have been successfully simulated using SPH [77-81]. SPH is noted as one of the very promising CFD methods for slamming research by Kapsenberg [8] in 2011 in his review of slamming in ships.

The wedge water entry problem has been simulated by SPH by several authors. For example, Oger et al. [82] included simulation of an imposed velocity drop test, a 1DOF wedge free fall and 3DOF wedge drop. This work showed excellent agreement with experiments for free fall wedge simulations. Brizzolara et al. [83] and Viviani et al. [84] included comparison of various CFD approaches to wedge water entry problem. It was concluded that the Finite Volume method and SPH have performed best across a range of simulations among other methods. Some real vessel sections such as a frigate bow section and a catamaran section were simulated via SPH by Veen et al. [85]. Not very satisfactory results were achieved for the more complex sections with convex forms such as the frigate bow section with a bulbous bow. Veen et al. [86] also combined the 2-D drop simulations with a strip theory to create a single 3-D slam event for the frigate.

SPH is a relatively new method which is capable of modelling violent flows involving complicated sprays and large fluid deformations. In the present work it was decided to use SPH for simulating slamming of catamarans with centrebows mainly for three reasons: first, generation of input data is faster compared to other conventional methods [82, 84, 87]. Secondly, large surface deformations and sprays are better captured with SPH because of its meshless nature compared to other grid based methods [8, 82-84]. Thirdly, the involvement of Graphic Processing Units (GPU) technology with high computational abilities in SPH simulations has made the method a lower cost option among other methods which are not yet fully integrated with this technology [77, 88, 89]. New particle neighbour searching techniques and new parallelisation techniques are also boosting the speed of simulations with SPH. The open source software SPHysics and Dual-SPHysics from a joint European-based research group is chosen to be used for the simulations in the present work [77, 88, 89].

1.3.3. Numerical 3-D ship slamming problem

Ship slamming is a 3-D event that occurs in waves with forward ship speed. Hence, to simulate this complex event by only 2-D drop tests naturally introduces large questions about relevance and

accuracy. Analytical or numerical investigations have therefore moved toward 3-D either by integrating 2-D results in vessel length (strip theory methods) or by direct fully 3-D simulation of the ship.

Rigid body motions by full 3-D CFD methods have also been performed more recently by various methods using various software packages. 3-D BEM solvers or panel methods such as ANSYS-AQWA have been used on offshore vessels successfully. This method however, is valid only for low Froude numbers [90]. The LAMP program [37] is another example of the 3-D panel method solvers which is also used for catamaran wetdeck slamming simulations.

Marcet et al. [91] suggest using a linear frequency domain or time domain method to predict the motions, then to select critical situations based on slamming criteria (such as relative vertical velocity), run a CFD code to predict the pressures and input these results to an FE model for hydroelastic structural response prediction.

Kapsenberg, Thornhill and Sames [92, 93] have used a 3-D VOF method to predict motions of the vessel and calculate the slam loads on the bow section in waves. Although they could not simulate properly steep waves and also waves with a length comparable with the ship length, the ship motions and number of slams on the bow visor were captured well. Wave propagation in time and problems with damping in the fluid domain end were reported to be key difficulties in these simulations. The bow section loads achieved by integrating the pressure matched fairly with experiments. Mousaviraad [94] have calculated RAOs of a vessel in waves by 3-D VOF method with their RANSE solver called CFDSHIP-Iowa. No validation study was reported.

3-D simulations with SPH have been recently performed by the joint works of ECN and HydroOcean in Nantes (France) on various naval applications [95]. Novel methods have been used to overcome numerical instabilities, the SPH scheme inaccuracies and high computational costs. The method has been tried on various cases such as a 2-D ship deck wetness problem, sphere impact case and a life boat drop. The results, however, show that for better resolutions in these cases, high numbers of particles are necessary for simulations.

In summary, SPH is not as developed as FVM methods for fully 3-D applications; however, it is increasingly being used for naval applications including slamming events. The new computing technologies with the implementation of GPU computational abilities have given a boost to 3-D SPH simulations. In 2-D though, it has shown good advantages over other numerical methods due to its Lagrangian nature.

1.4. Thesis arrangement

Concluding the above review of the slamming problem of large high-speed catamarans, it is evident that hull form, especially bow shape, can have a substantial effect on the seakeeping and slamming

behaviour of these vessels. Reviewing the slam investigation methodologies proposes the benefits of hydroelastic segmented model testing and also the use of SPH as a promising computational model. Therefore, work in this thesis aims to answer the following research questions:

- What are the effects of different hull shapes on the seakeeping and slamming behaviour of large high-speed catamarans at sea?
- What effect does changing the bow shape have on the magnitude of the slam loads (both vertical and horizontal components) and vertical bending moment?
- Can SPH be used to simulate the slamming of catamaran hull shapes and accurately predict the slam loads for different geometries in both two and three-dimensions?

To approach these research questions, a research methodology was developed. The thesis structure follows this methodology as outlined below.

Chapter 1 has highlighted the definition of the problem and provides a review of previous work; following on, in Chapter 2, a practical insight is provided on existing large wave-piercing catamarans to understand the influence of hull form features on slamming behaviour. The approaches of pioneers in this field, such as INCAT Tasmania and Austal Ships in designing hull forms for slamming are discussed. Two hull form parameters of the wave piercer bow configuration, the tunnel clearance and centrebow length are identified to be important for further investigation.

In Chapter 3, the design of a hydroelastic segmented model to investigate the effect of various hull forms on slamming and seakeeping behaviour of large wave-piercing catamarans is presented. Lessons learnt from a previous hydroelastic segmented model built in AMC were applied to the new model. A 2.5m scaled model of the INCAT 112 m catamaran was designed including the effect of tunnel clearance and longitudinal distribution of centrebow volume. The construction, instrumentation and calibration of the model are presented in chapter 4.

The experimental test program took place in late 2011 in the AMC towing tank facility. The results of the hull motions and loads acting on the hull segments and centrebow were measured in regular waves in head-seas and are reported in Chapter 5. The responses of the vessel and its structure were extracted from the model instrumentation, processed and plotted against various wave environments in the towing tank. In total, three centrebow length configurations at one wave height and one vessel speed were tested and the results are presented at model scale and also in non-dimensional forms for full-scale usage. Insight into the recorded slam forces and the centrebow inertia effects reveals new knowledge on the slamming mechanism of the centrebow. The implications and relevance of the test results for the industry are discussed at the end of this chapter.

To investigate the slamming behaviour of various hull forms numerically, water entry simulation of catamaran sections in SPH were undertaken and are reported in Chapter 6. First, simple wedge

geometries in 2-D were simulated and validated with published experimental results. The technique is extended to consider the full catamaran bow section with centrebow. The applicability of using SPH over conventional water entry techniques for more complex shapes such as catamaran's bow slamming is discussed. At this stage, this approach ultimately aims to find a shape in the bow which leads to lower local pressures and smaller vertical slamming forces.

Finally, Chapter 7 outlines the outcomes and conclusions of this research with recommendations for industry and further research.

2. Wave-piercing catamarans hull form and slamming: an exploratory study

Large high-speed catamarans are relatively novel craft and there is not a large database of designs for designers and classification societies to use to make clear design judgments. In Australia, INCAT Tasmania and Austal Ships have been the world's pioneers in building large high-speed catamarans and a review of their different approaches to design for improving seakeeping performance and minimising wave loads is presented here. An exploratory approach is taken by looking at the major vessel characteristics and the evolution of the designers' approach to this problem.

2.1. High tunnel clearance approach to catamaran design

Austal Ships and STENA have developed semi-SWATH hull forms and Z-shape demihull bows [96]. The water plane area is minimised to reduce motions in high frequency waves. The Z-shape bow makes a fine entry to reduce hull resistance and also provide reserve buoyancy in forward part of the ship. Figure 2.1, shows the Z-shape bows in a 41 m Austal catamaran. There is a mild flare above the water line in the forward half of the demihulls, allowing the reserve buoyancy to act against large pitch motions. Due to the slender demihulls, the vessels can experience high pitch motions in large waves and wetdeck slamming could occur. A high tunnel clearance and a mild longitudinal curvature in wetdeck profile are the measures taken to mitigate this undesired phenomena (tunnel clearance is the relative distance between the wetdeck and calm water level at the design waterline; see Figure 2.3). By increasing the wetdeck height it is expected that in the severe sea conditions the water surface will not impact the wetdeck to initiate large slam events.



Figure 2.1: Trinidad and Tobago 41m Water Taxi built by Austal Ships. The Z-shape demihull bow and high tunnel height is of some important features of these catamarans (www.Austal.com).

There are drawbacks to this approach, particularly for large catamarans, since increasing the height of the wetdeck to avoid slamming can create practical complications. Loading and discharging Ro-Ro cargo and passengers where the cargo deck is high compared to the wharf level can mean that a heavy ramp should be fitted to the vessel or complex infrastructure installed on the wharf at each point. Structural complications also arise from high demihulls, since to account for split and pitch connecting moment loads in oblique seas, additional strength is needed in the cross deck structure which will increase the overall vessel lightship weight and limit the cargo carrying space. High demihulls themselves also increase the vessel's lightweight without producing useful cargo space. The crew of these vessels should also be well experienced in the determination of when to slow down in high seas to avoid slamming, since serious damage could occur if the flat wetdeck is designed for less severe impact pressures.

2.2. INCAT approach to catamaran design

INCAT Tasmania and Revolution Design Pty Ltd use a different strategy to account for seakeeping and wave loads. Various demihull bow shapes have been used by INCAT: conventional bow shapes, sharp-edge elliptical bows and semi-oval wave-piercing bows. An example for each of these bow types is shown in Figure 2.2. The difference between the sharp edge and the semi-oval wave-piercing bows is the underwater shape. In INCAT's more recent catamarans, the demihulls commence with a relatively long semi-oval volume that is mainly underwater in the bow that pierces the water and encountered waves leading to both low resistance and low wave impacts on the demihulls. These stretched demihulls provide extra forward buoyancy to achieve the designed trim condition.

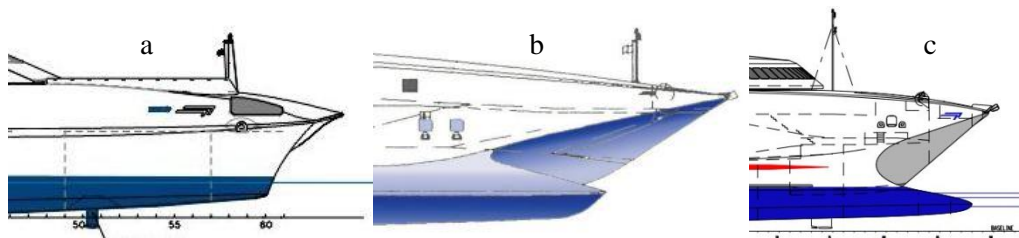


Figure 2.2: INCAT large catamarans demihull bow shapes. (a) conventional demihull bow (INCAT K-class); (b) sharp elliptical demihull bow (waterline below the tip – 78 m WPC); (c) semi-oval surface-piercing bow (waterline above the tip – 112 m WPC); (www.incat.com.au).

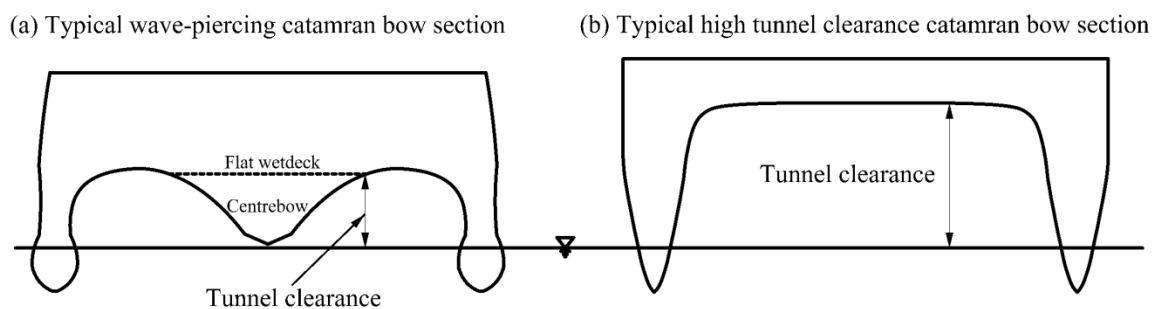


Figure 2.3: Typical bow profiles of WPCs and conventional catamarans. Narrow water-plane area of demihulls, low tunnel clearance and centrebow are the main characteristics of INCAT large WPCs.

A photo of an INCAT 112 m WPC is shown in Figure 2.4. Over time, the vessel lengths have increased in new INCAT designs mainly to increase payload and improve seakeeping behavior. Table 2.1 shows a summary of the INCAT-built catamaran lengths and displacements that are referred to in this chapter. Note that the 125 m and 130 m WPC (118.8 m and 123 m demihull length) are in the concept design stage; also SFM in this table stands for the designer Stuart Freizer Marine.



Figure 2.4: Natchan Rera, INCAT 112 m wave-piercing catamaran (www.INCAT.com.au) showing the fine entry demihull bows and the centrebow

Table 2.1: INCAT Catamarans Specifications

Vessel name	Length Over All	Demihull Length (DL)	Displacement
SFM 27m WPC	27 m	26.00 m	-- tonnes
SFM 29m WPC	29 m	28.77 m	-- tonnes
SFM 40m WPC	40 m	39.60 m	-- tonnes
74m WPC	73.6 m	61.45 m	-- tonnes
78m WPC	77.46 m	64.90 m	-- tonnes
81m WPC	81.15 m	67.30 m	-- tonnes
85m WPC	84.64 m	80.34 m	-- tonnes
86m WPC	86.62 m	76.70 m	-- tonnes
91m WPC	91.3 m	81.54 m	-- tonnes
96m WPC	95.47 m	86.3 m	-- tonnes
98m WPC	97.22 m	92.40 m	-- tonnes
112m WPC-Overload	112.6 m	105.60 m	-- tonnes
112m WPC	112.6 m	105.60 m	-- tonnes
125m WPC (concept)	125 m	118.80 m	-- tonnes
130m WPC (concept)	130 m	123.60 m	-- tonnes

-- Deducted due to commercial sensitivity

In these surface-piercing catamarans, the demihulls are characterised by having little reserve buoyancy (small water plane area) above the waterline in the bow area as illustrated in the bow

section in Figure 2.3. As the small water plane area reduces the vessel response to local water elevations, this feature helps to reduce the motion response to high frequency waves.

2.2.1. Tunnel clearance

INCAT wave-piercing catamarans tend to have relatively low tunnel heights compared with conventional catamarans. The INCAT wave-piercing catamarans tunnel clearances were compared with the DNV guideline for no slam condition tunnel clearance as detailed by Equation (2-1):

$$H_L = 0.22L(0.3 - \frac{0.8}{1000}L) \quad (2-1)$$

in which H_L is the necessary vertical clearance from the waterline to the load point (wetdeck) to avoid slamming for catamarans and L is the vessel length. Figure 2.5 is a comparison of INCAT catamarans tunnel clearance and the DNV guideline; noting that these tunnel clearance values are for mid ship and longitudinal upward archway curves of the bow of these vessels are not considered.

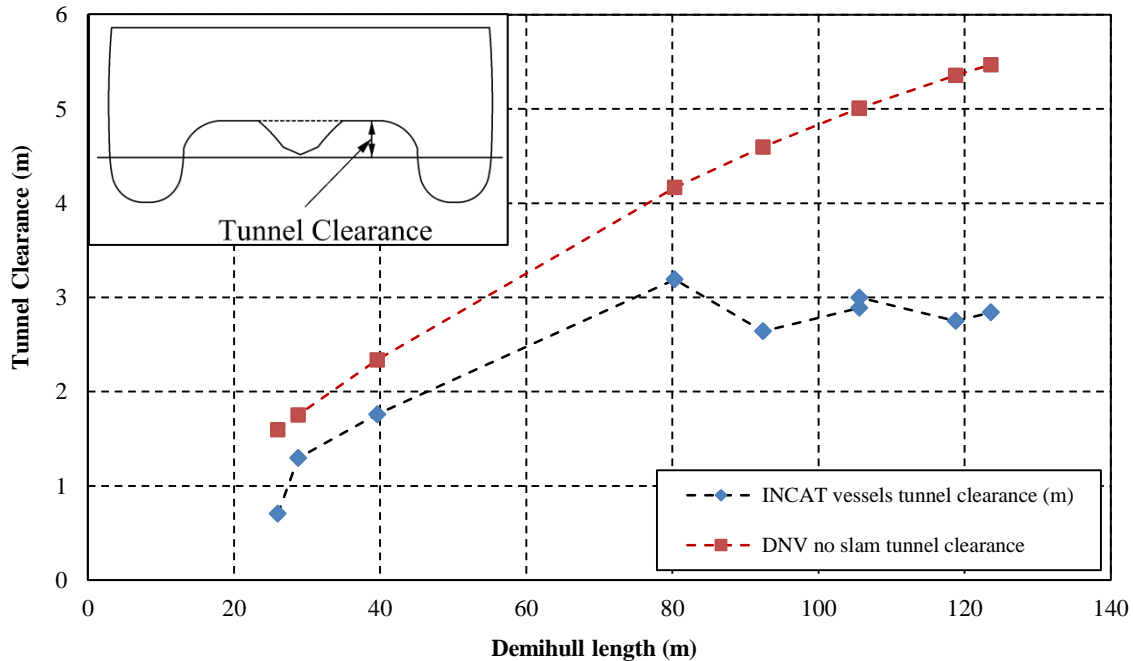


Figure 2.5: Tunnel clearance of some of INCAT catamarans and DNV recommendations. INCAT catamarans have lower tunnel clearance

The tunnel clearance, as shown in Figure 2.5, has increased with increasing demihull length up to 80 m and then it has tended to remain relatively constant for larger vessels. The main reason for limiting the tunnel height has been the practical considerations: having too high a tunnel will increase the height level between the wharf and the vehicle deck, meaning either a special wharf needs to be built or a large ramp installed on the ship. This is a very important consideration for reducing operational costs [97]. Another reason for selecting mainly low tunnel heights could be that in larger catamarans, the tunnel clearance is high enough compared to the design sea states, which are mainly less than 5 m significant wave height. The 30% to 100% difference between the vessel's tunnel clearance and the

DNV guideline especially for larger vessels also could be justified by the fact that these wave-piercing catamarans are not conventional catamarans.

Normally, the cross deck structure in large INCAT vessels has two or three decks with no major longitudinal or horizontal bulkheads, facilitating the easily accommodation of trucks and cars. The decks are predominantly supported by vertical cross bracing manufactured from steel square sections. Keeping the tunnel height low increases the cargo volume. However, it has some structural implications such as reduction in vessel longitudinal strength due to the reduction in sectional second moment of inertia. This problem could be somewhat mitigated by using different structural design systems such as having raised side shells especially in the mid-ship region, having continuously plated upper decks over the whole length of the vessel and cross bracing in decks under the superstructure to increase vessel longitudinal bending strength. A hybrid of plating and cross-bracing system could have the best results for both longitudinal and torsional strength [10].

2.2.2. Centrebow

Although a small water-plane area results in reduced motion in high frequency waves, this can lead to low pitch motion stiffness. There may be insufficient reserve buoyancy to stop the vessel from experiencing large pitch motions, especially in following seas where deck diving could occur. To counteract deck-diving a centrebow has been introduced, acting as extra reserve buoyancy at the bow of the vessel. The wetdeck is also modified in the fore part of the vessel with an upward slope towards the bow giving increased bow tunnel clearance. This results in two arch-shaped tunnels between each demihull. Longitudinally orientated hard chines are also used on the centrebow to direct displaced water sideways in the early stages of an impact. The centrebow keel profile is designed to remain out of the water under calm conditions and thus to reduce calm water resistance. However, the keel is close enough to the water surface for a fast response to large encountered wave motions. The side profile of the demihull upper bow edge and the centre bow outer edge makes a jaw shape curve which is referred to as the jaw-line.

Each INCAT wave-piercing catamarans has a unique centrebow shape and volume. Figure 2.6 shows the trend of the change of the centrebow volumes as length has increase for these vessels. The centrebow volume is defined here as the volume contained between centrebow surface and the extended horizontal flat wetdeck plane (see Figure 2.8).

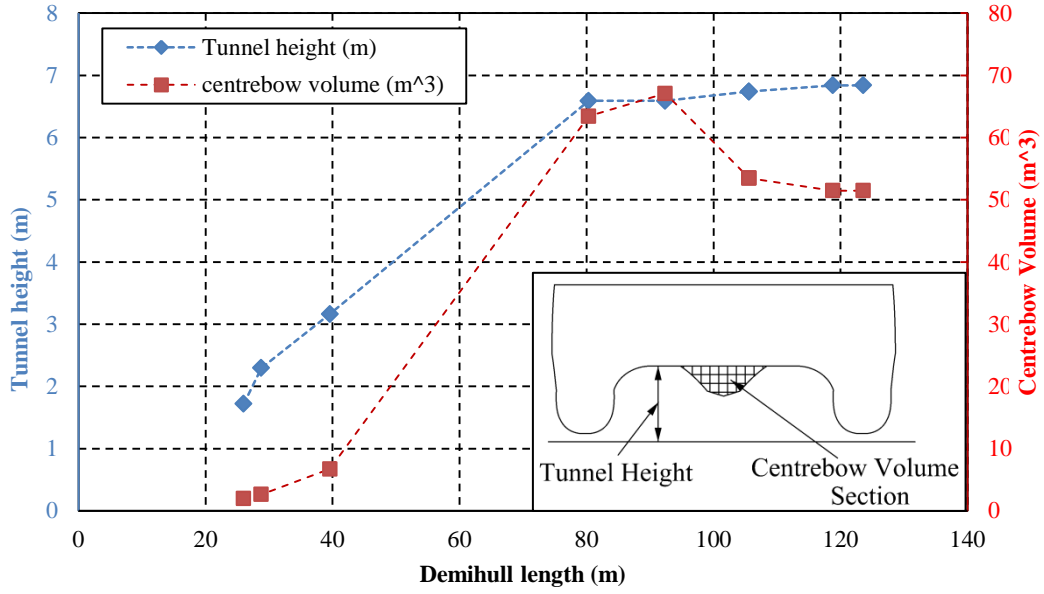


Figure 2.6: Evolution of the centrebow volume in INCAT wave piercing catamarans.

Figure 2.6 shows that the centrebow volume has not increased linearly with vessel length. It has increased in proportion to the vessel size, up to a demihull length of 85-98 m, then it has decreased slightly to be approximately constant for larger catamarans. The reason for effectively shortening the centrebow in larger catamarans will be discussed in the following sections. If the centrebow volume and tunnel clearance are non-dimensionalised respectively by demihull displaced volume and demihull length, the trends appear as shown in Figure 2.7. The ratios are defined as Equation (2-2) and Equation (2-3).

$$\text{Tunnel Clearance Ratio (TCR)} = \frac{\text{Tunnel Clearance}}{\text{Demihull Length}} \quad (2-2)$$

$$\text{Centrebow Volume Ratio (CBVR)} = \frac{\text{Centrebow Volume}}{\text{Demihulls Volume (V)}} \quad (2-3)$$

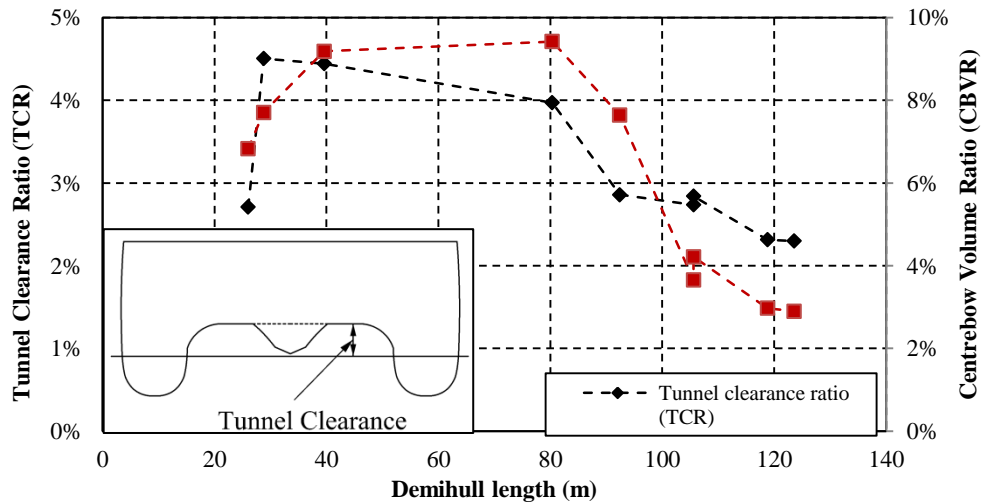


Figure 2.7: Tunnel clearance ratio (TCR) and centrebow volume ratio (CBVR) for INCAT wave-piercing catamarans versus demihull length.

It can be seen in Figure 2.7 that the centrebow volume tends to increase with demihull length for lengths less than 40m and then decreases after 85 m LOA. The centrebow volume ratio in the 85m WPC is 9.4% and reduces dramatically to 2.8% as the vessel length increases. The TCR however, tends to stay within a smaller range between 4.5% and 2% for all vessel lengths. As with the CBVR, the TCR tends to decrease from 4% in the 85m WPC down to 2.2% in the larger vessels. It can be concluded that the larger is the TCR, the larger the centrebow volume becomes. This is because the centrebow volume has to increase to fill the higher tunnel clearance as the centrebow keel remains close to water surface.

2.2.3. Reserve buoyancy

During severe bow down pitch motions, the forward half of the demihulls volume and the bow cross structure volume provide the necessary restoring buoyancy force to resist the downward pitch in conventional catamarans. The centrebow volume adds substantially to this reserve buoyancy in WPCs. A reserve buoyancy indicator (RBI) is defined in Equation (2-4) where the referred volumes are illustrated in Figure 2.8. The RBI with and without centrebow of some INCAT WPCs have been plotted against the demihull length in Figure 2.9.

$$\text{Reserve Bouyancy Indicator (RBI)} = \frac{\text{FWD demihulls volume} + \text{centrebow volume}}{\text{vessel displaced volume (V)}} \quad (2-4)$$

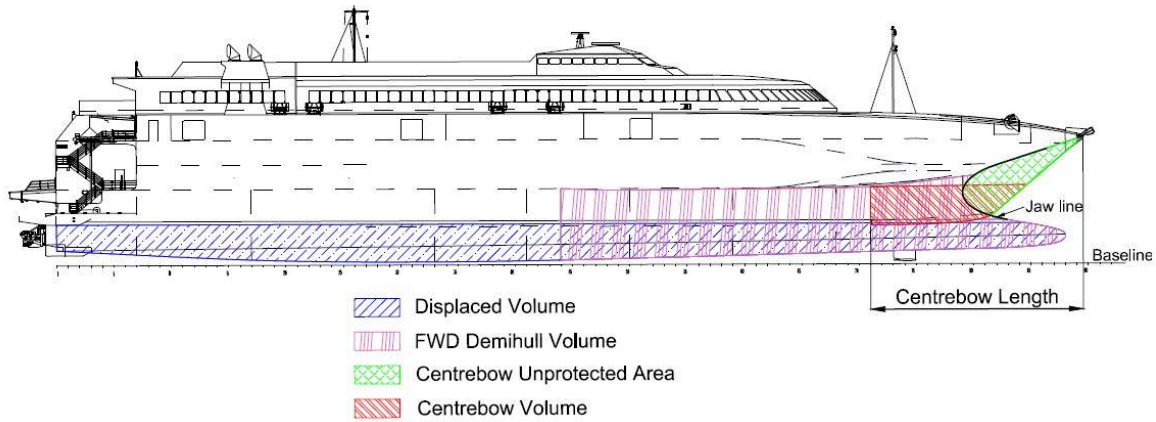


Figure 2.8: INCAT 112m wave-piercing catamaran; the forward demihull volume, centrebow volume, unprotected area and the centrebow length definitions are illustrated.

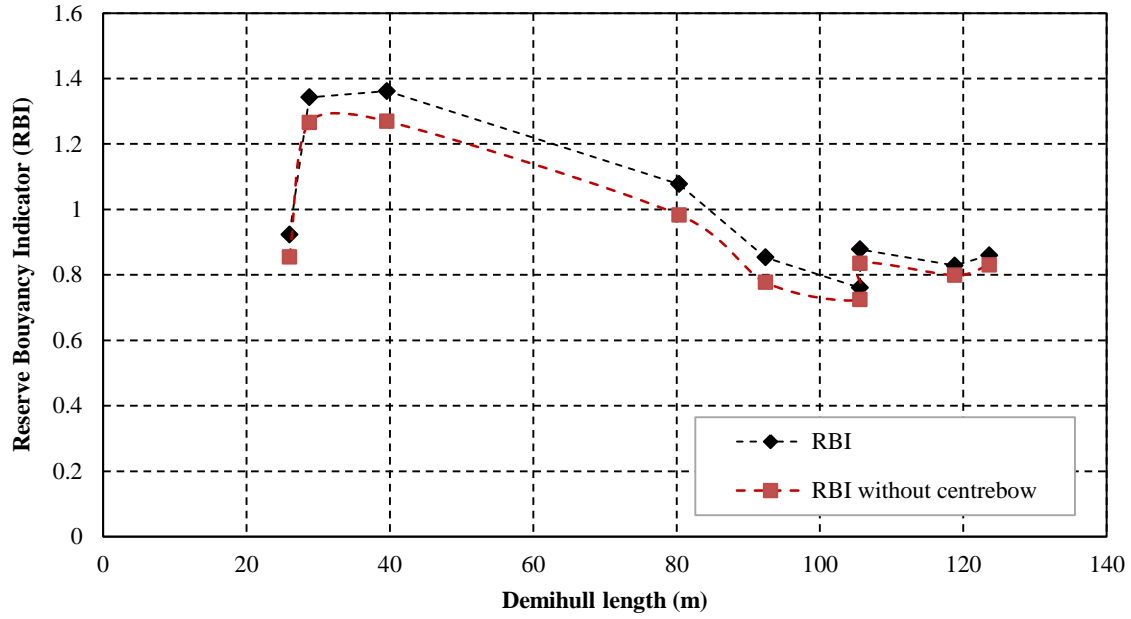


Figure 2.9: Reserve buoyancy indicators of INCAT wave-piercing catamarans versus demihull length.

It can be seen in this graph that for vessels greater than 30 m, the RBI has a general trend to reduce and remains approximately constant for vessels more than 90 m in length.

Recent designs such as the 85 m, 112 m and 130 m high-speed WPCs have raised several design questions. These new vessels have different tunnel heights and centrebow shapes; however, there is insufficient knowledge about the real effects of these variations on vessel behavior at sea.

2.2.4. Centrebow length

In larger INCAT WPCs, the centrebows are usually truncated at their largest sectional area within the forward third of the vessel. In this work large WPCs are of key interest, so the centrebow length is defined as the distance between vessel cross-deck's most forward point (centrebow most forward tip) and the centrebow aft truncation as illustrated in Figure 2.8. To have a dimensionless value the Centrebow Length Ratio (CLR) is defined as Equation (2-5):

$$\text{Centrebow Length Ratio (CLR)} = \frac{\text{Centrebow Length}}{\text{Demihull Length}} \quad (2-5)$$

As shown in Figure 2.10 the centrebow length has tended to reduce as the vessel's length increases. Among the available data, the 81 m WPC has the highest CLR of 37%; it reduces down to 18% in the 130 m concept WPC. This reduction in centrebow length follows the decrease in the centrebow volume for larger vessels. It could be argued that the longer centrebow should reduce motions more and prevent severe wetdeck slamming. However, the precise effects of the centrebow length are unknown.

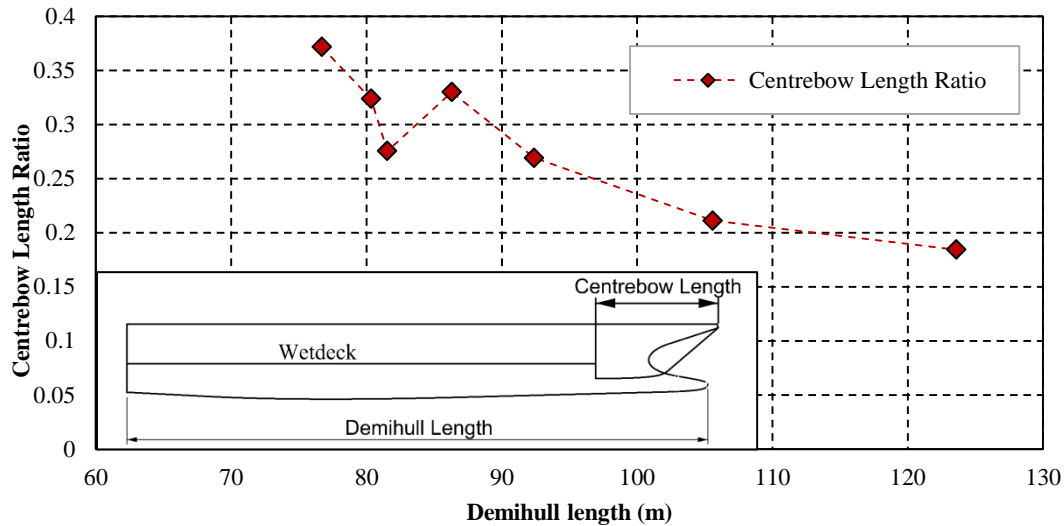


Figure 2.10: INCAT wave-piercing catamarans centrebow length ratio versus demihull length.

2.2.5. Centrebow unprotected area

As the centrebow enters water in bow down motions, the water runs up the sides of the centrebow. When this displaced water reaches the centrebow side knuckles ahead of the jaw, it deflects outwards like a jet flow, passes over the top of the demihull bow sections and does not get restrained by the demihulls. This water does not contribute in severe wetdeck slamming. The unprotected area of the centrebow is defined as the projected area of the centrebow in profile view which is not covered or protected by the demihulls (i.e. that region which is ahead of the jaw, see Figure 2.8 and Figure 2.11 for unprotected area). In protected areas i.e. between centrebow and demihulls, the upwash from both the centrebow and demihulls become restrained within the enclosed arch area where severe arch top slamming could then occur. Therefore, there can be significant differences in slam pressures in protected and unprotected areas. For example, Lloyd Register of Shipping design guidelines for special service crafts [98] recommends that the slam pressures in unprotected areas can be taken as half of the pressure values in protected areas. Having more exposed area or unprotected area in the centrebow may be a mechanism to reduce slamming loads. Having the centrebow extending more forward ahead of the demihulls or having wider open jaws are the possible approaches to reduce protected areas of the centrebow.

Various centrebow shapes with different unprotected area have been incorporated into the design of WPCs. Figure 2.11 shows the difference between unprotected areas of the centrebow in designs of the 78 m INCAT WPC, the 112 m INCAT WPC and the 95 m AMD1800 WPC. In the 78 m WPC, a large volume of the centrebow is located outside demihulls protection, whereas the centrebow is mainly protected in the 112 m WPC design. In the 95 m WPC (designed by Advanced Multihull Designs, AMD Australia) the jaw is moved a long way aft so as to let the displaced water escape sideways across the top of the demihull bow sections (<http://www.amd.com.au/designs>). For large high-speed catamarans, AMD have used both high tunnel height configuration and WPC with

centrebaw. The distinct difference between WPCs from INCAT and AMD is the unprotected area which is much larger in AMD designs.

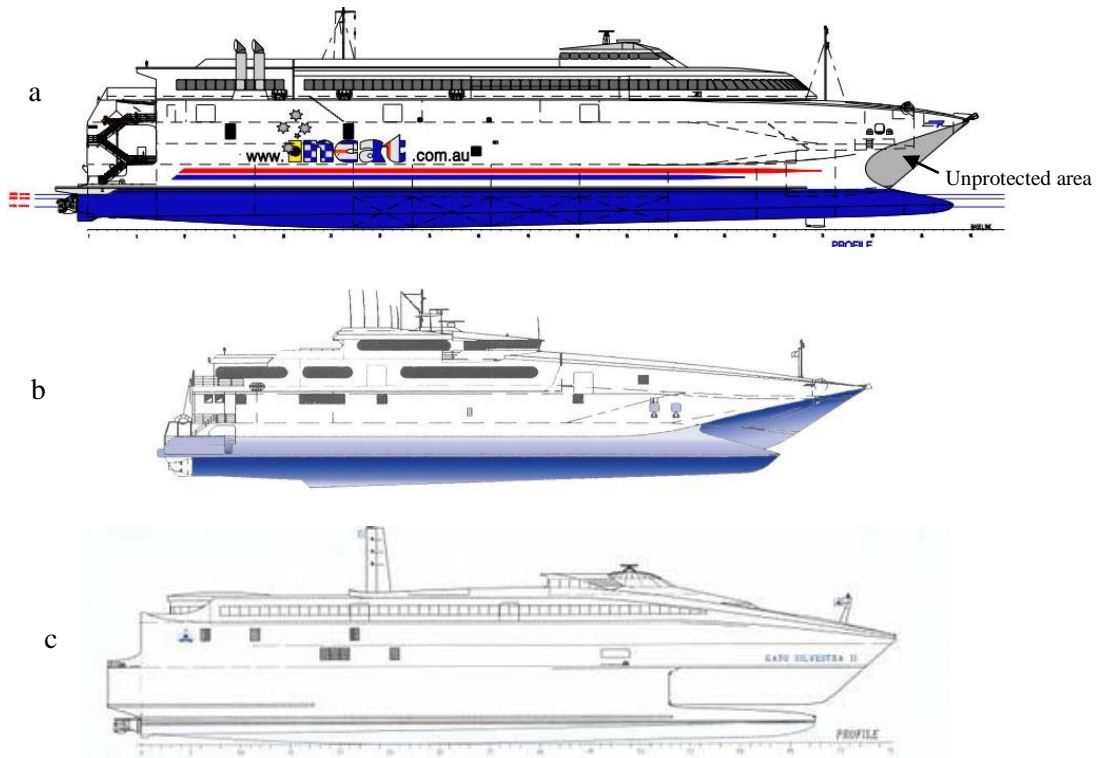


Figure 2.11: (a) INCAT 112m WPC; (b) INCAT 78m WPC (www.incat.com.au); (c) AMD1800, the 95 m WPC. The unprotected centrebow area in 78m vessel is much larger than the 112m WPC. In the 95 m WPC the jaw is moved a long way aft (<http://www.amd.com.au/designs/amd1800.php>)

For the INCAT WPCs, as in Figure 2.12, it is seen that as the vessel size is increased, despite the significant variations, the unprotected areas of the centrebaws has not increased. The reason for this is the tendency to increase the demihull lengths whilst the LOA remains the same to improve the seakeeping behaviour of the vessels. Extending the centrebaws too far forward also could make it difficult to maintain the design trim. Moreover, in larger vessels the structural strength necessary to withstand the high stresses in the jaw region of the vessel can cause complications.

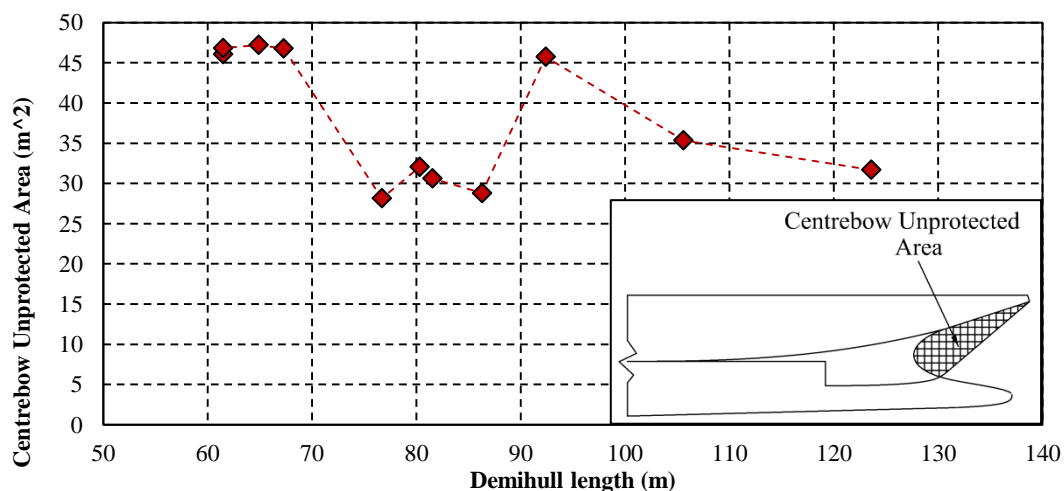


Figure 2.12: INCAT wave-piercing catamarans unprotected centrebow area

2.3. Summary

From a review of wave-piercing catamaran designs, it is evident that parameters such as tunnel clearance, centrebow volume, centrebow length, jaw-line profile and unprotected area have varied significantly through the evolution of these vessel designs. However, a clear evaluation of the different designs on the basis of full-scale studies is not possible due to the difficulty of conducting full-scale experiments as explained in the previous chapter. Improving the seakeeping and slamming behaviour of large WPCs requires a methodical investigation of the effect of these various design parameters under controlled test conditions. In the following chapters, two different methodologies are chosen for the present investigation. Firstly, physical model experiments were carried out using a hydroelastic segmented model designed to allow different hull forms to be compared by towing tank tests. In the present work, variations of centrebow length were investigated. Secondly, modelling was carried out as the basis of investigating the effect of different hull cross-sectional parameters.

3. Hydroelastic segmented model development

Hydroelastic segmented models (HSMs) are one of the experimental approaches that can be used to investigate wave induced loads and their effects on ships. Much research has been conducted into sea loads, slamming, structural behaviour, whipping vibration and local pressures, as well as the hydroelasticity effects of ships; this past work was overviewed in Chapter 1, Section 1.2.3.

A collaborative research project commenced in 2004 between UTAS, AMC and INCAT Tasmania to experimentally investigate the seakeeping behaviour and structural loads of large high-speed wave-piercing catamarans (WPC) using hydroelastic segmented models. The objective of the research was to establish reliable methods to accurately predict wave loads. In this chapter a brief overview on the initial HSM will be presented; this model is referred to as HSM01. A new set of design objectives are then outlined, including improvements over HSM01. The design, construction and instrumentation of this new model, HSM02, are detailed in this chapter.

3.1. Hydroelastic segmented catamaran model (HSM01)

The HSM01 was a model of the 112 m INCAT full-scale vessel with a design displacement of 2500 tonne. Based on the size and capabilities of the AMC test facility, the chosen scale ratio was defined as 1/44.8, resulting in a model of length 2.5 m and mass of 27.12 kg. The model was designed to have each demihull split into three segments, the segment cuts being at 40% and 60% of the model length from the transom. The two demihulls and the wetdecks (mounted between the hulls) were joined using transverse aluminium beams. The three segments were connected using aluminium elastic links, strain gauges fitted to these links allowed the vertical bending moments (VBM) to be measured. An outline of the model is presented in Figure 3.1.

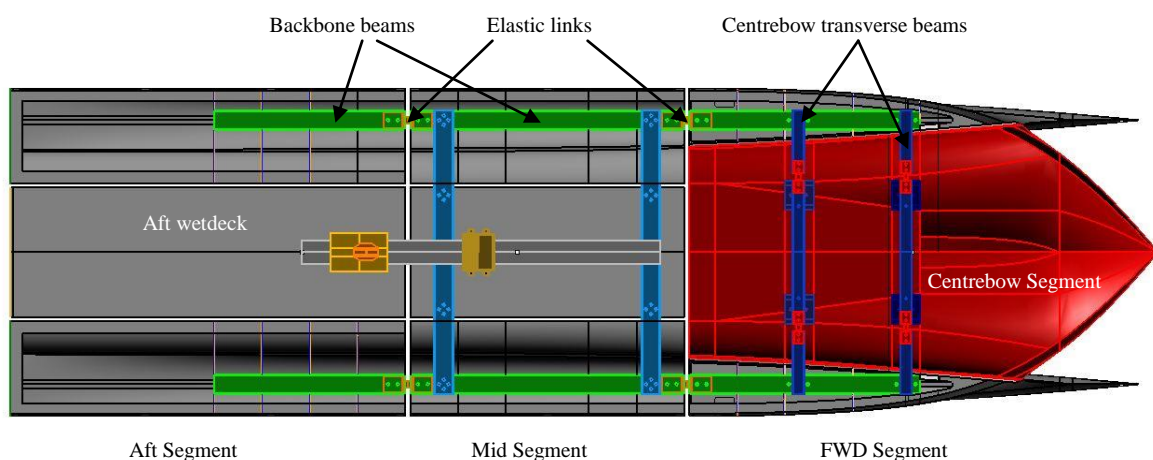


Figure 3.1: The first AMC-UTas segmented catamaran model HSM01 with its main components and elastic links

The model was constructed using sandwich panels of carbon fibre and Divinycell foam core, whilst the elastic links were fabricated from aluminium square section fitting into a hollow square section backbone beam embedded into each segment. This backbone beam ensured that each segment was rigid and flexibility only occurred at the segment gaps through the elastic links.

The elastic link dimensions were designed to ensure that the whipping vibratory response replicated the full-scale vessel behaviour. Since the 112 m WPC was not built at the time of HSM01 design, the measured modal frequencies of the 86 m and 96 m INCAT catamaran were extrapolated to obtain an estimate of first longitudinal mode whipping frequency based on the 112 m catamaran. Hence, from the similarity scaling, the target modal frequency of the HSM01 was designed to be 13.79 Hz from similarity scaling [50]. As also seen in Table 3.1, following the sea trials of the 112 m WPC, the average frequency was measured to be 2.29 Hz [51], corresponding to 15.33 Hz at the model scale. It was recommended that stiffer links should be used in the future to provide a more accurate structural representation of the full scale vessel [50].

Table 3.1: First longitudinal modal frequency of the 112 m vessel and its scaled values for 2.5 m model

Vessel	First longitudinal modal frequency	
	Predicted Before construction	Measured after construction
112 m vessel, Hull 064	2.06 Hz	2.29 Hz
Scaled value for 2.5 m model	13.79 Hz	15.33 Hz

The centrebow was isolated from the forward demihull segments so that slam loads could be measured. Two transverse beams with four elastic links located the centrebow and measured the vertical loads on the centre bow. The centrebow was also fitted with pressure transducers on the archway to measure slam pressures.

The model HSM01 was tested in various sea conditions to measure motions, loads and slamming behaviour in both regular and irregular waves as follows:

- Investigation of mode shapes and the effect of hydroelasticity on vessel motions at varying speeds in regular waves by Matsubara and Lavroff [50, 51, 99-101].
- Pressure mapping on the centrebow section at various speeds and wave heights in order to produce full-scale load cases for finite element analysis models by Amin [20].
- Global motions, VBM and slam loads in regular waves by Matsubara and Lavroff [50, 51].
- Vessel response in irregular waves and the characterisation of slamming behaviour by French and Winkler [1, 102, 103].

Although scaling the slam loads is difficult, the results from this extensive set of experiments have been verified against full-scale results. One interesting result is that both the model and full-scale INCAT vessels have experienced slams with a magnitude greater than the vessel displacement [1].

Figure 3.2 shows some structural elements of HSM01 where a longitudinal cantilever beam connects the aft wetdeck tray to the mid segment transverse beams; the aft tow post was attached to this beam.

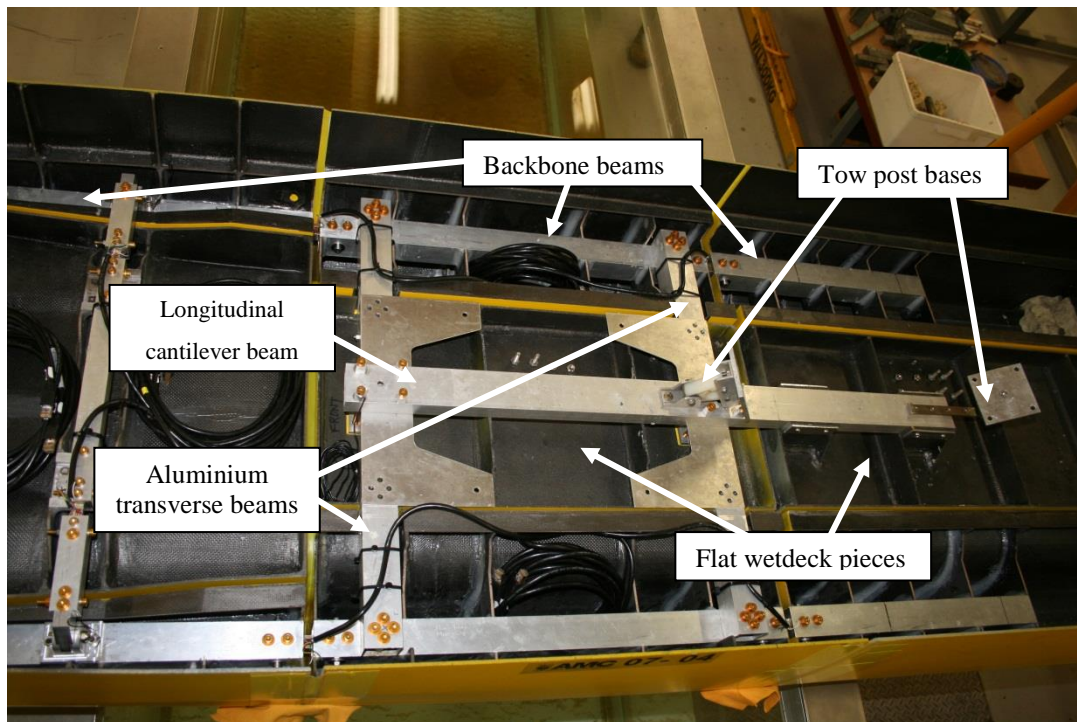


Figure 3.2: HSM01 transverse beam and cross-deck system. Two aluminium transverse beams connected to demihull backbone beams hold the demihulls together in mid segment. Aft wetdeck is attached to another cantilever beam extended from mid segment

By reviewing the model design, construction techniques and the test results from HSM01, the following issues were considered:

- It was noted through studying videos of test runs that the model, when tested at higher speeds, tended to run horizontally into waves rather than slam vertically caused by pitch and heave motions. This indicated that there could be a significant horizontal slamming force present on the centrebow. However, the HSM01 centrebow force measuring system could only measure vertical slam components. Hence, to better understand and measure slam forces it was recommended that loads in both the horizontal and vertical directions be measured.
- The centrebow force calibration of the HSM01 required the introduction of correction factors due to internal structural cross-torques and friction generated at the hinge supports of the bow transverse beams [51, 104]. It was proposed that a major review on the centrebow load measuring system should be completed to provide a more direct measurement system. This would also help to understand why there was uncertainty in the slam magnitudes measured in equivalent sea conditions [1, 102].
- A longitudinal cantilever beam connected the aft wetdeck tray to the mid segment. Since the aft wetdeck was actually a member of the mid segment, as demonstrated in Figure 3.3, any vertical wave forces on the aft wetdeck would be transferred to the mid segment instead of the aft segments. It was proposed that the connection between the aft wetdeck and mid segment be eliminated so transferring the loads to the segments realistically.

- The robust and light weight properties of the carbon-fibre with Divinice cell foam core. The resin was infused to carbon-fibre sandwich by vacuuming technique. More than 2,300 runs in slamming conditions were completed in the towing tank and model test basin. The model went under repair only in one case which the model disconnected from the tow post and struck the towing tank wall.
- The friction locked ball joint mount used for towing the model was replaced with a mechanically locked connection to increase the safety and avoid disconnecting from the tow post in heavy seas.
- The number of structural elements and instruments used in the model HSM01 increased the model light weight and therefore the model was difficult to trim. It was necessary to use a 3D solid modelling CAD package to enhance design efficiently and track the masses and LCG of the many structural elements.
- The effectiveness of the sealing method between segment gaps was to be improved. Using double sided tapes on the hull, applying light latex to seal the gap and on top each side, the use of water proof sticky tapes was found to be satisfactory. However, in some gap junctions such as where the forward cut and centrebow gap meet, especial care has to be taken to avoid leakage without transferring any loads across the flexible seal.

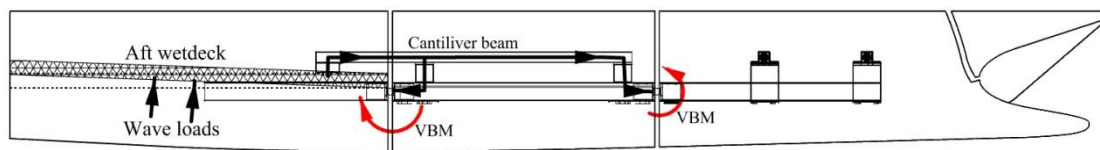


Figure 3.3: Aft wetdeck in HSM01 is attached to a cantilever beam extended from mid segment. In case of wave loading on the aft wetdeck, the VBMs are transferred to both sides of the mid segment

3.2. The new HSM design objectives

There is continued industry interest in the effect of tunnel height and centrebow shape on the slamming and seakeeping behaviour for new vessel designs. Whilst the effect of bow flare shape and general body form for the seakeeping and slamming of monohulls has been investigated (e.g. Kapsenberg et al. [47], Hermunstad et al. [105] and Bereznitski [106]) there is little data available on the effects of catamaran hull form on seakeeping, slamming and structural loads. The only work on the effect of WPC hull forms on slamming was conducted by Whelan [33] who conducted drop tests with various catamaran bow shapes to provide design guidance to reduce slam loads. He showed that outboard movement of the top of the arches between centre bow and demihulls alleviated slam loads somewhat.

The overall aim of the design of the new HSM model was to allow the investigation of hull form changes on the vessel's motions and slam severity. From this major aim, a set of design objectives of HSM02 were derived:

- 1- The design of the HSM of the INCAT 112 m wave-piercing catamaran should have two transverse cuts (three segments) and a separate centrebow, so the vessel motions, VBM, slam pressures and centrebow loads can be measured.
- 2- The centrebow volume, length and tunnel clearance are to be adjustable allowing variations and combinations of these parameters to be investigated. The new body lines are to be designed based on parameters derived from full-scale WPCs. In case of various tunnel heights, the wetdecks should move up and down to properly model the new designs.
- 3- An improved method of measuring centrebow loads is to be developed to accurately measure slam loads, both vertical and horizontal, and their location along the bow central axis.
- 4- The segments are to be designed and built separately so as to model the correct dynamic behaviour and avoid VBM confusion between segments. This will be achieved by modifying the wetdeck system; in particular, the longitudinal beam system is to be eliminated and the aft wetdeck attached to the aft demihull segments.
- 5- The Rhinoceros 3D CAD package is to be used for designing the new bodylines, shop-drawing and tracking the masses.
- 6- Similar shell material to HSM01 is to be used for model construction and the same model maker Stuart Philips is to build the model.
- 7- The lessons learnt from the design, construction and testing of HSM01 should be considered. For example the use of new weight reduction techniques such as reducing aluminium components are amongst the highest priorities so as to make trimming at design displacement less problematic.

3.3. New hull forms for application to the HSM02 model

As described in Chapter 2, WPCs use several key parameters to define the hull form including tunnel clearance, centrebow volume (length), reserve buoyancy and unprotected area of centrebow (the area of the centrebow which is not protected by demihulls). In this work the two parameters chosen that were likely to have the greatest effect on seakeeping and slamming behaviour were centrebow volume and tunnel clearance. Also, these two parameters include the crucial differences between the two strategies taken by the two peer catamaran designers explained in Chapter 2 to reduce or avoid slamming; the choice between having a high tunnel height or having a lower tunnel height but introducing a centrebow. A major design objective was to be able to model changes in these hull form parameters without changing other particulars of the demihulls. It should be noted that this author designed and commissioned the model to allow investigation of both the centrebow length and tunnel clearance effects. However only the effect of centrebow length was examined experimentally at this stage of the project, the tunnel clearance effect is to be examined at a later stage as a part of the ongoing industry collaborative project. The next sections describe the methodologies used to define

the hull form parameters, design the required hull forms using these parameters and manufacture the model.

3.3.1. Variation of centrebow length

The centrebow length has varied as the INCAT catamaran designs have evolved. As seen in Figure 3.4, the Centrebow Length Ratio (CLR), defined in Equation (2-5), has decreased from 37% to 18% as the vessel length has increased. The HSM02 is modelled on the 112 m catamaran that has a 21% CLR and it is referred to as “parent” Centrebow.

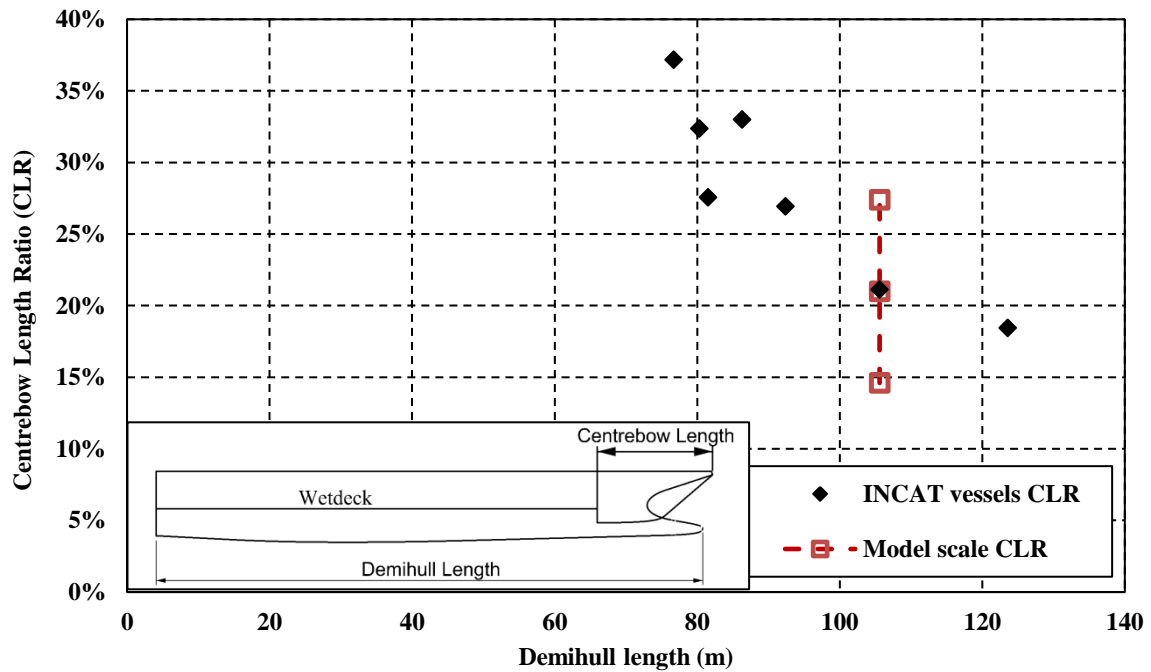


Figure 3.4: Centrebow length ratio (CLR) of INCAT large wave-piercing catamarans and this ratio variation tested in model scale

The new centrebow lengths were created by removing a 6.72 m (150 mm model-scale) section from the end of the parent centrebow model to make a short centrebow and extending the body lines of the parent centrebow aft for 6.72 m by adding model centrebow segments under the wetdeck to make the long centrebow. As seen in Figure 3.4 the CLR covered by this variation is 6.4% higher and lower than the parent design. Figure 3.5 illustrates how the added and removed sections create the three centrebow lengths. As seen in this figure, the centrebow volume is defined as the volume of the centrebow bounded by the keel line of the centrebow and the flat horizontal wetdeck plane extended forward. The centrebow volume is varied significantly between these three centrebow lengths and it is expected to play an important role in the vessel’s slamming [104]. Figure 3.6 shows the sectional view of the short, long and parent centrebow at their truncation points.

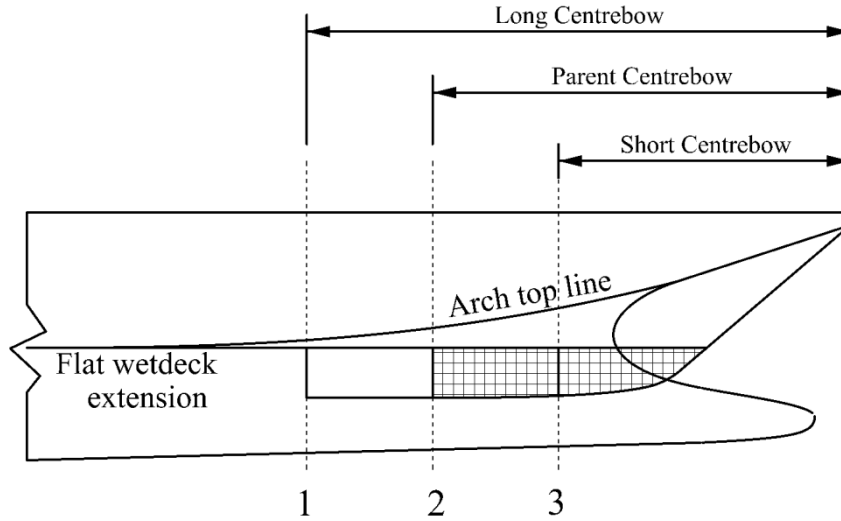


Figure 3.5: The creation of three centrebow lengths by adding and cutting out 150 mm pieces from the model parent centrebow truncation. The hatched area shows the parent centrebow volume

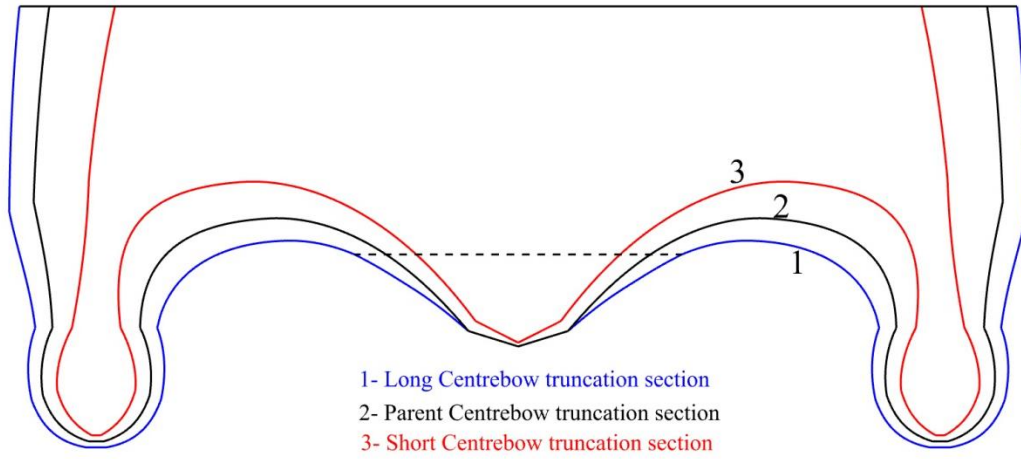


Figure 3.6: The transverse truncation section of the long, parent and short Centrebows

During slamming, flow blockage between demihulls and centrebow can influence the severity of the slam events in the vertical direction [50, 102, 104]. In the horizontal direction, the centrebow partly blocks the water flow under the wetdeck. The blocked area by the centrebow and the clearance area under the wetdeck are parameters that can affect this flow blockage; hence, it is considered that they can influence the magnitude of the horizontal slam forces. Figure 3.7 shows the centrebow truncation section of the 112 m WPC with the blocked and clearance areas defined.

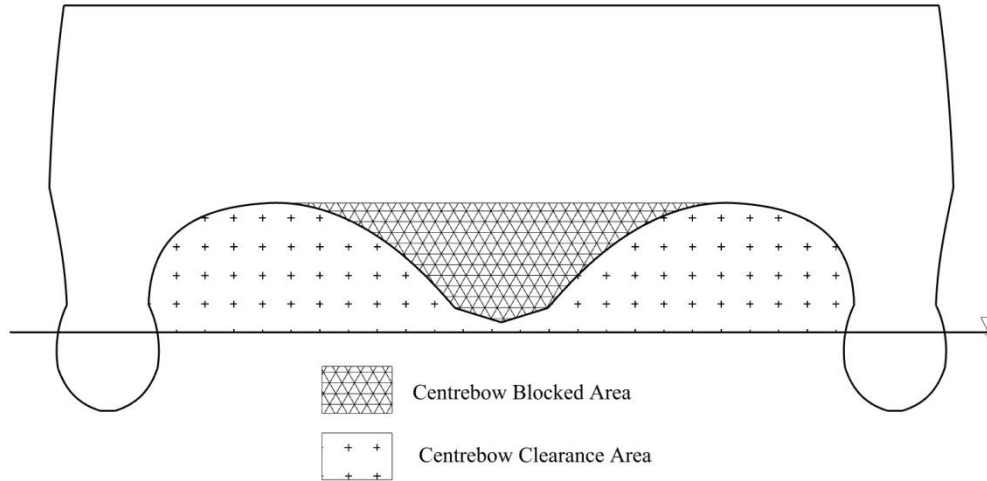


Figure 3.7: The definition of centrebow clearance area and blocked area shown for a catamaran bow section

A Tunnel Blockage Factor (TBF) has been defined as the ratio of centrebow blocked area to the total clearance area (without the centrebow) at the truncation section as Equation (3-1),

$$\text{Tunnel blockage Factor (TBF)} = \frac{\text{Centrebow blocked area}}{\text{Clearance area} + \text{Centrebow blocked area}} \quad (3-1)$$

Some of the characteristics of these three centrebow lengths are given in Table 3.2. The CBVR in this table is defined as the ratio of the centrebow volume to the displaced volume.

Table 3.2: Three Centrebow Length Dimensions Designed for Experiments

Model Name	Centrebow Length (m)	CLR	Centrebow Volume (m ³)	TBF	CBVR
Short Centrebow	0.348	14.6%	4.0696×10^{-4}	0.237	1.44%
Parent Centrebow	0.498	21%	11.8934×10^{-4}	0.265	4.22%
Long Centrebow	0.648	27.4%	21.5579×10^{-4}	0.272	7.64%

Figure 3.8 shows the final three centrebow lengths before painting. The extensions to the centrebows were attached to the hull section using three bolts and the gaps filled with plasticine to make the surface smooth and sealed. The weight of the short-parent extension piece was 0.198 kg and it was 0.202 kg for the parent -long extension piece.



Figure 3.8: Three centrebow length segments under construction. The short centrebow achieved by cutting 150mm from centrebow aft and a separate segment was built to form the long centrebow

3.3.2. Various tunnel clearance

Varying the catamaran wetdeck height can have a significant influence on the occurrence and severity of the wetdeck slamming in waves. As explained in Chapter 2, having too high a tunnel height conveys some operational and structural complications. Therefore, the use of lower tunnel heights with the introduction of a centrebow has been the preferred design configuration used by INCAT Tasmania. Investigating the effect of tunnel height on the vessel motions and wetdeck slamming is an important component of this overall project and therefore has to be accommodated in the design of HSM02.

The tunnel clearance ratio (TCR) describes the height of the wetdeck above the calm water surface and is defined as the ratio of the tunnel clearance to the demihull length of the vessel (see Equation (2-2)). The TCR of several INCAT WPCs are shown in Figure 3.9 where the TCR varies between 2.3% and 4.5%. Note that in this figure, the two largest vessels are in concept design stage.

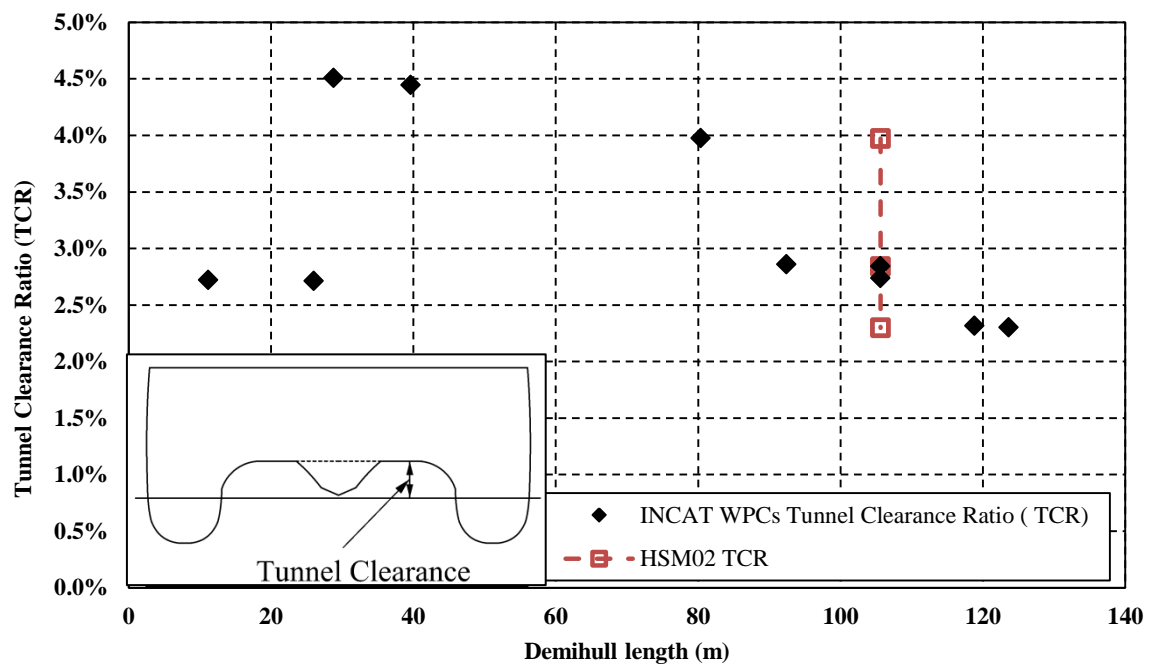


Figure 3.9: Tunnel clearance ratio of INCAT WPCs and the HSM02. The 112 m WPC is the parent hull configuration. The tunnel clearance is illustrated in the bottom left corner figure

This figure shows that in vessels with a length greater than 40 m, the larger the vessel size, the lower the tunnel clearance tends to be. The 112 m vessel has 2.84% TCR which is within the maximum and minimum TCR range among the other vessels. Therefore, the decision was made to have the dimensions of the existing 112 m WPC model with 2.84% TCR as the intermediate point or “parent hull”. Two extra tunnel heights were designed above and below this TCR allowing for the effect of the tunnel clearance on loads and motions of large WPCs to be more clearly determined. Selected principal particulars for the three vessels that provide the selected TCRs are shown in Table 3.3.

Table 3.3: The Three Designed WPC Specifications with Various Tunnel Heights

WPC Name	LOA (m)	Displacement (tonnes)	TCR	Tunnel Height (m)	Tunnel clearance (m)	Centrebow Volume (m ³)
High Tunnel Height	112	2500	4%	7.96	4.22	198.245
Parent Hull	112	2500	2.8%	6.74	2.95	106.936
Low Tunnel Height	112	2500	2.2%	6.06	2.35	104.805

As seen in Table 3.3, the centrebow volume varies significantly by increasing the tunnel height. The new centrebows were designed so that the demihull geometry and the centrebow keel line remained constant; the arch area was also faired for each new tunnel height into the components of the hull that remained constant. The centrebow truncation remained in the same position as the parent hull. The final bodylines of the “high tunnel height”, “parent hull” and “low tunnel height” are shown in Figure 3.10 and Figure 3.11. The final design tunnel clearances in the model-scale are given in Table 3.4. The high and low tunnel height bows were designed without removable segments at the single parent hull length.

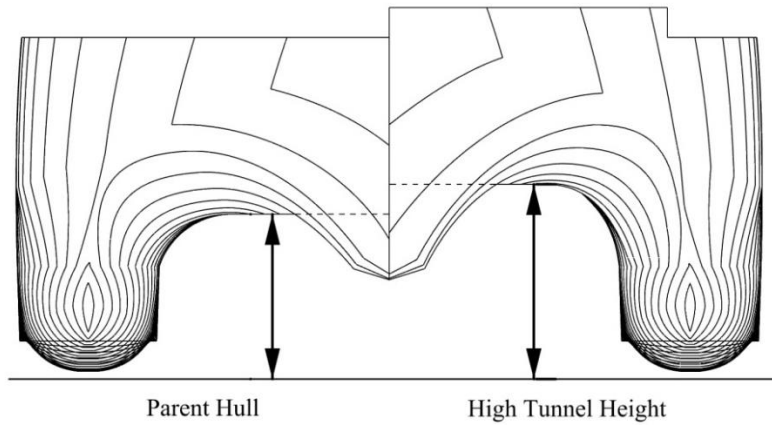


Figure 3.10: High tunnel height centrebow body plan (right), compared to parent hull bow form (left)

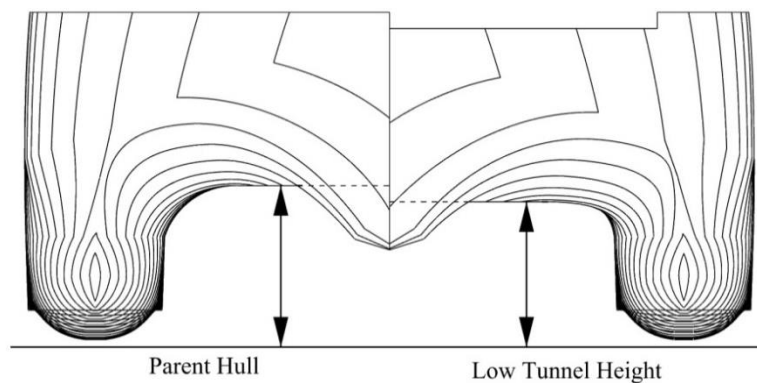


Figure 3.11: Low tunnel height bow body plan (right), compared to parent hull centrebow (left)

Table 3.4: Tunnel Clearance of Three Different Model Tunnel Clearance Ratio Configurations in HSM02

Model Name	TCR	Tunnel Height (mm)	Tunnel Clearance (mm)	Centrebow Volume (m ³)	CBVR
High Tunnel Height	4%	177.8mm	94.2mm	$2.2048 \times 10^{-3} \text{ m}^3$	7.81%
Parent Hull	2.8%	150.45mm	66mm	$1.1893 \times 10^{-3} \text{ m}^3$	4.22%
Low Tunnel Height	2.2%	135.3mm	51.9mm	$1.1656 \times 10^{-3} \text{ m}^3$	4.13%

3.3.3. Adjustable flat wetdeck design

To allow for testing of the three tunnel heights, the wetdeck of the model needed to be adjustable in vertical position. The wetdeck also needed to provide a strong and rigid connection between the two demihulls while being lightweight. To achieve these requirements three configuration options were investigated:

- **Aluminium transverse beams configuration:** using one set of aluminium cross-beams to connect the two mid demihull sections and then a separate set to connect the two aft demihulls, with an adjustable wetdeck suspended from these beams. The transverse beams would be placed higher for the highest tunnel height and the wetdeck trays connected to the beams with variable height attachments. The advantage with this option would be the ease of changeover between different tunnel heights. However, the drawback would be the significant weight of the 4 beams.
- **Carbon-fibre beam configuration:** this option would be similar to the aluminium transverse beams, but using carbon fibre instead of aluminium for the beams. The advantage would be weight reduction, but to ensure adequate strength the beams would be oversized thus limiting access and space.
- **Carbon-fibre wetdeck box configuration:** this option would consist of a carbon-fibre sandwich wetdeck box connecting the demihulls together. This wetdeck box would be attached directly to the demihulls via steel bolts and aluminium reinforcing plates. The box would consist of a top plate, a bottom plate and longitudinal and transverse bulkheads between them to provide bending and torsion stiffness. The height adjustment would be achieved by having aluminium reinforcing plates inside the demihulls with three set of holes. The aft towing tank carriage tow post would be connected to the aft segment wetdeck.

The carbon-fibre wetdeck box was chosen as the preferred option since it would provide a light weight solution with sufficient strength and ease of adjustment. The aft segment and mid segments are completely separate in this configuration. A schematic of the wetdeck box configuration with the 3 mm thick aluminium reinforcing plates is shown in Figure 3.12. The wetdeck boxes and plates can be adjusted vertically at steps equivalent to the difference in wetdeck height.

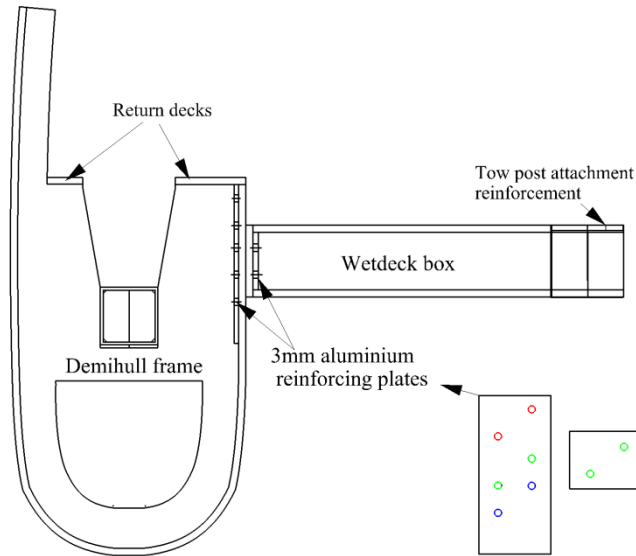


Figure 3.12: Schematic port side cross section of the carbon wetdeck box and its attachment to the demihull. The aluminium reinforcing plates with three premade 3 mm holes for height adjustment are shown in the bottom right of the figure

Figure 3.13 shows the profile view of the wetdeck box and aluminium reinforcement plates arrangements along the hull. In the designed wetdeck, the shell layup was a 3 mm laminate with 0.1 - 0.3 mm carbon/resin and 2.4 mm Divinycell foam core. Figure 3.14 shows a photo of the mid segment assembly of the demihulls and the wetdeck box. As seen, holes were made on the top wetdeck shell to both to reduce the weight and enable access to the inside reinforcement plates.

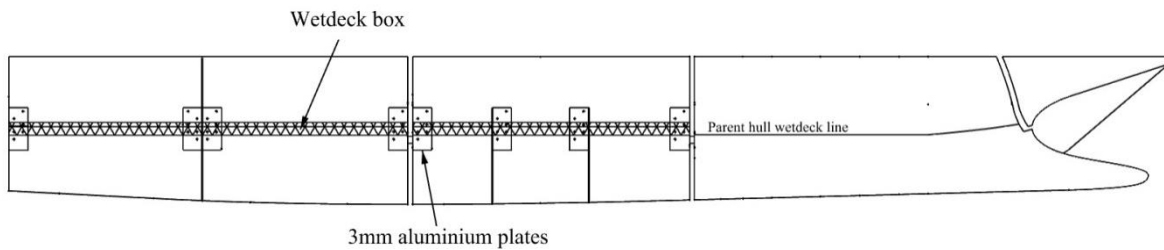


Figure 3.13: The location of wetdeck box and the arrangement of the reinforcing plates along the hull. The wetdeck box can move up and down the plates to change tunnel height



Figure 3.14: HSM02 mid segment wetdeck and demihulls assembly configuration

3.4. Flexural rigidity and vibratory response of the model

The hydroelastic behavior of the model needed to represent the 112 m INCAT WPC with a first longitudinal mode whipping frequency of 2.29 Hz of [51]. According to the scaling laws the modal frequencies are as given by Equation (3-2),

$$f_m = f_s \sqrt{\frac{L_s}{L_m}} \quad (3-2)$$

where f_m and f_s are the model and full-scale frequencies respectively. The desired model wet modal frequency is therefore 15.33 Hz. By assuming rigid segments in the model, the wet vibratory response is determined by the stiffness of the elastic links, the mass distribution of the model, the body form and the surrounding water. Using the method described by Lavroff [50] for a three degree of freedom model shown in Figure 3.15, the appropriate dimensions of the elastic links (dimensions of the square cross section and the link length) were obtained using the required model stiffness.

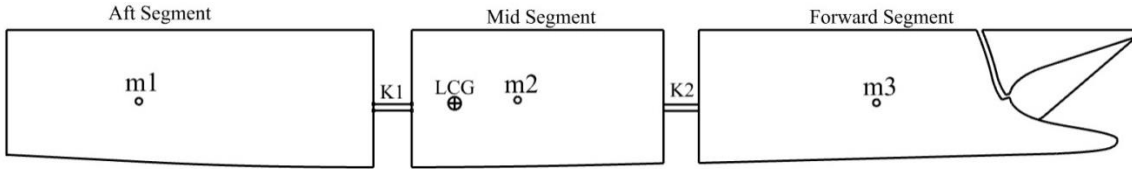


Figure 3.15: The three degree of freedom model of HSM02 to obtain the first modal frequency and the dimensions of the elastic links

Figure 3.16 shows a photo of one of the aluminium elastic links used in the model. Both ends of the elastic links were fabricated to fit inside the backbone beams with three aluminium bolts (two vertical and one horizontal).

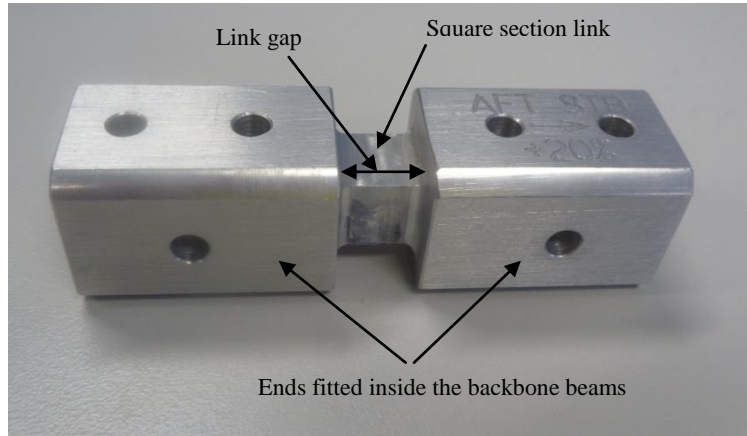


Figure 3.16: Fabricated HSM02 elastic link configuration

To ensure rigidity of the demihull segments, aluminium square section backbone beams were introduced to the demihulls and attached to the carbon-fibre hulls at multiple frames. The aluminium square sections for the backbone beams were specified as 32×32×1.6 mm and lengths of 225 mm in the forward section and 260 mm in the aft segment. As seen in Figure 3.17, the backbone beams were

supported at least at three points by the transverse frames and bulkheads. Carbon-fibre longitudinal return decks were also assembled on top of the transverse frames to provide increased rigidity to the segments.

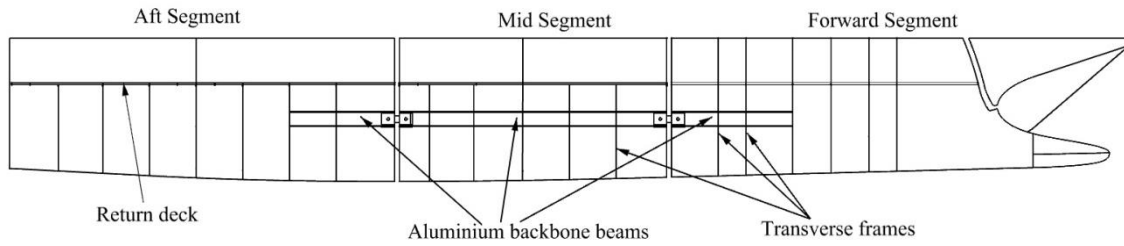


Figure 3.17: Backbone beams and the transverse frames arrangement in HSM02

Figure 3.18 shows a photo from the assembly of the transverse frames and the backbone beams in the two demihulls under construction. The backbone beams were joined to the transverse frames using epoxy resin. The total weight of the backbone beams in HSM02 is 1.112 kg: therefore, the weight saving was 1.237 kg compared to HSM01.

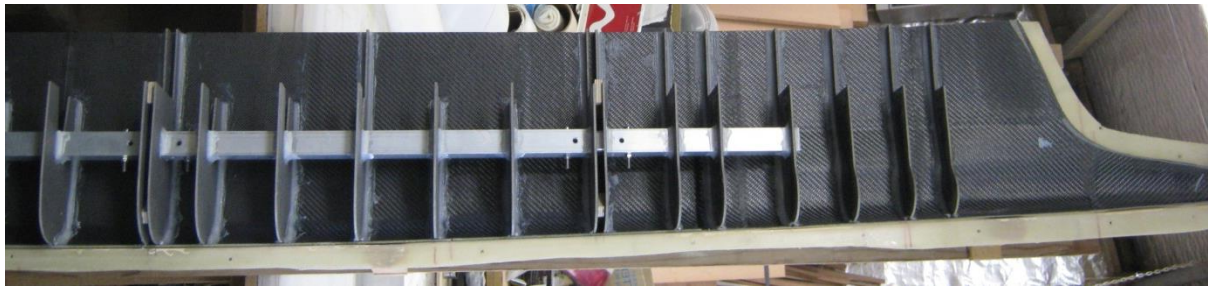


Figure 3.18: The HSM02 assembly of backbone beams and transverse frames under construction. Epoxy glue was used to connects various parts together

For practical reasons, such as knowing the exact mass distribution before model construction and also not having ideally rigid segments, predicting the exact whipping frequency of the model is difficult. Therefore, impulse experiments were conducted with various elastic link dimensions so as to measure the whipping frequency directly, changing the stiffness by modifying link dimensions accordingly. The results of these experiments to obtain the final 14.7 Hz of the whipping frequency of HSM02 with the nominal link stiffness of 2271.6 Nm/rad is detailed in Chapter 4.

3.4.1. Strain gauges and VBM calibration

The relation between the full-scale and model scale vertical bending moment is defined in Equation (3-3),

$$VBM_m = VBM_s \left(\frac{L_m}{L_s} \right)^4 \quad (3-3)$$

where VBM_m and VBM_s are the vertical bending moment of the model and the ship respectively. Based on full-scale investigations by Lavroff [50] on an INCAT wave-piercing catamaran, the model should withstand maximum 24 Nm of VBM. As seen in Figure 3.19, the VBMs were to be measured

at two longitudinal locations along the hull in the segment cuts. Sagging VBM is positive and hogging is considered negative. The designed elastic links should provide sufficient strength to withstand the predicted VBMs, which was accomplished using the dimensions obtained from the flexural vibratory experiments.

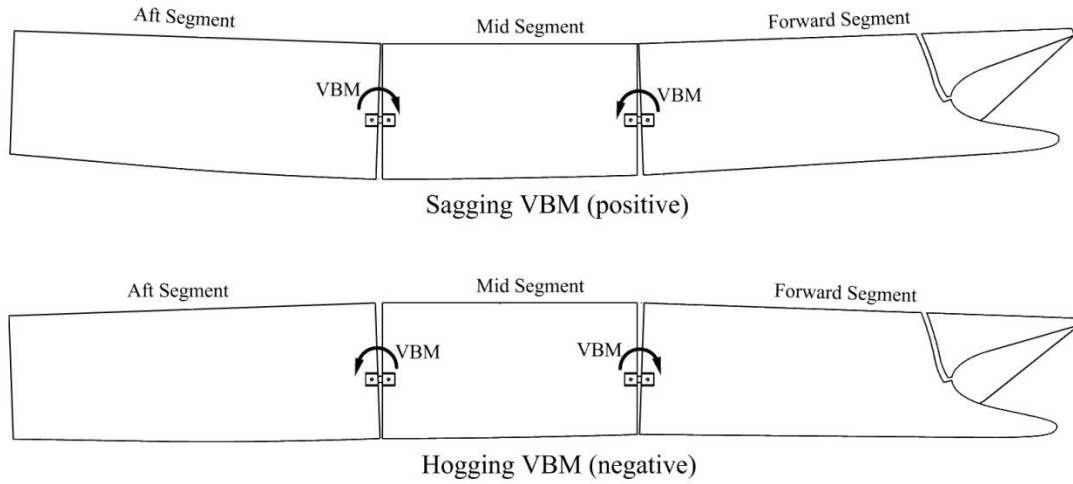


Figure 3.19: The sagging and hogging VBMs are measured in two segment cuts of the HSM01

To measure the VBM, strain gauges were glued to the top and bottom of the final elastic link square sections. The strain gauges were metallic foil gauges and were made by Vishay Micro-Measurements with resistance (R_G) of $350.0 \pm 0.3\%$ Ohms and gauge factor (GF) of $2.145 \pm 0.5\%$. The excitation voltage (V_{EX}) of the half bridge circuit was 10 Volts. The surface strain (ϵ) is obtained from the half bridge circuit using Equation (3-4),

$$\epsilon = \frac{2V_o}{V_{EX} \cdot GF} \quad (3-4)$$

where V_o is the output voltage [107]. Figure 3.20(a) shows how the loads can be measured on a beam by measuring strains on both side of it and Figure 3.20(b) shows the metal film strain gauge.

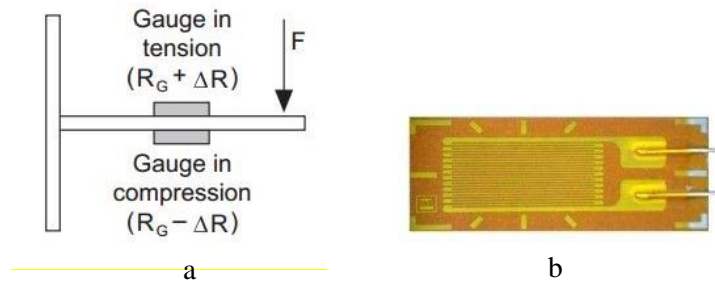


Figure 3.20: (a) Locating strain gauges on both sides of a bar to measure strains by change of grid resistance; (b) metal wire strain gauge (www.ni.com/white-paper/3642/en)

The size of these strain gauges was small (6 mm) which allowed mounting in the relatively small gap on both sides of the elastic links. The half-bridge circuit electronics were placed on the demihull return decks as in Figure 3.21. A Signal Conditioning Amplifier 2100 from Vishay Measurement Group Inc. and a Matronix (towing tank custom made) gain and filter box were used for conditioning

the strain signals; anti-aliasing (analogue) filters of 1000 Hz were applied in measuring VBM in the experiments.

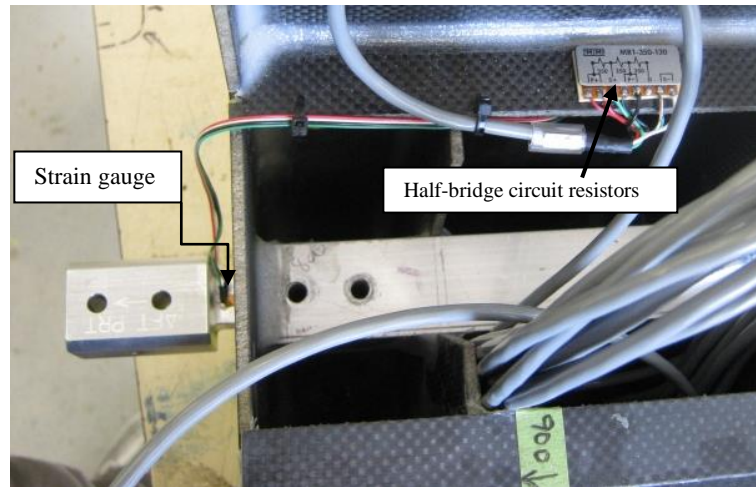


Figure 3.21: The strain gauges on the link and the Wheatstone half-bridge circuit

The four elastic links were named Forward Starboard, Forward Port, Aft Starboard and Aft Port elastic links based on their location in the two forward and aft cuts in the model. The VBM calibration process and the calibration factors are presented in Chapter 4.

3.5. Centrebow load measuring system

In both HSM01 and HSM02 the centrebow and arch area are isolated as a separate segment to capture the slamming loads. As seen in Figure 3.22, the cuts were made in locations in the demihulls to include all the centrebow and archways and having minimum water flow disturbances.

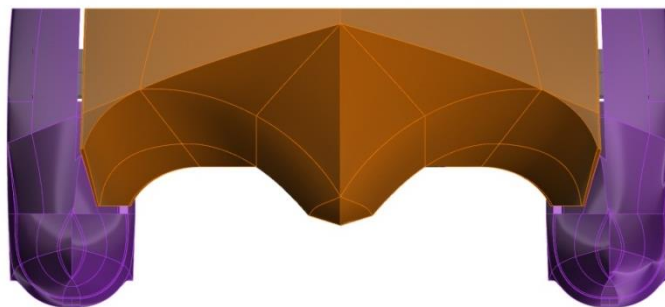


Figure 3.22: The centrebow isolation technique. The cuts are made so the slam loads can be captured by the centrebow segment alone

To increase the accuracy of the load measurements and remove the uncertainties arising from the HSM01 centrebow load measuring system, it was decided to use 6DOF force transducers which would allow for the measurement of both the vertical and horizontal centrebow forces. This would provide more fundamental knowledge about the nature of the slam forces and their locations. To measure the centrebow slam forces accurately, the 6DOF sensors needed to satisfy these criteria:

1. The maximum expected load must not exceed the transducers limit and there should be a safety margin in case of extreme slam loads. Meanwhile, the capacity of transducer should not be too high; otherwise the resolution of measurements for small forces would be insufficient.
2. The system should be lightweight and the dimensions of the transducer should be appropriate to fit in the model.
3. The system should be robust and have a high frequency response to extreme and asymmetric loads.

As the maximum slam loads in irregular waves could be up to about the model weight [102], to have a safe margin in extreme cases it was decided to choose a transducer with a capacity twice the maximum force to be measured. For this reason, the ATI MINI45 Force transducer was found to be in the appropriate range. This transducer is a semi-conductor silicon strain gauge 6DOF sensor with a cylindrical shape, 45 mm diameter, 15.7 mm height and 0.092 kg weight with 1/8 N force resolution. In extreme overloading it can withstand 5.7 to 25 times the rated loads, making it a very robust sensor. This sensor has various load range calibrations such as the SI-290-10 option which is calibrated to 580 N in Z-direction (vertical slam forces) and 290 N in both the X- and Y-direction (longitudinal and transverse). Figure 3.23 shows the MINI45 sensor and its axis, where F_x , F_y and F_z are the forces in X-, Y- and Z-directions and T_x , T_y and T_z are the torques measured by this sensor. This sensor has a tool side to connect to the load source and a mount side to be bolted to a rigid support. Table 3.5 shows the sensing range and measurement uncertainties in each loading axis for this sensor.

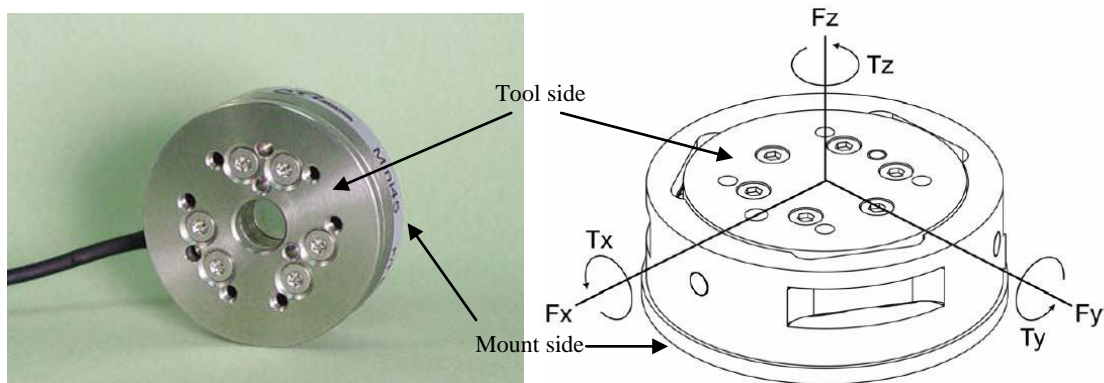


Figure 3.23: ATI MINI45 Force transducer and its load axes. The Z-axis will be used for vertical slam force measurements. Tool side is attached to the tool (centrebow) and mount side is attached to the support

Table 3.5: Load Capacity of MINI45 Force Transducer And Its Measurement Uncertainty (95% Confidence Level, Percent Of Full-Scale Load). The Calibration Is Done by The Manufacturer

Axes	Sensing range	Measurement Uncertainty
$F_x, F_y (\pm N)$	290	1.00%, 0.75%
$F_z (\pm N)$	580	0.75%
$T_x, T_y (\pm Nm)$	10	1.25%, 1.50%
$T_z (\pm Nm)$	10	1.00%

3.5.1. Feasibility study of installing 6DOF Force transducers

Employing MINI45 Force transducers required the installation of a rigid base to locate the sensors. The rigid mounting base was provided by transverse frames attached to demihulls at each end. Various configurations of sensor/frames were investigated for measuring centrebow forces. The first option was to use a single sensor and one frame; however, the small diameter of the sensor compared to the centrebow segment size increased the risk of failure where a severe slam occurred far from the sensor. Utilising three sensors was a structurally sound and reliable option but the weight and cost issues were drawbacks. Therefore, to reduce both weight and cost, the feasibility of utilising two sensors longitudinally in line was investigated. The proposed configuration is illustrated in Figure 3.24.

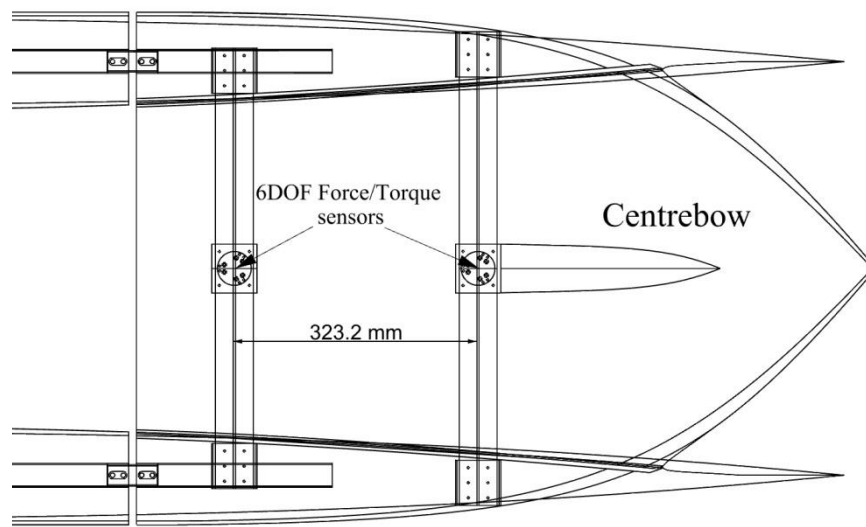


Figure 3.24: The proposed configuration of centrebow load measuring system where two aluminium transverse beams location the centrebow and the 6DOF force transducers

The designed load measuring system must prove to be reliable, accurate and also with minimum deflections under symmetric and asymmetric loads. Although it is normal to only expect symmetrical loads on the centrebow in the transverse direction in head seas, due to the strong and extreme nature of slamming, it is possible that there will be some uneven slam forces with asymmetric components on the centrebow due to small irregularities in the wave environment.

Since the centrebow is supported only at two points in the longitudinal direction, the only support to resist the asymmetric forces and moments is the bending stiffness of the transducers and their attachment bolts.

To investigate the system response against centrebow asymmetric forces, an extreme asymmetric force on the centrebow was applied and the deflection of the centrebow side edges measured. If the deflection was less than a defined threshold, it could be assumed to be an appropriate measurement system. By assuming rigid mounting frames, the deflection of the centrebow side edge would be due only to the flexibility of the centrebow structure plus the flexibility of the sensors themselves. The two

deflection sources were determined as follows: the deflection due to the sensor flexibility was determined by using the sensor's stiffness provided by the manufacturer. By assuming 60N asymmetric force on the top of the archway, the centrebow edge deflection was calculated to be 0.092 mm. For the deflection due to centrebow structure flexibility, a mock up configuration of the load measuring system with an existing centrebow model and a stiff dummy load cell was designed. By loading the centrebow in various locations on the archways and measuring the deflections at the edges, plots similar to Figure 3.25 were drawn. Therefore, maximum deflections due to asymmetric centrebow loading were obtained. More details are given in appendix 1.

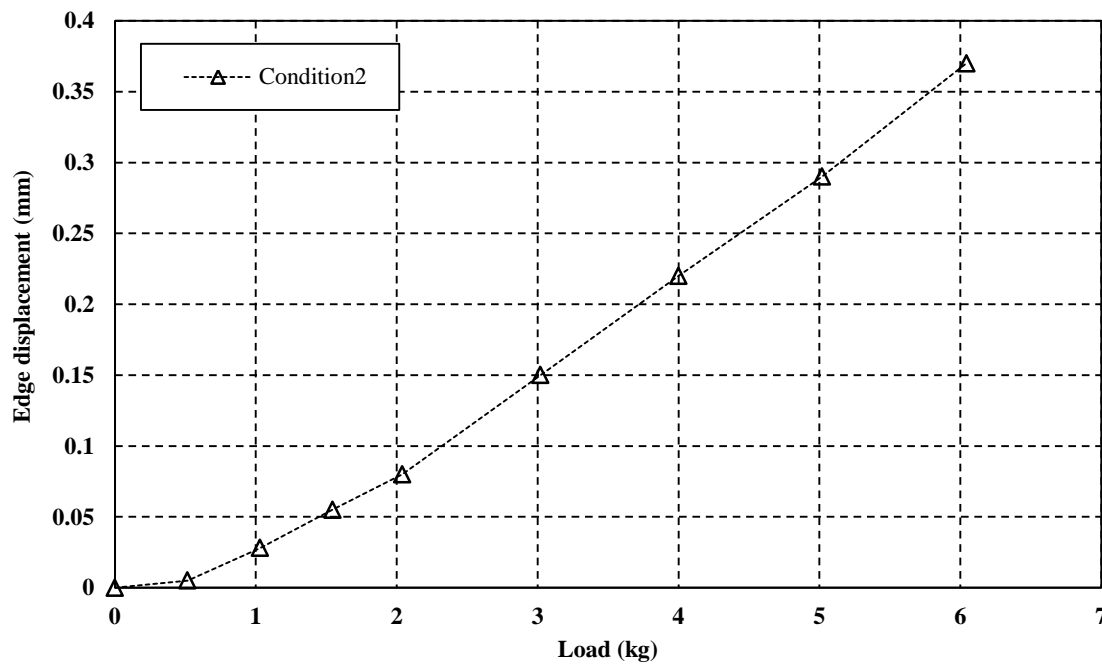


Figure 3.25: The side edge displacement of centrebow by loading asymmetrically on the archways close to centrebow truncation

By adding the two maximum edge displacements from the transducer and centrebow structure resulted in a maximum edge displacement of 0.5 mm which was considered very small, and within the required threshold. Visual and manual inspections also demonstrated that the system was sufficiently rigid and safe.

3.5.2. Load measuring system final configuration

To support the centrebow, two *T*-bar sections 50×50×3 mm aluminium beams proved to be the best option in terms of weight and strength. The transducer attachment section of the beam was strengthened by adding extra 3 mm plates on the *T*-bar flange. To avoid large moments from slam occurring outside the region between the two sensors, efforts were made to maximise the distance between the two *T*-bars. However, it was difficult to move the forward beam from the position in HSM01 since the demihulls become very fine at the bow. Hence, only the aft *T*-bar could be moved (100 mm) astern of the same location in HSM01.

There were also some difficulties in rigidly connecting the T-bars to the demihulls as the backbone beams were shorter in HSM02 compared to the HSM01. Hence, the T-bars could not be connected to the backbone beams directly. Therefore, it was decided to use a sandwich carbon-fibre deck plate providing the base support for the beam ends. Cradle shape bases were also designed to provide a rigid support for the T-bar ends. As seen in Figure 3.26, underneath the transverse beam ends, vertical frames were incorporated inside the demihulls for additional strength.

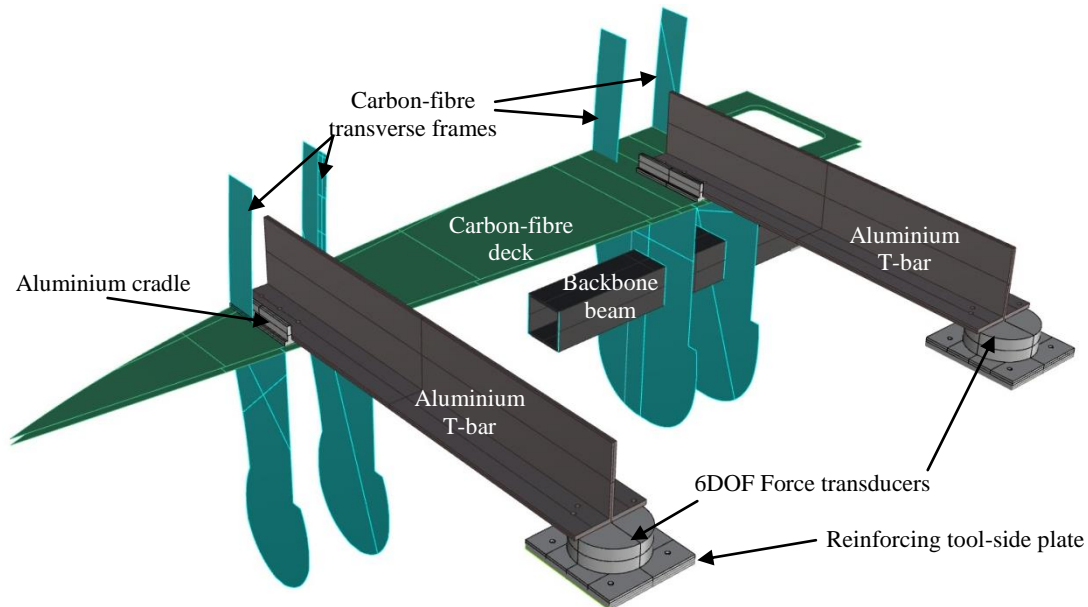


Figure 3.26: The connection of transverse T-bars and the demihull via a carbon-fibre deck and transverse frames inside the demihulls. Aluminium cradles were designed to rigidly attach the T-bars to the deck (note that the demihull shell has been removed in this rendering)

For the centrebow side of the transducers (facing down), a square aluminium plate was manufactured. As seen in Figure 3.27, this plate was mounted on another square plate attached to the centrebow. This arrangement allowed for ease of change over between centrebows without needing to remove the transverse beams, also easing consistent alignment.

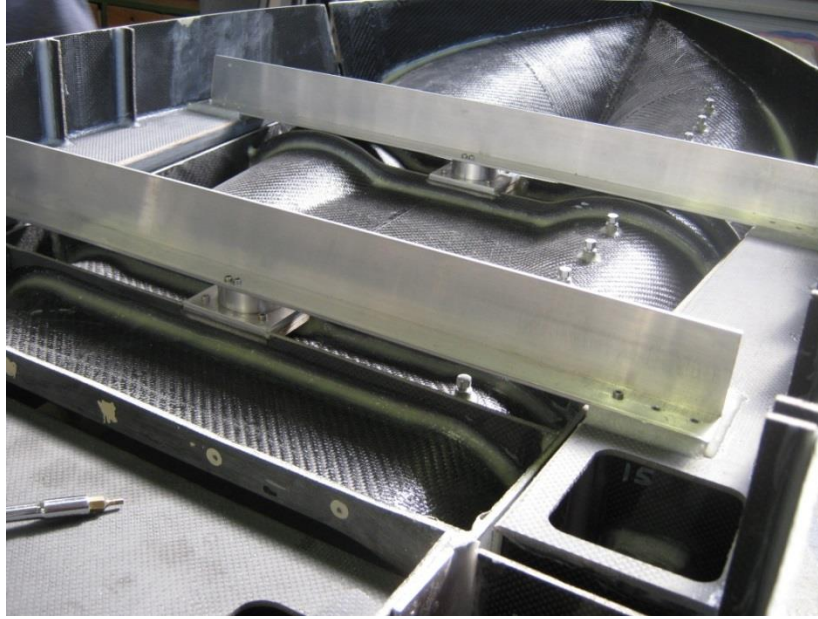


Figure 3.27: Centrebow segment transverse beam arrangement and 6DOF sensors. A stiffened carbon-fibre sandwich deck provides the base support for the beams

3.5.3. Extracting centrebow loads from the 6DOF Force transducers

To extract the total force and location of the slam forces on the centrebow, the static force and moment equations in equilibrium were derived. Figure 3.28 is a schematic of the centrebow profile view, points *A* and *B* are the 6DOF sensor positions, *d* is the distance between the two sensors and the location of the resultant slam force is at point *F* with distances to the frame of reference of *x* and *z*.

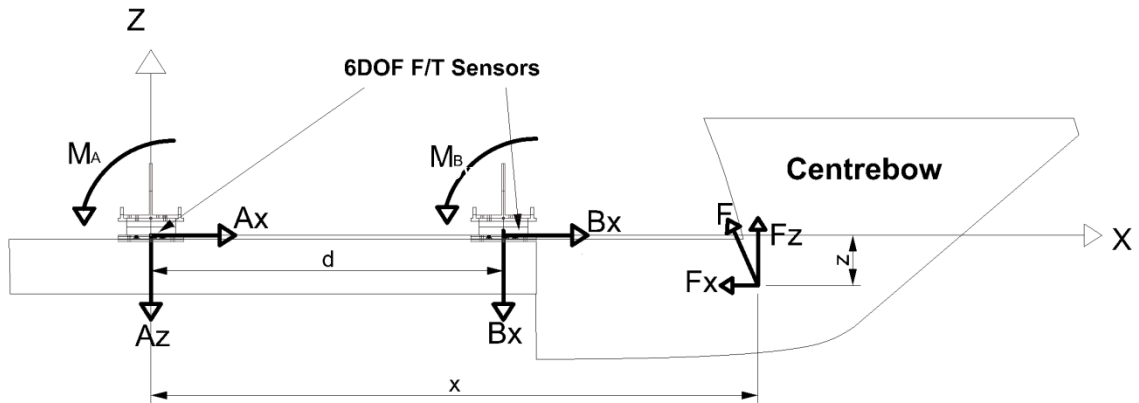


Figure 3.28: Centrebow free body diagram. Two 6DOF Force transducers measure the slam force

By writing the equations of equilibrium, the forces F_x and F_z can be calculated from Equations (3-5) and (3-6),

$$\sum F_x = 0 \Rightarrow Ax + Bx - F_x = 0 \rightarrow F_x \text{ will be known} \quad (3-5)$$

$$\sum F_z = 0 \Rightarrow Az + Bz - F_z = 0 \rightarrow F_z \text{ will be known} \quad (3-6)$$

Also, slam load angle can be calculated by Equation (3-7) by

$$\tan(\theta) = \frac{F_x}{F_z} \quad (3-7)$$

Solving Equations (3-5) and (3-6), the total slam force in both the horizontal (F_x) and vertical (F_z) directions can be determined. The moments about point A in the X-Z plane are given by Equation (3-8) and (3-9),

$$\sum M_A = 0 \Rightarrow Bz \cdot d - F_x \cdot z + F_z \cdot x + M_B + M_A = 0 \quad (3-8)$$

$$-F_x \cdot z + F_z \cdot x = -M_A - M_B + Bz \cdot d \quad (3-9)$$

where M_A and M_B are the moments around transverse axis (Y-axis) and z is the vertical distance of slam resultant force to X-axis. The x is the intersection of the slam line of action with the X-axis and is found using Equation (3-10).

$$x = \frac{-M_A - M_B + Bz \cdot d}{F_z} \quad (3-10)$$

This intersection point can be taken as the slam location if it is assumed that the slam resultant force is aligned vertically to the X-axis ($z \cong 0$, close to the arch top) where high pressures normally occur.

The size of these MINI45 transducers is small, thus the strain measured by the strain gauges inside the transducer are not isolated for each axes. Therefore, the calibration factor for each 6DOF sensor comes as a 6×6 matrix as demonstrated in Equation (3-11).

$$\begin{bmatrix} F_x \\ F_y \\ F_z \\ M_x \\ M_y \\ M_z \end{bmatrix}_{6 \times 1} = [\text{Calibration matrix}]_{6 \times 6} \times \begin{bmatrix} Sg0 \\ Sg1 \\ Sg2 \\ Sg3 \\ Sg4 \\ Sg5 \end{bmatrix}_{6 \times 1} \quad (3-11)$$

where $Sg0$, $Sg1$, $Sg2$, $Sg3$, $Sg4$ and $Sg5$ are the recorded signals from six channels and the F_x , F_y , F_z , M_x , M_y and M_z are the forces and the moments respectively shown in Figure 3.23 (letter T from torque is substituted with M as the moment). The sensors are factory calibrated and the calibration factors and the calibration check results for both individual sensors and the total centrebow load measuring system are given in Chapter 4.

3.6. Slam pressure measurement and instrumentation

Measuring pressures on the model is vital for predicting full-scale slam pressures (with significant care) for local strength analysis. Also, mapping the slam pressure helps identify high slam pressure regions on the vessel which could help develop case-loads for FEM analysis. In addition, it is valuable to compare peak pressure magnitudes and peak pressure locations between various hull forms in slamming.

Amin [20] completed extensive slam pressure mapping experiments on HSM01. The results indicated that the maximum slam pressures occurred close to the top of the arch top of the centrebow. The peak pressures occurred very rapidly and appear in the data from pressure gauges as very sharp spikes in the time series. The slam peak pressures did not occur simultaneously along the archway surface with high pressures moving aft and forward in relation to the initial impact during a single slam event. The location of the maximum slam pressures also changed with incident wave frequency; lower frequencies tended to induce pressures further forward on the centrebow. Maximum pressure reported was 13 kPa (1.9 psi) in 90 mm wave height.

ENDEVCO piezoresistive pressure transducer Model 8510C-50 along with DC amplifier Model 136 from ENDEVCO were chosen for measuring pressures on HSM02. The pressure range of these transducers is 0 to 50 psi and work in both wet and dry conditions. The ENDEVCO pressure sensors have shown robustness and linearity throughout all experiments in the towing tank. More information about these pressure sensors is given in Appendix 3.

As pressure mapping was not the primary objective of the HSM02 design, it was decided to locate the pressure transducers only in locations where high pressures were expected on the centrebow and to record the pressures simultaneously with the other loads and motion signals in the runs. Therefore, there were 9 channels available on the 32 channel DAQ card for pressure signals. Aluminium casings were manufactured and glued to the holes drilled on the centrebow shell to locate these transducers on the archway. Figure 3.29 show the location and arrangement of pressure transducers on the centrebow segment starboard side. The measurement locations were chosen sufficiently spatially spread to capture peak pressures at various incident wave frequencies, wave heights and for all three centrebow truncations. For the experiments conducted, pressure transducers were located at nine frames 60, 64, 66, 70, 74, 76 and three on frame 72. Three transducers at frame 72 were located transversely to capture transverse pressure distribution. The final configuration of the centrebow and the pressure gauges after construction is shown in Figure 3.30.

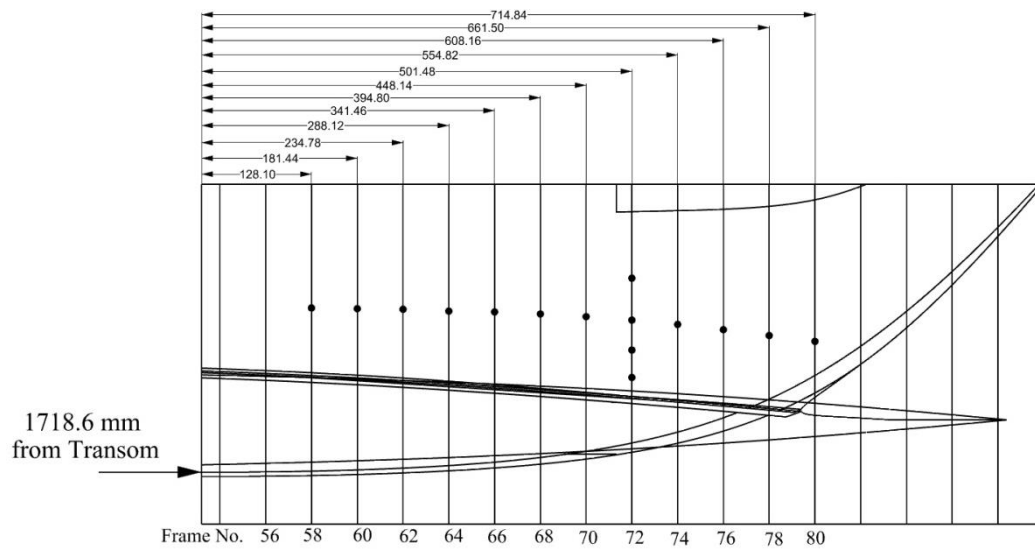


Figure 3.29: Pressure transducer casing arrangement on the centrebow starboard. The fittings are arranged in a longitudinal manner along the top of the arch with three transverse locations close to parent centrebow truncation



Figure 3.30: The centrebow with pressure transducer casings installed after construction

4. Hydroelastic model commissioning tests and calibration

The new hydroelastic model HSM02 was designed in three segments and constructed using carbon-fibre shell and aluminium backbone beams in the demihulls. The model should however show appropriate dynamic behaviour similar to the full-scale 112 m INCAT wave-piercing catamaran, hence it should be commissioned to measure the response and be corrected if necessary. The model also is to be used for measuring VBMs in the segment cuts; therefore, the elastic links between the segments were calibrated on the model to ensure the measurement accuracy. The centrebow is also built isolated using two 6DOF force transducers to measure the centrebow slam forces. The accuracy of the individual sensors and also working together on the model were examined in measuring the centrebow forces and predicting the applied force location. This chapter explains the above calibration procedures and shows the results of these commissioning and calibrations tests.

4.1. Modal structural frequency tests

The desired wet modal frequency of the model was 15.33 Hz, based on a value of 2.29 Hz for the full-scale vessel [51]. The model vibratory response of the model is largely dependent on the stiffness of the elastic links. As seen in Figure 4.1, the dimensions of the elastic links, the gap and the cross section (w), determine the nominal stiffness of the elastic links. Two 6 mm bolts from the top and one from the side make the connection to the backbone beam in each end.

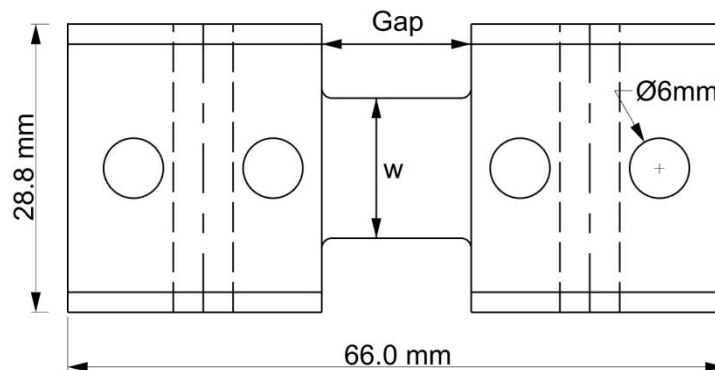


Figure 4.1: The elastic links from the top view. The cross section and the gap size determine the stiffness of the link

The model vibratory response of the model in water was measured by impulse tests in the wet dock of the towing tank. Lavroff [50] has shown that the effect of forward speed on whipping frequency is relatively small, although whipping damping increases moderately with forward speed. Impulses were applied to the most forward point of the model when it was at design displacement and with zero trim. The response of the model was measured by an accelerometer, which was placed at various points along the model at 100 mm increments from the transom as shown in Figure 4.2.

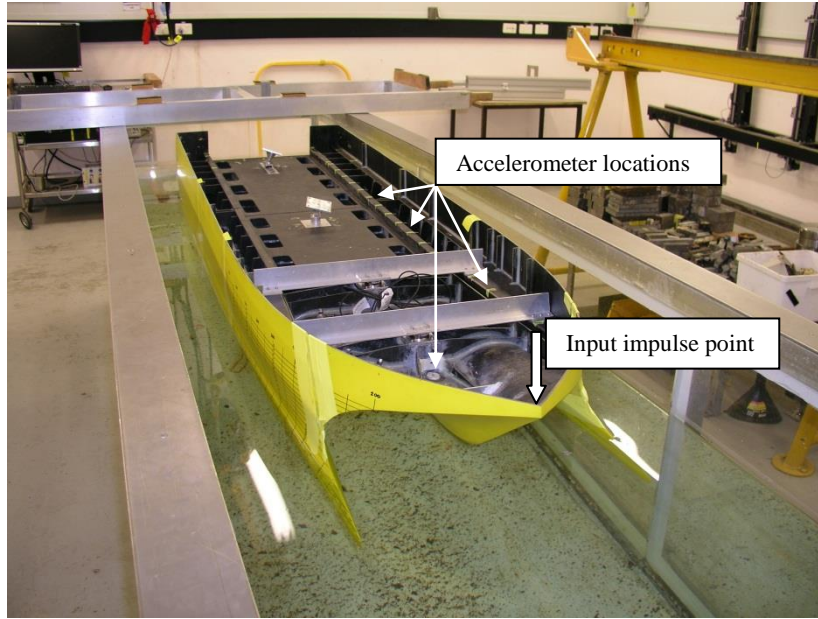


Figure 4.2: The impact test setup for measuring modal frequency. The centrebow tip was impacted and the accelerations were measured along the hull

The accelerations were measured via a piezoelectric seismic-mass accelerometer type 4370 B&K and a conditioning amplifier type 2626 was used for amplifying the accelerometer electric charges. Specifications of these instruments are given in Appendix 4. The amplitude response ($\pm 10\%$) of the accelerometer is at 0.1 Hz – 4800 Hz and the low end response of the type 2626 charge amplifier is 0.3 Hz (see appendix 4), which therefore, becomes 0.3 Hz in total; suitable for current measurements.

With the 14 mm square section and 15 mm gap (similar to HSM01) the average measured modal frequency was 13.47 Hz, which was less than the desired frequency of 15.33 HZ. It was also less than 13.79 Hz from the HSM01. This was somewhat expected due to the use of lighter backbone beams which led to a more flexible model.

The final frequency was achieved by a stiffer elastic link square section of 15 mm with the gap 13 mm between the two ends. The nominal stiffness of the link was calculated to be 2271.6 Nm/rad and the average whipping frequency obtained was 14.7 Hz which corresponded to 2.2 Hz at full-scale.

Figure 4.3 shows a time series collected in one of the impact tests, the accelerations are oscillating in time while being slowly damped. Figure 4.3 shows a time series collected in one of the impact tests, the accelerations are oscillating in time while being slowly damped. The average damping value for the first 12 cycle was 0.015 calculated from Equation (4-1),

$$\zeta = \frac{\ln\left(\frac{x_1}{x_{m+1}}\right)}{2\pi m} \quad (4-1)$$

where ζ is the damping ratio for small damping values, x_1 and x_{m+1} are the peak value at times of t_1 and t_{m+1} in m cycles. The damping value would decrease if the further smaller cycles are taken into account. The damping value for HSM01 was 0.0105 reported by Lavroff [50].

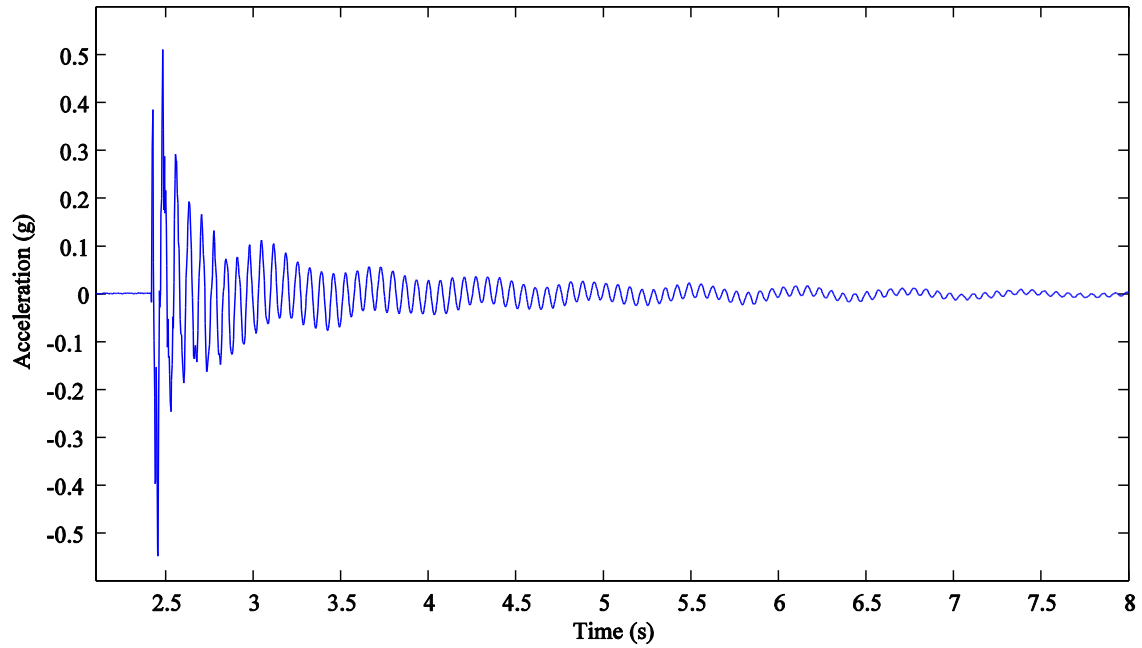


Figure 4.3: A sample time series of impact test accelerations of the model in the water. The whipping oscillations start after the impact and continue while getting damped slowly

Figure 4.4 shows the Fast Fourier Transform (FFT) analysis for the sample time series. This graph shows that the first fundamental longitudinal mode (hogging and sagging) is the dominant natural structural frequency (14.72 Hz) and the effects of higher modes are very small. Also an initial frequency of 1.685 Hz is present which is due to the pitch motions in the water.

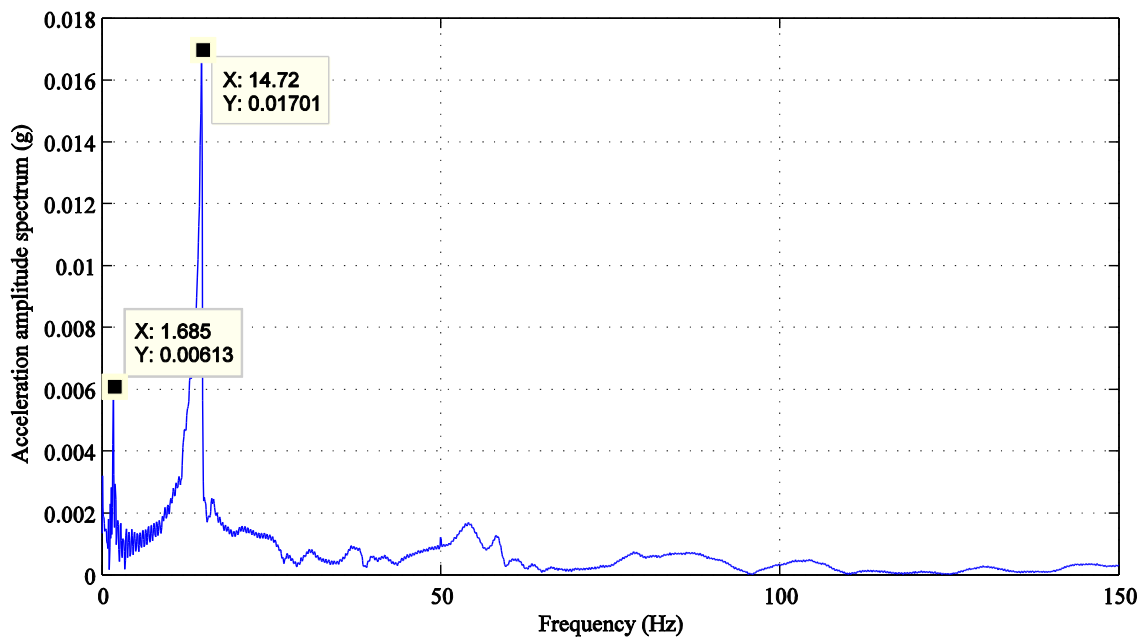


Figure 4.4: An impact test sample FFT analysis of the accelerations on the model. The analysis shows 14.72 Hz as the fundamental mode whipping frequency and 1.685 Hz as the rigid body motion response of the model inside the water

4.2. Strain gauges and VBM calibration

Strain gauges were glued to the top and bottom of the final elastic link square sections to measure VBM. For calibration of VBM on the model, as shown in Figure 4.5 and Figure 4.6, the model was placed on the edge of the wet dock of the towing tank with one segment hanging out as a cantilever beam. Weights were hung certain distances along the model; thus the VBM was calculated as the weight multiplied by the distance to the middle of the elastic link. The model was tested in both the upright and upside down positions and the calibration factors were averaged for hogging and sagging conditions. The sagging VBM was taken as positive VBM and the hogging moment as negative. Tests were carried out before and after the tank testing programme.

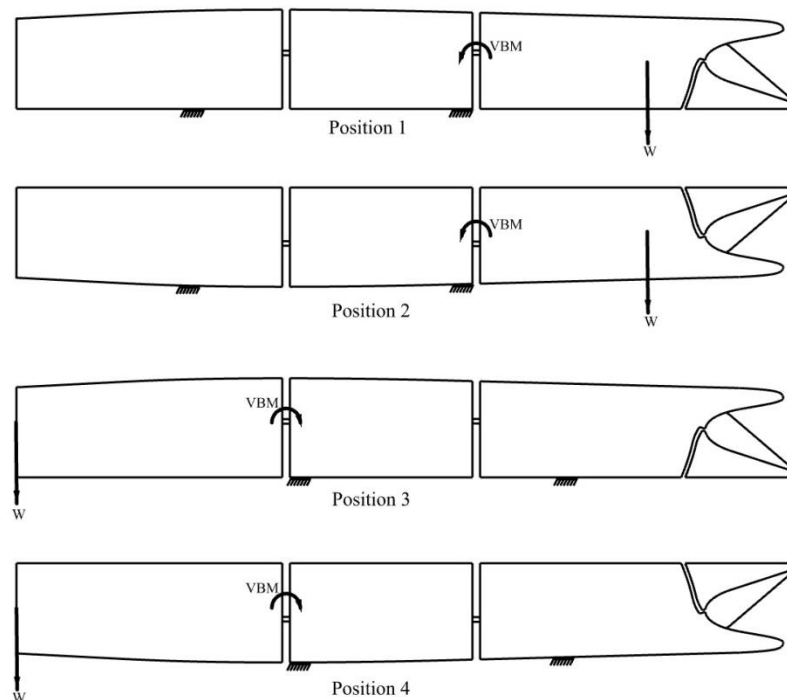
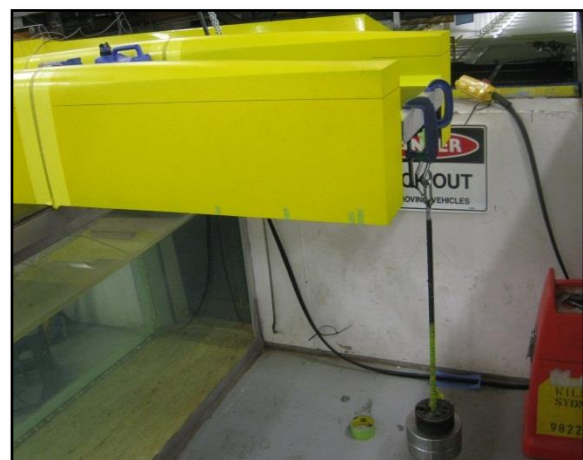


Figure 4.5: The position of the model and the supports location during loading for bending moment calibration



(a) Loading the model for Forward cut VBM calibration in Position 2



(b) Loading the model from transom to calibrate VBM in Position 3

Figure 4.6: The model was set up on the wet dock edges of the towing tank and loaded with a hook and string

The elastic links were named Forward Starboard, Forward Port, Aft Starboard and Aft Port elastic links based on their location in the two forward and aft cuts in the model. The loading results of the elastic link strain gauges before and after tests are presented in Figure 4.7. The calibration factor of each elastic link was calculated from the slope of VBM graph.

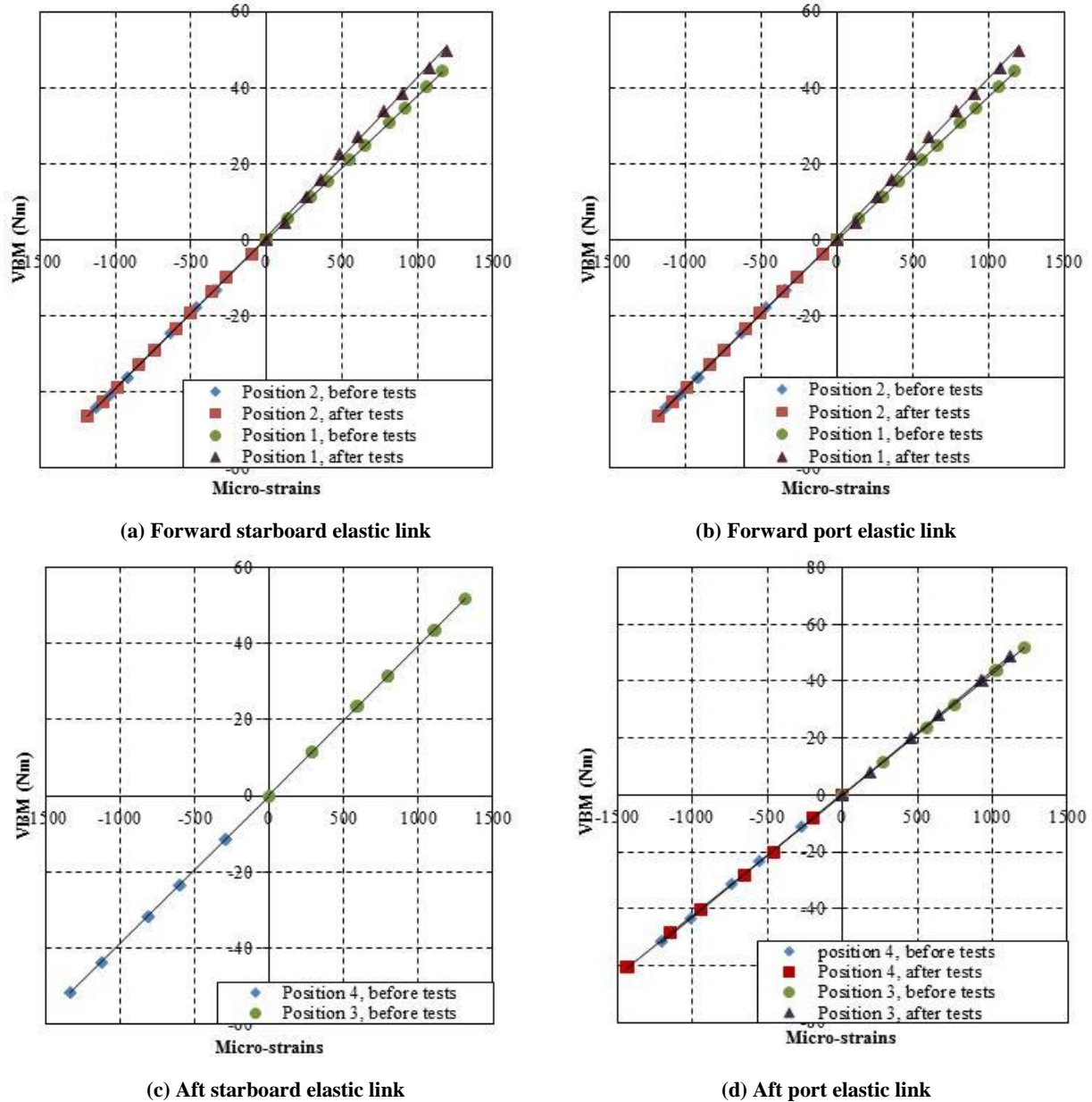


Figure 4.7: Elastic link strain gauge calibration graph. The calibration factor is taken as the average slope of the graph for different positions before and after tests

Figure 4.7(a) and (b) show that VBM calibration factors before tests in forward links are somewhat different from those measured after. This was due to the effects of tape and the latex sealing between the model segments. In the upside down position, the segment gaps open up and the rubber latex stretches at high VBMs. After tests because of the cyclic loadings, the sticky tapes and latex would sustain permanent deformation thus having a reduced effect on measured strains. The average calibration factors taken from before and after tests are presented in Nm/V in Table 4.1 where the

total signal gain was 600. The Mean Square Error (MSE) in measuring the VBM calibration factors was 0.5 which is in the acceptable range.

Table 4.1: Elastic Links vertical Bending Moment Calibration Factors in Nm/Volts

Elastic link	Before test Cal. factor	After tests Cal. factor	Average Cal. factor
Forward Starboard	6.358	6.143	6.2505
Forward Port	6.181	6.049	6.115
Aft Starboard	6.075	NA	NA
Aft Port	6.58	6.587	6.538

The aft starboard elastic link strain gauges glue failed and after several days of experiments exhibited strong effects of hysteresis in the results. However, because of the similarity of VBM magnitudes for the aft port and aft starboard elastic links in head seas, it was decided to use the portside demihull VBMs and assume the same value for the starboard strain gauge.

4.3. Centrebow load calibration

As mentioned in Chapter 3, section 3.5, the calibration factor for each 6DOF Force transducer is a square matrix as shown in Equation (3-11),

$$\begin{bmatrix} F_x \\ F_y \\ F_z \\ M_x \\ M_y \\ M_z \end{bmatrix} = [\text{Calibration matrix}]_{6 \times 6} \times \begin{bmatrix} Sg0 \\ Sg1 \\ Sg2 \\ Sg3 \\ Sg4 \\ Sg5 \end{bmatrix} \quad (3-11)$$

where $Sg0$, $Sg1$, $Sg2$, $Sg3$, $Sg4$ and $Sg5$ are the recorded signals from six channels and the F_x , F_y , F_z , M_x , M_y and M_z are the forces and the moments respectively. The load cells are factory calibrated and the calibration factors for the forward and aft sensor are given in Table 4.2 and Table 4.3 respectively.

Table 4.2: The Calibration Matrix for Forward Force Transducer

-0.2785	0.202407	1.788225	-44.6952	-1.81246	48.2805697
-2.33037	53.44771	0.886298	-26.2054	1.139556	-27.7213097
66.63692	-1.82108	65.99514	1.931545	66.75537	-3.88160105
-0.02327	0.370261	-1.07653	-0.2134	1.061903	-0.25187072
1.239785	-0.03864	-0.64308	0.292034	-0.59219	-0.29983543
0.03922	-0.68743	0.010628	-0.65487	0.030917	-0.70530096

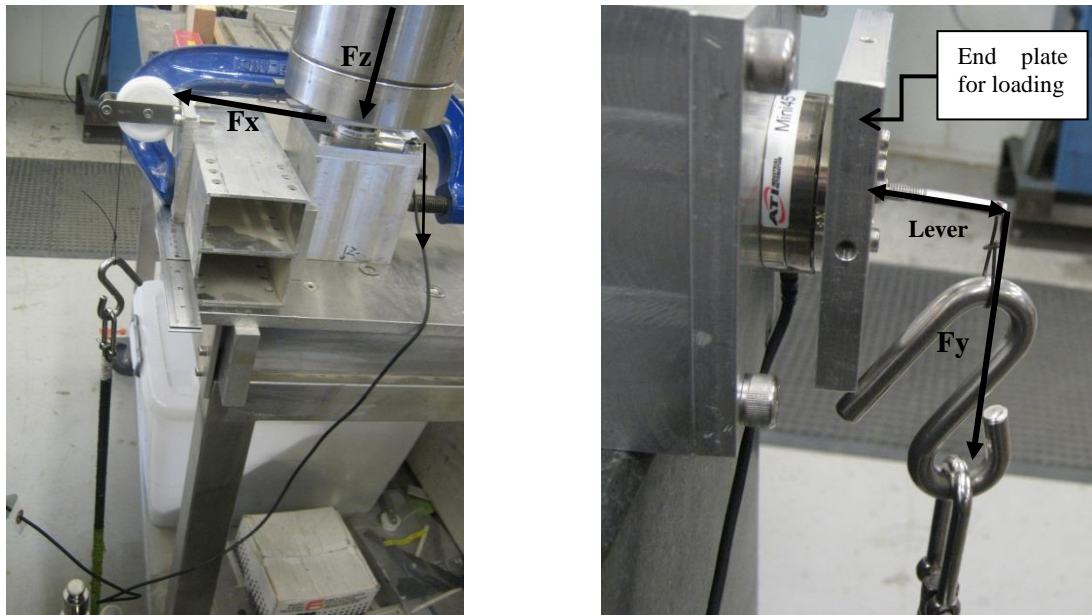
Table 4.3: The Calibration Matrix for Aft Force Transducer

0.63155	0.212611	0.254298	-44.3706	-0.22076	45.8508298
-1.70411	53.48305	0.171458	-26.0937	0.137037	-26.6726899
68.04531	-3.19484	68.24643	-2.33417	67.02297	-1.91046562
-0.02653	0.371649	-1.10583	-0.14711	1.085227	-0.21316571
1.239406	-0.05649	-0.65435	0.32754	-0.61449	-0.29949682
0.03534	-0.67932	0.008857	-0.65724	-0.01081	-0.67452842

A comprehensive set of calibration tests was required to integrate and determine the calibration matrixes. Since the MINI45 Force transducer is calibrated in the factory with high accuracy, it was decided to conduct only calibration checks to ensure the correct DAQ system setup and accuracy of the total centrebow load measuring system in situation. The calibration check involved two stages for this work; firstly, each individual sensor was exposed to combination of loads and secondly, the centrebow load measuring system including both sensors on the model was tested.

4.3.1. Individual 6DOF force transducer calibration check

To check each sensor individually, an aluminium rigid mounting block was manufactured to locate the 6DOF force transducer. The calibration rig being clamped on a rigid table is shown in Figure 4.8 where moments were applied by applying weights on a lever arm to the end plate. Loads were applied in various combinations to the sensors and by using factory calibration factors, the measured loads were compared with the actual loads.

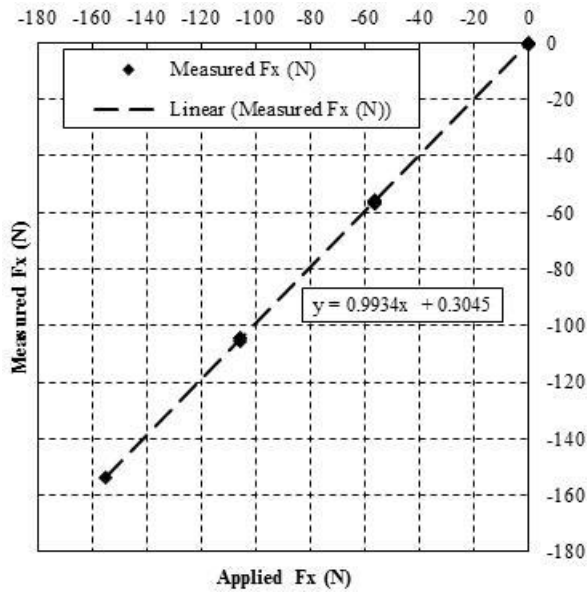


(a) The combination of F_x and F_z applied simultaneously to the sensor

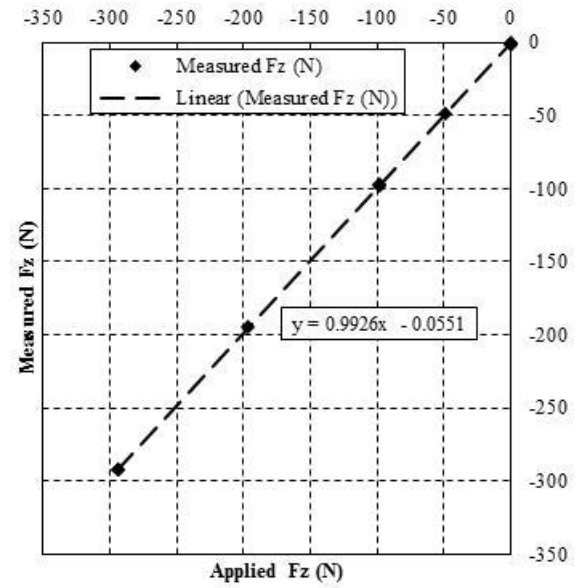
(b) Applying M_x and F_y on the end plate of the calibration rig

Figure 4.8: Some of the load combinations applied on individual 6DOF Force transducers. An especial rig including a rigid base and an end plate were designed for this purpose

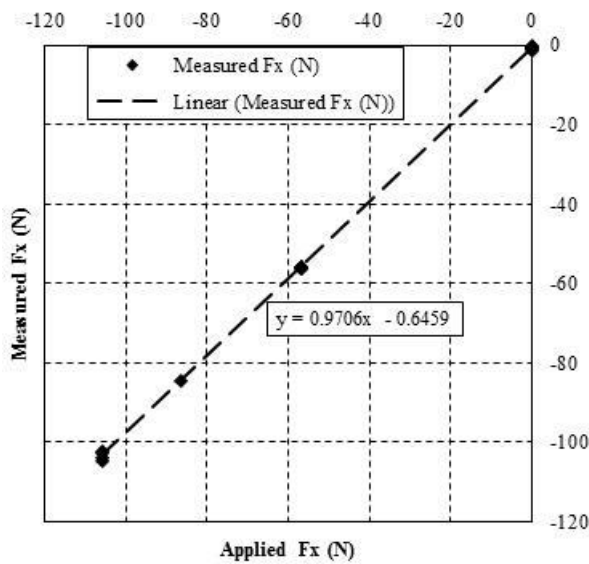
Figure 4.9 shows the result from the applied and measured forces demonstrating the accuracy of the sensors. The force measurement errors are less than 1% in both the horizontal and vertical direction for the forward sensor. For the aft sensor, the errors were less than 0.05% and 3% in vertical and horizontal directions respectively. Both sensors showed acceptable accuracy and hence, no further calibration was considered necessary.



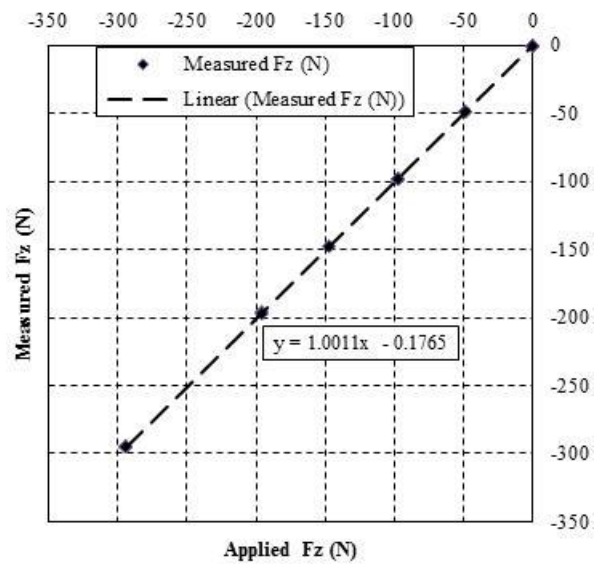
(a) Forward Sensor, F_x shows less than 1% error



(b) Forward sensor, The F_z shows less 1% error



(c) Aft sensor, The measured F_x shows less than 3% error



(d) Forward sensor, the measured F_z shows less than 0.02% error

Figure 4.9: Results of calibration check for the individual forward and aft 6DOF force transducers

4.3.2. Calibration check for centrebow load measuring system

For calibration of the centrebow in measuring loads and predicting the slam locations, the model was placed on a rigid frame and the centrebow was loaded by point loads in various locations. As seen in Figure 4.10, to load the centrebow upward, the model was placed upside down and six attachment points were located inside the centrebow. The weight application points were labelled Point1 to Point6 from the aft to forward positions as illustrated in Figure 4.11.

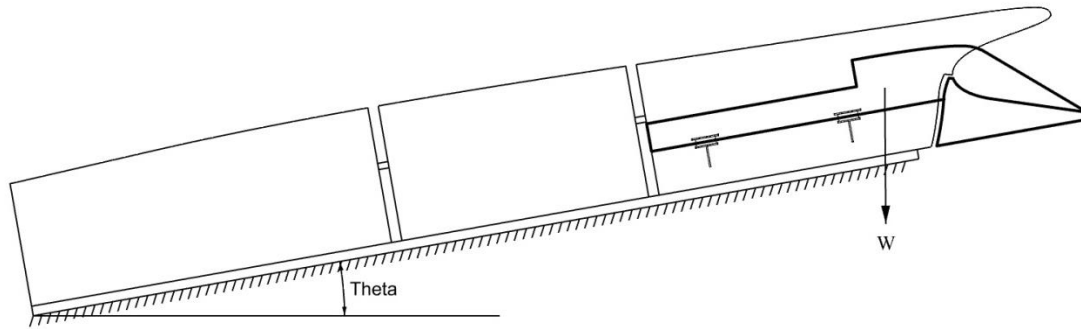


Figure 4.10: The centrebow loads calibration setup. The model was set upside down and loaded in angles to evaluate the accuracy of the load measuring system

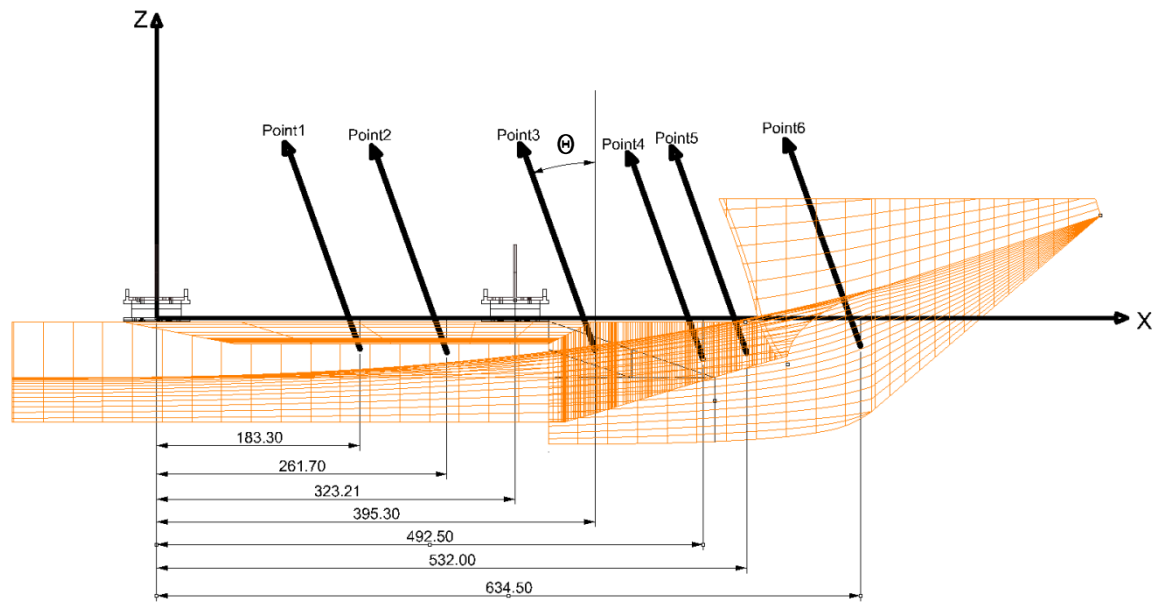


Figure 4.11: Centrebow load application points locations measured from the aft sensor (distances are in millimetres)

Table 4.4 show the coordinates of the load points from the local origin set at the tool side of the aft sensor. Each point was loaded by varying loads from 2 kg up to 30 kg using a hook and string. Since slam forces at an angle needed to be measured (with a horizontal component), it was decided to evaluate the centrebow load measuring system against both vertical and inclined loads. Therefore, loads were applied at various positions including vertical, 4.65°, 9.35° and 19.7°. By adding the results of both sensors together, the total measured loads were calculated.

Table 4.4: Loading Conditions and The Location of The Application Points (W:with; W/O:without)

Location	X-Coord. (mm)	Z-Coord. (mm)	Inclined angles (Θ)			
			0 degree (vertical)	4.65 degree	9.35 degree	19.7 degree
Point 1	183.3	-27.8	W- W/O tapes	W. tapes	W. tapes	W. tapes
Point 2	261.7	-30.95	W- W/O tapes	W. tapes	W. tapes	W. tapes
Point 3	395.3	-29.1	W- W/O tapes	W. tapes	W. tapes	W. tapes
Point 4	492.5	-37	Discarded	Discarded	Discarded	Discarded
Point 5	532	-31.7	W. tapes	W. tapes	W. tapes	W. tapes
Point 6	634.5	-25.2	W. tapes	W. tapes	W. tapes	W. tapes



(a)The model set up in 19.7 degree Position for loading the centrebow



(b)The weights were hung with ahook and string from the centrebow

Figure 4.12: The centrebow loads calibration setup. The model was set upside down and loaded in angles to evaluate the accuracy of the load measuring system

Figure 4.13 shows the result from the calibration tests on the applied and measured loads in the Z-direction. It is seen from this plot that the system has less than 1% relative error in measuring F_z independent of load application point (when loads are vertical). The calibration experiments were also conducted for the same conditions without sealing rubber tapes to investigate the effect of tapes on the measured loads. The results showed that in all loading conditions the sealing effect is less than 1.5% of the applied loads.

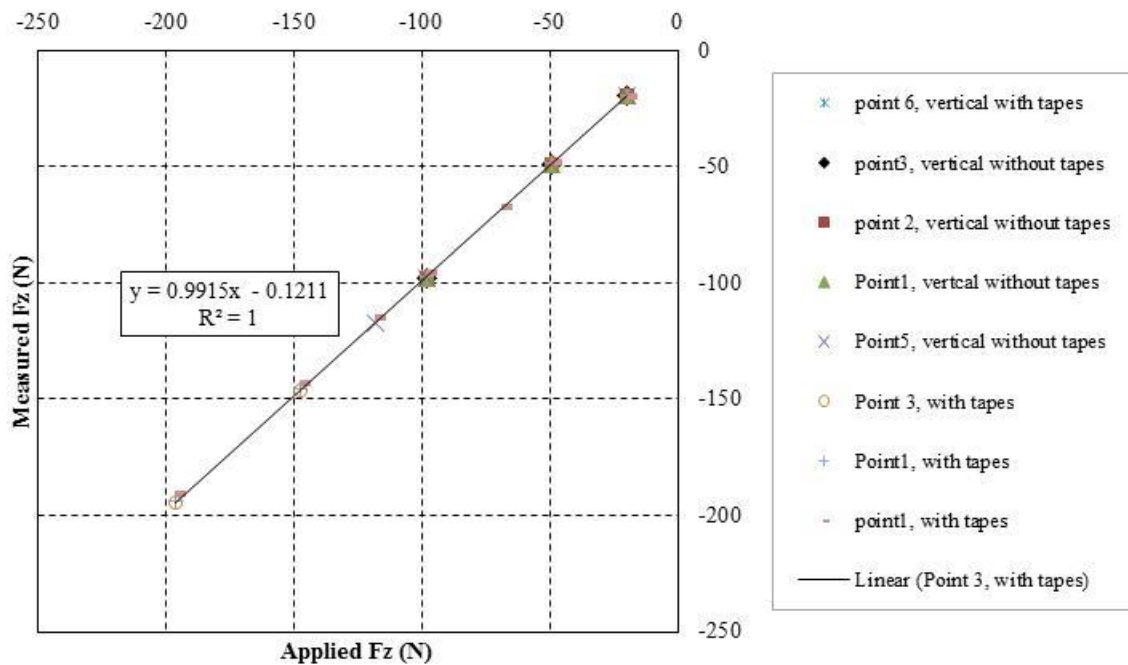


Figure 4.13: Measured vertical applied load and the measured vertical loads (F_z) in vertical loading setup

Comparing this graph with HSM01 results from Matsubara [51, 104] indicates the improvement achieved by changing to the new centrebow load measuring system. Figure 4.14 shows individual centrebow transverse beam forces in one of the calibration cases in which the forces were applied

vertically on the centrebow, 1.956 m from transom. The adjusted points are after Matsubara correction efforts. As seen the second row graphs, the force discrepancies for the HSM01 model are significant. This issue has since been resolved for HSM01 by relocating the four transverse beam mounting pivots on that model in the plane of the transverse beams instead of below that plane.

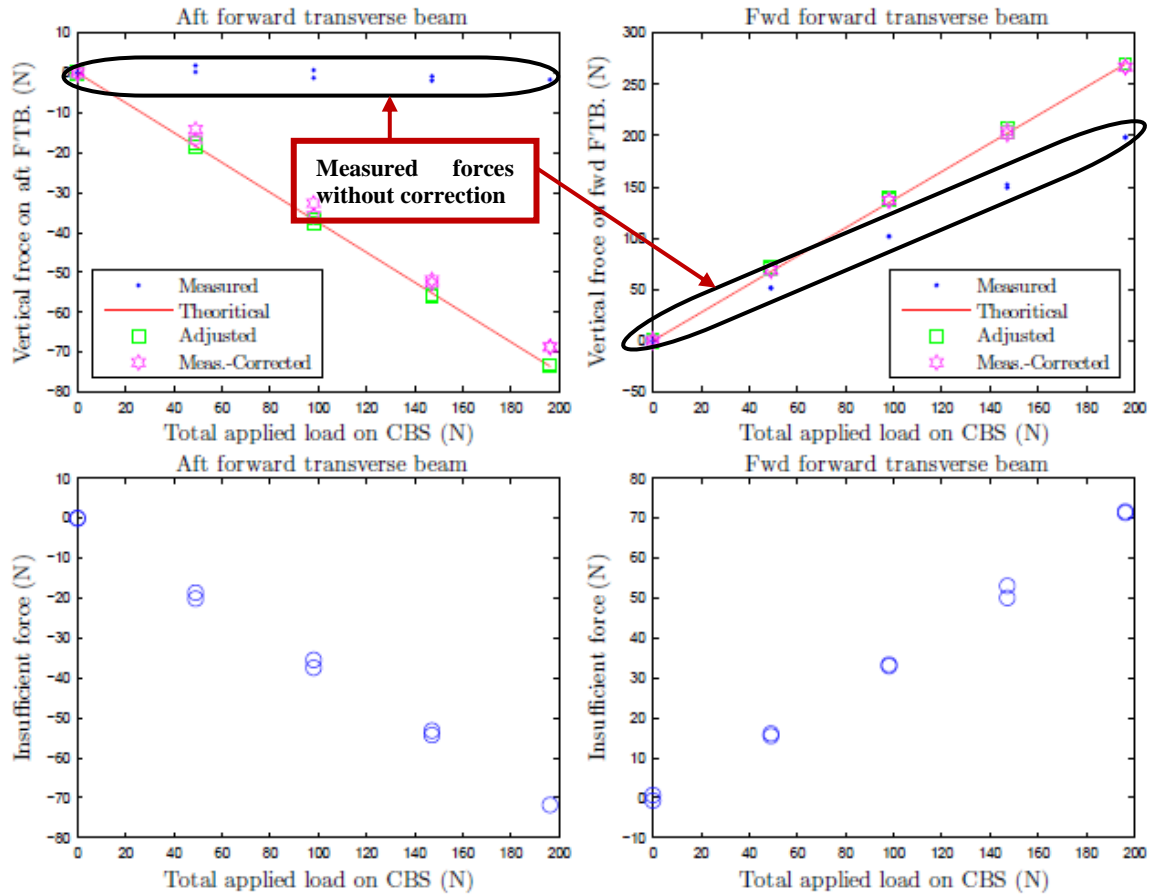


Figure 4.14: Applied load and the measured forces in HSM01 performed by Matsubara (thesis, page 80) [51]. The first row shows the applied and measured vertical forces 1.956 m from transom, versus the 1:1 line. The left is for the aft transverse beam (FTB) and the right is for the forward beam gauges. The second row graphs show the insufficient forces predicted by each transverse beam (CBS stands for centrebow segment)

Figure 4.15 shows that the centrebow load measuring system has less than 0.5% error in predicting the applied load location when applying vertical forces. Again comparing these results with HSM01 results in predicting the force locations as seen in Figure 4.16 shows the improvement achieved by applying this method [51].

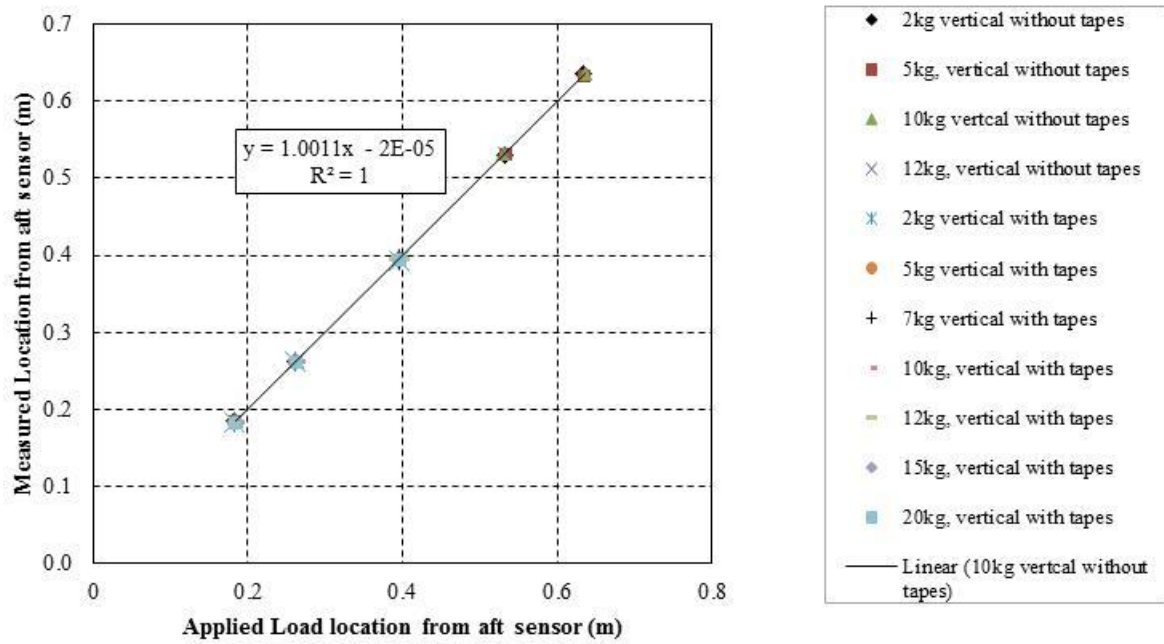


Figure 4.15: Applied load location and the measured location from the aft 6DOF force transducer. The trend line slope shows less than 0.5% error in predicting locations

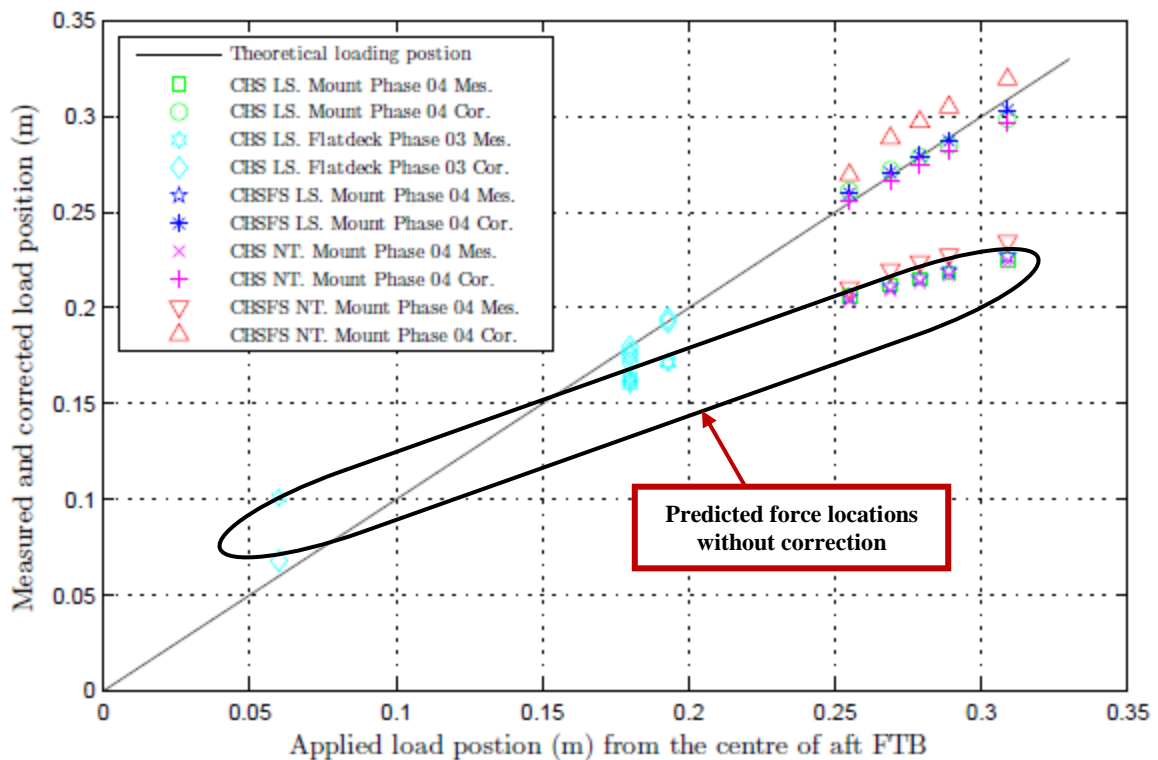


Figure 4.16: Applied load location and the measured location from the aft centrebow transverse beam (FTB) in HSM01 performed by Matsubara (thesis, page 83) [51]. The results before applying correction could predict the forces up to 80 mm astern the actual location

The results for inclined setups are shown in Figure 4.17. There is under 2% error in 19.7 degree setup, and under 4% and 5% error in 9.35 degree and 4.6 degree setups respectively. The reduced accuracy in smaller angle setups could be due to the centrebow structure and the frame deflections which makes the definition of the small angles difficult.

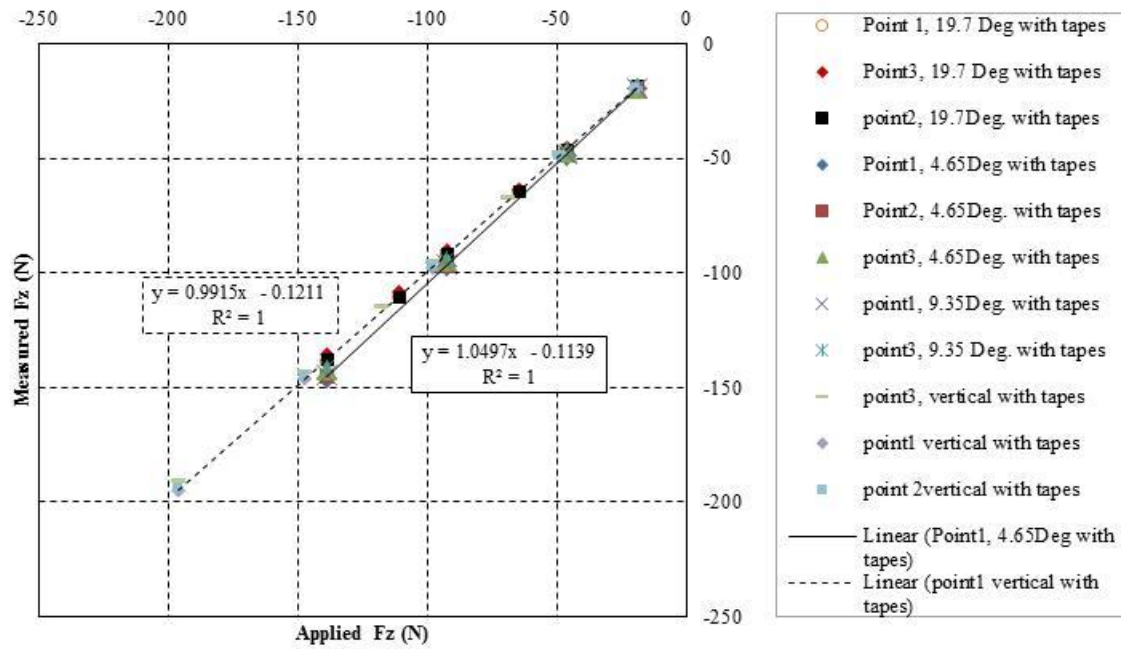


Figure 4.17: Measured vertical loads versus applied vertical loads (F_z) in different loading angle setup. The vertical setup and higher angles setups show less than 1.5% error in measuring the applied loads; for small application angles the relative error could be around 5%

In Figure 4.18 the results of horizontal component measurements are shown. The horizontal centrebow force calibrations show less than 1% relative error in 19.7° about 12% in 9.35° and 23% relative error in 4.6° The reduced accuracy in smaller angles can be attributed to the structural deflections and adding the large noise to signal ratio effects. Later in the tank tests, the angle of the slam loads was measured to be between 15° to 33° where the calibration results in horizontal direction are considered to be in the acceptable range.

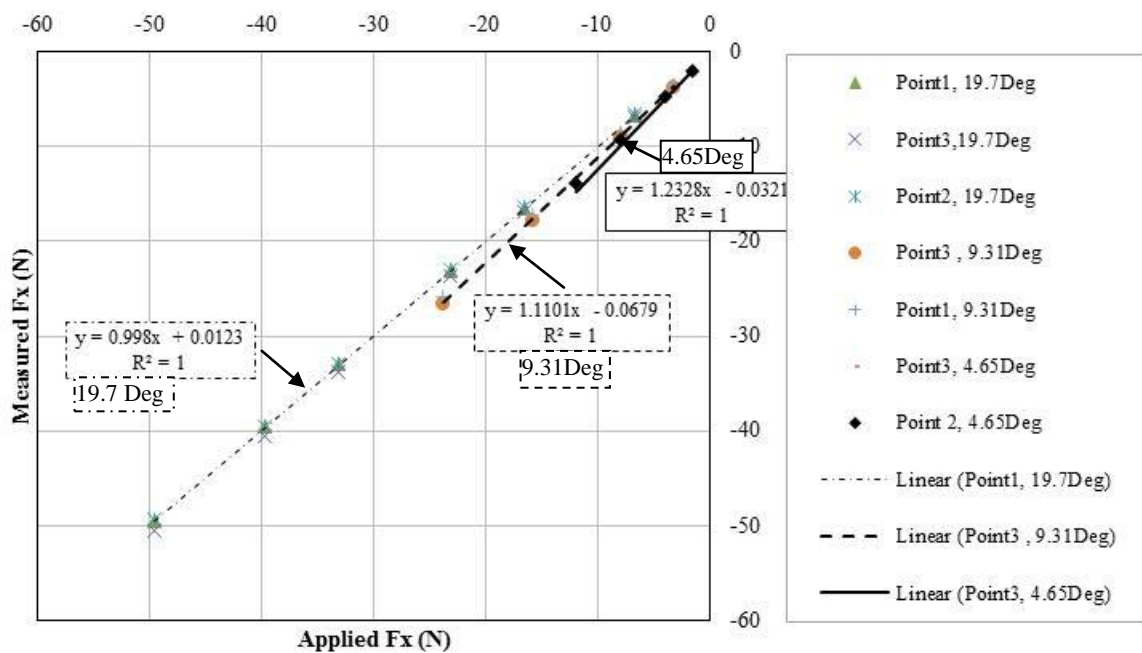


Figure 4.18: Measured horizontal load versus applied Horizontal force (F_x) in different inclination setups. The larger the angle, the more accurate is the load measurement

4.4. Summary

As presented in this chapter, the designed and constructed hydroelastic segmented model HSM02, by having 14.7 Hz whipping frequency, demonstrates the correct dynamic behaviour similar to the full-scale 112 m INCAT wave-piercing catamaran. The elastic links incorporated in between the segments can be used to measure VBM confidently, since the calibration process showed acceptable accuracy. Also the HSM02 does not have the problems with the aft wetdeck and VBM transfer from loads on the aft wetdeck to the model mid-segment. The possible modal confusion caused by having the aft wetdeck as a cantilever beam is also removed. Overall, the model is simpler than HSM01, eliminating the bulky aluminium beams used in HSM01. The total light weights of both models were quite similar, due to the addition of adjustable bow components in HSM02.

The calibration of the new centrebow load measuring system using two 6DOF force transducers showed high accuracy in measuring vertical (less than 1% error) and inclined centrebow forces (less than 4% error). The predicted force location on the centrebow also showed very high accuracy (being less than 0.15% of overall hull length in error) in vertical loading conditions and of acceptable accuracy (less than 0.5% of overall length) in inclined loading conditions. Comparing these forces with the results of HSM01, we see that there is a significant improvement in accuracy of measuring the slam forces on the centrebow. The horizontal centrebow forces have also been calibrated successfully without any corrections on the model. The calibration results showed that by increasing the inclination angle, the accuracy increases such that in 20 degrees the average error is less than 0.3% in measuring horizontal force components.

5. Effect of centrebow length on motions and loads: experimental process, results and discussion

In this chapter, the experimental facilities, test conditions and results of the experiments on the hydroelastic segmented catamaran model (HSM02) are presented. The seakeeping behaviour, slam loads and VBM of the HSM02 in head seas were all investigated in relation to the centrebow design. The three centrebow shapes, as explained in Chapter 3, the “long centrebow”, “parent centrebow” and “short centrebow”, were tested in controlled environmental conditions and the results compared. These results are interpreted and conclusions are drawn on the effect of centrebow length on the motions and loads of large high-speed wave-piercing catamarans.

5.1. Experimental Procedure

5.1.1. Facility

The experiments were conducted in the Australian Maritime College (AMC) towing tank facilities in October and November of 2011. The towing tank is 100 m long, 3.5 m wide and 1.5m deep and incorporates a carriage that runs on rails positioned on the tank walls, up to speeds of up to 4.5 m/s. The model was towed using a two post towing system, allowing the model to freely heave, pitch and roll. Figure 5.1 shows a photo of the carriage and the towing tank. The data acquisition system (DAQ) and the operator are onboard the carriage whilst it is in motion along the tank.



Figure 5.1: The towing tank carriage and the HSM02 on the water

The speed of the carriage is measured by use of the encoders installed on the casted wheels of the carriage and is recorded as the first channel in the DAQ system. The towing tank is equipped with a

hydraulically-powered positive displacement wave maker at the end of the tank that can generate waves of various heights and frequencies. A sloped beach wave absorber is positioned at the other end of the tank to absorb the incident waves. There is also a side beach in the tank that can be used to accelerate the dampening of the waves between runs. In the experiments, the carriage was set in motion before the waves reached the end of the tank to avoid wave reflections; hence the first few acquired encountered waves data were disregarded in the analysis.

5.1.2. Model setup

After the model dimension checks, the sensors and other instruments were installed and the model was ballasted at level trim. The LCG of the model and each segment were also measured by balancing the model on a rod on a smooth table. The pitch radius of gyration (RoG) of the model was determined by using the Bifilar technique [3]. For this method the model was hung using two strops from an aluminium horizontal beam. As seen in Figure 5.2 the beam itself was hung from two long steel cables allowing the model to swing around its LCG in horizontal plane with small angles. The period of the swings was then used to calculate the pitch RoG of the model.



Figure 5.2: The set up for Bifilar swing test to estimate the model pitch radius of gyration

The centrebow had a main piece and two extension pieces to create the parent and the long centrebow. The weight of the main piece or the short centrebow was 2.42 kg; the weight of the parent centrebow extension piece was 0.198 kg and the additional long centrebow extension piece was 0.202 kg. To keep the three centrebow mass distributions consistent, the heavier long centrebow configuration was taken as the base and counterweights were used for the parent and short centrebows (when the extension pieces were out). The dimensions and other model particulars and their corresponding full-scale values are given in Table 5.1.

Table 5.1: HSM02 Model Particulars

Item	Model scale	Full-scale
Scale factor	1/44.8	1
Length overall	2.5m	112 m
Demihull length	2.35 m	105.6 m
Displacement	27.7 kg	25530 tonnes
LCG	0.941 m from transom	42.15 m from transom
Radius of gyration (RoG)	0.67 m from LCG	30.16 m from LCG
Forward segment mass, LCG	8.37 kg, 1.804 m	-
Mid segment mass, LCG	7.57 kg, 1.298 m	-
Aft Segment mass, LCG	11.76 kg, 0.381 m	-
Trim	0 degrees	0 degrees
Fundamental structural modal frequency in calm water	14.7 Hz (measured)	2.2 Hz

5.1.3. Instrumentation and data acquisition

Wave measurement: to measure the wave elevation, resistance wave gauges were used. These wave probes are used for measuring rapidly changing water levels by measuring the current that flows between two stainless steel wires immersed in water. The current is then converted to voltage and amplified through a wave probe conditioner. The output voltage is proportional to the water surface height between the rods. One static wave probe, located 5 m from the wave maker, and two moving wave probes on the carriage were used to measure the wave elevations. Figure 5.3 shows a photo of the static wave probe in front of the wave maker; Figure 5.4 shows the wave probe conditioner, which is a 3 channel Wave Monitor made by Churchill Controls Ltd.

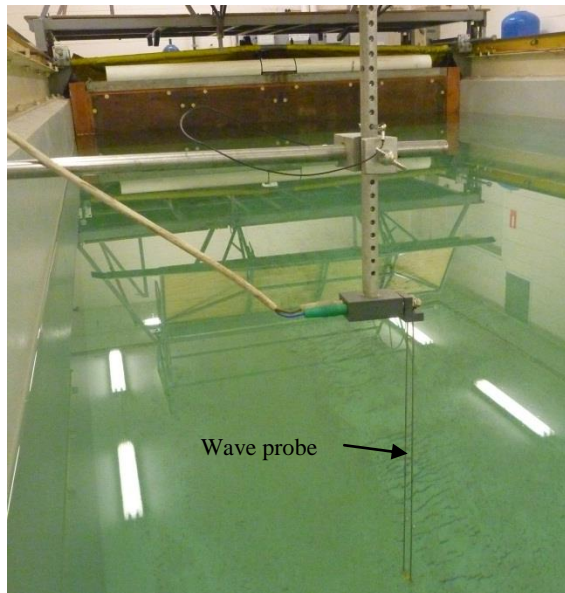


Figure 5.3 The static resistance wave probe which was located 5 m from the wave generator

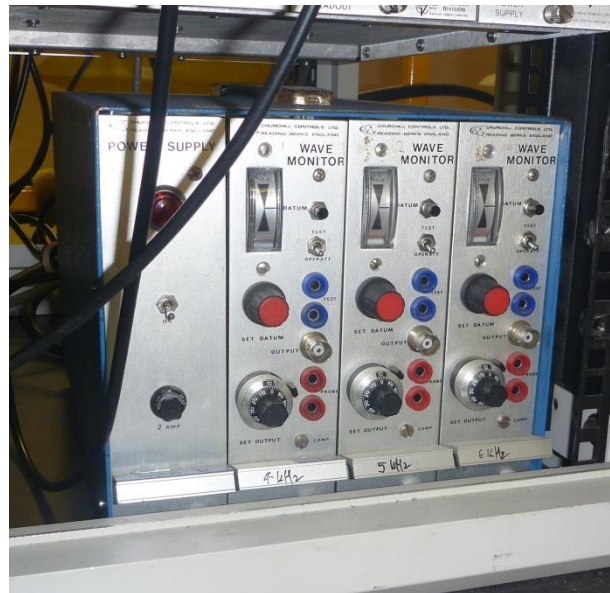


Figure 5.4: The wave probe signal conditioner

Using the static wave probe, the generated waves were measured for 10 seconds before each carriage run, since the towing tank carriage had to be detached from connectors before starting the run. The moving wave probes were installed under the carriage, one in-line with the model LCG and one in-line with the parent centrebow truncation point. The moving wave probes were placed at a sufficient

distance (approximately 0.8 m away from the model side-walls) from the model to not be affected by the model/wave interactions.

During the tests the wave probes were calibrated every morning to help ensure the accuracy of the results. The gain was 2.5 and the signals were analogue low-pass filtered at 1 kHz. The gauges were calibrated to plus and minus 60 mm from the calm water level. Table 5.2 presents the calibration factors of the final three days of testing where the errors are presented as Mean Square Errors (MSE). As seen in the table, the errors are less than 2% full-scale and are considered sufficiently accurate.

Table 5.2: Wave Probes Calibration Factors and the Errors Involved in Three Days of Testing

Wave probe	Day 1 (parent centrebow)		Day 2 (short centrebow)		Day 3 (long centrebow)	
	Cal. Factor	Error (MSE.)	Cal. Factor	Error (MSE.)	Cal. Factor	Error (MSE.)
Ch4- Static wave probe	8.4179	0.03	8.4154	0.05	8.3677	0.04
Ch5- Centrebow wave probe	5.5852	0.33	5.6127	0.21	5.6262	0.4
Ch6- LCG wave probe	10.142	0.92	9.9803	1.52	10.038	1.54

Model motion measurement: the forward post towed the model and the aft post, connected to a longitudinal slider, prevented the model from yawing or swaying. The tow posts could freely move up and down, hence the model could heave and pitch freely; the model was also free to roll due to the ball joint at the base of each post. Figure 5.5 shows the arrangement of the two posts in the model. The relative motions of the two posts and their position to the LCG enabled the heave and pitch magnitudes to be determined. The distance between the two posts was 764.5 mm and the the forward tow post was located 17.6 mm ahead of LCG.

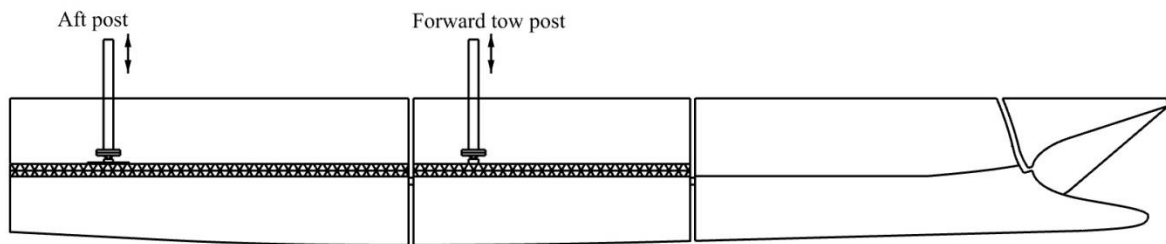


Figure 5.5: The arrangement of the posts connecting the model to the carriage. The forward tow post tows the model and the aft post is located on a longitudinal slider. The motions of the model are calculated from the relative vertical motion at the two posts

Each post had a Linear Variable Differential Transformers (LVDT) attached to measure the vertical motions. The LVDTs use a moving ferromagnetic core that changes the induced voltages between a primary coil and two secondary coils. The voltage signals were conditioned through LVDT conditioners and then digitised and recorded onto the DAQ card. The forward and aft LVDTs were calibrated to plus and minus 120 mm and the calibration factors and mean square errors through the three days of the experiments are shown in Table 5.3. As seen, the calibration factors have barely changed over different days and the very small errors indicate highly accurate vertical motion measurements.

Table 5.3: Calibration Factors and Errors of LVDT Motion Sensors during Three Main Test Dates

LVDT	Day1 (parent centrebow)		Day2 (short centrebow)		Day3 (long centrebow)	
	Calibration Factor	Error (MSE)	Calibration Factor	Error (MSE)	Calibration Factor	Error (MSE)
Ch1_FWD LVDT	-12.63	0.01	-12.627	0.01	-12.629	0.01
Ch2_Aft LVDT	-12.677	0.06	-12.677	0.06	-12.678	0.06

The DAQ card used was a 32-bit National Instrument PCI-6254 M Series, which takes the analogue signals from two 16 channel BNC-2090 racks. All the signal cables were terminated with a BNC connector to enter the DAQ card. The sampling rate was set to 5000 Hz for all the data channels to capture pressure peaks with sufficient resolution. This sampling frequency was chosen with reference to Amin [20] who conducted slam pressure mapping on the HSM01. Later in this chapter, the result of using this sampling frequency on pressure signals is discussed. As mentioned in Chapter 3, the pressure transducers are ENDEVCO piezoresistive differential pressure transducer Model 8510C-50 along with DC amplifier Model 136 from ENDEVCO.

During the experiments, there were 32 channels of signals recording on the DAQ card. One channel was for recording carriage speed, two channels for recording motions (LVDTs), one channel for recording centrebow accelerations, three for recording wave probes signals, four to record strains in the elastic links, 12 channels for the two 6DOF force transducers and nine channels to measure pressures. Table 5.4 shows the channels and the signal conditioning units used on the DAQ card. The speed of the carriage was measured by use of the encoders installed on the cast wheels of the carriage. A video camera recorded the tests from the starboard side of the model capturing the bow-wave interactions. The details of the pressure transducers, 6DOF force transducers and the strain gauges in this table are outlined in Chapter 4.

Table 5.4: DAQ Card Set Up For Recording the Sensor Signals and Each Channel's Signal Conditioning Units

Ch. No	Channel name	Instrument	Signal conditioning unit	Sample Rate
1	Ch0_Speed	Carriage speed	Carriage dynamometer	5kHz
2	Ch1_Fwd LDVT	Forward LVDT	LVDT conditioner	
3	Ch2_Aft LVDT	Aft LVDT		
4	Ch3_Accellerometer	Accelerometer on centrebow	B&K 2626 Charge Amplifier	
5	Ch4_Static WP	Static wave probe	Churchill Controls Wave Monitor	
6	Ch5_Centrebow WP	Moving wave probe; in-line with centrebow truncation		
7	Ch6_LCG WP	Moving wave probe; in-line with LCG		
8	Ch7_Pressure 1	Pressure gauge, Frame 72 inside	ENDEVCO Amplifier 136 #1	
9	Ch8_Pressure 2	Pressure gauge, Frame 76		
10	Ch9_Pressure 3	Pressure gauge, Frame 74		
11	Ch10_Pressure 4	Pressure gauge, Frame 72 arch-top	ENDEVCO Amplifier 136 #2	
12	Ch11_Pressure 5	Pressure gauge, Frame 72 outside		
13	Ch12_Pressure 6	Pressure gauge, Frame 70		
14	Ch13_Pressure 7	Pressure gauge, Frame 66	ENDEVCO Amplifier 136 #3	
15	Ch14_Pressure 8	Pressure gauge, Frame 64		
16	Ch15_Pressure 9	Pressure gauge, Frame 60		
17	Ch16_SG FWD STBD	Demihull strain gauge, forward starboard	Vishay Signal Conditioning Amplifier 2100	
18	Ch17_SG FWD Port	Demihull strain gauge, forward port		
19	Ch18_SG Aft STBD	Demihull strain gauge, aft starboard		

20	Ch19_SG Aft Port	Demihull strain gauge, aft port		
21	Ch20_SG0-1	Forward centrebow 6DOF Force transducer (FT1)	Power Supply and Interface box#1 (IFPS1)	
22	Ch21_SG1-1			
23	Ch22_SG2-1			
24	Ch23_SG3-1			
25	Ch24_SG4-1			
26	Ch25_SG5-1			
27	Ch26_SG0-2	Aft centrebow 6DOF Force transducer (FT2)	Power Supply and Interface box#2 (IFPS2)	
28	Ch27_SG1-2			
29	Ch28_SG2-2			
30	Ch29_SG3-2			
31	Ch30_SG4-2			
32	Ch31_SG5-2			

The forward tow post was located on the mid-segment and the aft tow post was located on the aft-segment of the HSM02. This raised the possibility of model flexibility affecting motion measurements with tow posts. Therefore, in addition to the signals acquired above, an IMU440 Crossbow inertial system (see Figure 5.6) was located on the wet deck at the LCG to measure pitch angles and linear accelerations. The Crossbow was connected to a RS232 port on the computer and was recording in a separate file with a 100 Hz sample rate. The result of the pitch motions analysis showed that the difference between LVDTs and Crossbow was an average 2% of the measured angle.



Figure 5.6: Crossbow IMU440 inertia system to measure pitch motions and linear accelerations

5.2. Test conditions

The three centrebow configurations were tested at 1.53 m/s and 60 mm of wave height, which correspond to 20 knots and 2.688 m of wave height at full-scale. Due to the complexity of the instrumentation and model set up for testing in different conditions, the main aim was to obtain high quality results for limited conditions rather than testing many conditions. Regular waves were generated from frequencies of 0.4 Hz up to 1.2 Hz, with intervals of 0.5 Hz or 0.25 Hz. More resolution around resonant peaks was achieved by conducting tests at smaller frequency intervals. Table 5.5 shows the test conditions at model and full scale. The water depth was set to 1.4 m to avoid collisions between the top of the model and the lower frames of the carriage during severe motions. The average water temperature was 18°C, the average air temperature was 21°C and the density of the water was 998.85 kg/m³ during the experiments.

Table 5.5: Towing Tank Test Conditions for testing HSM02 Model

Condition	Model speed		Wave height (mm)		Wave frequency (Hz)	
	Model (m/s)	Full-scale (knots)	Model (mm)	Full-scale (m)	Model (Hz)	Full-scale (Hz)
Condition 1- parent centrebow	1.53	20	60	2.688	0.4 - 1	0.06 - 0.14
Condition 2-short centrebow	1.53	20	60	2.688	0.4 - 1.2	0.06 - 0.18
Condition 3- long centrebow	1.53	20	60	2.688	0.4 - 1.2	0.06 - 0.18

5.3. Results and discussion

In this section, the motion and loads results are presented and discussed. The slam resultant force locations and slam directions are also presented. One particularly interesting case which showed clearly the interaction between slam events and the motions of the vessel is also discussed.

5.3.1. Motions

Sample time series data for the heave and pitch are shown in Figure 5.7 (at run 45 at a wave frequency of 0.75 Hz). The heave and pitch values for a run were calculated as the magnitude between the average of peak values and the average of trough values when the motions were steady. The ramping up of the wave height can be clearly seen. As mentioned earlier, these first encounters were ignored.

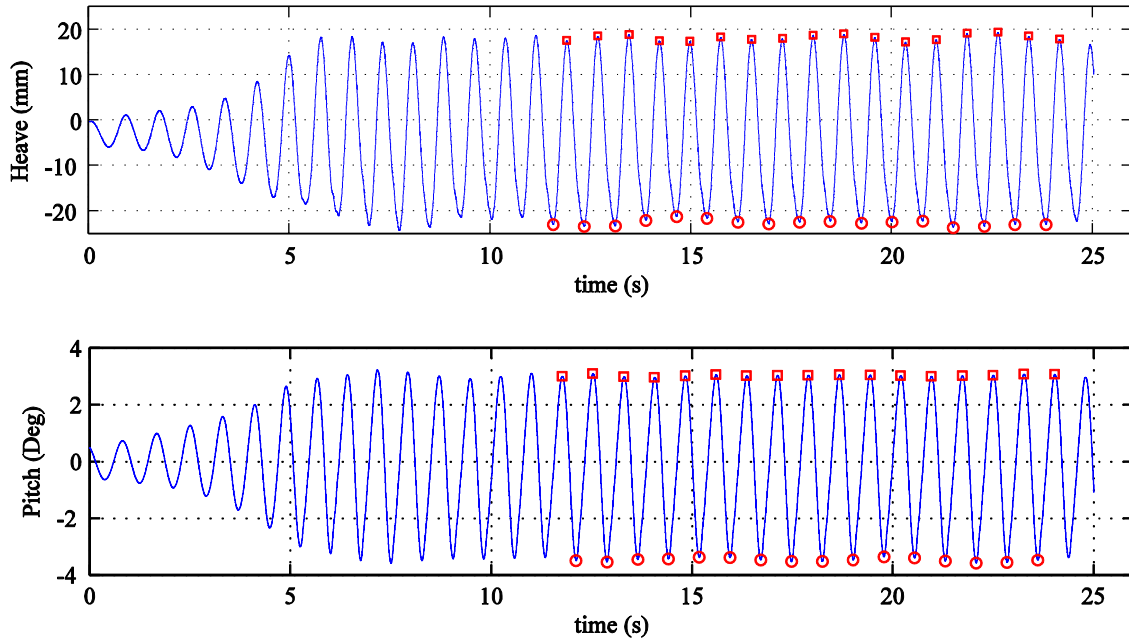


Figure 5.7: Sample heave and pitch raw data (run 45, $H_w=60$ mm, $H_w=60$ mm, speed=1.53 m/s, wave frequency=0.75).

Motion results for seakeeping experiments are usually presented in non-dimensional values. Non-dimensional heave is the ratio of heave to wave height, as seen in Equation (5-1) where ξ is the wave height and η_3 is the heave value. The non-dimensional pitch is the ratio of pitch value (η_5) to wave slope as defined in Equation (5-2),

$$\text{Non_dimensional Heave} = \frac{\eta_3}{\xi} \quad (5-1)$$

$$\text{Non_dimensional Pitch} = \frac{\eta_5}{k \xi} \quad (5-2)$$

where k is the wave number. Wave slopes for the low frequency waves were corrected for shallow water effects based on semi-empirical dispersion formula provided by Fenton and Mckee [108, 109]. The motions are plotted against non-dimensional encounter wave frequency (ω_e^*) calculated based on equation (5-3),

$$\omega_e^* = 2\pi \times f_e \times \sqrt{L/g} \quad (5-3)$$

where L is the vessel overall length, g is the gravitational acceleration and f_e is the encountered wave frequency observed by the moving wave probes. Figure 5.8 shows the heave response of the HSM02 for the three centrebows. As expected, the heave response in high frequency waves is very small and in the long waves (low frequencies) the heave response tends to one, also there is a local maximum (resonance) around $\omega_e^* = 3.7$.

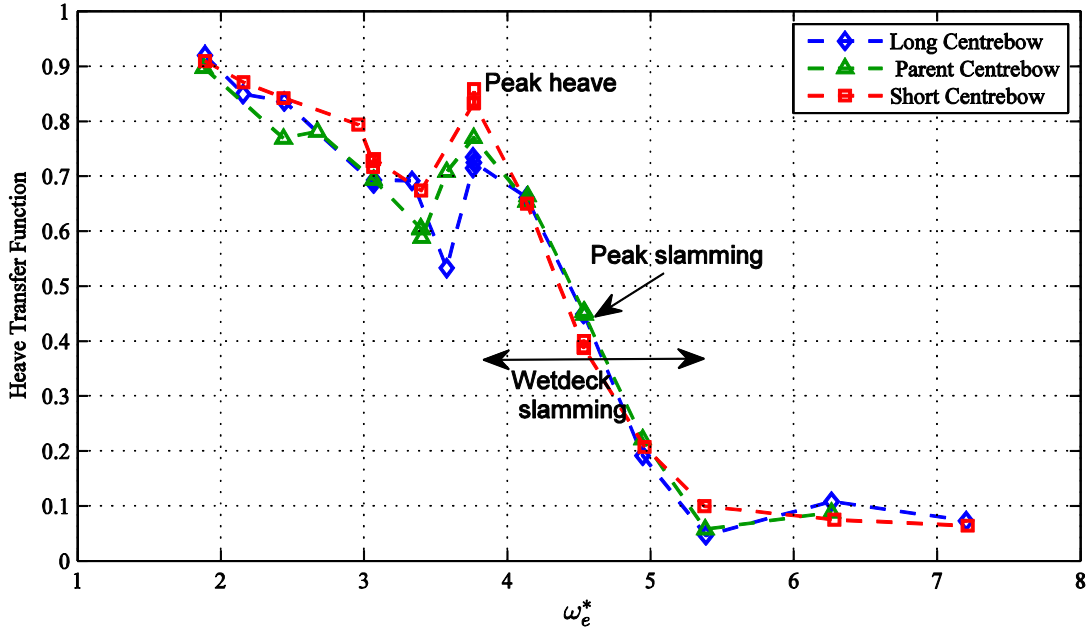


Figure 5.8: Non-dimensional heave response for various centrebow lengths in HSM02 ($H_w=60$ mm, speed=1.53 m/s)

The heave results show that for high and low frequencies, the results for the three centrebows are quite similar; whereas in the resonance frequency region ($3.4 \leq \omega_e^* \leq 4$), the short centrebow has about a 13% higher response compared to the long centrebow. Tests were repeated at $\omega_e^* = 3.7$ to confirm the differences and ascertain the experimental uncertainty. The standard error for non-dimensional heave values was less than 1% for three repeat runs.

Figure 5.9 shows the heave resonant peak versus the three Centrebow Length Ratio (CLR, centrebow length to demihull length) and Centrebow Volume Ratios (CBVR, the ratio of the centrebow volume to total vessel displaced volume). As seen, the resonant heave is higher in shorter centrebows and the reason could be the increased stiffness for longer centrebows due to a larger centrebow volume. In

this plot, the heave responses for the peak slamming condition ($\omega_e^* = 4.53$) are also compared; here the shorter centrebows have slightly (not significantly) lower heave values.

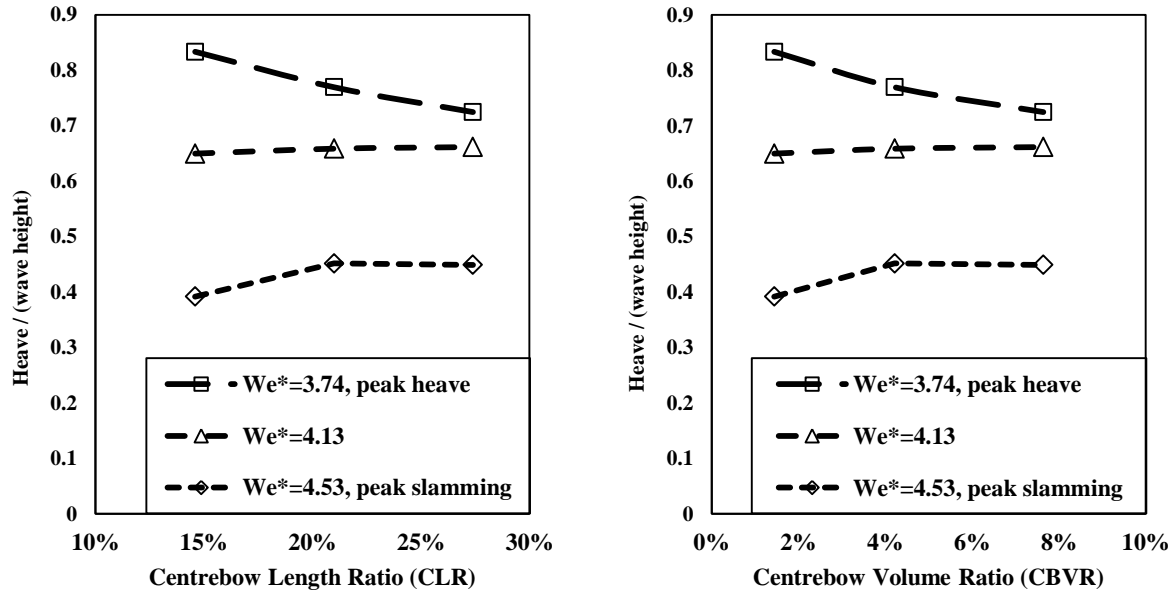


Figure 5.9: Non-dimensional heave response with respect to Centrebow Length Ratio and Centrebow Volume Ratio in different encounter wave frequencies ($H_w=60$ mm, speed=1.53 m/s)

Figure 5.10 shows the non-dimensional pitch response of the three centrebows. As seen, the pitch response also tends to one at low frequency and reduces to zero at high frequency. The pitch motion resonance occurs between $\omega_e^* = 3$ and 3.4 which is slightly lower than the heave resonance frequency. Similarly, less than 1% standard error was observed in the non-dimensional pitch values for three repeat runs.

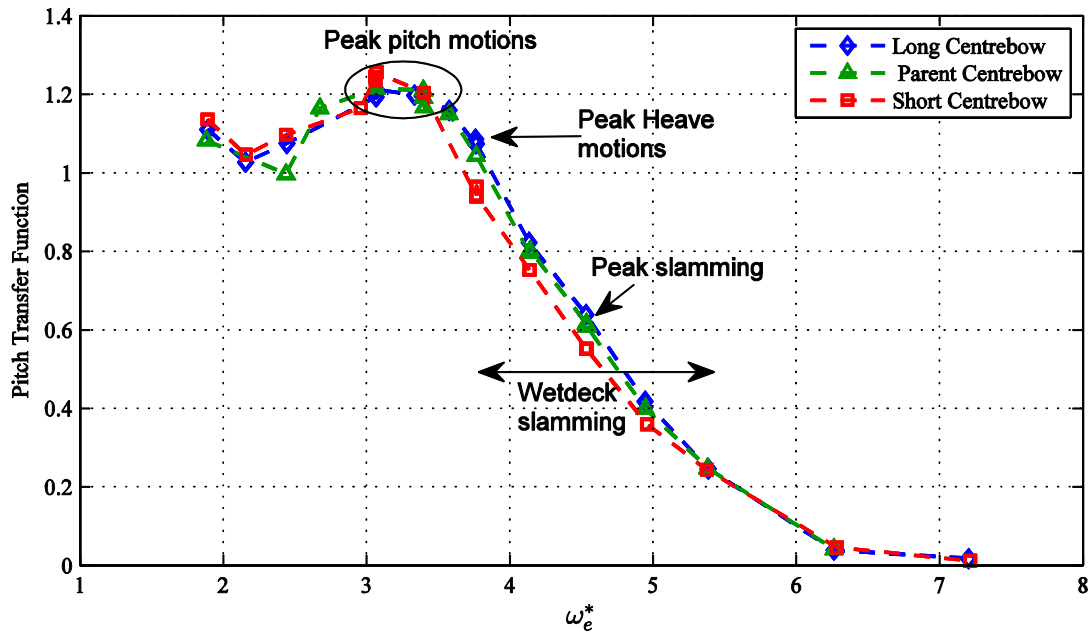


Figure 5.10: Non-dimensional pitch response for the three centrebow lengths in HSM02 ($H_w=60$ mm, speed=1.53 m/s)

The pitch motions show negligible differences between the three centrebow lengths in the resonance frequencies. There is also a slight shift in the pitch resonance frequency between the three centrebow lengths, with the short centrebow having the smallest resonance frequency. If modelling the motions of a vessel by linear equations of motion (spring-damper-mass system), the resonance frequency (ω_n) can be estimated by Equation (5-4),

$$\omega_n = \sqrt{\frac{\text{stiffness}}{\text{Inertia}}} \quad (5-4)$$

where the stiffness of the model is defined by the hydrostatic forces and the inertia of the model is a representative of the mass, mass distribution and the added mass of the vessel. Having the response of a spring-damper-mass system, a shift in the resonance frequency from $\omega_e^* = 3.4$ to $\omega_e^* = 3.05$, with negligible change in the resonance magnitude, can mean that the change in stiffness is more than the change in inertia [110]. The long centrebow has an extension of 150 mm behind the parent centrebow truncation, and the short centrebow is reduced in length by 150 mm. So the lesser volume, in the short centrebow, creates less pitch stiffness compared to the other two centrebows. This is for the pitch resonance frequencies ($3 \leq \omega_e^* \leq 3.7$) where the effect of slamming is very minimal. In frequencies between $\omega_e^* = 3.7$ and $\omega_e^* = 5$ where severe wetdeck slamming occurred during the runs, the pitch response of the short centrebow is on average 5% less than for the long centrebow. The reason for this difference will be discussed in more details in the following sections when the slam loads are compared.

Figure 5.11 shows the comparison of non-dimensional pitch values of the three centrebows for pitch resonant peak value and for peak slamming condition. As seen the resonant peak values reduce only marginally between the three bow lengths but the pitch values at the peak slamming condition increase slightly as the centrebow volume/length increases.

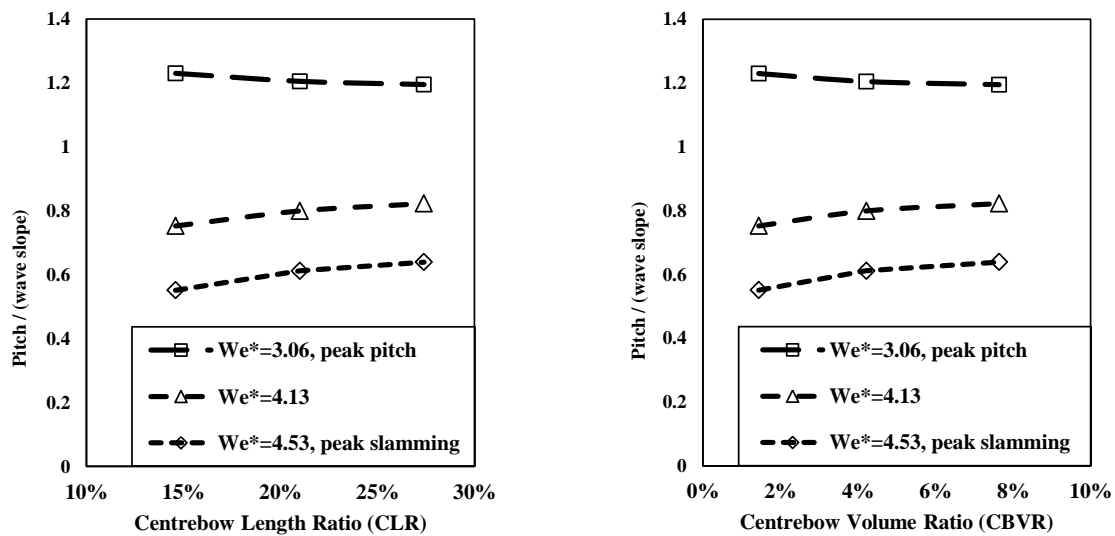


Figure 5.11: The non-dimensional pitch results versus the Centrebow Length Ratio and Centrebow Volume Ratio of the three centrebows in different encounter wave frequencies ($H_w=60$ mm, speed=1.53 m/s)

5.3.2. Centrebow loads

As outlined in Chapter 3, the centrebow load measuring system consisted of two ATI Mini45 6DOF force transducers, which connected the centrebow to the two T-bar transverse beams attached to the demihulls. As shown in Figure 5.12, the upward vertical force and the forward surge direction force on the centrebow are taken as positive. The coordinate axis is attached to the model and moves with it.

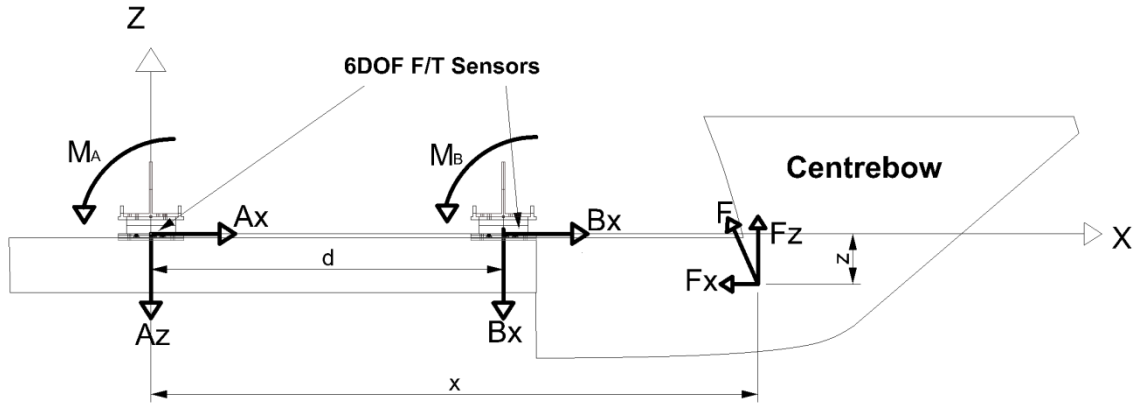


Figure 5.12: The centrebow forces and moments on force transducers. The centrebow force is calculated as the addition of the two sensors' readings

The time series of centrebow vertical (F_z) and horizontal (F_x) forces were calculated from equation (5-5) and (5-6) where B_x and B_z are forward sensor forces and A_x and A_z are the aft sensor forces. The negative in equation (5-6) is to achieve a positive upward slam force, since the sensors were mounted upside down.

$$F_x = A_x + B_x \quad (5-5)$$

$$F_z = -(A_z + B_z) \quad (5-6)$$

The noise to signal ratio in the centrebow force signals for some loading conditions was found to be quite high. Therefore, it was decided to filter the signals digitally. A study was undertaken to find the best low pass filtering frequency to minimise the noise whilst not losing resolution of the force peaks. Figure 5.13(a) shows the time series of the recorded F_z force in run 45 and Figure 5.13(b) shows a close up of the recorded signals for F_z and F_z after being 3 decibel (3db) low-pass filtered with a 500 Hz cut-off frequency. The filtering was performed digitally in MATLAB using a second order Butterworth Filter [111]. The slam-induced forces are present as sharp peaks at each encounter wave frequency.

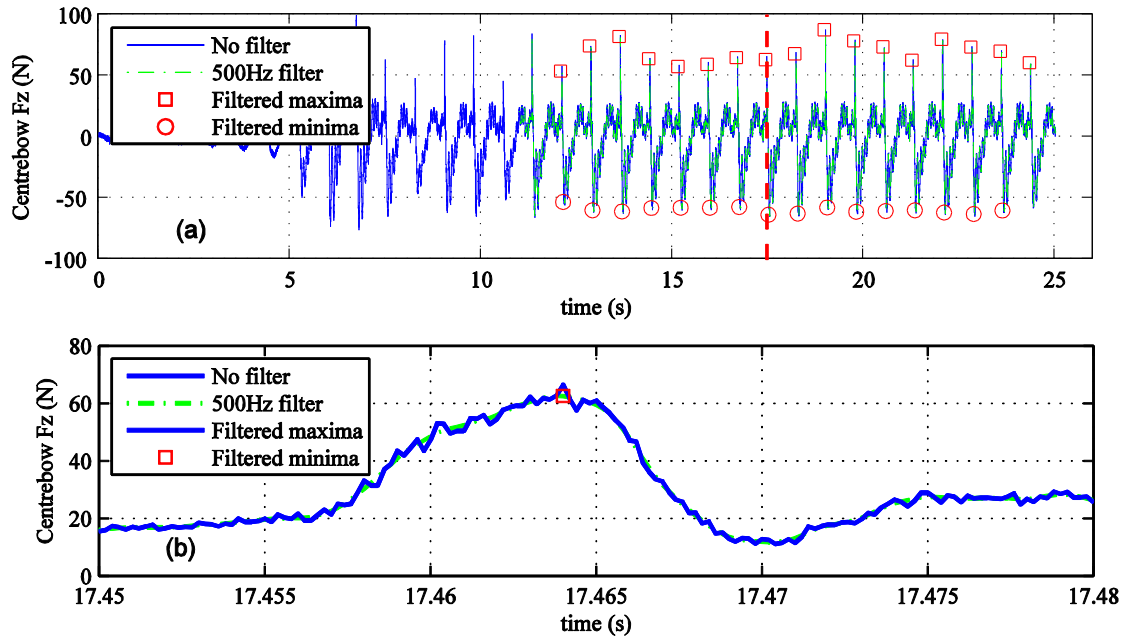


Figure 5.13: The centrebow F_z in run 45, (a) the raw forces and the filtered 3db low pass 500 Hz cut-off frequency; (b) the graph zoomed to show one single slam spike ($Hw=60$ mm, speed=1.53 m/s, $\omega_e^*=4.136$)

Figure 5.14 shows the peak values of the centrebow forces after filtering with various cut-off frequencies. When increasing the 3db low pass cut-off frequency beyond 500 Hz, there was a negligible effect on peak values. The slam peak duration is around 0.015 of a second and filtering with a low pass cut-off of 500 Hz will not distort the sharp peaks.

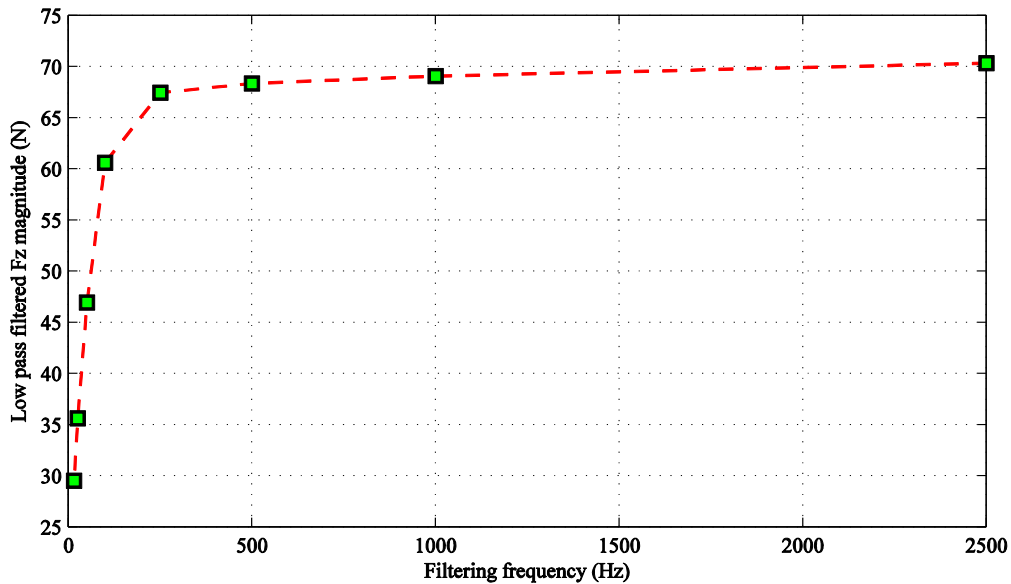


Figure 5.14: Change in magnitude picked up in various 3db low pass cut-off filtering frequencies ($Hw=60$ mm, speed=1.53 m/s, $\omega_e^*=4.136$). 500 Hz was chosen to be the best filtering frequency. The sampling frequency is 5 kHz, thus 2500 Hz means no filtering

5.3.3. Vertical centrebow force results

Figure 5.15 shows a close up of the sample time history of recorded F_z in run 45. As seen in the force signal is combination of the underlying wave encounter frequency, first longitudinal mode (whipping) frequency and sharp peaks representing the wetdeck slam forces. The higher frequency vibrations in the hull, whipping cycles, start immediately after the slam peaks as downward forces, and shift the direction slowly while being damped before the next slam event. These downward forces after the first upward impact are due to added mass effects, where a substantial mass of water is attached to the centrebow and accelerates with the hull.

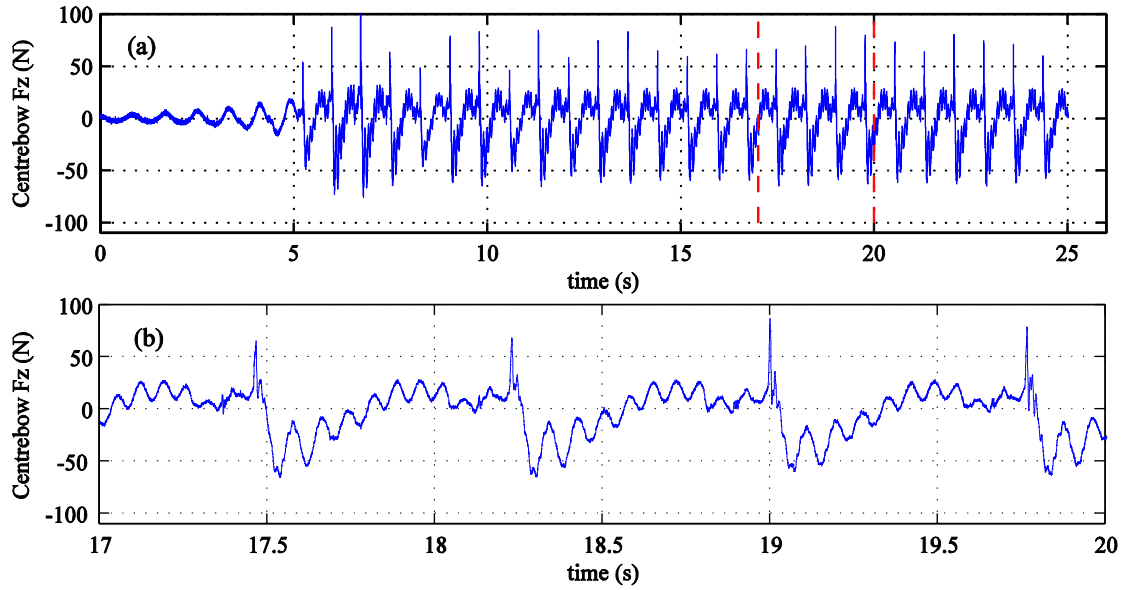


Figure 5.15: (a) Recorded centrebow vertical forces (F_z) from the run 45 ($H_w=60$ mm, speed=1.53 m/s, $\omega_e^*=4.136$); (b) close up of the graph (positive is upward force). The sharp peaks from slamming and the more frequent oscillations from the whipping are clearly seen.

The Fast Fourier Transform (FFT) of the slam signal is shown in Figure 5.16. This graph has been extracted by dividing the time signal into bins with the width of two wave encounter frequency (1.45s), using Hamming window [112] to taper both ends of each bin, taking FFT of all the individual bins and then averaging them over the run. As seen in the graph, the lowest frequency results from the wave encounter frequency, but the frequency is not picked well, since the time bins were relatively small. The second peak is from the first longitudinal vibratory mode of the model and is around 12.82 Hz. The energy of whipping oscillations is spread around the whipping frequency and is not concentrated on one peak. The reason could be the little differences between the whipping oscillation periods between the two slams depending on the proximity to the slam events on both sides. The hydrodynamic loading on the model is transient between the slams and affects the modal whipping frequencies.

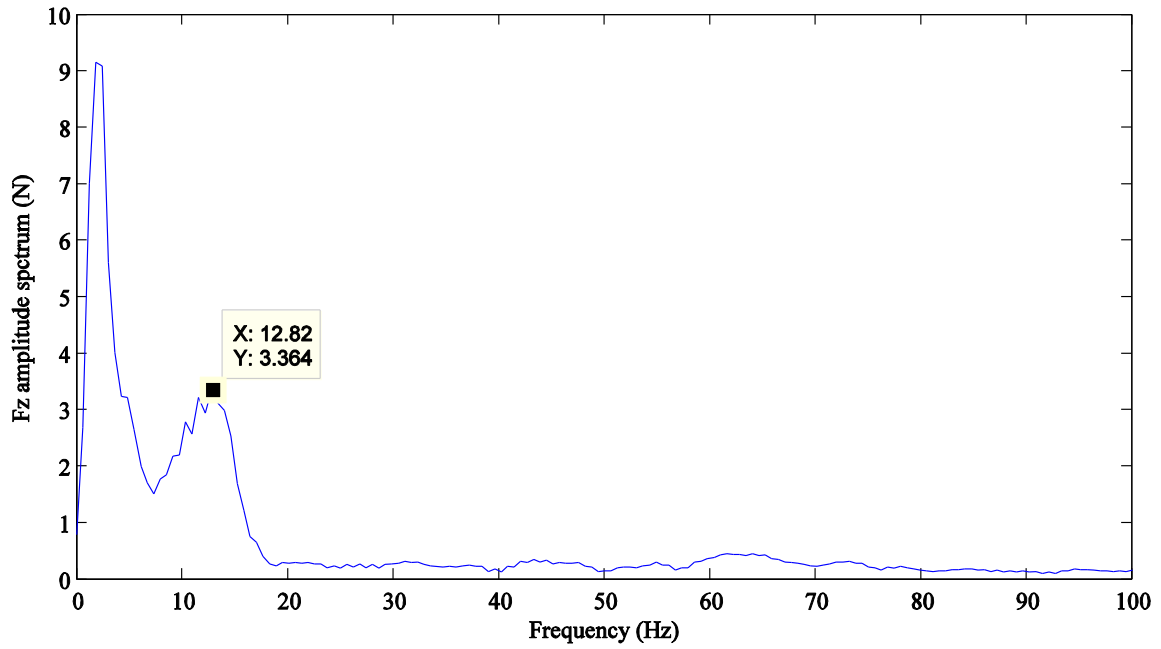
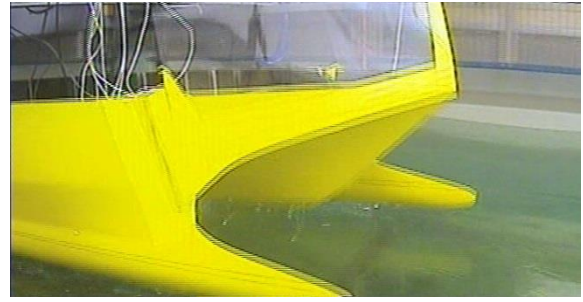


Figure 5.16: Spectral analysis of the centrebow forces in run 45 ($Hw=60$ mm, speed=1.53 m/s, $\omega_e^*=4.136$)

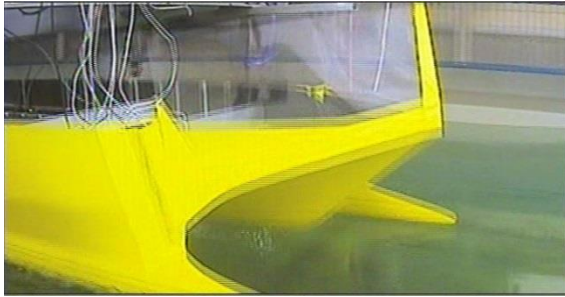
As shown in Figure 5.17, the snapshots of recorded video in run 45, the model bow moves in and out of the water during each wave period. Whereas in Figure 5.15, the whipping induced forces are present in the measured force signals even when the centrebow is out of the water. This means that these forces are not induced by water directly, but the first longitudinal mode in action. Accordingly, the measured forces are not directly the slam forces. As a result, to identify slam forces, an analysis on the external forces, force transducers measured forces and the centrebow mass inertia is required.



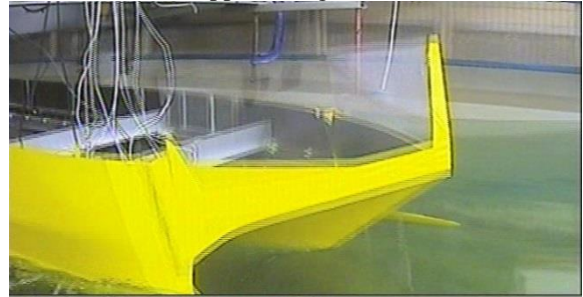
a- The bows out of the water



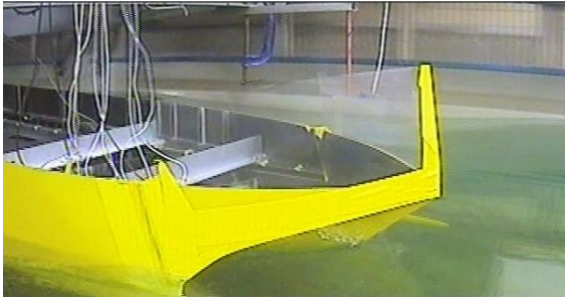
b- The bows approaching water



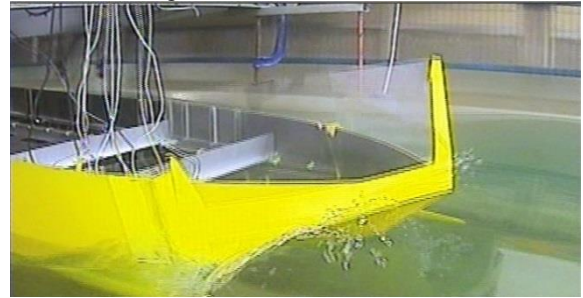
c- Demihull bows and wave surface meeting



d- Demihull bows submerged, centrebow partly submerged



e- Demihull bows and centrebow submerged



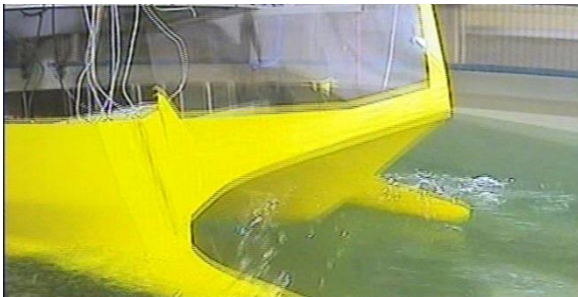
f- Wave crest meeting the arch top, wetdeck slamming occurs



g- Water starts splashes outboard, bow up motion starts



h- Bow comes up further, the water splash extends forward



i- Bow up, the piled up water drains, the centrebow exits the water



j- Both the centrebow and demihull bows emerge from water again

Figure 5.17: Still sequences of snapshots from one encounter frequency of HSM02 with the parent centrebow in run 45 ($H_w=60$ mm, speed=1.53 m/s, $\omega_e^*=4.136$)

Figure 5.18 shows the free body diagram of the centrebow in front view where F_z is the centrebow forces measured by the two force transducers, F_{ex} is the external force and a is the acceleration of the centrebow. The weight of the centrebow is not present in this diagram, as it was cancelled out by biased recording before the runs.

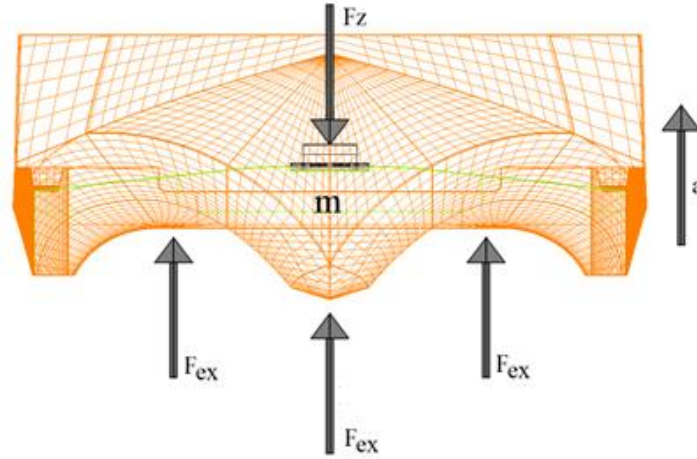


Figure 5.18: Free body diagram of the centrebow and the acceleration. F_z is the reaction of the 6DOF sensors and F_{ex} is the external forces acting on the centrebow.

The acceleration of the centrebow was measured by the B&K piezoelectric accelerometer on the centrebow, close to its LCG. Using Newton's second law, the force and acceleration equation could be written in the form of Equation (5-7) and (5-8),

$$\sum F = ma \rightarrow F_{ex} - F_z = ma \quad (5-7)$$

$$F_{ex} = ma + F_z \quad (5-8)$$

where m is the mass of the centrebow and ma is the inertia component. The recorded accelerations are noisy, due to the inclusion of some local structural high frequency components. The acceleration signals were low-pass filtered by a fifth-order Butterworth with a 150 Hz cut-off frequency. This frequency was chosen to both eliminate the high frequency components and retain resolution of the slam peaks. Figure 5.19 shows F_z , ma and the resulting F_{ex} in the run 45 with $\omega_e^* = 4.136$. The plot of external force shows that the slams start with a small peak from the centrebow keel slam followed by an increase in the forces until the large wetdeck slam occurs, followed by two large downward force periods, which causes a hogging response in the model.

The wetdeck slam sharp peak and the following few sharp peaks have the period of about 15 milliseconds. The sharp wetdeck slam force duration is then around 7.5 milliseconds (half period) and is somewhat similar between all the wetdeck slamming events in different runs.

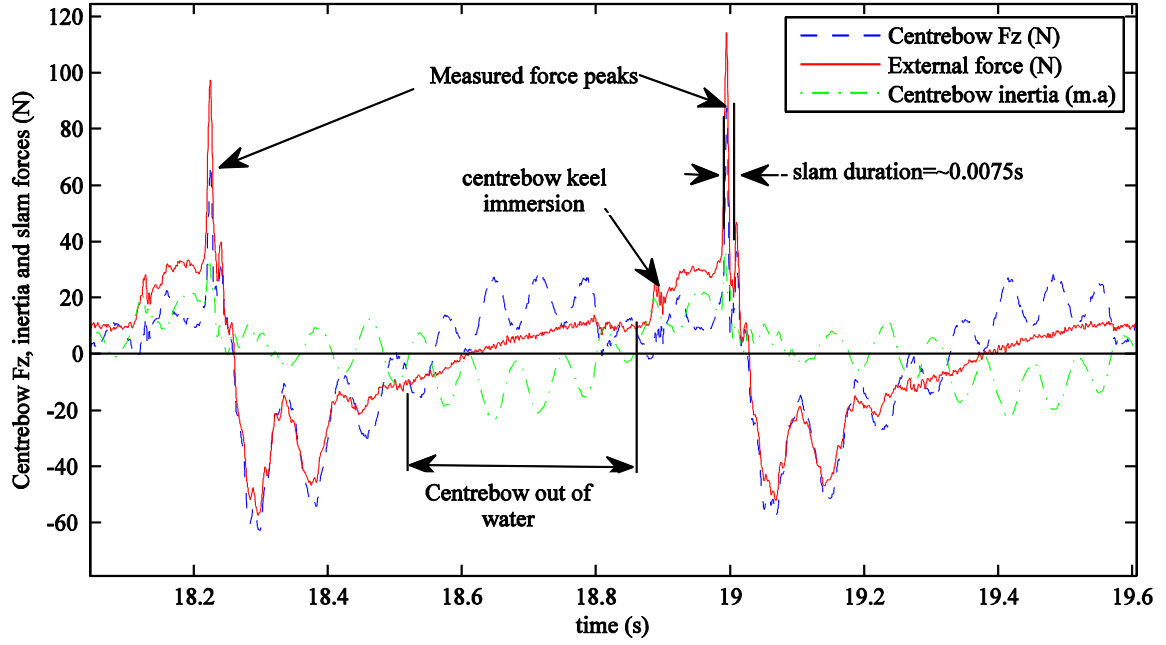


Figure 5.19: The centrebow and slam force for run 45. Including the inertia removes the whipping oscillations from the centrebow measured forces ($Hw=60$ mm, speed=1.53 m/s, $\omega_e^*=4.136$).

As seen in Figure 5.19, inclusion of the inertia removes the whipping oscillations when the centrebow is out of the water. Also, this analysis shows that there exists an underlying sinusoidal loading in between two slams at the wave encounter frequency. In order to clearly differentiate the slam forces on the centrebow from the underlying forces, the external force records were high-pass filtered at the encountered wave frequency. The magnitude of such underlying forces can contribute up to an average 15% of the total external force. The final centrebow force signals were called slam forces (Fs).

As shown in Figure 5.20, when the centrebow is out of the water, the F_s is nearly zero. The relative displacement was defined as the distance between the centrebow keel at centrebow truncation and wave elevation records from the moving wave probe in-line with the truncation. When the relative displacement reaches zero, meaning the centrebow keel touches the water, a small slam occurs as seen in the slam force trace. The F_s ramps up after centrebow submersion until the water reaches the wetdeck, where the severe wetdeck slamming occurs. After the slam, the relative velocity remains zero for a short time, the relative displacement maximises (in negative direction, more immersion of the bow). At this point, a small twist in vessel pitch motion trace can be seen; and thereafter the vessel pitch returns until the centrebow re-emerges from the water. The effect of the slamming on the vessel motions can be clearly seen the time series of the pitch, relative velocity and relative displacement.

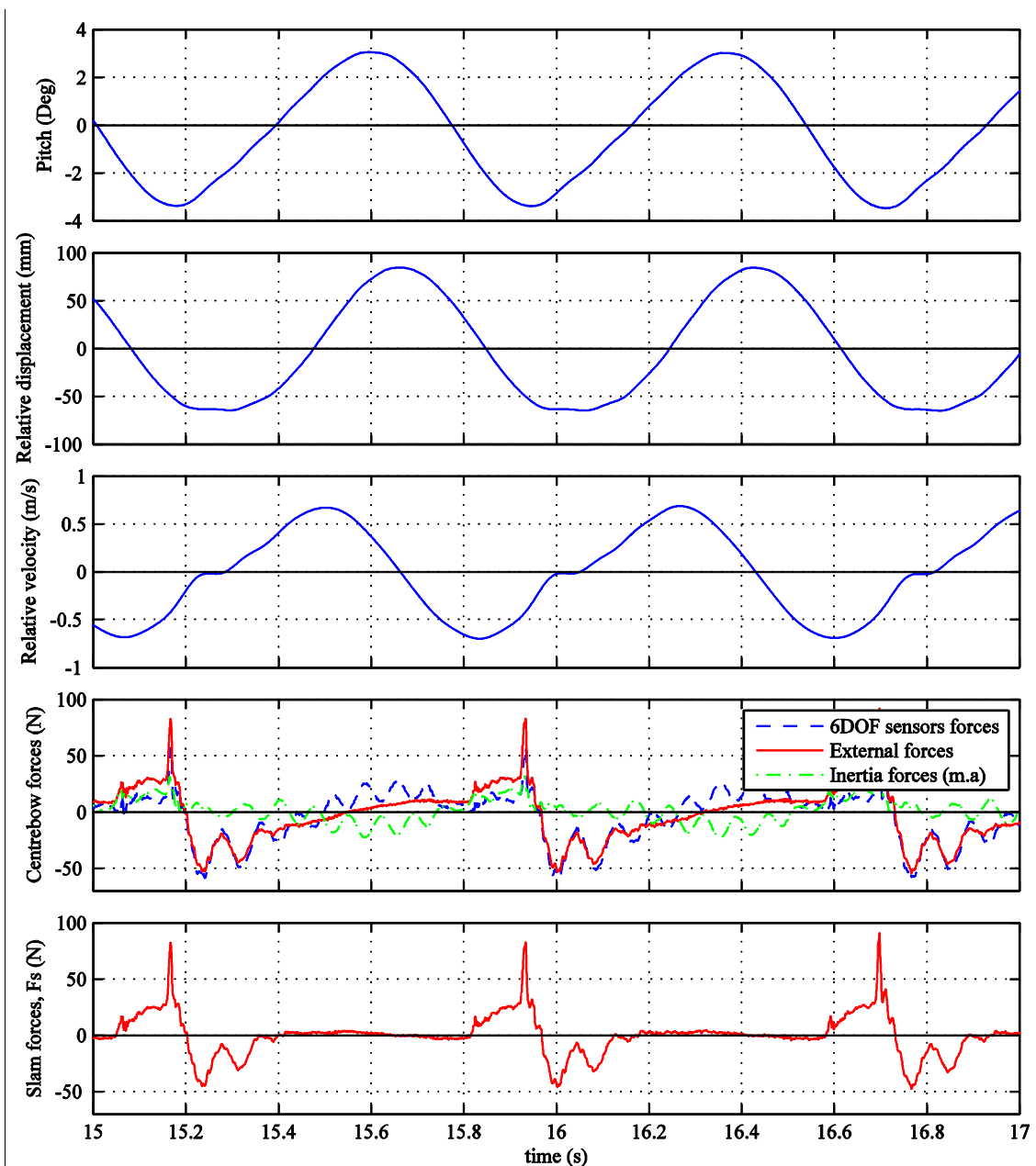


Figure 5.20: Sample time series of centrebow forces and motions from run 45 ($H_w=60$ mm, speed=1.53 m/s, $\omega_e^*=4.136$).

Similar reasoning can be applied to the towing tank runs on shorter or longer waves. As an example Figure 5.21 shows the time series of pitch angle, relative displacement, bow relative velocity and centrebow slam force for run 38 on a short wave with $\omega_e^* = 5.37$. As seen, the pitch motions and relative displacements are smaller than run 45, especially the relative velocity trend does not show the twist after the slam event as could be seen in run 45. The magnitude of slam forces is low (12 N in sagging and 20 N for hogging) and the wetdeck slamming is only a small peak. However, the centrebow keel immersion moment before slamming is clearly seen in the slam force plot.

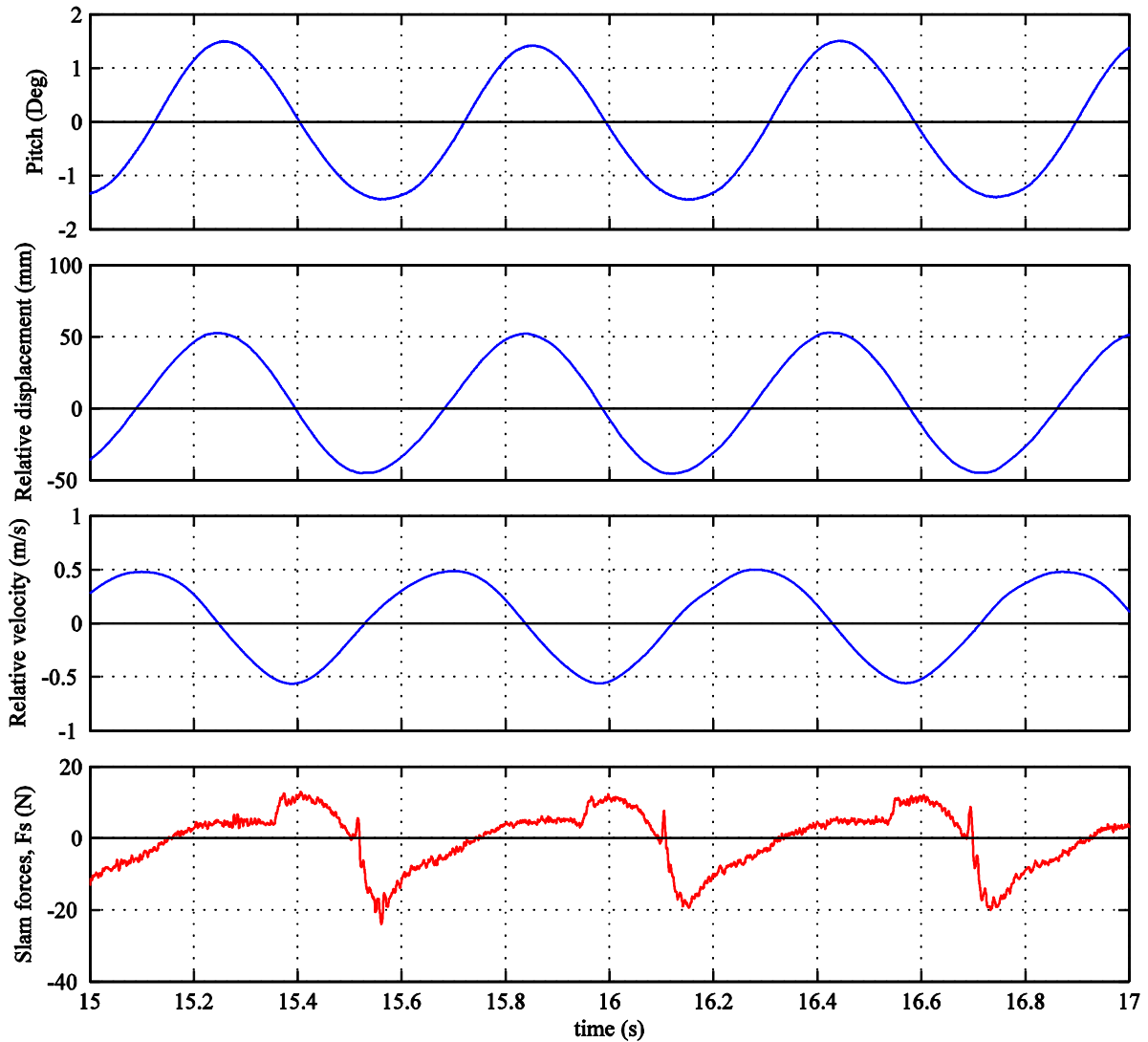


Figure 5.21: Sample time series of centrebow forces and motions from run 38 on a short wave ($Hw=60$ mm, speed=1.53 m/s, $\omega_e^*=5.37$)

As an example of running in long waves is shown in Figure 5.22 recorded in run 44 with $\omega_e^* = 3.39$. In this run the pitch motions are quite large, but the bow relative velocity is small. As seen in the slam force plot, the magnitude of centrebow force is very small (less than 4 N) and because of the scale of the plot, the centrebow keel entry force shows itself clearly. It can be said that in run 44, low relative bow velocity has prevented wetdeck slamming.

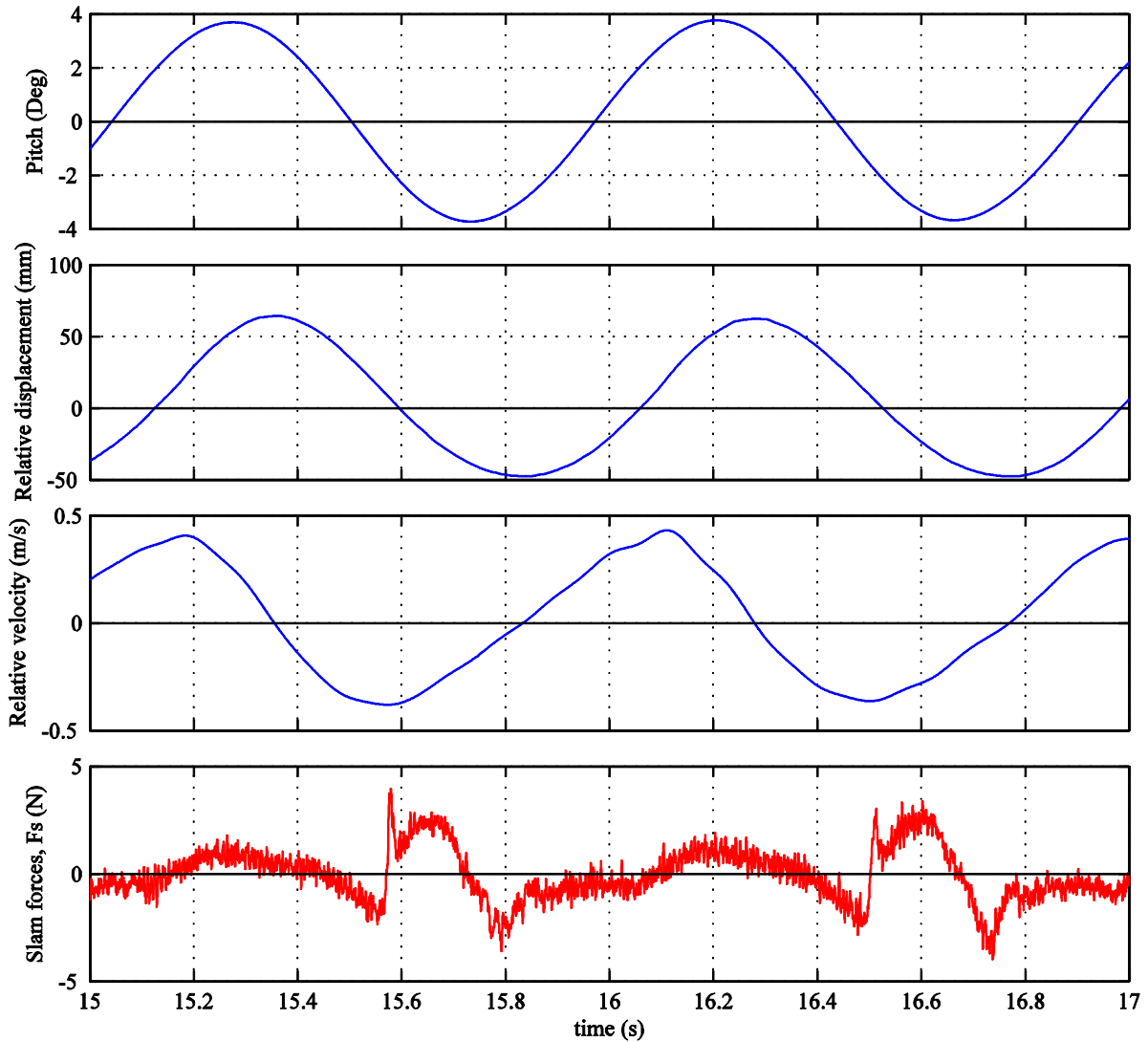


Figure 5.22: Sample time series of centrebow forces and motions from run 44 on a relatively long wave ($Hw=60$ mm, speed=1.53 m/s, $\omega_e^*=3.39$)

5.3.4. Vertical slam load magnitudes

A sample time series of slam forces for the parent centrebow is shown in Figure 5.23. The bottom figure shows the response to short wave lengths and the top graphs show the longer encountered waves. In very short or very long wave lengths, wetdeck slamming does not occur. However, in mid frequency ranges ($3.75 \leq \omega_e^* \leq 5$) the centrebow submerges and wetdeck slamming occurs. As seen, the waves condition with $\omega_e^* = 4.53$ shows the highest slam impulses.

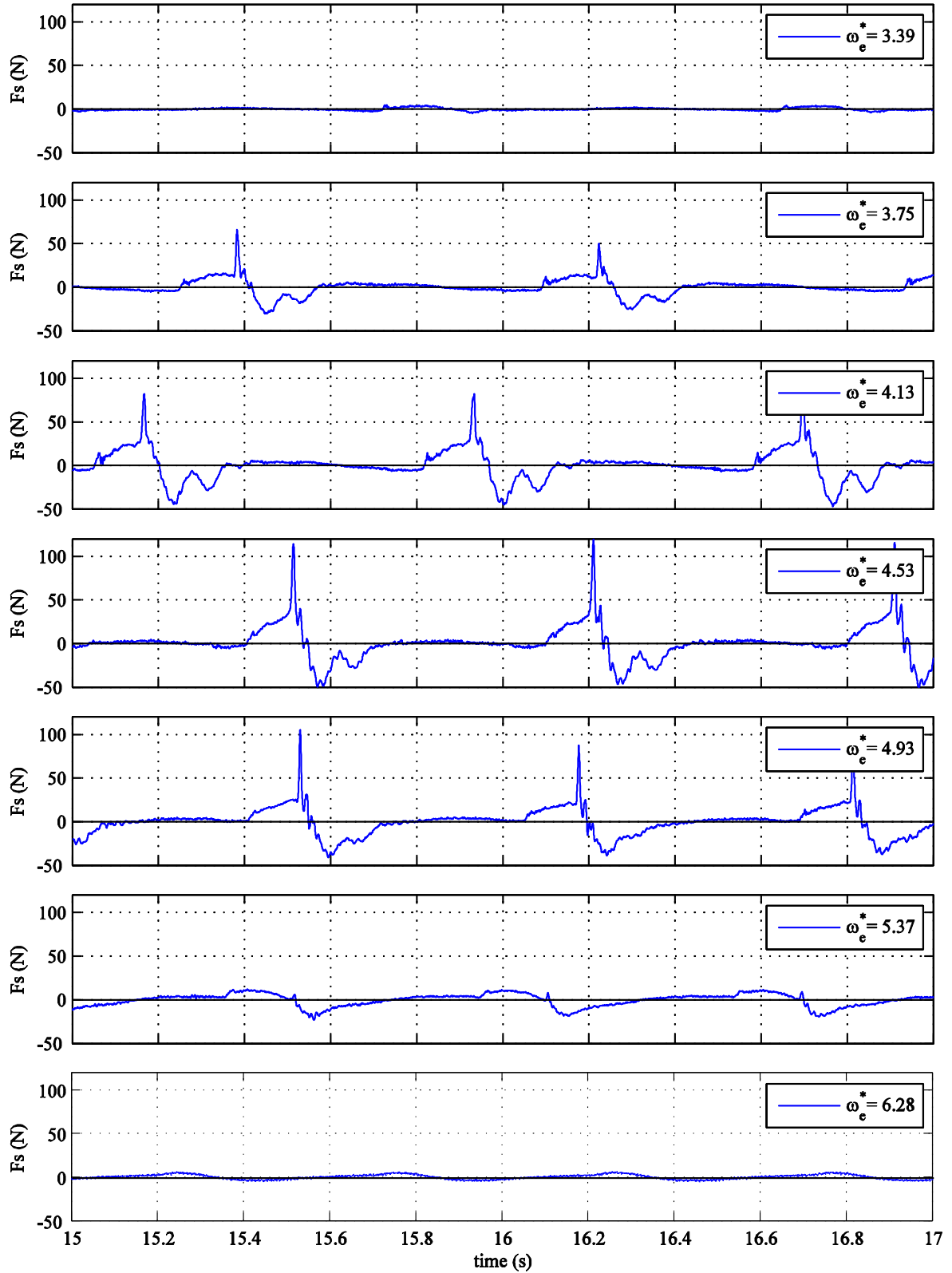


Figure 5.23: Sample time series of the parent centrebow slam forces (F_s) in various encounter wave frequencies. The slam forces are greatest in mid-range frequencies ($H_w=60$ mm, speed=1.53 m/s)

Figure 5.24 shows the result of slam forces (F_s) for all three centrebow configurations for varying encounter frequency. The positive values are sagging (upward) slam forces which are calculated as the average of the peak slam force values in each run. The negative values are the average of the hogging (downward) force peaks in each run. The results are presented with error bars showing 95% confidence intervals for predicting the mean of the slam peak values. The use of 95% confidence intervals means that the total population mean will fall into this region with less than 5% error. In other words, it demonstrates how accurately the mean of the sample population can be estimated. The formula to calculate the confidence intervals of each sample is given in Equation (5-9) to Equation (5-11),

$$\text{Confidence Interval} = \bar{x} \pm t_z \frac{S_n}{\sqrt{n}} \quad (5-9)$$

$$S_n^2 = \frac{1}{n-1} \sum (x_i - \bar{x})^2 \quad (5-10)$$

$$\bar{x} = \frac{x_1 + \dots + x_n}{n} \quad (5-11)$$

where \bar{x} is the sample mean, S_n^2 is the samples variance, S_n is the sample standard deviation; n is the number of samples and t_z is the critical value extracted from the peak values distribution. The distribution of the slam load peak values is taken as Student's T-distribution [113]. The student's T-distribution is similar to normal distribution (symmetric around the mean with a bell curve) but with heavier tails; meaning that the possibility of values far from the mean is quite high. This distribution is usually used when the sample number is small (less than 30). The Student's t-distribution, with confidence intervals, is useful when predicting the mean of different populations, i.e. comparison between loads from different centrebow lengths. The procedure of proving normal distribution is similar to that explained further in Section 5.3.8 for vertical bending moments. Table 5.6 presents the t_z used for 95% confidence intervals of a two-tailed student's T-distribution, knowing that t_z for a normal distribution equals 2. Using larger critical values (t_z) creates larger error bars, meaning that the mean of the peak slam values can vary in a larger range if the tests are repeated or longer distance runs are performed.

Table 5.6: The T-Value Of Student's T-Distribution For 95% Confidence Interval [113].

Number of samples (n)	6	7	8	9	10	11	12	13	14	15	16	17	18	19	20	21	22-26	27-31
t_z	2.57	2.45	2.36	2.31	2.26	2.23	2.2	2.18	2.16	2.14	2.13	2.12	2.11	2.1	2.09	2.09	2.07	2.05

The reason why the slam peaks vary significantly in one run can be summarised as:

- Considering the very transient nature of a slam event, the slam forces are quite sensitive to the precise detail of each slamming event. The environmental effects such as wave surface could be slightly different for consecutive slams

- The interaction of vessel motions and slam loads. Slams alter the pitch and heave and consequently the pre-slam bow velocities and motions will be different for the next slam.
- The whipping frequency of the model is not an exact multiple of slam occurrence frequency, thus each slam will have a pre-slam modal condition which can affect its severity.

As seen in Figure 5.24, the hogging (downward) forces do not show significant variations among the three centrebows. Similarly, at high or low wave frequencies ($\omega_e^* \leq 3.3$ and $\omega_e^* \geq 6.3$), the centrebow loads are small and comparable for all three centrebows. The slam forces increase as the wave length becomes closer to the vessel length and the maximum loads occur in the mid frequency range ($4 \leq \omega_e^* \leq 5$). The difference between the forces for three centrebows also increases as the model goes through the severe wetdeck slamming region. The maximum load frequency is similar between the three centrebows; however, the results clearly indicate that there are significant differences in slam values.

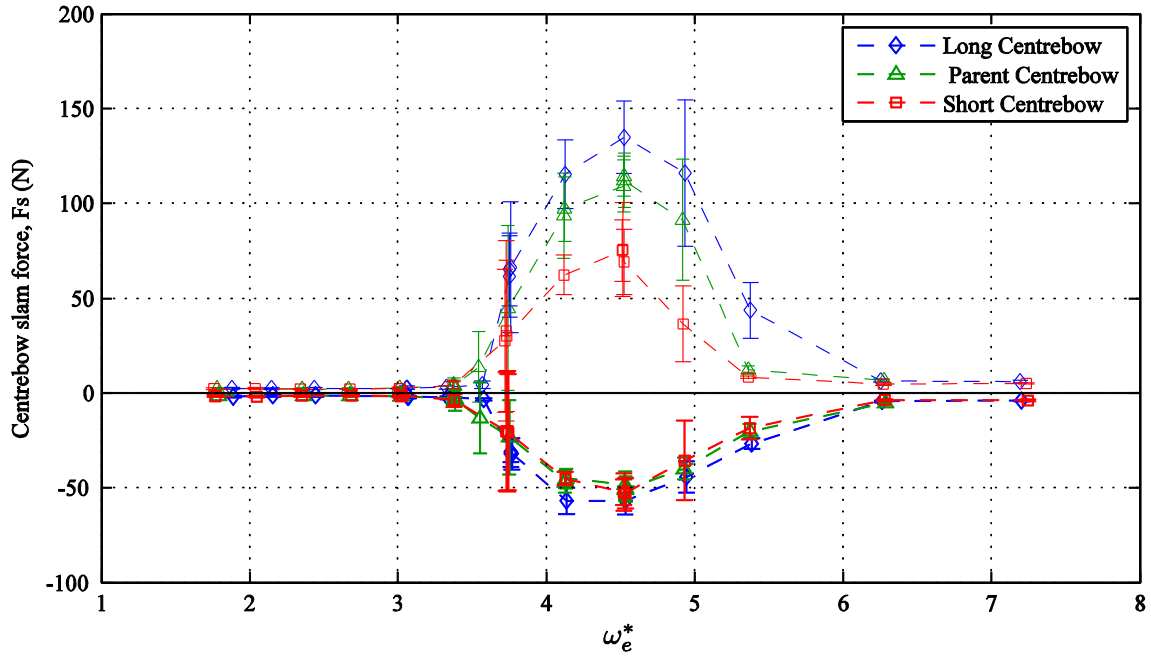


Figure 5.24: Vertical centrebow slam forces for three centrebow lengths in HSM02 ($H_w=60$ mm, speed=1.53m/s, positive shows upward slam forces and the bars show the 95% confidence intervals)

The non-dimensional slam forces (F_s^*) were calculated based on the method used by Colwell et. al [51, 114] where significant influencing parameters such as wave height and vessel weight are considered. F_s^* is calculated from Equation (5-12),

$$F_s^* = \frac{F_s}{\rho g H_w \nabla^{2/3}} \quad (5-12)$$

in which H_w is the wave height, ∇ is the vessel displaced volume, ρ is the water density and g is the gravity acceleration. The non-dimensional slam forces are shown in Figure 5.25 in terms of non-dimensional encounter wave frequency.

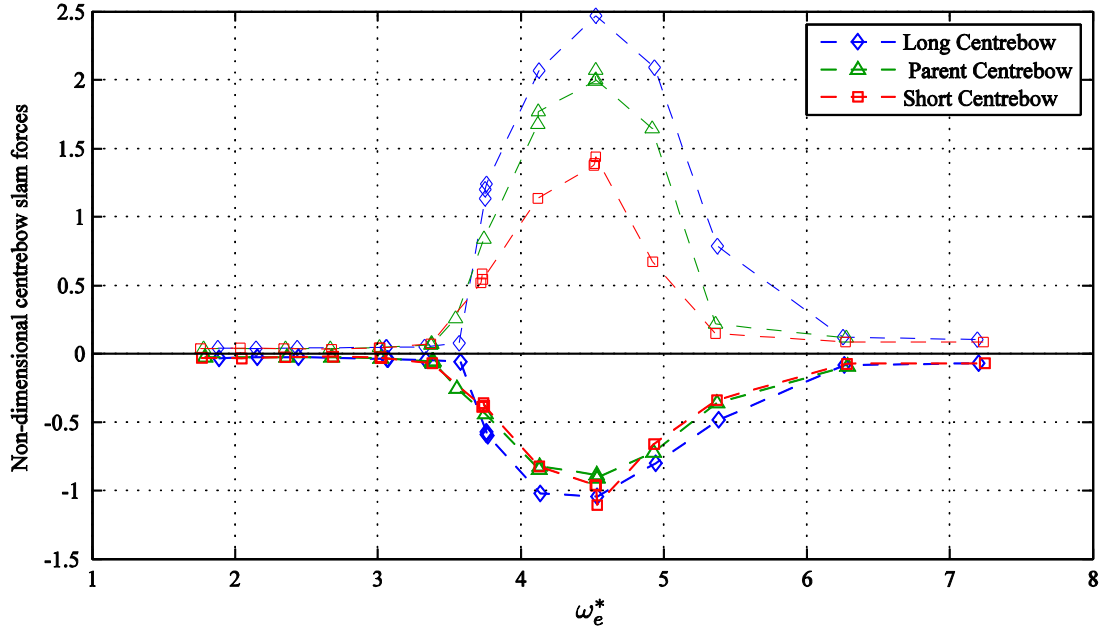


Figure 5.25: Non-dimensional vertical centrebow slam forces ($F_s^* = \frac{F_s}{\rho g H_w \nabla^{2/3}}$) for three centrebow lengths in HSM02

The long centrebow has around 25% higher slam forces, compared to the parent centrebow and the parent centrebow experiences around 40% higher slam forces than the short centrebow. The aim is to achieve the lowest slam forces for similar wave and speed condition, thus the short centrebow is the most promising from this perspective. However, the motion results need to be considered as well.

To find the reason for this large difference, an examination of the mechanism of slamming under the archways is required. As the centrebow enters the water due to bow down motion, the water runs up the sides of the centrebow. As illustrated in Figure 5.26, when this water reaches the knuckles forward of the jaw line, it deflects outwards like a jet flow and does not get restrained by the demihulls. This water does not significantly contribute to severe wetdeck slamming. However, behind the jawline, the upwash water from demihulls and centrebow becomes constrained under the enclosed archways and creates a large confluent impact in the area at the top of the arch. The further the archway extends aftward, the more water becomes restricted and so larger slams are created. Therefore, the shorter centrebow experiences the smallest and the long centrebow the largest slam forces.

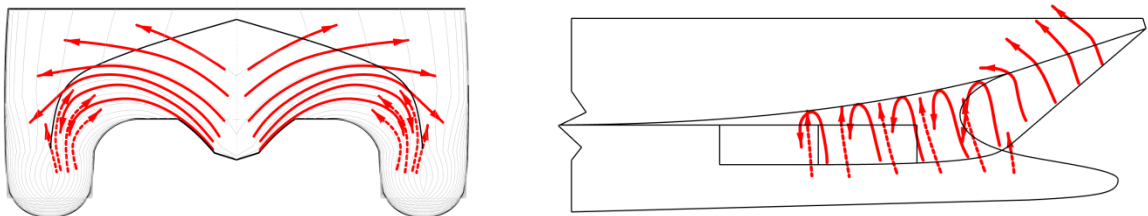


Figure 5.26: The slamming upwash water exits the centrebow in open jaw, but becomes restricted under the archway behind the jawline

The impact forces alter the motions of the vessel in slamming conditions. The short centrebow works even more effectively by reducing pitch motions in severe slamming frequency range ($4 \leq \omega_e^* \leq 5$).

Figure 5.27 shows the comparison of slam force and pitch time histories for the three centrebows in the same wave condition ($\omega_e^* = 4.136$). As seen, the pitch troughs are somewhat the same, but the bow-up pitch values for the longer centrebows are higher. This creates asymmetric pitch angles, where there is a limit for the downward angle, imposed by archway fill-up in the slam events. The reason could be the similar archway height for all the three centrebows which results in the same bow-down limit. The higher bow-up pitch for larger centrebow was expected to be due to the larger upward slam forces experienced in the slam events.

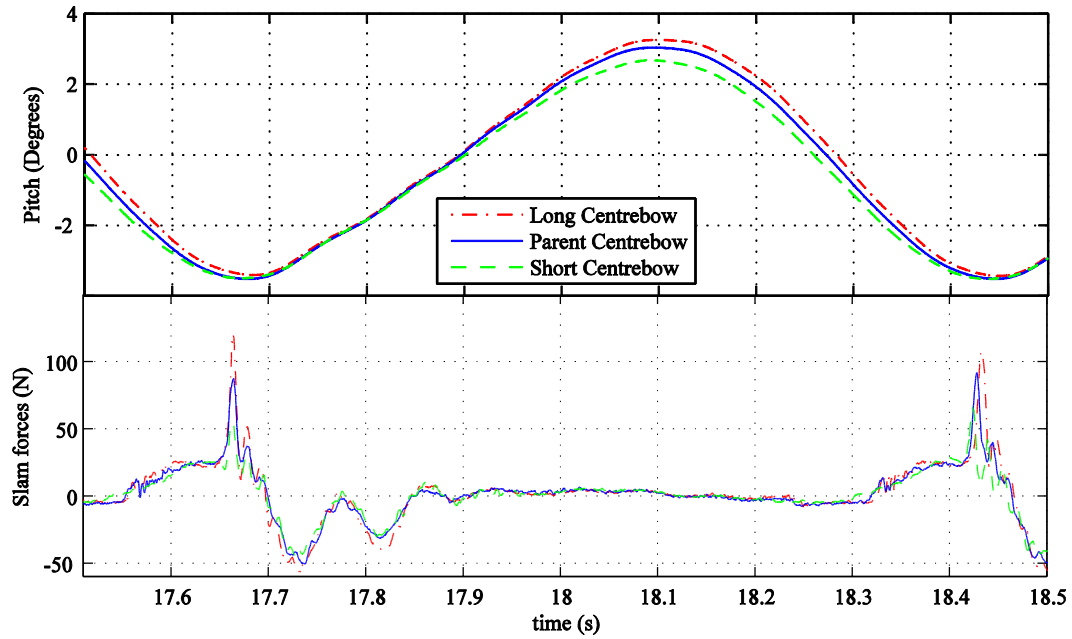


Figure 5.27: The time histories of slam force and pitch response of the three centrebows. The time axis is shifted for better visual comparison ($H_w=60$ mm, speed=1.53 m/s, $\omega_e^*=4.136$)

Figure 5.28 compares the non-dimensional pitch and slam force values for the peak slamming condition $\omega_e^*=4.53$. As seen, in the peak slamming condition, the pitch and vertical slam forces are greater for the long centrebow and less for the short centrebow. This shows the improved performance of the short centrebow in both loads and motions in 2.69 m wave height.

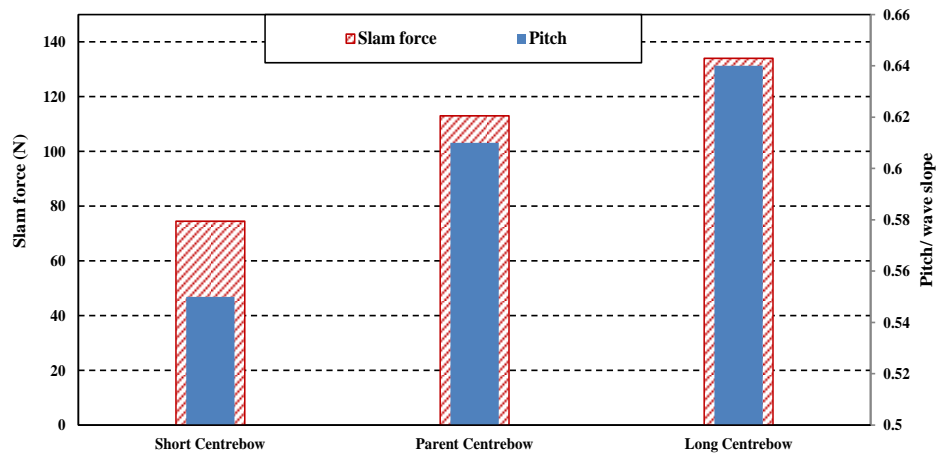


Figure 5.28: The pitch motion and slam forces of the three centrebows for the peak slamming condition ($H_w=60$ mm, speed=1.53 m/s, $\omega_e^*=4.53$).

The effect of the slamming on motion can be seen in the pitch or heave time series both in sinusoidal form and in the magnitude. In the case of the short centrebow, these effects are more visible when slams do not occur in every encountered wave. Figure 5.29 shows the time series of run 60 with $\omega_e^* = 4.9$ where the slams occur on every two encountered waves. As can be seen in the pitch data, the motions are irregular with peak values alternating in each period. The slam event slows the motions sufficiently to prevent a slam on the subsequent wave, but the motions then increase sufficiently to produce a slam in the next cycle. The occurrence of slamming is on a border line and a very small variation in initial condition can dramatically affect the result. Therefore, in presenting the mean slam force peak value for this run, only the slamming events were counted for averaging, even when the model was in regular waves.

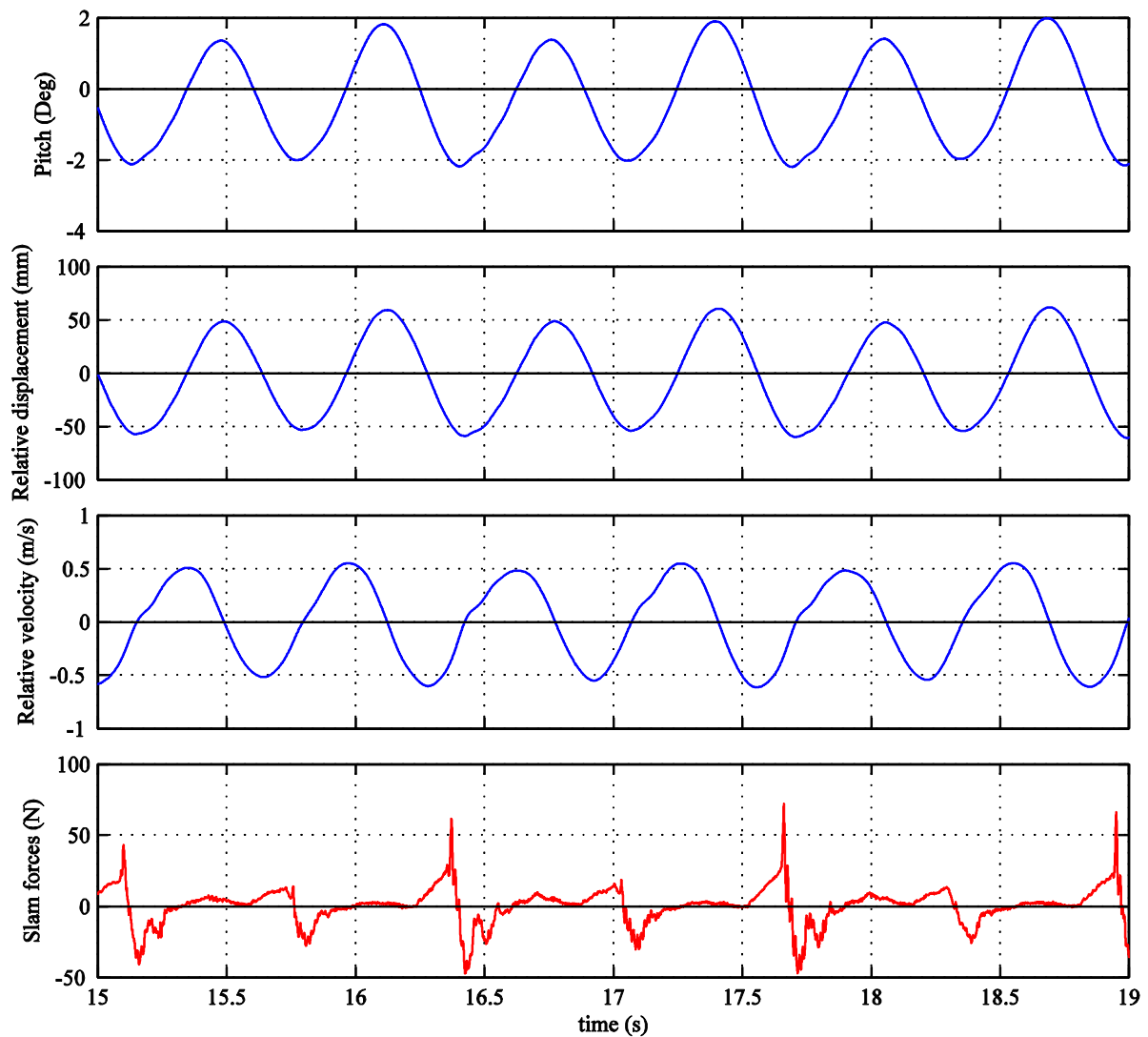


Figure 5.29: Sample time series from run 60 with the short centrebow. In this run, a slam slows the relative motion to prevent a slam on the next wave, but the motion then increases for the next wave encounter ($Hw=60$ mm, speed=1.53 m/s, $\omega_e^*=4.9$)

To understand the effect of centrebow parameters on the slam behaviour of the vessel the slam forces can be related to geometric differences between these three centrebows. Figure 5.30 shows the peak

slam force at $\omega_e^* = 4.53$ as a function of the Centrebow Volume Ratio (CBVR) and Centrebow Length Ratio (CLR) of the three centrebows. As seen the slam forces are more severe as the centrebow length increases. The prime reason for this, as already explained is that for the longer centrebow volume more water is constrained between the centrebow and demi-hulls in the archways which increases the severity of the impacts with the longer centrebows. The other reason which could be of interest for the following stages of the project is the effect of tunnel clearance which is different between the three centrebows at their truncation section. The short centrebow has a higher tunnel clearance at that section because of the longitudinal slope of the archways under the wetdeck. It appears that the lower wetdeck configurations will likely give rise to larger slam forces.

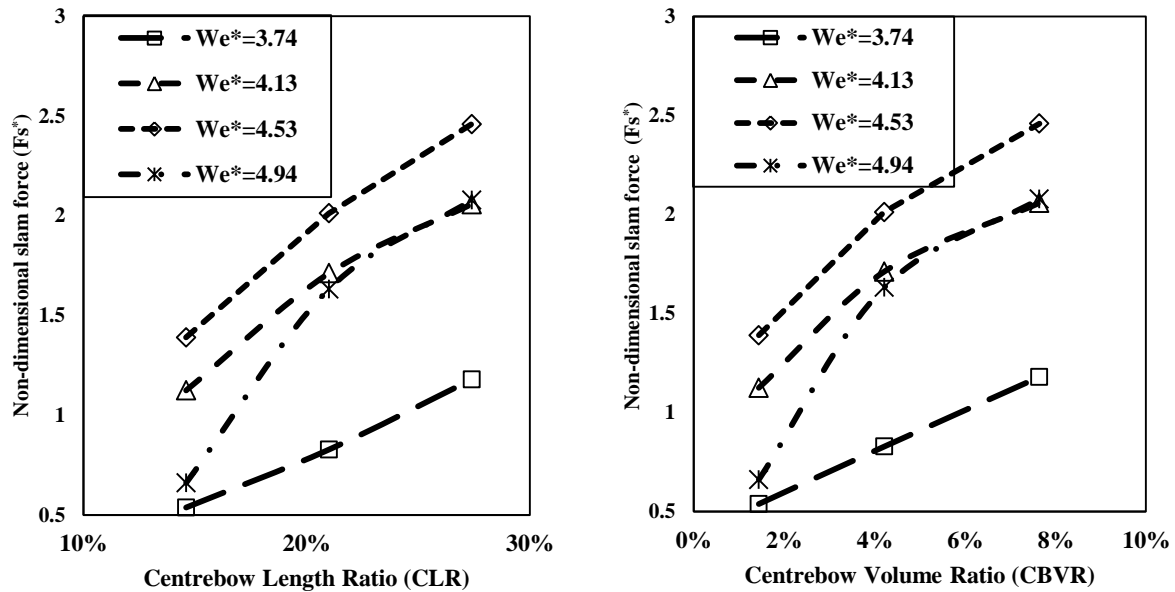


Figure 5.30: The non-dimensional slam forces ($F_s^* = \frac{F_s}{\rho g H_w \nabla^{2/3}}$) for the peak slamming condition as a function of the Centrebow Length Ratio (CLR) and Centrebow Volume Ratio (CBVR) of the three centrebows

5.3.5. Horizontal centrebow forces

The horizontal slam forces were measured on the model by adding the X-direction component forces from the two 6DOF sensors. Figure 5.31 shows a time series of horizontal (F_x) forces recorded during run 45. As indicated in this graph, for each impact there is initially a ramping up of force in the negative (backward) X-direction followed by a sharp peak in the aft direction at the instant of the wetdeck slam. After the impact, the force is reduced until it changes direction to positive X and cycles two times before returning to zero and then oscillating around the node line. Even though the model's first longitudinal mode causes vertical accelerations, because of the longitudinal (and transverse) curvature of the centrebow, the positive (forward) forces are most likely caused by added mass effects where the centrebow is accelerated by the model's whipping frequency. The oscillations of F_x between two slam events, where the centrebow is out of the water is not as regular as the vertical forces.

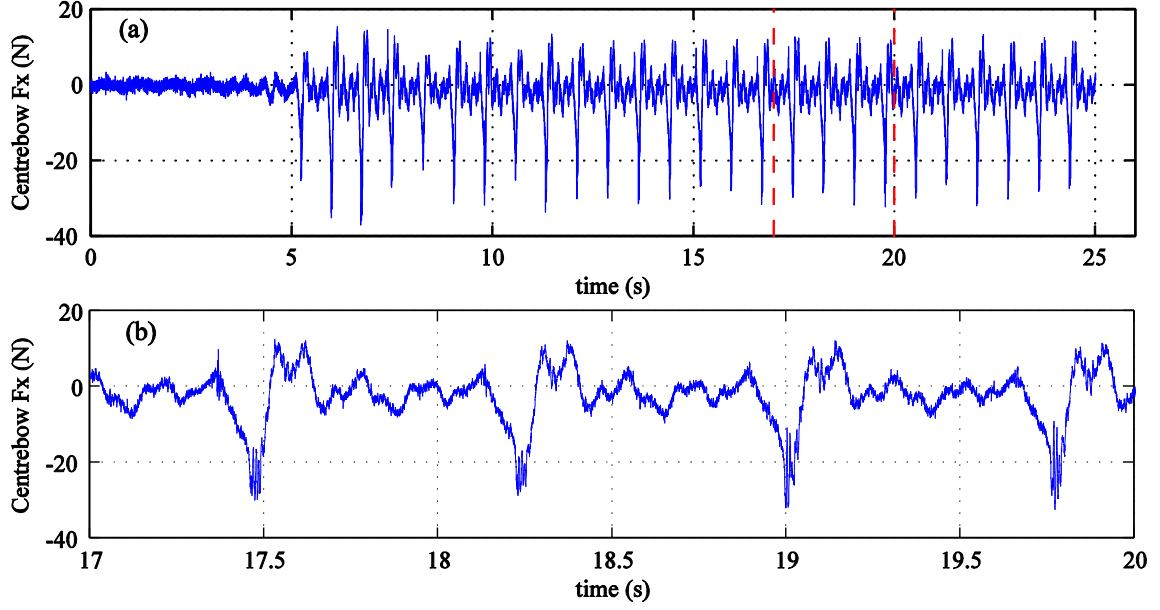


Figure 5.31: Horizontal centrebow forces for three centrebow lengths in HSM02. Negative is the aftward direction ($Hw=60$ mm, speed=1.53 m/s, $\omega_e^*=4.13$).

Figure 5.32 shows the mean and 95% confidence intervals of the measured peak horizontal forces in each run, for the three different centrebows. The positive in this graph shows aftward horizontal forces. Since there was no accelerometer to measure the X-direction accelerations, the forces presented here are not corrected for centrebow inertia effects. As seen in the graph, in either short waves or long waves ($\omega_e^* \leq 3.3$ and $\omega_e^* \geq 6.3$), the resultant horizontal forces of all the three centrebows are very similar, because the wetdeck slamming does not occur and the water flows smoothly on the centrebow. For mid-range encounter wave frequencies ($4 \leq \omega_e^* \leq 5$), the difference between the horizontal centrebow forces increases. As indicated in the graph, in slam conditions the long centrebow experienced slightly higher horizontal slam forces compared to the parent centrebow (around 10% in $4 \leq \omega_e^* \leq 5$). The smallest horizontal forces were recorded for the short centrebow, which showed around 16% less than the parent centrebow. The negative (forward) forces are smaller and much closer together for the three centrebows, except at one frequency ($\omega_e^* = 4.53$) where the long centrebow has about 60% higher value than the short centrebow and the parent centrebow is between the other two.

Figure 5.33 shows the non-dimensional horizontal centrebow forces measured in the model. Equation (5-12) was also used to normalise the horizontal forces. Peak horizontal force occurred at $\omega_e^* = 4.13$ which is lower than $\omega_e^* = 4.53$ for the vertical forces, meaning that horizontal force peaks occur between peak slamming and peak motions frequency.

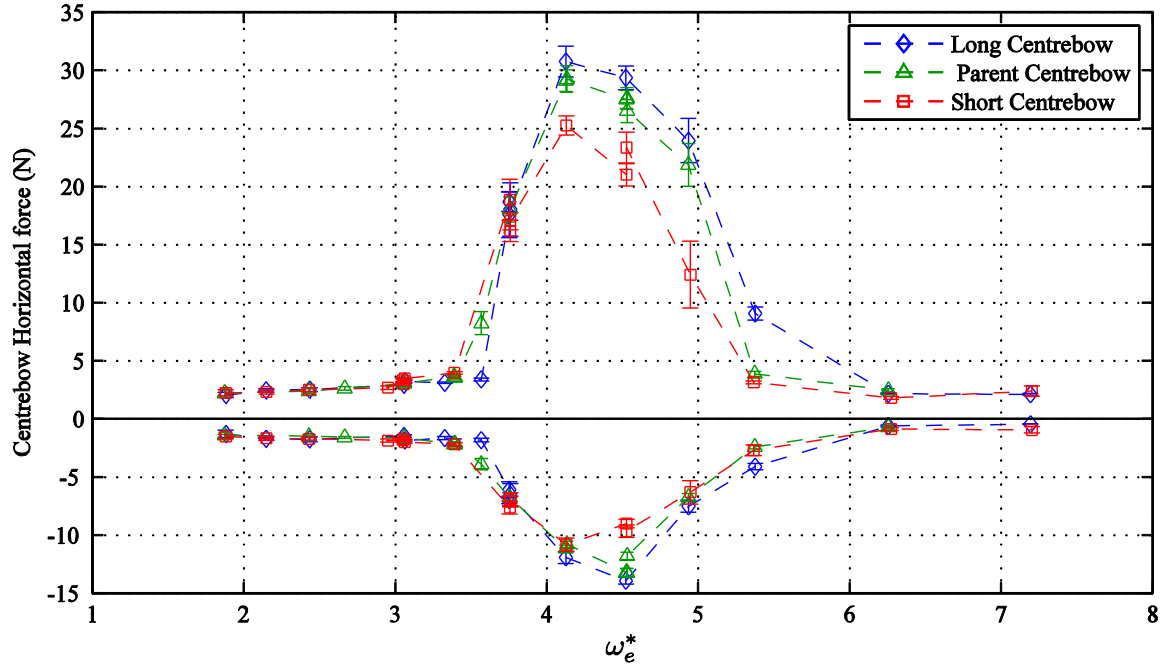


Figure 5.32: Horizontal centrebow forces for three centrebow lengths. Positive is the aftward direction

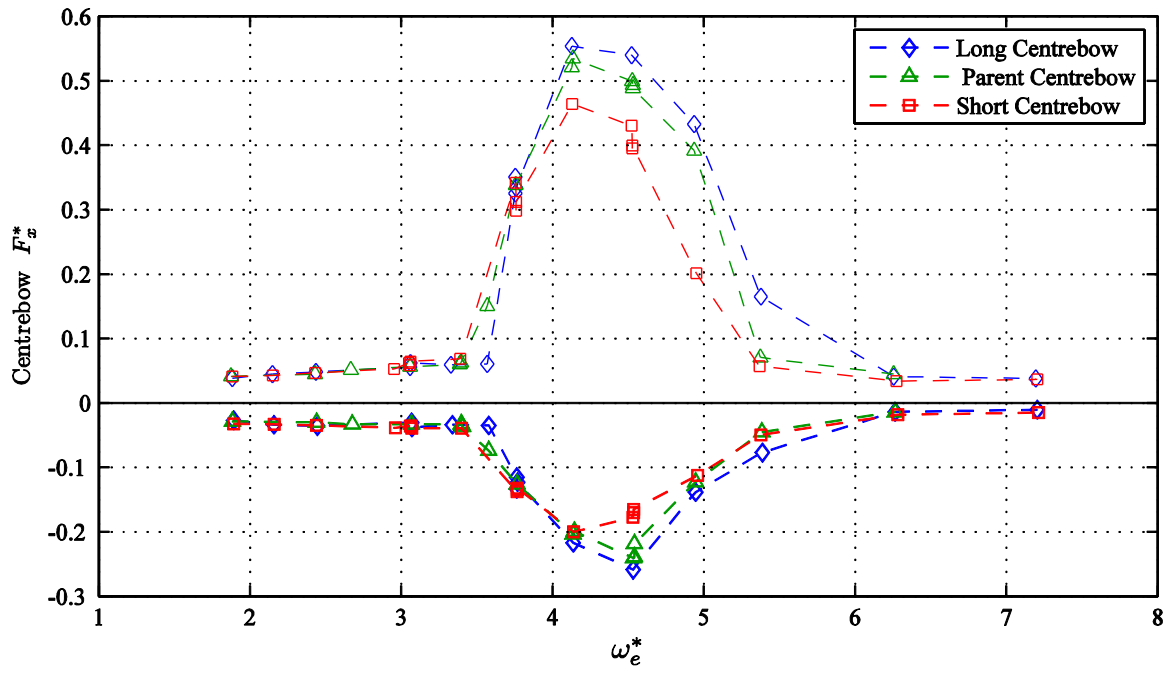


Figure 5.33: Non-dimensional horizontal centrebow force ($F_x^* = \frac{F_x}{\rho g H_w \bar{v}^{2/3}}$) for three centrebow lengths

The explanation for the larger horizontal forces for the longer centrebows can be found by looking closely at the geometrical differences between the three centrebows. The long centrebow is extended aftward compared to the parent and short centrebow. As seen in Figure 5.34, the transverse curvature of the centrebow surface varies less between the long and parent centrebow, whereas the curvature changes more significantly between the parent and short centrebow. Also, the centrebow blockage area and the normal angle between the water and centrebow surface vary significantly between the centrebows. As defined in Chapter 3 and shown on Figure 5.34, Tunnel Blockage Factor (TBF) is the projected area of the centrebow divided by the clearance area of the truncation section under the archways.

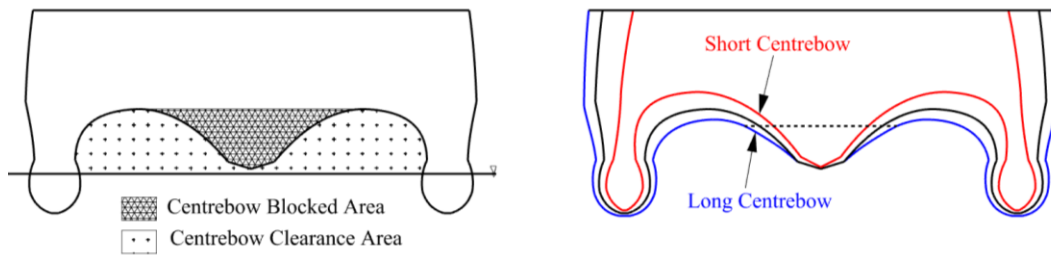


Figure 5.34: The variation of the tunnel blockage at the centrebow truncation between the three centrebows

Figure 5.35 shows the horizontal slam forces of each centrebow versus centrebow length ratio and tunnel blockage factor in peak slamming condition ($\omega_e^* = 4.53$). As can be seen there is a more linear variation of the non-dimensional horizontal forces with the TBF than with the CLR. This linear relationship can also be seen in most of the other slamming conditions. Therefore, it can be concluded that the horizontal slam forces applied to the centrebow increase linearly as the area blockage of the centrebow under the wetdeck increases. From a design perspective, if horizontal slam forces are important, large blockage of the tunnel should be avoided.

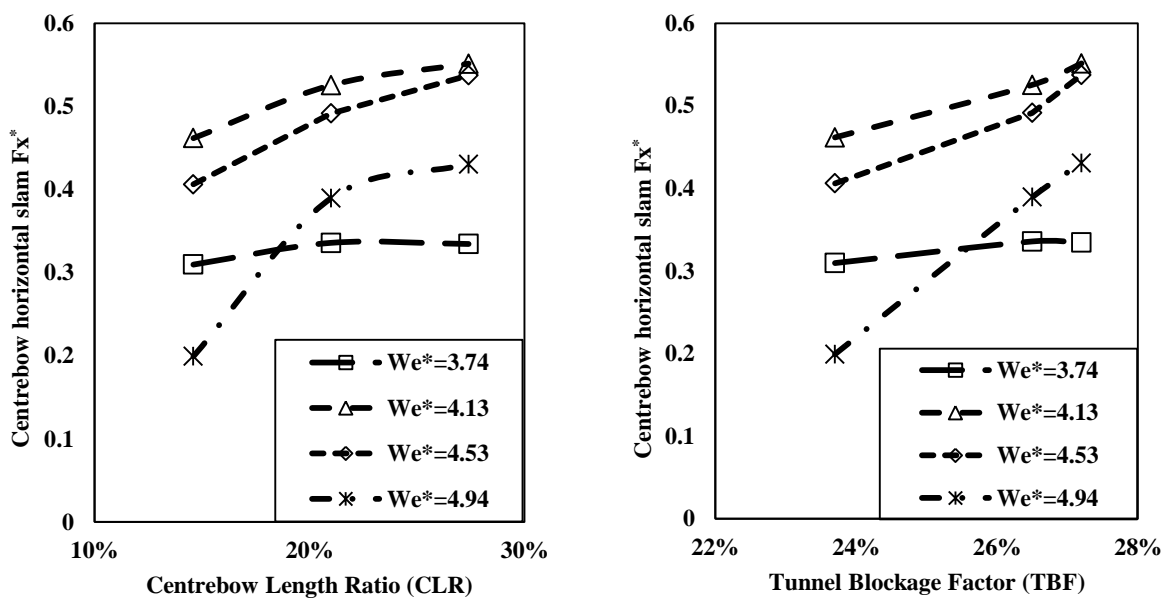


Figure 5.35: The non-dimensional horizontal force ($F_x^* = \frac{F_x}{\rho g H_w V^{2/3}}$) in slamming conditions in the three centrebows versus Centrebow Volume Ratio (CBVR) and Tunnel Blockage Factor (TBF)

5.3.6. Slam force direction

As shown in the previous sections, the centrebow slams forces have both vertical and horizontal components. The slam angle (force direction) is defined as the ratio between the upward vertical force (F_z) and the aftward horizontal force (F_x) as per equation (5-13) and Figure 5.36,

$$\theta = \tan^{-1} \left(\frac{F_x}{F_z} \right) \quad (5-13)$$

where θ is the slam force angle taken from the Z-axis. The slam direction was calculated based on the magnitude of the F_z and F_x in each slam event and then it is presented as the average value of slam angles for each run.

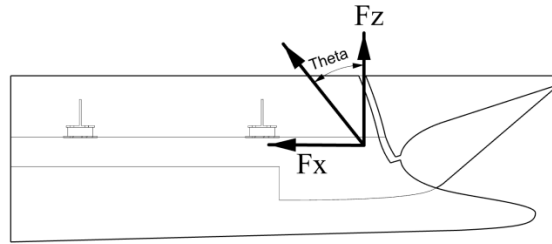


Figure 5.36: The definition of the slam angle (direction). F_x and F_z are the average peak slam forces measured for each slam event

The slam direction varies for different encountered wave frequencies. Figure 5.37 shows the slam angles for the three centrebows with the bars showing the 95% confidence intervals. The graph shows that the slam angles ranged from 14° to 35° where the long centrebow had the lowest slam angles and the short centrebow resulted in more vertical slams. Even though the long centrebow had larger horizontal forces, the even larger vertical forces in the long bow caused its slam angles to be smaller than the shorter bows. The slam angles are approximately constant for $4.53 \leq \omega_e^* \leq 5$ for each centrebow and become larger only in the longer waves.

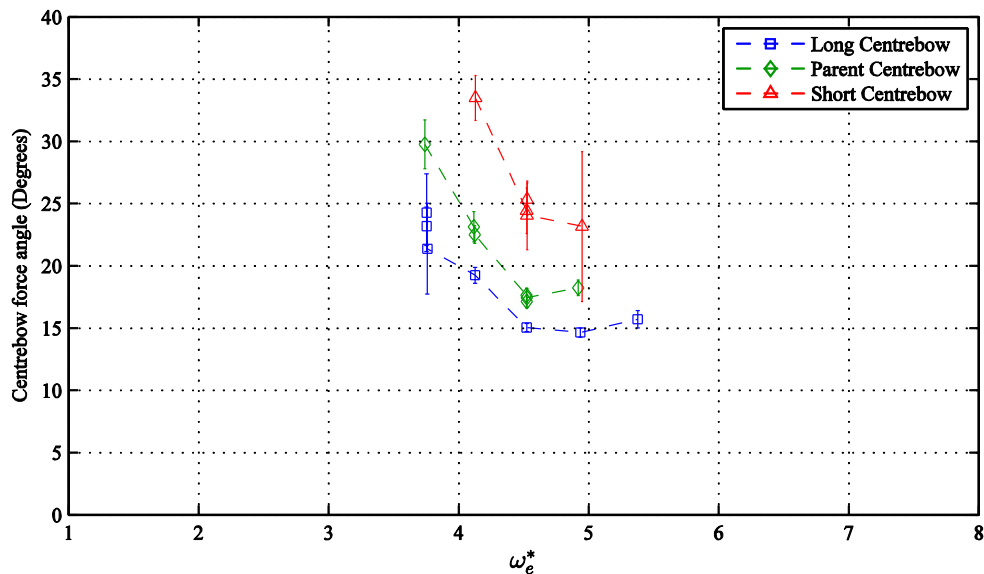


Figure 5.37: The slam angles for slamming conditions for three centrebows (speed = 1.53 m/s, $H_w = 60$ mm)

Figure 5.38 shows the slam direction versus centrebow length ratio and tunnel blockage factor of the three centrebows at the peak slamming condition ($\omega_e^* = 4.53$). As can be seen, the slam angles reduce as the centrebow length increases. Similar to the horizontal forces, the slam angles appear to have a more linear relationship with tunnel blockage. Even though the short centrebow has the least horizontal slam force (due to smaller TBF), its ratio of horizontal and vertical slam components gives rise to a larger slam angle.

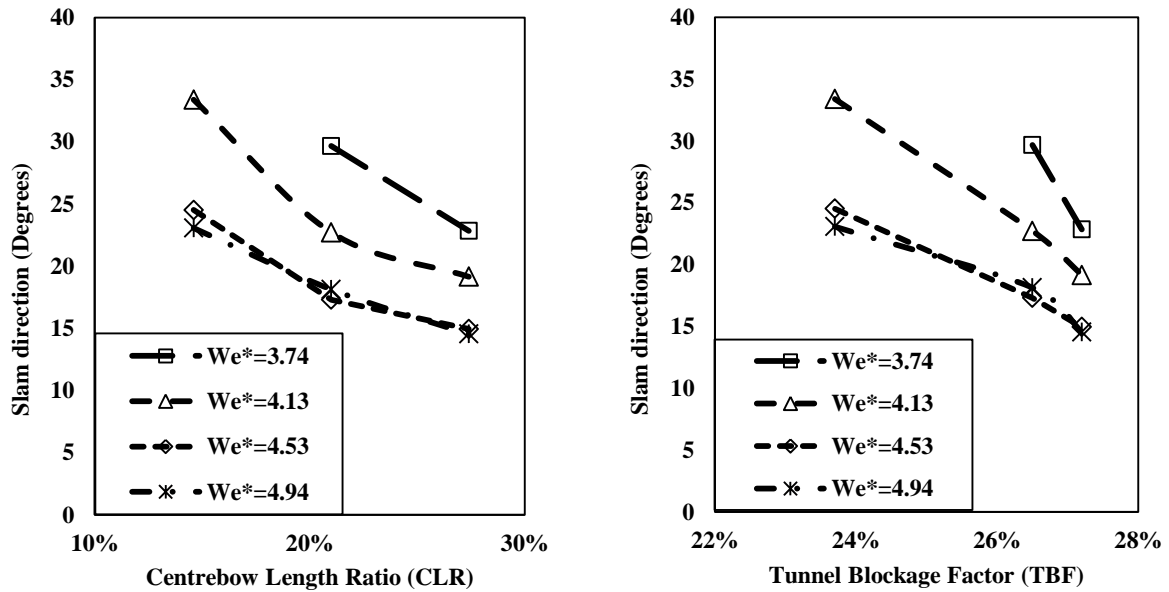


Figure 5.38: Slam directions versus Centrebow Length Ratio (CLR) and Tunnel Blockage Factor (TBF) of the three centrebows in slamming conditions.

5.3.7. Slam locations

The slam resultant force locations (x) as described in Chapter 3, section 3.5.1, can be calculated using Equation (5-14),

$$x = \frac{-B_z \cdot d + M_B + M_A}{-F_z} \quad (5-14)$$

where B_z is the aft force transducer force, M_B and M_A are the moments recorded by forward and aft sensors respectively and d is the distance between the two sensors.

Figure 5.39 shows the slam locations for the three centrebows for the slamming wave encounter frequencies. The slam locations are calculated for each slam event and have then been averaged over each run. As seen, the slams occurred mainly in the region forward of the parent centrebow truncation with $\omega_e^* = 3.7$ having the most forward located slams. In the short and parent centrebow, for the lowest and highest frequencies shown, the severity of slamming (bow diving) reduces and only the aft end of the centrebow encounters the wave upwash; therefore, the slam locations are behind the centrebow truncations.

At $\omega_e^* = 5.4$ the slams occurred further aft, close to the long centrebow truncation: the reason could be the combination of vessel motions and the wave profile, which caused a slam for only the long centrebow configuration.

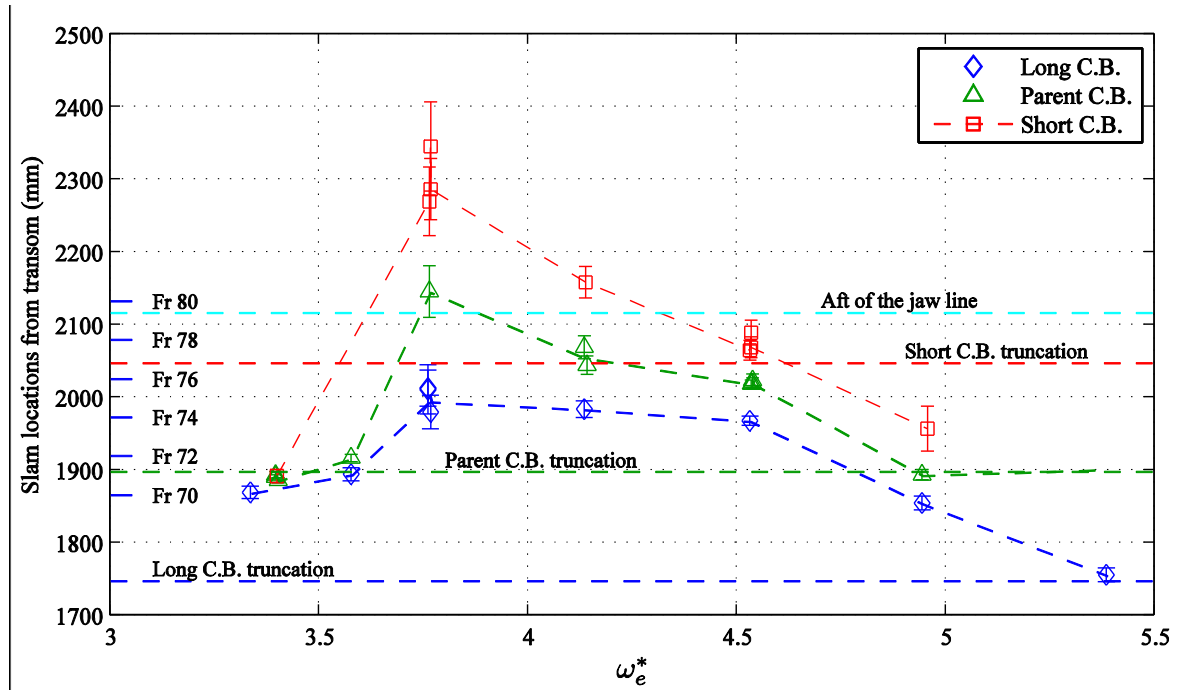


Figure 5.39: Centrebow resultant force locations for three centrebow lengths. The centrebow truncations and the aft of the jaw-line of the bow profiles are shown.

This trend for aftward movement of the slams in the shorter waves follows a trend for reduction of heave and pitch magnitudes as seen in Figure 5.40, meaning that the larger the motions are the further forward the slams occur. This is due to the increased downward motion of the centrebow which enters the water more deeply further forward when experiencing larger motions.

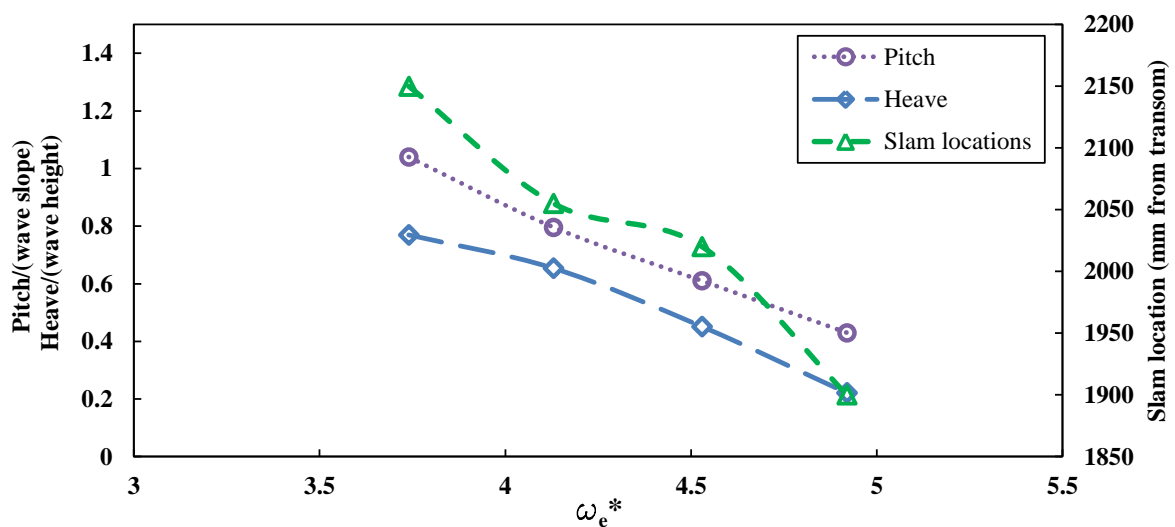


Figure 5.40: Trends of slam locations pitch and heave motions in the mid frequency range (slamming zone) for the parent centrebow

Slams occurred further forward on the short centrebow, followed by the parent centrebow and the most aftward slam locations were for the long centrebow. The reason for this trend was that the long centrebow has a larger volume extended astern thus increasing the length of the constrained archway region; thus the location of the forces moves aftward Figure 5.41 illustrates a schematic location of the slam resultant forces for the three centrebows at the peak slamming condition ($\omega_e^* = 4.53$). As seen the short centrebow slams are smaller in magnitude, have larger horizontal components and occur further forward. The long centrebow slams are greater in magnitude, more vertical and occur further aft.

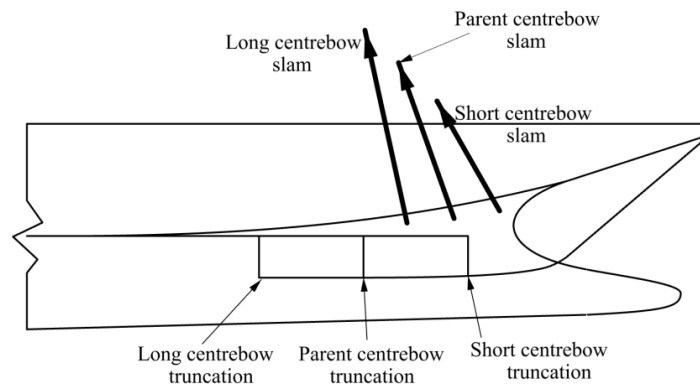


Figure 5.41: Schematic of the slam resultant force locations in peak slamming condition ($H_w=60$ mm, speed=1.53 m/s, $\omega_e^*=4.53$)

Also it is seen that for the short centrebow, the slam resultant force location is just aft of the jaw line, forward of which most of the centrebow upwash water can exit outboard without being constrained under the archways. This is another indication of why the smallest slam forces occurred on the short centrebow. From this figure it also might be interpreted that the resultant force locations occur vertically in-line with the centroid of the centrebow volumes in a bow down slam condition: as the centrebow length increases, the centrebow volume centroid moves aftward. Figure 5.42 shows a snapshot from the videos of the centrebow in a slam event where the upwash water exits outboards from the centrebow jawline.

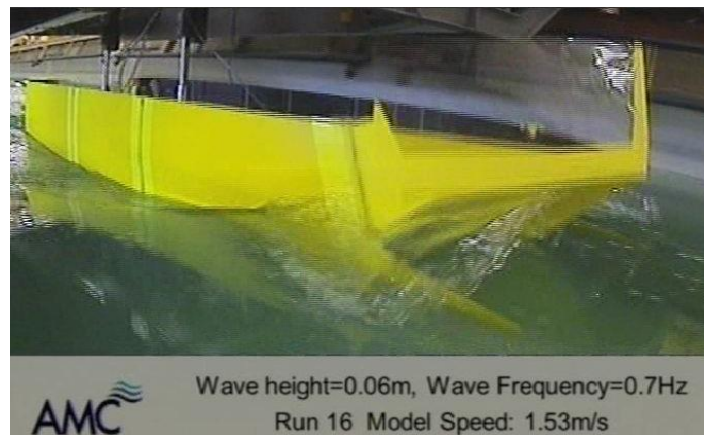


Figure 5.42: A photo of slamming for the parent centrebow configuration in the head seas ($H_w=60$ mm, speed=1.53 m/s and $\omega_e^*=4.136$). The spray pattern after the slam shows that water displaced by the centrebow passes outboard of the demihull, forward of the aftmost jaw point

Figure 5.43 shows the slam locations with respect to centrebow length ratio and tunnel blockage factor at the peak slamming condition ($\omega_e^* = 4.53$). As seen the slams are weaker and occur further forward as the centrebow length decreases. Also, the slam locations vary more linearly with the centrebow length than tunnel blockage. This further illustrates the effect of the constrained water under the archways on slam magnitude and location.

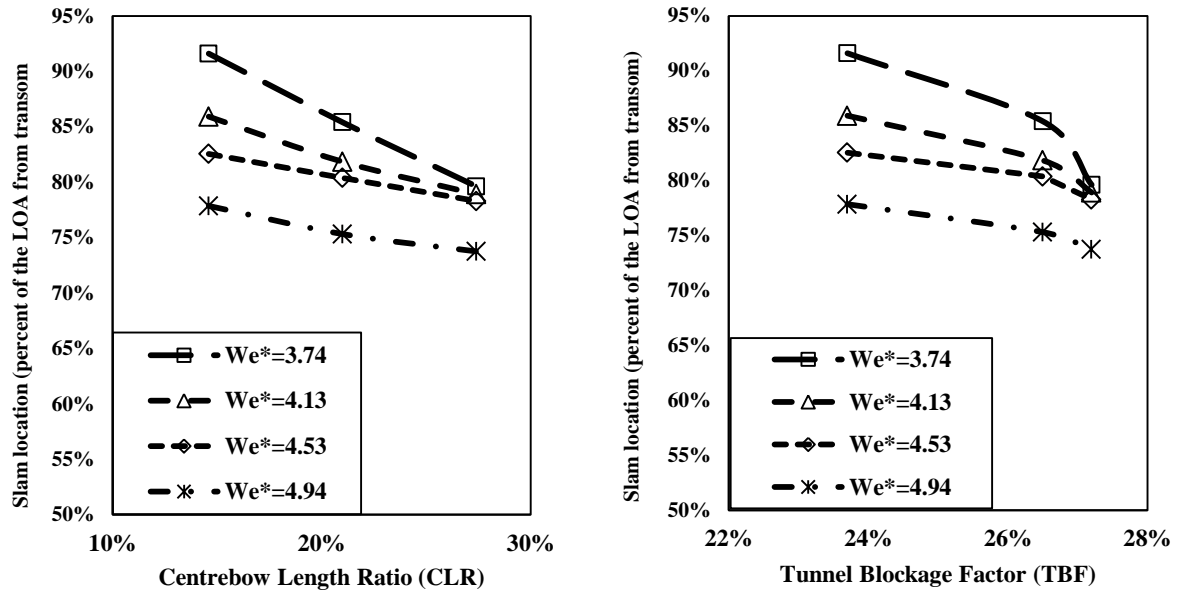


Figure 5.43: The slam resultant force locations in peak slamming condition ($H_w=60$ mm, speed=1.53 m/s) as a function of Centrebow Length Ratio (CLR) and Tunnel Blockage Factor (TBF) of the centrebow

5.3.8. Vertical Bending Moments (VBMs)

VBMs were derived from the strain gauges on the elastic links in the transverse cuts. The forward cut is at 1409 mm (56% of LOA) from the transom and the aft cut is located 820 mm (33% of LOA) from the transom. Figure 5.44 shows the location of the segment cuts and the directions of the VBMs, where the sagging VBM is positive and hogging VBM is negative.

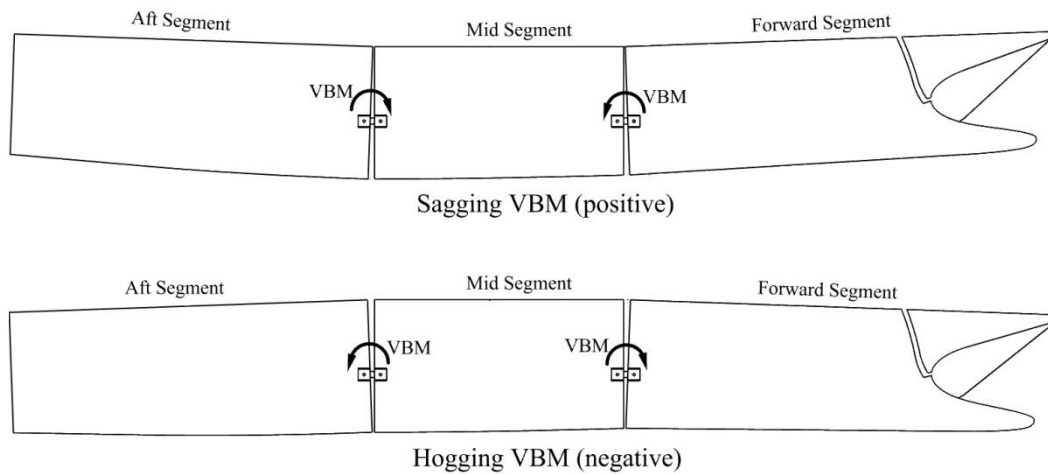


Figure 5.44: The hogging and sagging of the model and vertical bending moment in each segment cut. Sagging VBM is positive and hogging is negative

The VBM at each cut is the addition of the VBM from the starboard and port side elastic links. The procedure and calibration factors for VBMs of the model were presented in Chapter 4. Figure 5.45 shows a sample time history of the VBM recorded at the aft cut in run 45. The calm water, zero speed VBMs were first removed as bias signals. The graph clearly shows the slam induced sharp VBM peaks and the consequent vibrational loading or whipping. The peaks are visible after a peak slam sagging VBM and are followed by large oscillations around the mean line.

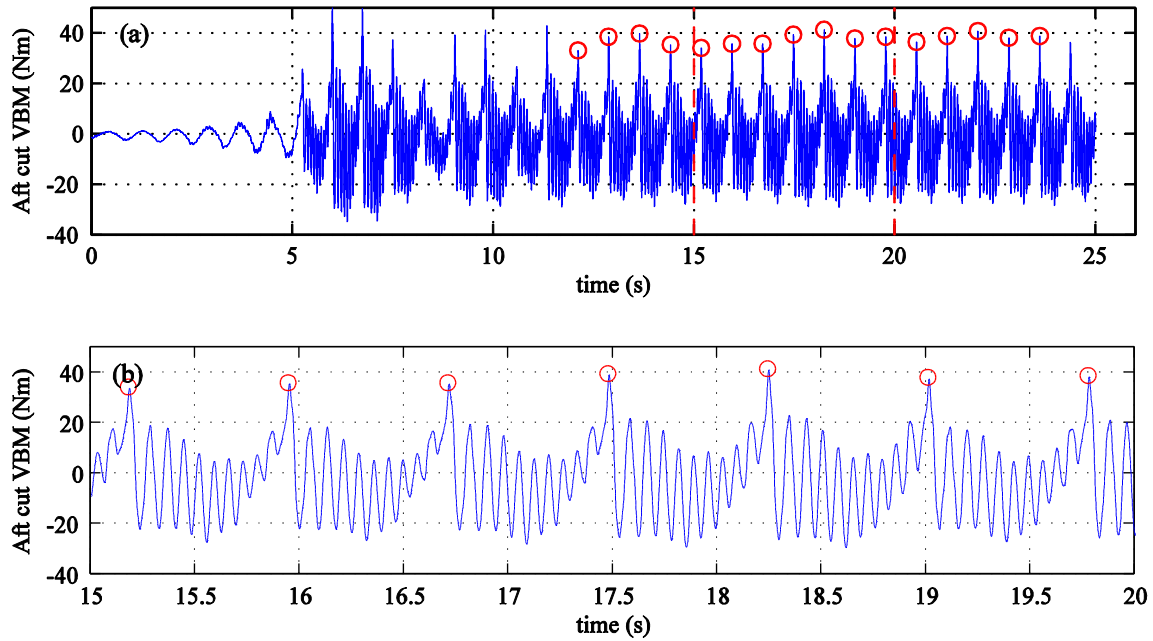


Figure 5.45: (a) Sample run recording data of aft cut vertical bending moment (VBM) for run 45 ($H_w=60$ mm, speed=1.53 m/s, $\omega_e^*=4.136$); (b) close up of the data. The more frequent oscillations are the whipping responses of the model, while the high peaks are slam induced VBMs.

The whipping effects are significant and they are not fully damped by the time the next slam is experienced. The average damping ratio of the VBMs for this run is around 0.023. This decay coefficient is greater than the value of 0.015 for the model in calm water and zero speed (see Chapter 4, section 4.1). Full-scale decay coefficients calculated by Thomas [115] on Hull 50 (96 m length) of INCAT wave-piercing catamarans through anchor exciter tests ranged between 0.01 and 0.06. This means that the model structural damping ratio is in a similar range to full-scale vessels. Figure 5.46 shows a sample strain gauge data from full-scale keel plate the Hull042 (86 m length) INCAT catamaran after being excited by a slam [115]. As seen, in full-scale, single slam occurs and it becomes fully damped whereas in the model, the next slam occurs before the whipping effects are totally damped. The comparison between the model raw data and full-scale data demonstrates the effectiveness of the model in replicating the dynamic behaviour of the full-scale vessel.

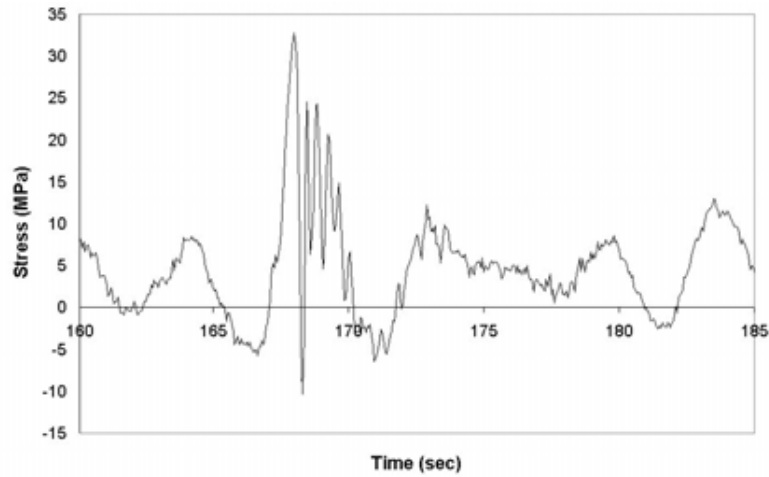


Figure 5.46: keel plate stresses frame 24.5 of full-scale measurements on INCAT Hull042 (86 m length) [115]

Figure 5.47 shows the power spectrum of the forward cut VBM signals. As seen, there are two main frequencies observable in the spectrum. Similar to centrebow forces, to obtain this spectrum, the VBM signal over the run was divided into bins of roughly two encounter wave periods, tapered with MATLAB Hamming window, performed FFT on the bin and then averaging the spectrums for the whole run. As seen, there are two peaks in the graph. The first one is close to the encounter wave frequency inducing the global wave loads (this is inaccurate, since less than two wave encounters were in each bin). The second group of oscillations are at peak 12.82 Hz which correspond to the whipping vibratory response of the model. Similar frequency was also seen in centrebow force responses. The whipping frequency peak in the spectrum is not very sharp and the energy is quite widely distributed; the reason is that the whipping oscillations between to slam induced peak differ slightly before and after the peaks due to variations in hydrodynamic loads.

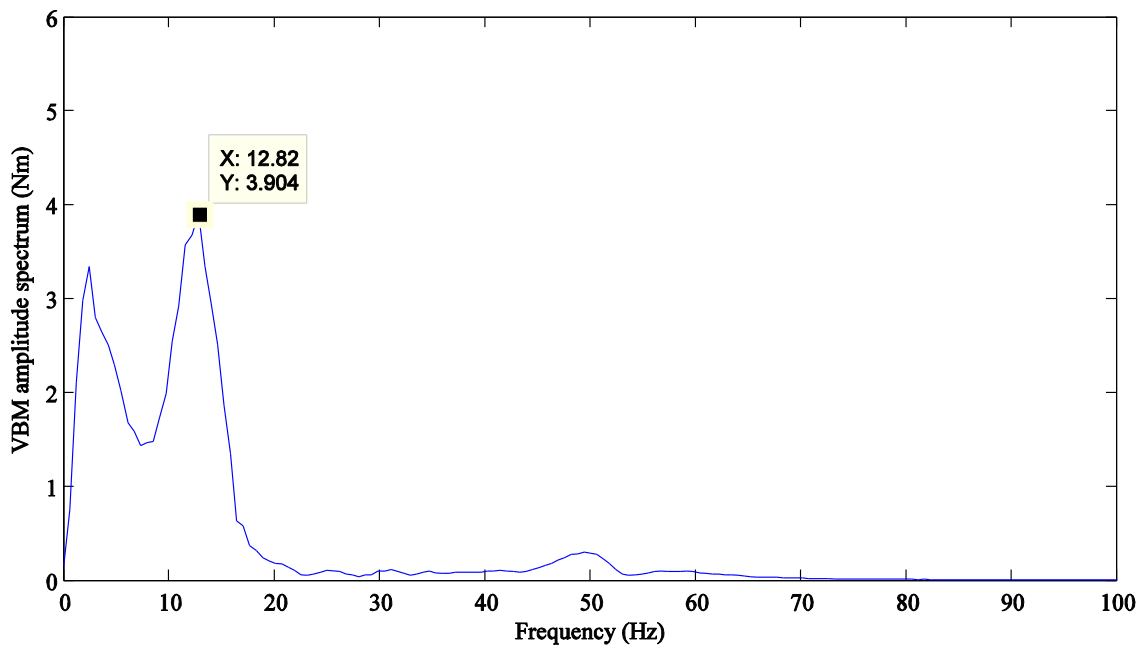


Figure 5.47: Amplitude spectrum of vertical bending moments of run 45 ($H_w=60$ mm, speed=1.53 m/s, $\omega_e^*=4.136$) extracted using FFT analysis

The VBM time series in Figure 5.45 also shows the variation of slam induced VBMs in one run; however, the peak value variations are less than the slam forces. The whipping cycles in VBM signals are seen to be damped more strongly when approaching the next slam by the hydrodynamic loads on the now partly immersed bow. However, similar to the slam loads, the whipping frequency is not an exact multiple of the slam frequency; hence, each slam induced VBM peak can vary as they are influenced by the slam loads severity and also the un-damped whipping effects. Observing such variations in VBM values lead to presenting the loads in a more probabilistic manner to show the uncertainty involved. In a given environmental condition, both the distribution of load values and the extreme loads can be important.

Depending on the encounter wave frequency, the number of steady wave loads in one towing tank run varied between 7 and 25 peaks. In the runs where slamming occurred the number of slams was between 12 and 20. To identify the distribution of peak values, as an example, the results of aft cut sagging VBM peak values from four similar runs with $\omega_e^* = 4.53$ (with largest slam loads) in parent centrebow were analysed. Figure 5.48 shows the histogram of these VBM peak values where, from the total 78 peak values, the mean is 38.48 Nm and the standard deviation is 2.79 Nm. It is seen that the samples are somewhat evenly distributed around the mean value and this suggests that the normal distribution can be assumed for the VBM values for a particular run.

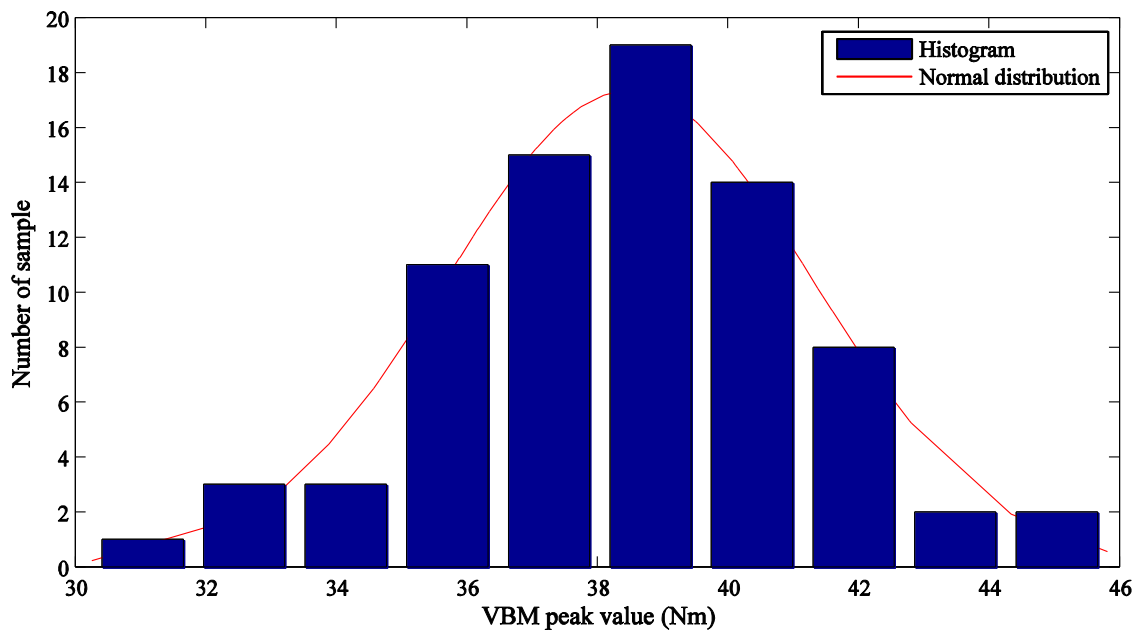


Figure 5.48: The histogram of slam induced VBM peak values for the forward cut during 4 runs ($H_w=60$ mm, speed=1.53 m/s, $\omega_e^*=4.53$). The mean is 38.48 Nm and standard deviation is 2.79.

To verify this assumption, a Kolmogorov–Smirnov test [116] (a test for the equality of continuous probability distribution) was performed on the data in MATLAB statistics toolbox, which showed that with 98.7% confidence the normal distribution can be accepted (or cannot be rejected) for this

distribution. Figure 5.49 shows the cumulative distribution function for the normal distribution and the sample data where a good concurrence is observed.

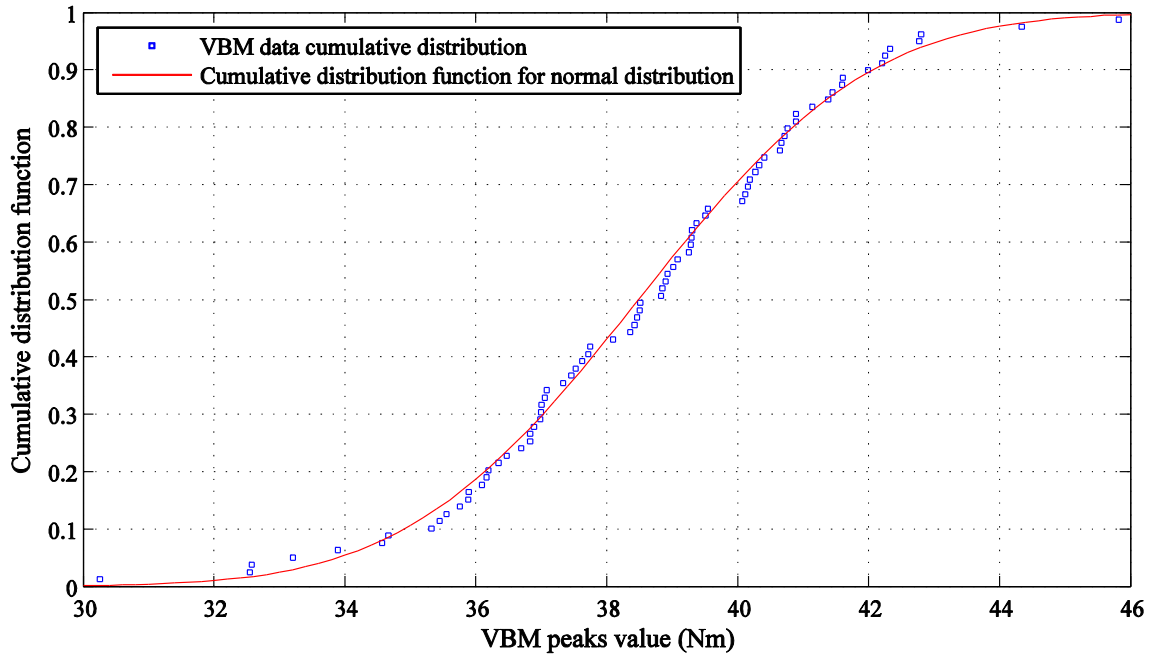


Figure 5.49: The cumulative distribution of the VBM peak values of parent centrebow compared to the normal distribution ($H_w=60$ mm, speed=1.53 m/s, $\omega_e^*=4.53$)

The VBM values in hogging or sagging condition was calculated as the mean of the peak values in each encountered wave when the run was in steady wave conditions. Figure 5.50 and Figure 5.51 show the measured peak forward cut and aft cut (56% of length overall (LOA)) and aft cut (33% LOA) VBM response of the three centrebows with 95% confidence intervals as a function of the non-dimensional encounter frequency. As seen, for high and low encounter wave frequencies, the measured VBM results tend to zero and there is negligible difference between the three centrebows. In the frequency range of slamming ($3.7 \leq \omega_e^* \leq 5$) the VBM values increase and there is an evident difference between the responses of the three centrebows. Although there is not a sharp peak, the VBM due to slamming is a maximum when $4.13 \leq \omega_e^* \leq 4.53$.

The hogging VBMs are smaller than sagging VBMs in the frequency range of slamming and it is difficult to draw a comparative conclusion between the three configurations for the hogging results. The reason for this is that the hogging peaks are the consequence of the slam induced sagging peaks which occur when the archways are filled up after a wetdeck slam. There is little difference between the three centrebows in terms of whipping frequency (12.82 Hz) and it could be concluded that the variations of added mass on the bow (causing the hogging response) are small.

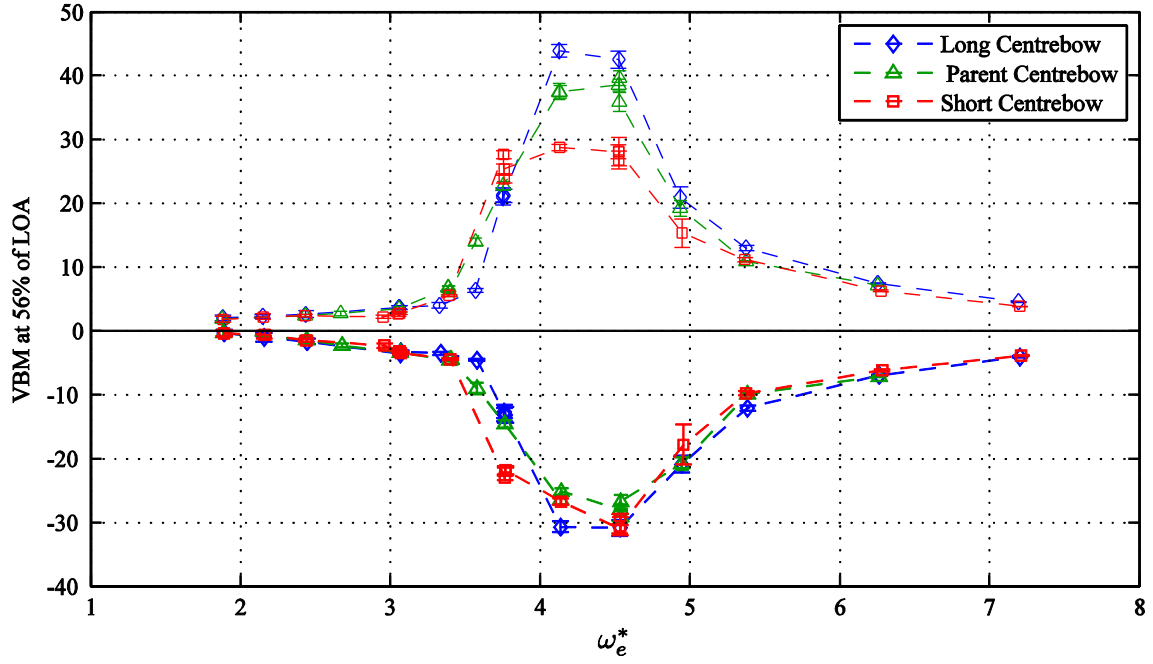


Figure 5.50: The measured forward vertical bending moment (VBM) for the three centrebow lengths. The positive shows sagging VBM values and the negative shows hogging VBM ($Hw=60$ mm, speed=1.53 m/s)

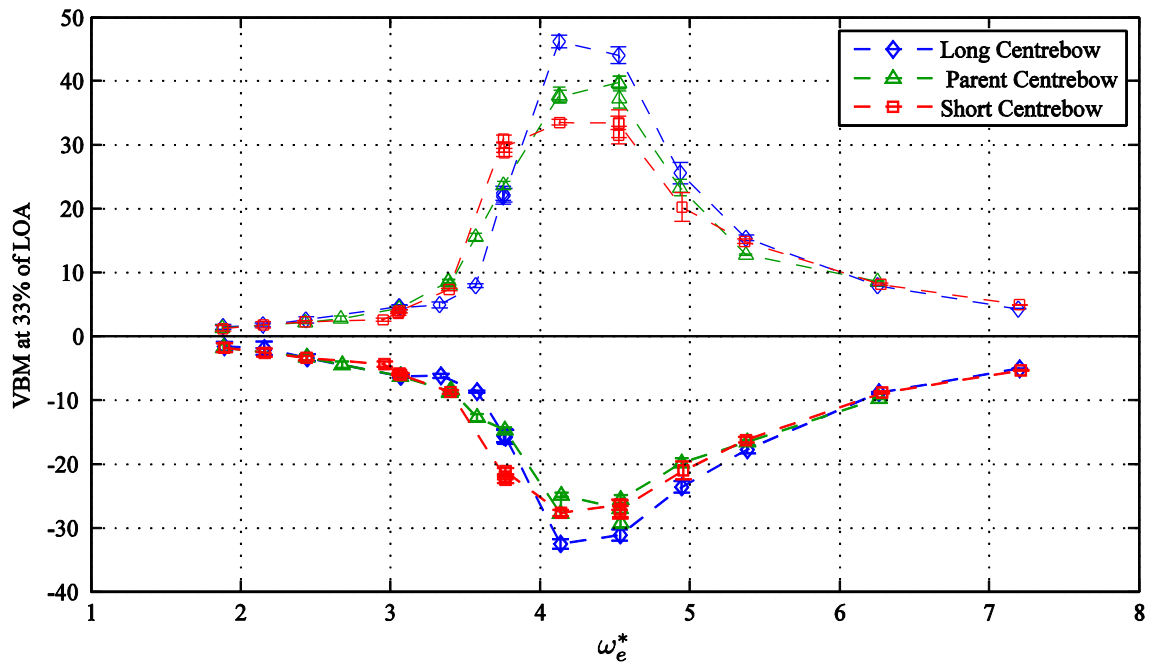


Figure 5.51: The measured aft cut VBM in the model for the three centrebow lengths. The positive shows sagging VBM values and the negative shows hogging values ($Hw=60$ mm, speed=1.53 m/s).

The non-dimensional bending moment, VBM^* is calculated by equation (5-15),

$$VBM^* = \frac{VBM}{\rho g H_w \nabla} \quad (5-15)$$

based on the method used by Colwell [114], where ρ is the water density, H_w is the wave height and ∇ is the vessel's displaced volume. Figure 5.52 and Figure 5.53 shows the results of non-dimensional VBMs for the three centrebow lengths in forward cut.

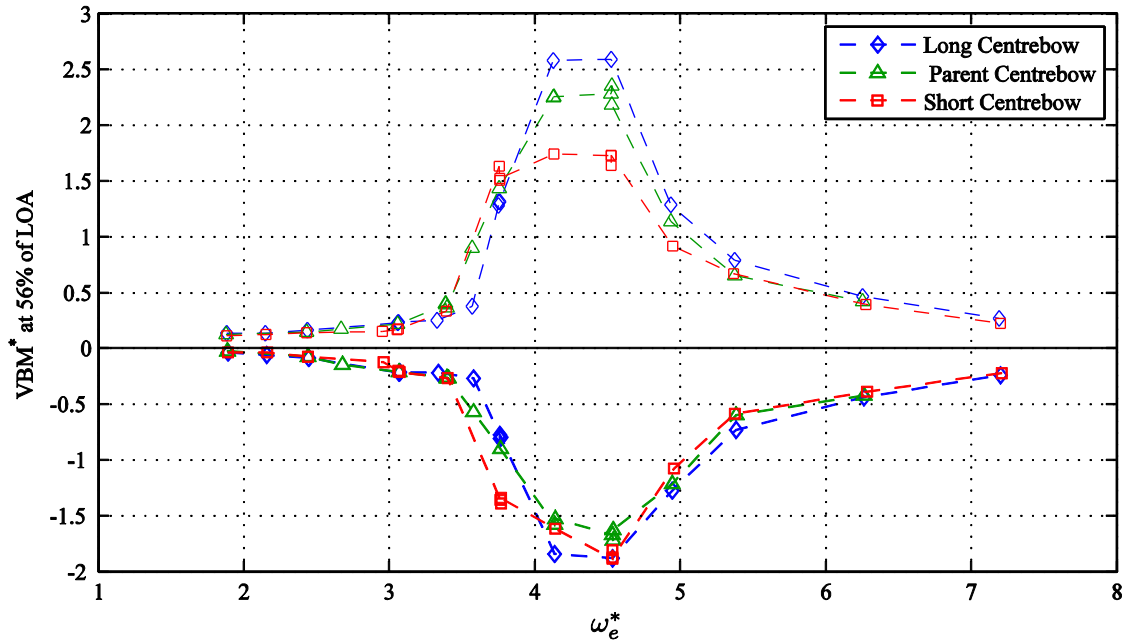


Figure 5.52: The non-dimensional forward cut (56% LOA) vertical bending moment (VBM^*) for the three centrebow lengths ($VBM^* = \frac{VBM}{\rho g H_w \nabla}$)

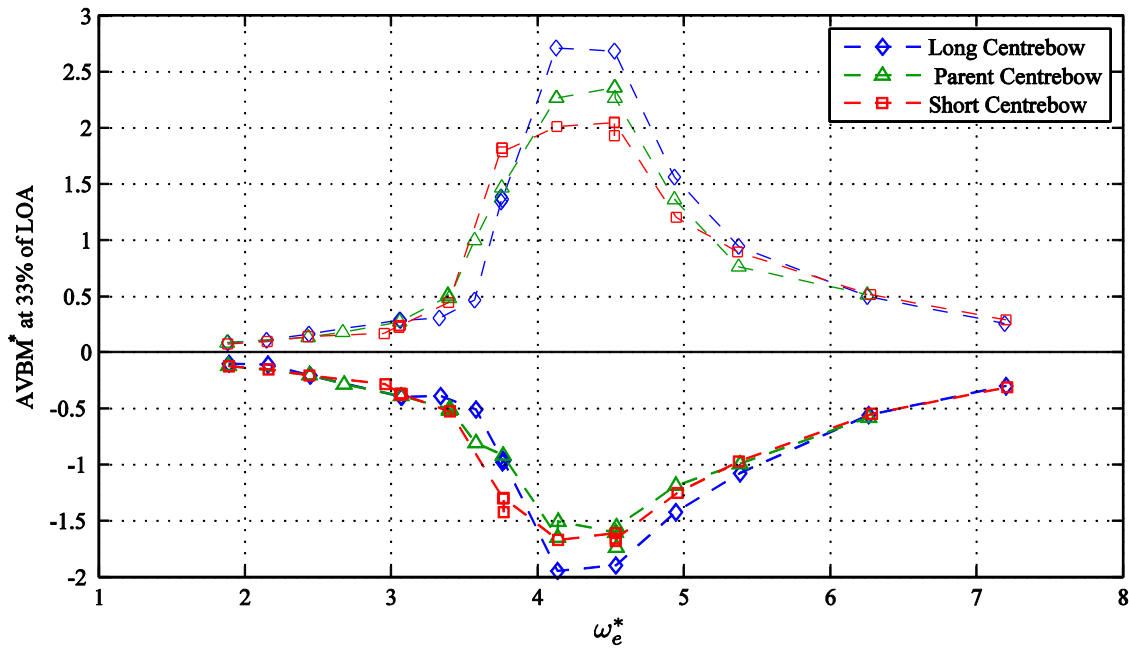


Figure 5.53: The non-dimensional aft cut (33% LOA) vertical bending moment (VBM^*) for the three centrebow lengths ($VBM^* = \frac{VBM}{\rho g H_w \nabla}$)

As seen in the above figures, the VBM results have a maximum in the range of $4.13 \leq \omega_e^* \leq 4.53$. Figure 5.50 and Figure 5.51 show that the average VBM peak value for the long centrebow was 52% and 40% higher than the short centrebow at the forward and aft cuts respectively. This difference can be related to higher slam forces recorded for the long centrebow compared to the shorter centrebows. The difference between the VBMs though was not as great as the slam loads differences between the three bows. The reason could be the rapid transient nature of the slam forces which would be rounded (filtered) by the model segment's inertia before turning into a peak vertical bending moment in the structure. The other reason could be the reduction in moment of the slam force with the long centrebow since the slams occurred further aft.

Figure 5.54 and Figure 5.55 show the non-dimensional VBM recorded in slamming conditions at the forward and aft cuts as a function of centrebow length ratio in different wave conditions. As can be seen, similar to the slam loads, the VBM peaks in slamming conditions increase approximately in proportion to the centrebow length ratio. In $\omega_e^* = 3.74$ the VBM decreases with regard to centrebow length which shows the difficulty of generalised explanations for such complex models.

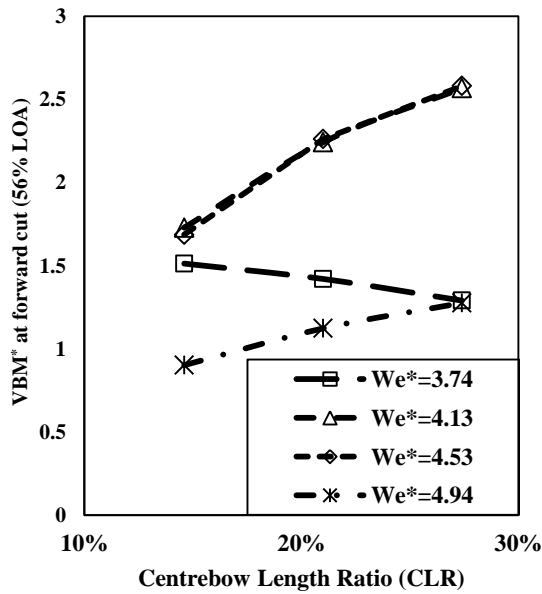


Figure 5.54: The vertical bending moment of the forward cut of the three centrebow lengths

$$VBM^* = \frac{VBM}{\rho g H_w \nabla}$$

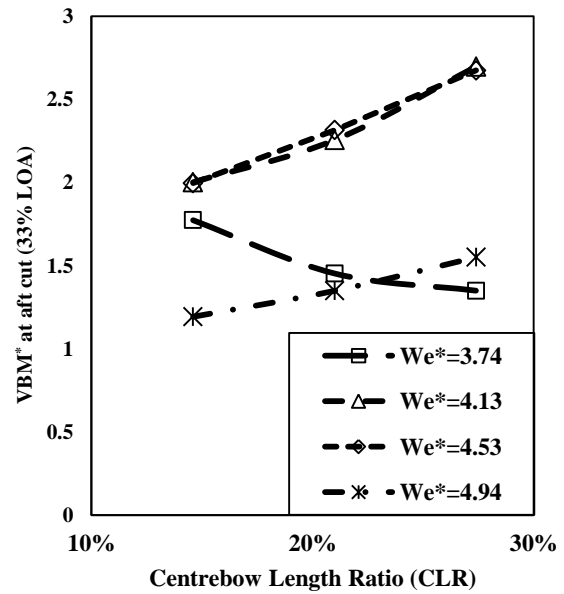


Figure 5.55: The vertical bending moments of the Aft cut of the three centrebow lengths

$$VBM^* = \frac{VBM}{\rho g H_w \nabla}$$

The VBM peak frequency is slightly lower than peak slam loads frequency ($\omega_e^* = 4.53$) but higher than the motion resonance frequency especially for the long centrebow. This could be due to the slam locations being more forward at lower encounter frequencies. Figure 5.56 shows the forward cut peak vertical bending moments and the product of slam force and the distance of the slam from the forward cut for the three centrebow lengths at the peak slamming condition. As seen, the product of slam force and slam distance from the forward cut is more than the induced VBM since the inertia loads from the forward segment demihulls and the VBM induced by the mid segment are not taken into account.

However, quite similar slopes are seen for these two plots. In summary the magnitude of the slam forces and their distribution can be key factors affecting slam induced VBM.

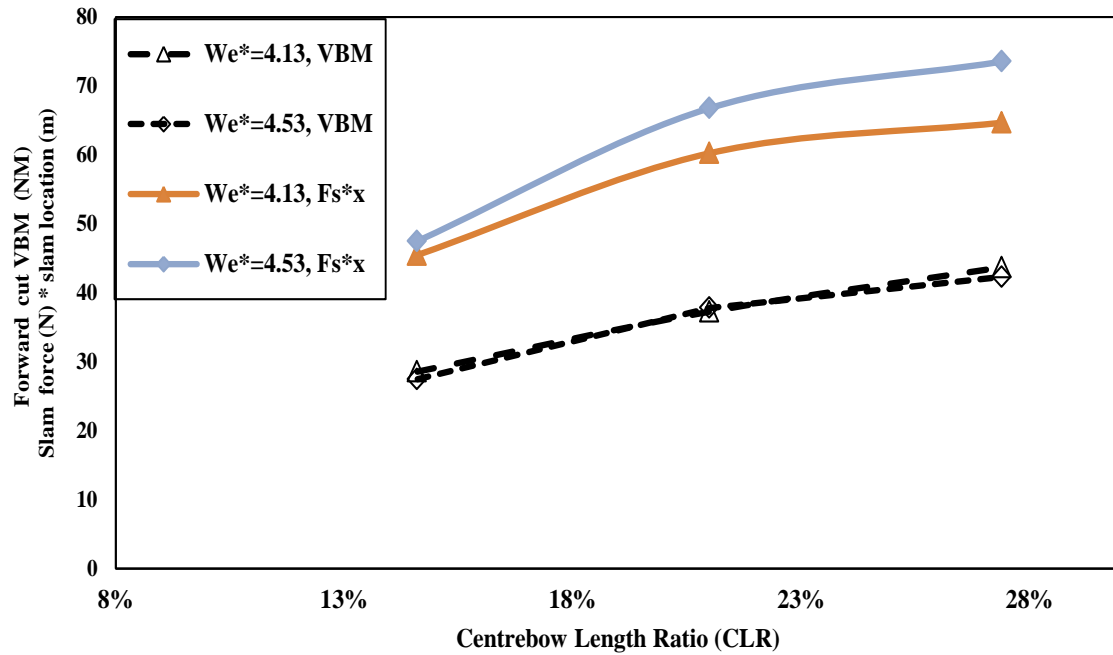


Figure 5.56: The relationship between the forward cut (56% LOA) vertical bending moments and the slam locations (x) multiplied by slam forces (F_s) in peak slamming conditions

5.3.9. Wetdeck archway pressure results

The time history of run 45 pressures at Frame 72, located 18.2 mm forward of the parent centrebow truncation, is plotted in Figure 5.57. As can be seen, the slams show themselves as very sharp peaks and are followed by negative pressures due to added mass effects. For this run the mean pressure peak value was 5.262 kPa; however, a significant variation in peak value is observed. The standard deviation of the peak value is 1.268 kPa with a maximum to minimum range of 4.745 kPa for the steady wave conditions. The variation is around $\pm 45\%$ of the mean value, which means that there are high variations (errors) in estimating the mean of peak pressures for each run. One reason for these variations is the remaining whipping oscillations prior to slam event which created variations in both slam loads and VBMs. The peak pressure appears to be quite sensitive to the precise detail of each slamming event, such as the exact water surface profile and the precise timing of hull and surface motions.

To investigate the source of this large variation, the pressure time histories were examined in detail. Figure 5.58(a) shows the pressures of one of the slams in run 45. The pressure peak is very sharp and is followed by two negative oscillations which are similar to the slam loads signals. Figure 5.58(b) shows a close up of the peak of this pressure signal where it can be seen that there were insufficient points to define the peak accurately. Although the condition of this particular slam event is quite extreme, it shows that the true peak could be either before or after the measured peak. This is due to the low sampling rate (5000 Hz) chosen for pressures referring to previous works on the previous

model, HSM01 by Amin [20]. The sample rate study in his work was comprised of recording and comparing the averages of the pressure peaks in three similar runs. At 5000 Hz, the mean of three runs worked out to be similar; however, the standard error in predicting the means was very high. According to more recent literature, the slam pressures should be sampled at around 20,000 Hz or above [117] in model tests for slamming. Therefore, the use of pressure peak results at this stage of the project can introduce high errors into the predictions.

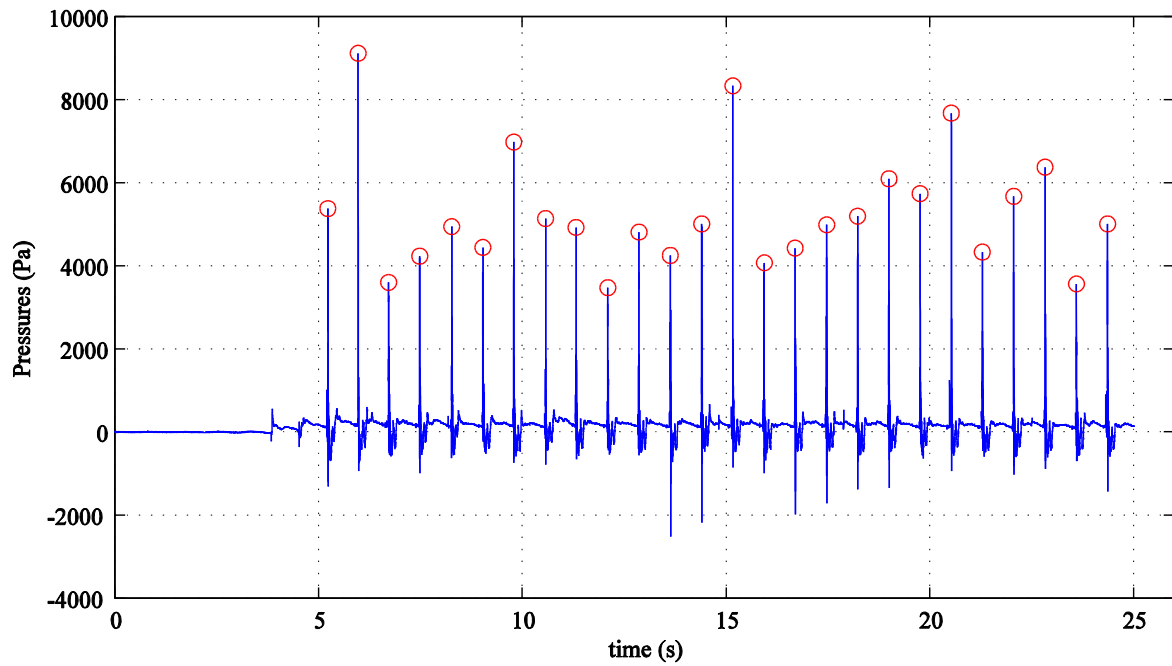


Figure 5.57: Time history of pressures at frame 72, top of the arch pressure transducer in run 45 ($\omega_c^*=4.136$)

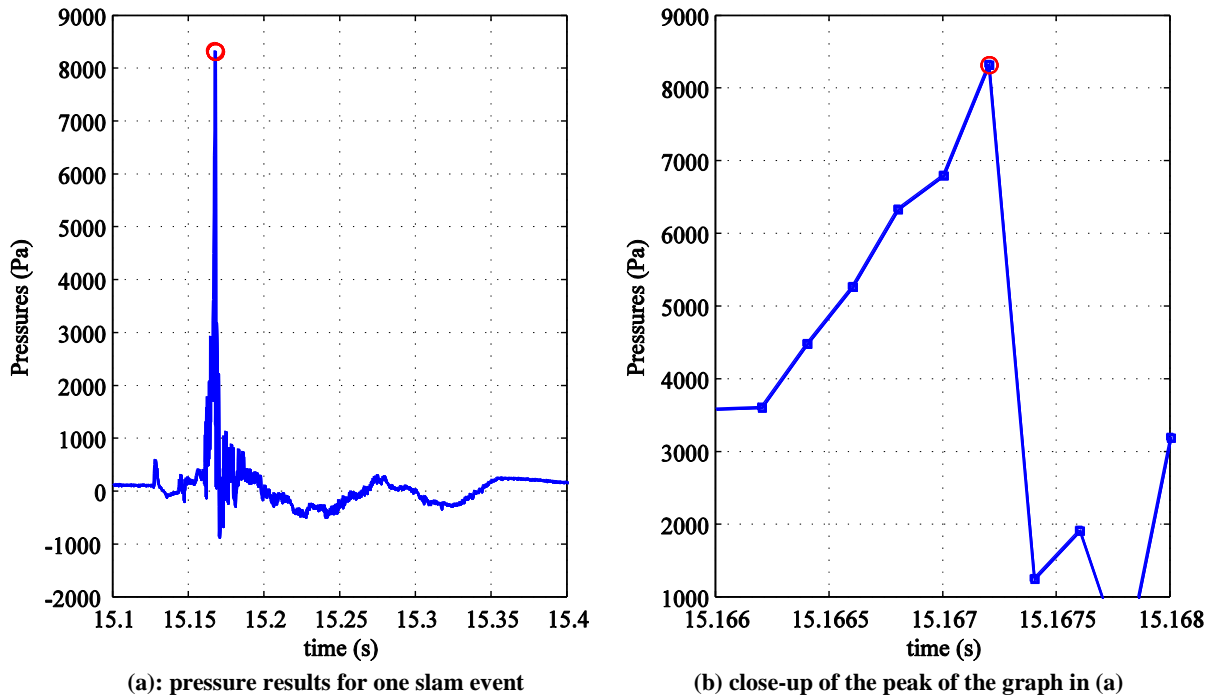


Figure 5.58: The pressure signal for one slam case in run 45. The (b) shows the peak of the (a) slam event. It shows strong effect of aliasing in finding the slam peak pressure

5.3.10. Further investigations into the centrebow force signals (a hypothesis)

As seen previously in Figure 5.19, when the centrebow is out of the water, the external forces show no oscillation after exclusion of the inertia. The underlying sinusoidal external force can be seen in between two slams at the wave encounter frequency, where it starts after the centrebow comes out of the water and peaks before wetdeck slamming. This force then cannot be distinguished from other external forces components during slamming. If the external forces are low-pass filtered at the wave encounter frequency, this underlying force can be seen as in Figure 5.60(b).

The nature of this force is not inertia (the accelerations effects from whipping and the global motions are removed) and it is an external force; therefore, the only option remaining is a force caused by air. The logic is that during the motions in waves, the small air pressure difference between the top and bottom of the wetdeck can generate a force over the quite large area (0.415 m^2) of the isolated centrebow segment. This is shown in the schematic diagram of Figure 5.59. The air becomes constricted under the wetdeck, inside the demihulls and water surface, whilst it deflects and increase speed (thus dropping pressure) on top of the wetdeck. Note that there was a light-weight shield installed on the centrebow to stop green water splashing into the model and the isolated bow segment is extended far beyond the centrebow truncation. The unforced ventilated air pressure acting as an air cushion has been used previously in designing some planning crafts to lift the boat to reduce drag [118]. The logic has been to naturally vent the air underneath the vessel through bow channels, use a transverse chine discontinuity and confine the air between the side hulls and vessel end. Similar phenomena appear to happen during slamming for catamarans with a truncated centrebow in forward speed in waves. The air blow around the jet of water outboard from the centrebow after slamming [119] can also be an indication of existence of such air pressure constriction prior to slamming.

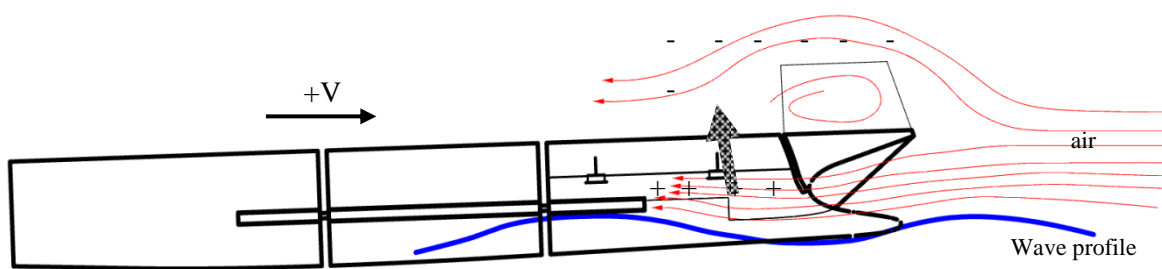


Figure 5.59: The schematic diagram of the air flow below and above the wetdeck when running in waves. An air pressure difference is generated applying a small upward force

Therefore, it is proposed (as a hypothesis) that the external forces can be divided in two components: water slam forces (F_s) and air pressure forces (F_a) as in Equation (5-16):

$$F_{ex} = F_s + F_a \quad (5-16)$$

where F_a is obtained by low-pass filtering the external forces. The slam forces (F_s) and air pressure forces (F_a) can be seen in Figure 5.60 for run 45.

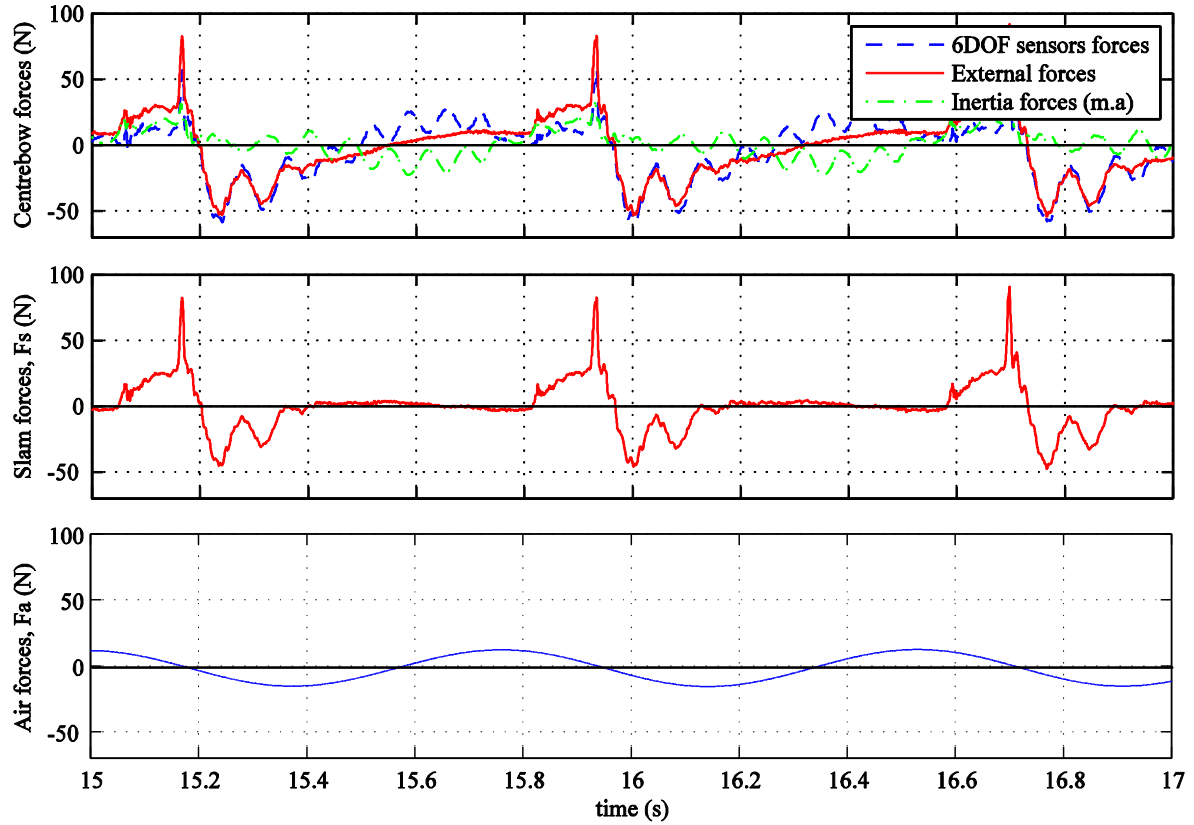


Figure 5.60: Sample time series of the centrebow forces (speed=1.53 m/s, $H_w=60$ mm, $\omega_c^*=4.136$). The centrebow external force can be divided into water slam forces and air forces

To further support this hypothesis, an investigation was conducted using pressure measurements during the runs in the waves. The pressure gauges were examined for linearity in measuring low pressures and the aerodynamic forces and the pressures are again in phase. Pressures transducers were located longitudinally along the arch top and recorded differential pressures (between top and bottom of the archway) during the runs. The average necessary pressure difference underneath the centrebow (P) to produce such aerodynamic force can be calculated from Equation (5-17):

$$F_a = P \cdot A \quad (5-17)$$

where A is approximated by the projected area of the centrebow from the top and equals 0.415 m^2 . The aerodynamic force in run 45 is about 14 N, therefore the necessary pressure difference is 34 Pascal (Pa).

Figure 5.61 shows the time series of the pressure gauge and its low-pass filtered signal in run 45 at the arch top, close to the centrebow truncation (frame 72). The filtered signal is in phase with the air forces, and when the centrebow is fully emerged (i.e. between the two red dotted lines), its mean to peak value is an approximately 80 Pa. Although the air pressure distribution on the centrebow surface is unknown, the 80 Pa pressure is sufficiently greater than the necessary 34 Pa to generate the 14 N force. The other pressure transducers along the arch top in this run also show more than 34 Pa of

gauge pressure. It should also be noted that these calculations for air forces are not valid when the centrebow is totally or partly submerged.

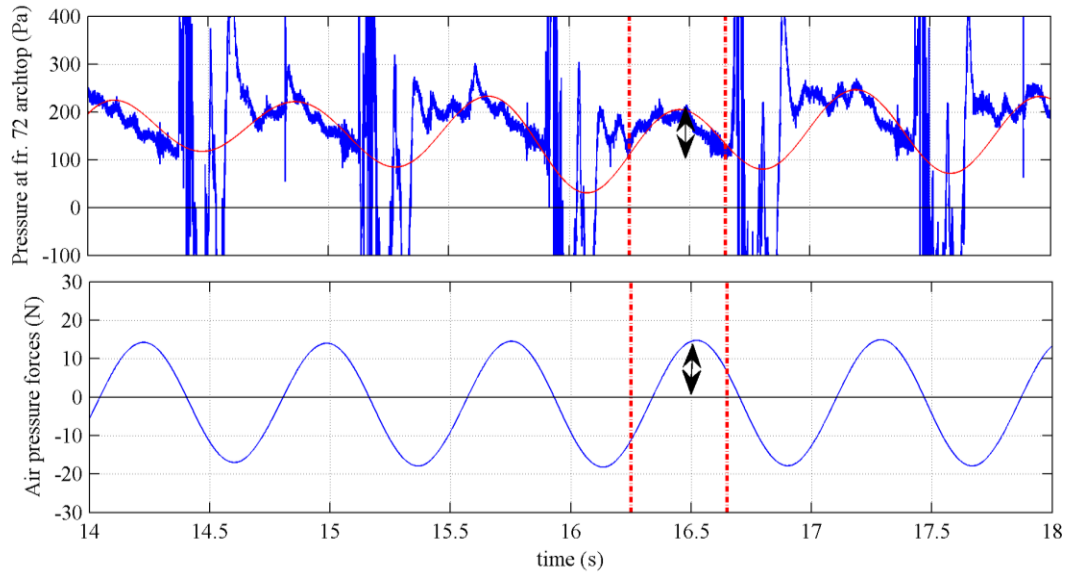


Figure 5.61: Sample time series of pressures in the transducer at frame 72 arch top and the calculated air pressure forces in run 45 (speed=1.53 m/s, $H_w=60$ mm, $\omega_e^*=4.136$)

Similar reasoning can be made for other wave frequencies and the alignment of air forces and pressures measured on the arch top.

The magnitude of air forces for the three centrebows is quantified and plotted against ω_e^* in Figure 5.62. The plot indicates that there is no significant difference between the three centrebows' air pressure forces and the slight differences can be explained by the filtering effects. Similarity in the air forces between the centrebows suggests that it is somewhat independent of centrebow length and is more closely related to slam load magnitudes.

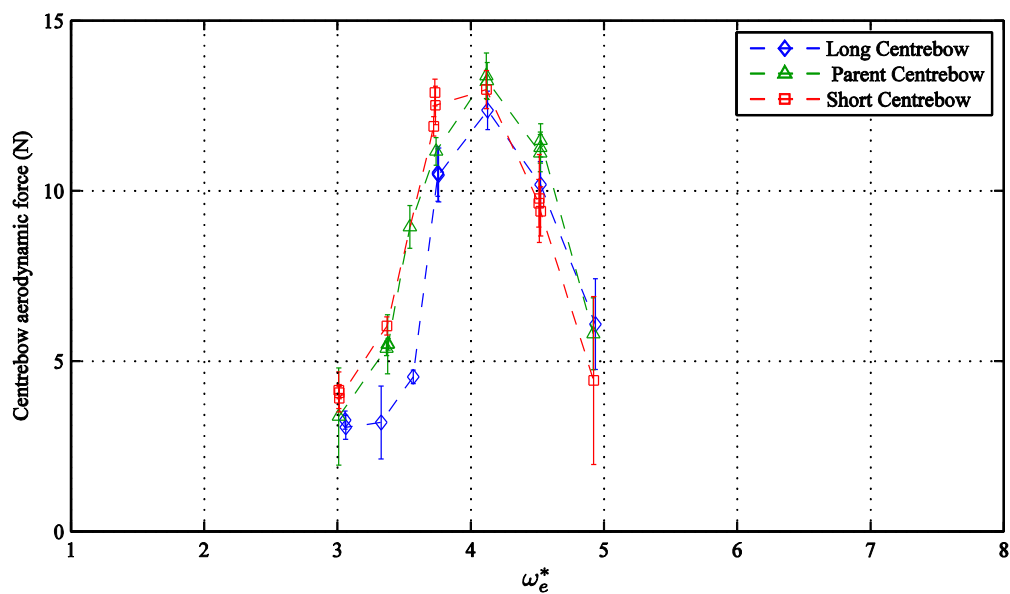


Figure 5.62: Air pressure forces under the centrebow archways (speed=1.53 m/s, $H_w=60$ mm)

In summary, it is proposed that there are sufficient indications to suggest that the air pressure difference between the top and bottom of the cross deck can generate a force albeit small under the wetdeck. Identifying this force component in catamarans is relatively novel; therefore, it is evident that further studies are necessary to further prove this phenomenon. These studies could include conducting experiments of the model in the air, swinging the model in pitch with a frequency between 1.1 Hz to 1.5 Hz (wave encounter frequency in slamming conditions), and sometime tapping the bow by hand to excite whipping mode while measuring centrebow forces and the bow accelerations. Removing bow mass inertia from the bow forces would give a good indication if the underlying forces are not solely from the global loads.

5.4. Summary

Measurement of motions and loads for each of the three models of varying centrebow length was undertaken successfully in regular waves of 60 mm height (2.68m full-scale) and at 1.53 m/s speed (20 knots full-scale) in different wave frequencies. The results could be summarised as following:

- The heave motions of the vessel showed a maximum at $\omega_e^* = 3.7$. The resonant peak of the short centrebow was higher than the parent, and the parent centrebow was higher than the long centrebow. At other frequencies, no significant difference between the centrebows was observed.
- The maximum peak of the pitch response of the vessel was in the range of $3 \leq \omega_e^* \leq 3.5$. No significant difference was observed between the peak values of the three model configurations; however a slight shift of the frequency of maximum pitch for the short centrebow toward lower frequencies was observed. The reason was likely to be due to the reduction in model hydrostatic stiffness with the short centrebow. The main difference was in the frequency range of slamming ($4 \leq \omega_e^* \leq 5$) in which shorter centrebows had an average 5% less pitch compared to the longer centrebows.
- The slam forces were measured in both the vertical and horizontal directions. In the vertical direction, the centrebow inertia was included successfully, leading to identification of external slam forces. This force showed to have a small local peak when the centrebow keel submerges and a sharp peak when the archway slamming occurs. Negative (downward) forces were seen right after the slamming where centrebow relative velocity was nearly zero and then the bow emerges from the water.
- The vertical slam loads were significantly different between the three centrebows, with the short centrebow having the minimum and the long centrebow having the maximum loads. This is due to the larger volume of water constrained under the archways with the longer

centrebowl. The vertical slam forces showed a clear linear relationship with centrebow length ratio (CLR).

- The external forces had a low frequency component which was evident even when the centrebow was out of water; this led to proposing (as a hypothesis) the existence of an aerodynamic component of external force which was explained more with the aid of pressure signals under the wetdeck prior to slam. These forces accounted for less than 15% of the total external vertical forces. More investigations are required in the future to fully test this hypothesis.
- The longer centrebows had a smaller pitch response in the frequency range of slamming and this was due to the larger upward slam force which pushed the model bow up more after a slam event.
- The slam resultant force locations were further forward with shorter centrebows. The reason was the location of constrained upwash water under the archways which was further forward with shorter centrebows. Also it was shown that, the larger the motions, the more forward the slams occur.
- The horizontal centrebow forces were also measured and identified to be aftward and around 24% to 70% of the vertical slam forces depending on the centrebow and encounter frequency. The horizontal forces had a clear linear relationship with the Tunnel Blockage Factor (TBF).
- The slam directions were calculated using the magnitude of vertical and horizontal component of slam forces. The slam angles were identified to be variant at different encounter frequencies and ranging between 15 to 33 degrees from the vertical axis. The shorter centrebows had more inclined slam angles. The slam angles also had a strong linear relationship with the horizontal tunnel blockage factor (TBF).
- The vertical bending moments were measured using strain gauges on the elastic links. The VBM peak values increased as the centrebow length increased in slamming conditions. The VBM peak distribution over a run was shown to be normal distribution. The VBM values difference was less than slam loads between the three bows due to model mass inertia and the location of the slams under the wetdeck.

In conclusion, for the conditions tested, the shorter centrebows are more effective in slamming conditions by reducing both motions and loads. The reason is that with shorter centrebows the displaced water exits from the sides and does not become constrained under the archways. The larger slam force appeared for longer centrebows and induces larger upward pitch motions which could intensify the slam condition further. This however, does not mean that the benefits of centrebow length reduction will increase if the centrebow is removed completely. Designers should note that

although shorter centrebows may give less loads and motions, the clear advantages of having a centrebow to prevent bow diving and the potentially more extreme nature of slams on flat a wetdeck should not be forgotten. The main message is that constraining the water between the centrebow and demihulls should be minimised as much as possible. This conclusion leads into a recommendation for future work to asses experimentally more hull forms in the bow region. Also due to nonlinearity of the vessel motions with respect to the wave height; it is also quite difficult to extrapolate the results for this condition to higher wave heights; therefore testing in harsher wave conditions is suggested for future works.

6. Numerical modelling of slamming using Smoothed Particle Hydrodynamics (SPH)

The slamming of monohulls has been studied quite extensively and various prediction models currently are in use to predict slam loads. For the more complex shapes such as catamarans with a centrebow however, there is still a large knowledge gap. Experimental studies of different types have been employed to investigate the behaviour of such complex vessel shapes and they offer valuable information. However, there are problems with experiments; they are expensive, there are scaling issues and more importantly these vessels' behaviour is nonlinear with respect to the input wave environment meaning that tests need to be performed for a series of wave heights to ascertain the influence of wave height on vessel behaviour. Therefore, having a reliable numerical model capable to predict the slamming behaviour of such vessels is of interest. Different Computational Fluid Dynamics (CFD) methods are available to approach this fluid-structure interaction phenomenon [83], one of which is Smoothed Particle Hydrodynamics (SPH). SPH has been identified as possible numerical model for slamming simulations with good prospects to provide accurate simulations [8].

There are some previous works modelling monohulls slamming, but to date only simplified theories have been used to predict slam loads on catamarans, for example the work of Whelan et al. [12, 33] who developed method based on conservation of momentum using the added mass method of von Karman [53]. This is mainly due to high level of complexity of the slamming problem for a catamaran with enclosed sections at very low deadrise angles of wetdecks. This current work seeks to develop a more advanced methodology to predict the slam loads. As identified in the research questions, the ability of SPH to simulate the slamming of catamaran hull shapes and accurately predict the slam loads for different geometries is investigated in this chapter. Answering this question would also fit into the AMC, UTAS and INCAT collaboration to further extend the studies of motions and loads of large high speed catamarans to further understand the effect of hull form in vessel's behaviour.

SPH is a numerical mesh-free particle method that approximates the solution of the equations of fluid dynamics, namely the continuity equation, the momentum and energy equation. The SPH technique discretises the material (fluid) into particles, free to move independently, interacting together through physics laws. SPH has some advantages over meshed methods in its capacity for capturing large deformations in free surface flows due to its Lagrangian nature, as well as its faster generation of input data [82, 84, 87]. Originally used for astronomical problems, Monaghan [74-76] was first to introduce SPH to solving free surface flows. However, it is now used for a wide range of problems including shock waves, hydraulic simulations such as dam break, sloshing, and maritime hydrodynamics.

SPH has been successfully used for two-dimensional (2-D) wedge water entry problems where there is relatively good agreement between SPH results and experiments [82, 84, 85, 87, 120]. Oger et al. [82, 95] applied SPH to model wedge water entry with different falling angles successfully capturing the spray root deformation, obtaining good results for the drop speed and pressure profile over surface, especially in the initial entry stages. Viviani and Brizzolara [83, 84] compared SPH with other numerical models in modelling impacting bow sections, resulting in reasonably good agreements for SPH. Veen et al. [85, 86, 121] modelled various wedge sections and frigate bow sections in 2-D, and extended his results to 3-D bow diving of frigate sections using strip theory. Most of the previous works have been modelling monohulls slamming, whereas, this work seeks to further the development and application of SPH for use in modelling two or three-dimensional water entry of wave-piercing catamaran with centrebow.

In this chapter, the SPH model with its basic formulations and implementation techniques are initially discussed. The application of SPH, for solving water entry of free falling objects in 2-D and 3-D is examined. A free falling 25° 2-D wedge section is selected as the benchmark model allowing the effect of various SPH parameters to be investigated, as well as conducting a particle density independency study. These optimal parameters are then used to simulate other wedge geometries extending to enclosed arch sections representing wave-piercing catamaran with centrebow. Detailed discussions of the results are presented for each geometry in 2-D; an exploratory study of the catamaran section in 3-D to capture the effects of water escaping through the tank wall clearance with conclusions drawn about the success and limitations of the SPH technique.

6.1. The SPH model

The formulation of SPH can be explained via two major steps; the integral representation of the field functions and the particle approximation of the represented integral form [73]. Various implementation techniques to discretise and stabilise the solution are used to make this formula functional in simulating various fluid dynamics problems. The open source code Dual-SPHysics (see <http://dual.sphysics.org/>), developed by a group of researchers mainly from the University of Vigo (Spain) and University of Manchester (UK) has been employed here. This code has been validated for various engineering problems [77, 88, 89]. A brief overview of the SPH model is given in this section, while notations are similar to Liu and Liu [73] and SPHysics user-guide [88, 89].

6.1.1. Basic formulations

In the SPH model, each of the field functions, $f(x)$ (e.g. density, mass, energy) can be represented as an integral form of the three-dimensional position vector x , as Equation (6-1),

$$f(x) = \int_{\Omega} f(x') \delta(x - x') dx' \quad (6-1)$$

where $\delta(x - x')$ is the Dirac delta function given by Equation (6-2) and Ω is the volume of the integral that contains x .

$$\delta(x - x') = f(x) = \begin{cases} 1, & x = x' \\ 0, & x \neq x' \end{cases} \quad (6-2)$$

If the Delta function kernel is replaced by $W(x - x', h)$ which W is “smoothing function” or “kernel function”, h will be the smoothing length. Using this kernel function gives an approximation to the function $f(x)$ as Equation (6-3),

$$f(x) \cong \int_{\Omega} f(x') W(x - x', h) dx' \quad (6-3)$$

Equation (6-3) generates the kernel approximation of the function which is applicable to discontinuous domains as well. Kernel functions that are used in SPH are usually even functions and have a Gaussian form with a cut-off radius of kh as seen in Figure 6.1, where k is a constant which defines the effective area of kernel function.

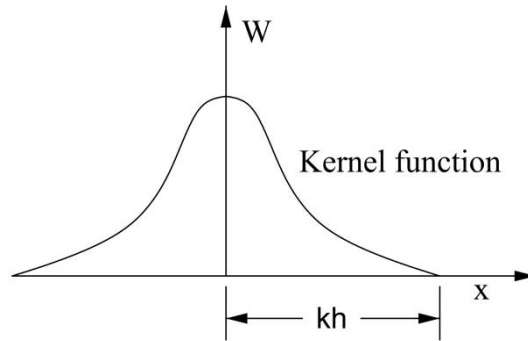


Figure 6.1: Smoothing function W and the support domain in SPH

The kernel function W should have some special properties to satisfy the approximation. First is the normalisation or unity condition as in Equation (6-4),

$$\int_{\Omega} W(x - x', h) dx' = 1 \quad (6-4)$$

The second is the condition that as the smoothing length approaches to zero, the function itself impends to the Delta function as Equation (6-5),

$$\lim_{h \rightarrow 0} W(x - x', h) dx' = \delta(x - x') \quad (6-5)$$

The third condition is the compact condition which states that by moving far enough from the particle, the function should approach zero as shown in Equation (6-6),

$$W(x - x', h) dx' = 0 \quad \text{when } |x - x'| > kh \quad (6-6)$$

The area which the kernel function is not zero is called the support domain for point x . By using the compact condition the integration over the whole domain reduces to the support domain only.

It can be shown that the spatial derivative of the field function $f(x)$ can be approximated by Equation (6-7),

$$\nabla \cdot f(x) \cong - \int_{\Omega} f(x') \nabla W(x - x', h) dx' \quad (6-7)$$

The kernel functions can take many forms, as Gaussian, Quadratic, Cubic spline and Quintic (Wendland) kernel functions and are described below:

a) The Gaussian kernel function as Equation

$$W(r, h) = \alpha_D \exp(-q^2) \quad (6-8)$$

where $r = x - x'$, $q = r/h$ and α_D is $1/(\pi h^2)$ in 2-D and $1/(\pi^{3/2} h^3)$ in 3-D [76]. This kernel has the problems of not having a cut-off domain so it never becomes zero [122].

b) The quadratic kernel function

$$W(r, h) = \alpha_D \left[\frac{3}{16} q^2 - \frac{3}{4} q + \frac{3}{4} \right] \quad 0 \leq q \leq 2 \quad (6-9)$$

where α_D is $2/(\pi h^2)$ in 2-D and $5/(4\pi h^3)$ in 3-D [122, 123].

c) The cubic spline kernel function with a higher order polynomial

$$W(r, h) = \alpha_D \begin{cases} 1 - \frac{3}{4} q^2 - \frac{3}{4} q^3 & 0 \leq q \leq 1 \\ \frac{1}{4} (2 - q)^3 & 1 \leq q \leq 2 \\ 0 & q \geq 2 \end{cases} \quad (6-10)$$

where α_D is $10/(7\pi h^2)$ in 2-D and $1/(\pi h^3)$ in 3-D [124-127].

d) The Quintic or Wendland [128] kernel function with a 4th order polynomial

$$W(r, h) = \alpha_D \left(1 - \frac{q}{2} \right)^4 (2q + 1) \quad 0 \leq q \leq 2 \quad (6-11)$$

where α_D is $7/(4\pi h^2)$ in 2-D and $21/(16\pi h^3)$ in 3-D [129].

Using higher order polynomials for the kernel function will generally increase the accuracy of the SPH simulations; however it would be computationally more expensive [130]. Amongst the above, the Wendland kernel has good accuracy while not being too computationally expensive.

Particle approximation: In SPH, the domain of fluid is represented by particles which have their own mass and support domain. The particle approximation of the field function is achievable by

converting the integration into a discretised summation over all the particles in the support domain. This is illustrated in Figure 6.2.

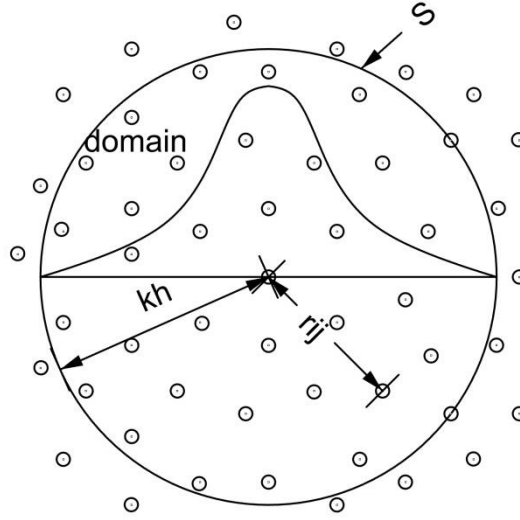


Figure 6.2: particles within support domain using of the smoothing function W for particle i . The support domain S is circular with a radius of kh and $r_{ij} = x_i - x_j$.

As mentioned the mass (m) of particle j ($=1,2,...N$) can be represented by the volume of the particle (ΔV_j) times the density (ρ_j) in which N is the number of particles in the support domain of particle j :

$$m_j = \Delta V_j \rho_j \quad (6-12)$$

By changing the integration to summation as and substituting the infinitesimal volume of the particle ΔV_j by the infinitesimal distance dx' , the field function for particle i can be approximated by Equation (6-13):

$$f(x_i) \cong \sum_{j=1}^N \frac{m_j}{\rho_j} f(x_j) W(x_i - x_j, h) \quad (6-13)$$

The particle approximation of the spatial derivative of the function can be written as Equation (6-14).

$$\nabla f(x) \cong - \sum_{j=1}^N \frac{m_j}{\rho_j} f(x_j) \cdot \nabla W(x - x_j, h) \quad (6-14)$$

Equation (6-14) can be rewritten for the particle i as well and be continued to depict all fluid properties and governing equations. Many techniques have been used to develop this idea and applied over fluids or structures [73].

Continuity equation: Fluid density changes can be calculated in SPH using the continuity density equation of the form of Equation (6-15),

$$\frac{d\rho_i}{dt} = - \sum_j m_j \vec{v}_{ij} \cdot \vec{\nabla}_i W_{ij} \quad (6-15)$$

where $\vec{v}_{ij} = \vec{v}_j - \vec{v}_i$ is the relative particle velocity and $W_{ij} = W(x - x_j)$. The introduction of velocity into density calculations is for fluids with a free surface since just averaging density over the surrounding particles in the free surface would lead to less fluid density [75]. When the simulation starts, the orientation of the particles changes and the surrounding particles are not symmetric any more. Also, close to the boundaries or free surfaces, the kernel is truncated on one side. Therefore, it is necessary in hydraulic problems to correct and renormalise the particle kernels and update them to keep the consistency and normalisation conditions [131, 132].

Using Equation (6-15) may also lead to pressure fluctuations and mass conservation problems which need to be smoothed and reinitialised over each particle, as applied by Colagrossi and Landrini [133]. This is done using quick and simple density filters such as Shepard filter (Zeroth-order filter) [76, 134, 135] usually every 30 time step as seen in Equation (6-16),

$$\rho_i^{\text{new}} = \sum_j \rho_j \tilde{W}_{ij} \frac{m_j}{\rho_j} = \sum_j m_j \tilde{W}_{ij} \quad (6-16)$$

Where the \tilde{W}_{ij} is the corrected kernel function using the same order correction as in Equation (6-17),

$$\tilde{W}_{ij} = \frac{W_{ij}}{\sum_j W_{ij} \frac{m_j}{\rho_j}} \quad (6-17)$$

Higher order corrections such as Mean Least Square (MLS) filter are also available [131, 134] but they are not discussed here as some studies such as the works by Gomez-Gesteria et.al [129] showed no significant advantages of them in slamming problems such as in dam breaking problems.

Momentum equation and viscosity: The momentum conservation equation in a continuum field is given in Equation (6-18),

$$\frac{D\vec{v}}{Dt} = -\frac{1}{\rho}\vec{\nabla}P + \vec{g} + \vec{\Theta} \quad (6-18)$$

where v is the velocity, P is pressure, g is the gravity acceleration and Θ refers to diffusion terms. The pressure gradient $\vec{\nabla}P$ can be written as Equation (6-19),

$$\frac{\vec{\nabla}P}{\rho} = \vec{\nabla}\left(\frac{P}{\rho}\right) + \frac{P}{\rho^2}\vec{\nabla}\rho \quad (6-19)$$

The acceleration equation using this method is symmetric and so the linear and angular momentum is conserved [135]. Artificial viscosity proposed by Monaghan and Gingold [76, 136] is a common way to approach momentum equation diffusive terms in free surface flows because of its ease of use and can be found in SPH literature as Equation (6-20),

$$\frac{d\vec{v}_i}{dt} = -\sum_j m_j \left(\frac{P_j}{\rho_j^2} + \frac{P_i}{\rho_i^2} + \Pi_{ij} \right) \cdot \vec{\nabla}_i W_{ij} + \vec{g} \quad (6-20)$$

where Π_{ij} is the artificial viscosity term and defined as Equation (6-21),

$$\Pi_{ij} = \begin{cases} \frac{-\alpha \bar{c}_{ij} \mu_{ij}}{\bar{\rho}_{ij}} & \vec{v}_{ij} \vec{r}_{ij} < 0 \\ 0 & \vec{v}_{ij} \vec{r}_{ij} \geq 0 \end{cases} \quad (6-21)$$

with $\mu_{ij} = \frac{h \vec{v}_{ij} \vec{r}_{ij}}{\vec{r}_{ij}^2 + \eta^2}$, $\vec{v}_{ij} = \vec{v}_i - \vec{v}_j$ and $\bar{c}_{ij} = \frac{c_i + c_j}{2}$, in which C is the speed of sound at each particle. $\eta^2 = 0.01h^2$ and α is a free parameter that can be selected according to each problem. There is no real relationship between this artificial viscosity and real viscosities, but it is designed to stabilise the simulations and allow shock waves to be simulated. Although, Monaghan [135] has related the fluid shear and bulk viscosities to ρ , c , α and h using certain simplifications. When two particles approach each other, artificial viscosity creates a repulsive force and when they move away from each other, it generates attraction.

The slamming problem is a fast transient phenomenon and there is insufficient time for large diffusion between the domain particles. Therefore, more complex diffusive terms such as laminar viscosity or sub-particle scale turbulence modelling described by Gotoh et al. [137] and Lo and Shao [138] are not discussed here. Shao [120] in his simulations of wedge water entry concluded that the influence of turbulent modelling is mainly upon the detailed flow near the splash region and the macroflow and fluid forces are not affected. However, the traditional XSPH smoothing velocity [135, 139] technique is used to reduce particle disorder and bring the particle velocities close to its average neighbour velocities. It is given in Equation (6-22),

$$\frac{d\vec{r}_i}{dt} = \vec{v}_i + \varepsilon \sum_j \frac{m_j}{\bar{\rho}_{ij}} \vec{v}_{ji} W_{ij} \quad (6-22)$$

where ε is a free parameter usually taken as 0.5 and $\bar{\rho}_{ij} = \frac{\rho_i + \rho_j}{2}$.

Equation of state and compressibility: Tait's equation [73, 140] is the equation of state for determining the fluid pressure where atmospheric pressure is negligible. This equation assumes the fluid as weakly compressible (as in real) and controls the density fluctuations [76, 136]. It has the form of Equation (6-23),

$$P = B \left[\left(\frac{\rho}{\rho_0} \right)^\gamma - 1 \right] \quad (6-23)$$

where $\gamma = 7$ for water and $B = \frac{c_0^2 \rho_0}{\gamma}$ in which ρ_0 is the reference density and $c_0 = \sqrt{\left(\frac{\partial P}{\partial \rho} \right) \bigg|_{\rho_0}}$ is the speed of the sound at the reference density. The density fluctuation is related to the maximum bulk velocity (v) of the fluid and speed of sound c_0 as Equation (6-24):

$$\frac{|\delta\rho|}{\rho} \sim \frac{v^2}{c_0^2} \quad (6-24)$$

Therefore, to keep the density fluctuations less than 1% in water, c_0 must be larger than 10 times the bulk velocity; this requires an estimate of maximum velocity in the fluid which is not very difficult [75, 76, 135]. To obtain the correct initial pressures at various fluid depths, at the start of the simulation an adjusted formula is used as $c_0^2 = C_{coef}^2 g h_{swl}$ where the h_{swl} is the still water level and C_{coef} is a coefficient which is recommended to be $10 \leq C_{coef} \leq 40$, which normally satisfies the minimum speed of sound requirement for hydraulic problems [88, 89, 141]. Table 6.1 shows various C_{coef} and their equivalent in c_0 if the water with $h_{swl} = 1$ m is considered.

Table 6.1: The Reference Speed of Sound (C_0) Calculated for Coefficients of the Speed of Sound (C_{coef}) for 1 m of Still Water Level

C_{coef}	C_0 m/s
10	31.32
15	46.98
20	62.64
30	93.96
40	125.28

Thermal energy equation: The thermal energy equation for SPH is present by Monaghan [75, 135] as in Equation (6-25),

$$\frac{d\vec{u}_i}{dt} = \frac{1}{2} \sum_j m_j \left(\frac{P_j}{\rho_j^2} + \frac{P_i}{\rho_i^2} + \Pi_{ij} \right) \vec{v}_{ij} \vec{v}_i W_{ij} \quad (6-25)$$

where u is the internal energy. The use of density filters also help conserve energy during simulations [129].

6.1.2. Time stepping

The physical quantities (velocity, density and position) are updated at each time step due to particle interactions. The new values of field parameters are calculated by integrating over the time using momentum, density, position and energy equations given in Equation to Equation (6-29);

$$\frac{d\vec{v}_i}{dt} = \vec{F}_i \quad (6-26)$$

$$\frac{d\rho_i}{dt} = \vec{D}_i \quad (6-27)$$

$$\frac{d\vec{r}_i}{dt} = \vec{V}_i \quad (6-28)$$

$$\frac{d\vec{e}_i}{dt} = \vec{E}_i \quad (6-29)$$

where \vec{V}_i is the velocity, \vec{D}_i is the velocity change, \vec{F}_i is the force and \vec{E}_i is the energy of particle i . Various schemes have been used in SPH simulations which are at least second order accurate, since the particles are moving in space [129]. These methods include the leap frog scheme, Runge-Kutta scheme, predictor corrector [75], Verlet scheme [77, 123, 126, 129, 142, 143], symplectic [135, 142] or Beeman scheme [130].

The symplectic scheme conserves momentum and energy and is reversible in time and is very attractive for SPH simulations especially when viscous diffusion is absent, such as drop tests [88, 135]. First, the values of density and acceleration are calculated at the middle of the time step; the pressures are then calculated from the equation of state. Then the final position and velocity of the particles in the final are calculated with the densities calculated using the updated values of position and velocity. Symplectic scheme have been adopted in this work; further details of the scheme can be found in Monaghan et al. [135] and Leimkuhler et al. [142].

Variable time step: The time step is controlled by Courant-Fredrich-Lewy (CFL) condition [144], the viscous diffusion terms and forcing terms. Therefore, a variable time step is used in SPH [145, 146] and is calculated based Equations (6-30), (6-31) and (6-32)

$$\Delta t = 0.3 \cdot \min(\Delta t_f, \Delta t_{cv}) \quad (6-30)$$

$$\Delta t_f = \min \left(\sqrt{\frac{h}{|f_i|}} \right) \quad (6-31)$$

$$\Delta t_f = \min \frac{h}{c_s + \max \left| \frac{h \vec{v}_{ij} \cdot \vec{r}_{ij}}{r_{ij}^2} \right|} \quad (6-32)$$

where $|f_a|$ is the force per unit mass, c_s is the speed of sound at particle i and Δt_f is the combination of Courant and viscous time step controls. This time stepping ensures that the information will not be sent more than one particle distance every time step.

6.1.3. Boundary conditions

There are four main types of solid boundary conditions considered in SPH; the solid boundary condition is to simulate the interaction between the fluid and solid boundaries either fixed like tank walls or moving with a known path like wave makers or free floating objects. Different methods are used to simulate the solid boundaries:

- 1- **Repulsive forces:** This boundary type locates ghost particles in the solid boundary which insert forces to the fluid particles as they approach the boundary by a known equation. These forces then are added to the momentum equation of the fluid particle to affect its motions. These repulsive forces are best described by Monaghan et al [75, 135]. This boundary type

sometimes causes large variation in the forces of a particle moving parallel to the solid boundary [135, 147].

- 2- **Ghost particles:** This is an additional layer of particles to the solid boundary particles which mirror the velocities of the fluid close to the boundary. These two type ghost particles for the solid boundaries are suggested by Liu et al. [73, 148] and have been used in many free surface flow problems such as works of Calogrossi et al. [133]. There are however, difficulties in placing the ghost particles in the concave corners where the boundary particles mount on each other.

A new version of these two type boundary particles are developed by Marrone et al. [149-151] in which the outer side ghost particles remain stationary. This resolves the issue of unstable boundaries in the previous ghost type where the boundary particles are instantaneous mirrors of fluid particles.

- 3- **The dynamic boundary condition:** In this method, the boundaries are simulated as essentially fluid particles but are fixed or bound to a known movement. The momentum equation, continuity equation and equation of state are applied, but the motion Equation (6-22) does not apply. This boundary type is best described by Crespo et al [152] and Dalrymple and Knio [123]. As illustrated in Figure 6.3, when a fluid particle approaches the solid boundary, the density increases based on the continuity equation and the pressure according to the equation of state. The particles can be placed in a staggered or straight-line sequence; the staggered arrangement is preferred for preventing the fluid particles from penetrating the boundary; however, the straight-line sequence can better represent smooth boundary surfaces. This boundary type is very simple to generate, robust and effective and has been shown to give good results [77, 88, 89, 125, 126, 129].

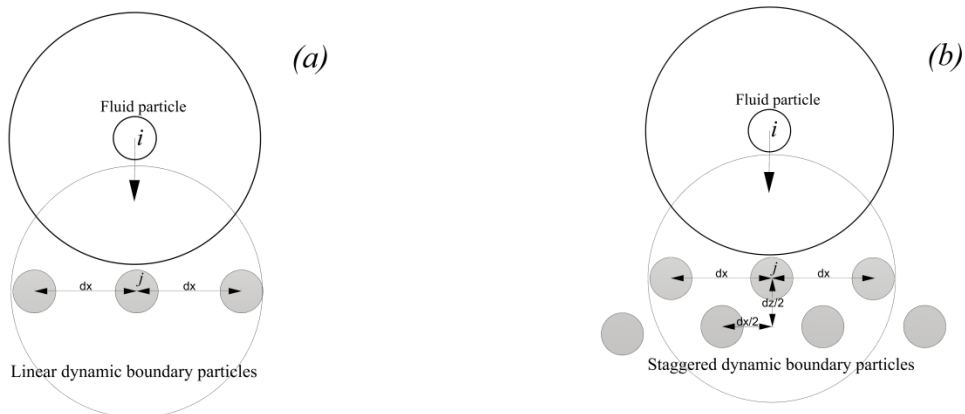


Figure 6.3: Dynamic boundary condition with (a) linear boundary particle arrangement and (b) staggered particle arrangement. The larger circles are support domains for particle i and j .

- 4- **Periodic open boundaries:** These boundary types do not use real particles on the boundary, instead the particles near the open lateral boundary interact with the particles near the lateral

boundary on the other side of the domain. The truncated support domain of fluid particles near the open boundary will be continued to the other side of the boundary particles. Figure 6.4 illustrates this boundary type where the top boundary particle supports are virtually filled up with bottom boundary particles [141]. As can be seen, to apply this boundary condition, two symmetric boundary walls are necessary.

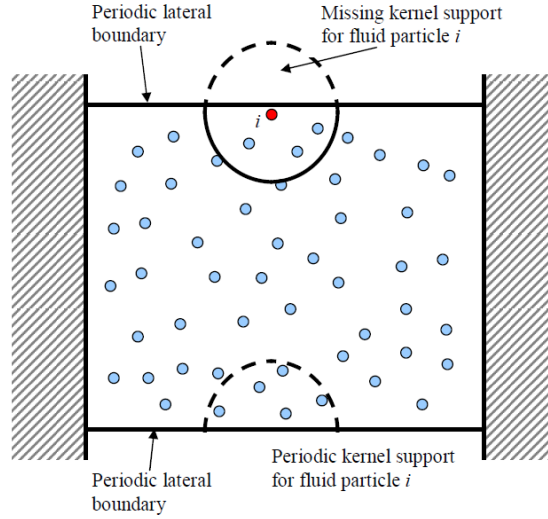


Figure 6.4: Open periodic boundary condition in SPH where the support domain of particle i is extended through the other side of the open periodic boundary (from SPHysics user guide [141])

6.1.4. Modelling of floating bodies

Floating bodies are modelled as a set of solid boundary particles but with rigid body motion dynamics applied to them. They exert a repulsive force as approaching other fluid particles. For example, in the case of a free falling wedge section into water, the wedge is modelled with fixed boundary particles which move with the wedge as it drops. Methods such as repulsive force boundary particles or dynamic boundary particles have been used widely in modelling floating objects [88, 89, 126, 146]. The translational and rotational degrees of freedom for the equation of the motion of a floating object is defined by Equations (6-33) and (6-34),

$$M \frac{dV}{dt} = \sum_{k \in BP} m_k f_k \quad (6-33)$$

$$I \frac{d\omega}{dt} = \sum_{k \in BP} m_k (r_k - R_0) \times f_k \quad (6-34)$$

where M is the mass of the object, m_k is the mass of the boundary particle, f_k is the total forces exerted to the boundary particle from all the surrounding fluid particles, V is the object velocity, ω is the rotational velocity, I is the floating object moment of inertia, r_k is the distance of the particle to the object centre of gravity, R_0 is the location of object centre of gravity and BP stands for boundary particles. The values of V and ω are predicted after integrating these two equations. Each boundary particle then will have a velocity (u_k) as in Equation (6-35),

$$\mathbf{u}_k = \mathbf{V} + \boldsymbol{\omega} \times (\mathbf{r}_k - \mathbf{R}_0) \quad (6-35)$$

The rigid floating boundary particles then will move by integrating this equation in time. This method conserves the linear and angular momentum [135].

6.1.5. Dual-SPHysics code and efficiency

As SPH is being used more extensively in engineering and science problems [129], a number of codes are reaching maturity in their development. SPHysics, an SPH code written in FORTRAN has been validated for various hydraulic problems such as dam breakings and wave breakings [123, 124, 126]. As with many new codes, SPHysics has a limited domain size and resolution caused by long computational times. Graphics processing Units (GPUs) have recently developed much faster than normal Central Processing Units (CPU) and can accelerate SPH simulations up to 66 times compared to single-core CPUs [77, 153]. Dual-SPHysics is the GPU version of SPHysics which can work both on CPU and GPU. This code is also open-source but written in C/C++ language and using Compute Unified Device Architecture (CUDA) framework. Using GPU computational abilities to parallelise and accelerate SPH simulations has shown to be effective (see Herada et al. [80] and Gomez-Gesteria et al. [77, 154]) . In the current work, a graphic card of GeForce 680 model with 2 gigabytes memory was employed to allow for a larger domain, increased number of particles to be modelled with reduced computation time.

The fluid domain in SPH is normally divided into square cells with size of $2h$ to reduce the number of interaction calculations in the domain in each time step [73]. The particles of each cell only interact with neighbouring cells and not the whole domain, traditionally reducing the number of interactions from N^2 to $N \log N$ if N is total number of particles [73]. Reordering the particle for faster access to memory, using symmetric force calculation between particles and the use of the best approach of neighbour list are the improvements of Dual-SPHysics [154, 155]. Figure 6.5 from Dominguez et al. [154, 155] shows the difference between the CPU and GPU version of the code in terms of steps in the calculations. The data are initialised in CPU, transferred to GPU for searching, particle interaction calculations and system updates, then occasionally sent back to the CPU for saving data. The whole process was performed previously on CPUs.

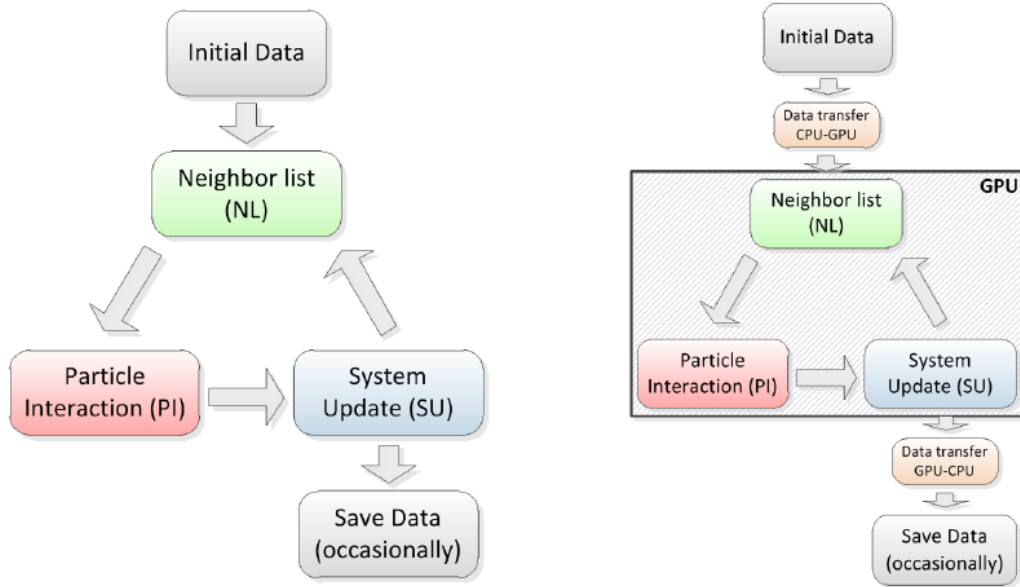


Figure 6.5: computational diagram for CPU (left) and GPU (right) implementation of Dual-SPHysics code [154, 155]

Dual-SPHysics is the open-source state of the art code designed to solve real-life engineering problems. The author had direct contact with the code developers, for advice and debugging, and to provide improvements to the code for solving more complicated floating object problems.

6.2. Implementation of SPH model for drop tests

6.2.1. Drop test experiments

Comprehensive drop test experiments were conducted by Whelan et al. [12, 33] at the University of Tasmania to investigate slamming of monohull and multihull vessel bow cross sections. The drop test facility developed by Whelan [33] is shown in Figure 6.6. It consists of a rising and falling system to allow for various sections to be dropped from various heights into a tank of water. The tank is made from glass to allow the water entry root to be visually captured with a high speed camera. The water depth was 1 m and the length of the tank was 2.4 m designed to avoid immediate reflections from the tank walls. The width of the tank was 0.3 m, close to the drop section width to minimise 3-D effects and keep the 2-D features of the drop experiments.

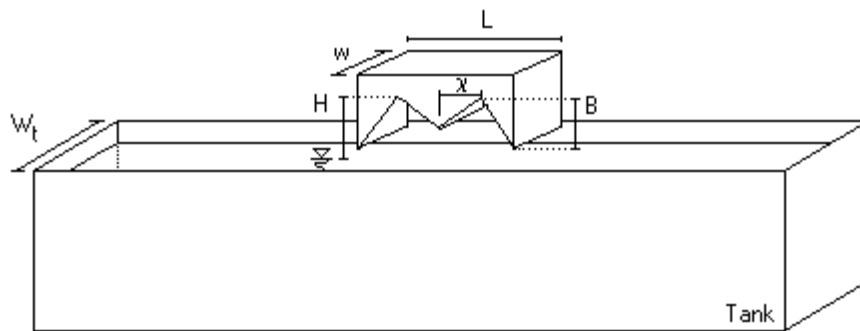


Figure 6.6: Schematic outlines of the drop experiments by Whelan [33] where H is the drop height

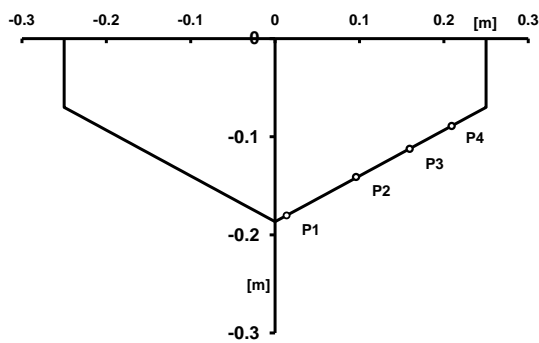
The drop heights, drop velocities and model masses were calculated from non-dimensional numbers replicating full-scale slamming data [33]. Normalised drop height (NDH) and mass number were defined as in Equation (6-36) and Equation (6-37),

$$\text{NDH} = \sqrt{\frac{2H}{L}} \quad (6-36)$$

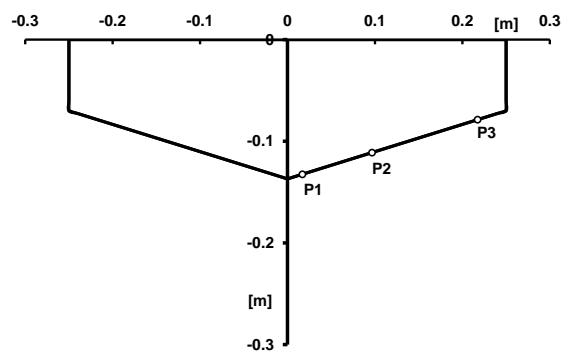
$$\text{mass number} = \frac{m_m}{\rho w L^2} \quad (6-37)$$

where H is the drop height measured from water surface to the top knuckle of the drop sections, L is the section length, w is the model width, ρ is the water density and m_m is the drop section mass (see Figure 6.6). Based on Whelan [33] work, full-scale trial results on a 96 m INCAT wave-piercing catamaran, the normalised drop height (NDH) range between 0.75 and 1.2 and mass number was mainly between 0.05 and 0.8. Two mass numbers of 0.29 and 0.58 were picked for model drop tests to effectively cover the full-scale mass number range for all the drop sections. Four NDH were tested for each section, which differed between models to account for the similarity in drop speed (due to top knuckle height difference).

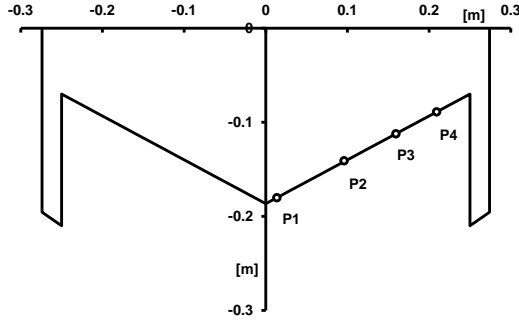
Four of the sections tested by Whelan [33] to evaluate slam kinematics and forces on various bow sections are shown in Figure 6.7. These four geometries were chosen for the study of the numerical model. The geometries were: a 25° wedge (Figure 6.7(a)), a 15° wedge (Figure 6.7(b)); a 25° wedge with vertical side plates (Figure 6.7(c)); and a wave-piercing INCAT catamaran with centrebow (called Incat1, Figure 6.7(d)). Various measurements such as drop velocity, drop acceleration and wall pressures, along with the video recording were performed during the drop tests. Pressure transducers (piezoresistive ENDEVCO 8510B-500 models with maximum of 447 kPa, face diameter of 3.8 mm and linearity of 0.25% full-scale output) using 7042 Hz sampling rate, were installed on the model symmetric plane, named P1 to P4.



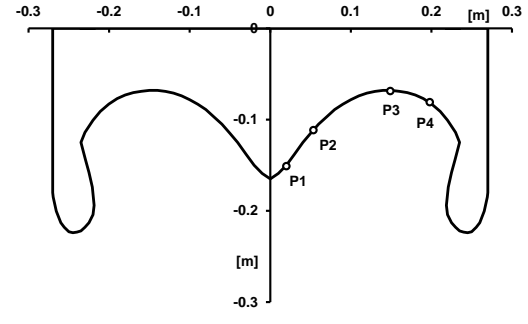
(a) The 25 degree wedge



(b) The 15 degree wedge



(c) The 25 degree wedge with side plates



(d) Incat1, INCAT wave-piercing catamaran with centrebow

Figure 6.7: Four of the drop geometries tested by Whelan [33], used for comparison in this work

6.2.2. SPH model configuration, boundaries and domain setup

To simulate the wedge water entry problem in 2-D, the 25° 2-D wedge section was chosen as the benchmark model allowing the effect of various SPH parameters to be investigated. Initially, a tank 2.4 m width and 1 m depth was created. Figure 6.8 shows the pressure distribution of the initial domain particle setup. The tank bottom boundaries were simulated by dynamic boundary particles (Dalrymple and Knio [156], Crespo [152]) and as mentioned earlier, they are essentially fluid particles that are fixed in space. The wedge was also generated as a line of dynamic boundary particles and was free to drop and float. The side boundaries were created using periodic open boundary condition which uses the particles from the other side of the domain to account for the truncated effective domain of the particles close to the boundary.

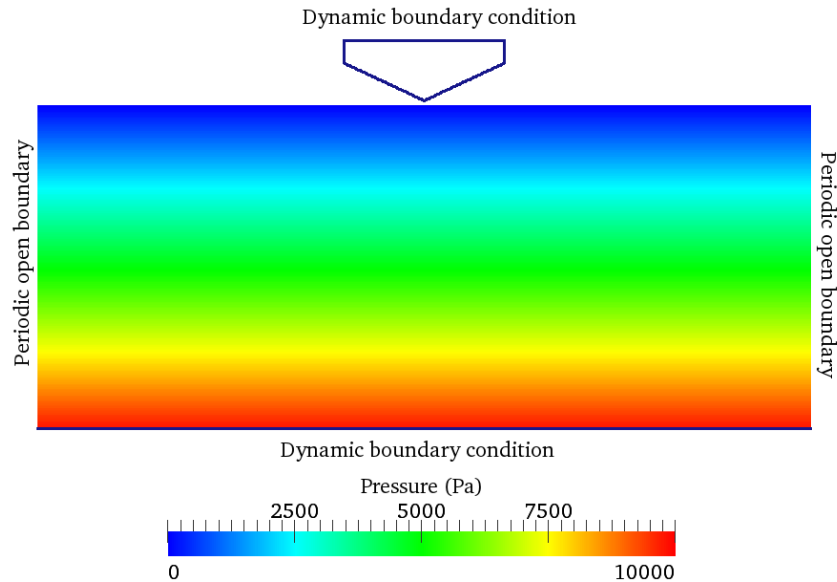


Figure 6.8: Initial 2-D particle arrangement, boundary conditions and pressure field of the tank and drop section in SPH

Figure 6.9 shows a close-up of the particle arrangement in the bottom right corner of the domain using two methods. The straight-line particle arrangement (Figure 6.9(a)) and the staggered arrangement approach (Figure 6.9(b)). For this problem, the linear arrangement was employed to help create a

smoother surface for the drop section (with less friction), although both arrangements showed similar trends in preventing particles from penetrating the boundary walls. The use of dynamic boundary particles all around the tank creates undesired pressure waves travelling and reflecting inside the domain, adversely affecting drop accelerations. This effect can be mitigated using periodic open boundary condition on the tank side walls, but the bottom solid boundary effects still remain.

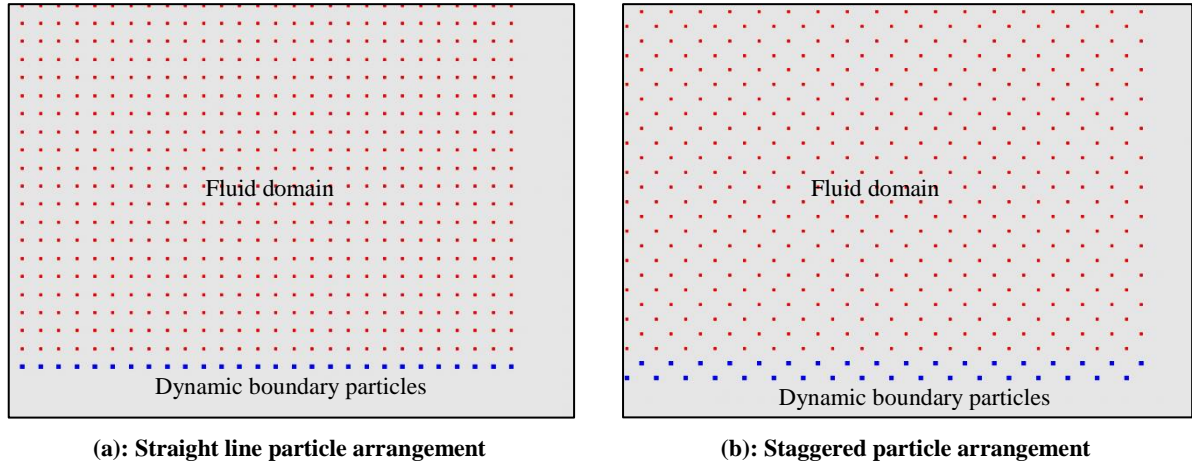


Figure 6.9: Particle arrangement on the bottom right corner of the tank. The blue (larger) particles are the boundary particles and the red (smaller) ones are the fluid domain particles.

The weight per length for the 25° wedge was extracted from the experiments as 72.5 kg/m with mass number of 0.29. In the first few simulations, the drop height was chosen so that the wedge velocity when it touches the water was the same as in the experiments. In later simulations, the drop section was modelled close to the surface and the drop speed of the wedge when it first touches the water was used as the initial condition; this helped to reduce computational time. In the experiments, the drop acceleration before touching the surface was approximately 9.2 m/s² which is less than 9.8 m/s² gravity acceleration possibly due to guiding pile friction or air resistance. This caused difficulty in adjusting the drop height in the simulations to achieve the initial section water entry velocity.

6.2.3. Speed of sound

The combination of Courant-Friedrichs-Lewy (CFL) stability criteria and speed of sound determines the maximum time step used for computations [88, 89, 144]. The CFL number is $\frac{u\Delta t}{\Delta x}$ where u is the speed of sound (c_0) for a compressible fluid, Δx is the distance between particles (DP) and Δt is the maximum time step. The CFL condition ensures that the information will not be sent more than one particle spacing at each time step.

The speed of sound mostly determines the computational time of the simulations in one particle spacing but also affects the compressibility of the fluid. A higher speed of sound results in smaller time steps, hence increasing the computational time required to complete the simulation. Thus, a study to determine the least speed of sound where it does not make the fluid too compressible (more than 1% compressibility strays from the liquids physical reality) was required. For this, it was necessary to

examine the maximum fluid velocity in the drop experiments. Figure 6.10 shows the photo of the drop experiment with an initial drop velocity of 1.22 m/s (NDH=0.89), 60 milliseconds (ms) after touching the water. As seen, the tip of the jet flow has travelled around 0.32 m from the initial state (assuming the jet tip particles were the ones under the centre knuckle at start) in 60 ms; so the maximum fluid velocity can be approximated as $v = \frac{0.32m}{0.06s} = 5.33 \text{ m/s}$. Taking into account the compressibility criteria, the speed of sound must be at least 10 times greater than this velocity, thus the minimum c_0 should be more than 53.3 m/s which corresponds to $C_{coef} \geq 17.02$ for water depth (h_{swl}) of 1 m. In the simulations the C_{coef} was chosen to be 20 corresponding to 62 m/s.

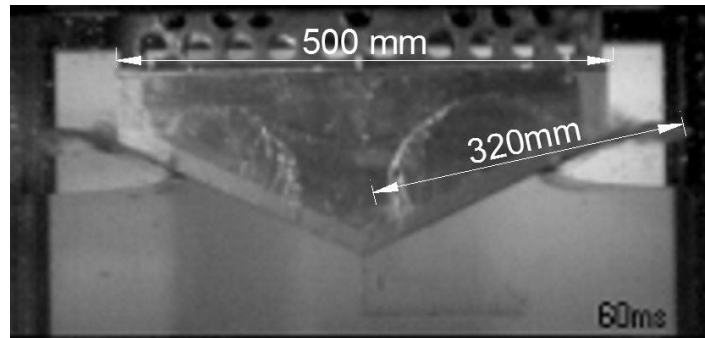


Figure 6.10: The approximate distance the jet flow under the 25 degree wedge has travelled in 60 milliseconds

6.2.4. Particle density independency study

The simulations were conducted using five different particle densities to study the effect of initial particle spacing (DP) and the trade-off between the accuracy and computational time. The acceleration results were used for comparison against the experiments since it is more sensitive to the dynamic variations compared to drop velocity and drop distance. Figure 6.11 shows the acceleration results for the 25° wedge with mass number 0.29 and dropping by inlet velocity of 1.22 m/s (for NDH=0.85) against different initial particle spacing. Some of the parameters used to perform these simulations are given in Table 6.2. The results are shown as a time series to enable comparison of both the trends and magnitude together; since comparing only the peak values without looking at the trends could be misleading as there are fluctuations in accelerations as time increases.

Table 6.2: The Simulation Parameters for Conducting Particle Density Independency Study

Features	Values
Geometry	25° wedge
Mass number	0.29
Normalised drop height	0.85, initial velocity=1.22 m/s
Time stepping algorithm	symplectic, variable time step
Speed of sound coefficient (C_{coef})	20
Speed of sound value (v_0)	62 m/s
Artificial viscosity coefficient (α)	0.01
Distance between particles (DP)	0.01 m, 0.005 m, 0.0025 m and 0.00125 m
Smoothing length	$h = 1.1 \sqrt{DP_x^2 + DP_z^2}$
Kernel function	Wendland (Quintic)
CFL number	0.3
ϵ in XSPH formulation	0.5

As seen in Figure 6.11 with $DP=0.01$ m, the drop acceleration shows significant oscillations in time. The peak value is also around 80% larger than the experimental acceleration peak. These oscillations are mainly caused by the pressure waves travelling through the tank which were not efficiently damped or resolved in space. Shorter period oscillations are seen in the results, caused by the roughness of the contact surface between the wedge and water due to large particle spacing. With $DP=0.005$ m the fluctuations are significantly reduced compared to $DP=0.01$ m. The results improved for $DP=0.0025$ m where the accelerations generally follow the experimental results. Figure 6.11 also shows the SPH drop acceleration results with $DP=0.00125$ m with 1,536,800 fluid particles in total in the domain. As seen the oscillations are well removed, the peak value is close to the experiments and the dynamics follows the physical event. Simulation with finer particles presented difficulties with regard to time and hardware memory.

It can be concluded from the simulations that the results improve as the space resolution increases, hence a $DP=0.00125$ m is taken as the base for further 2-D simulations as the accuracy is sufficient and it is not too computationally expensive.

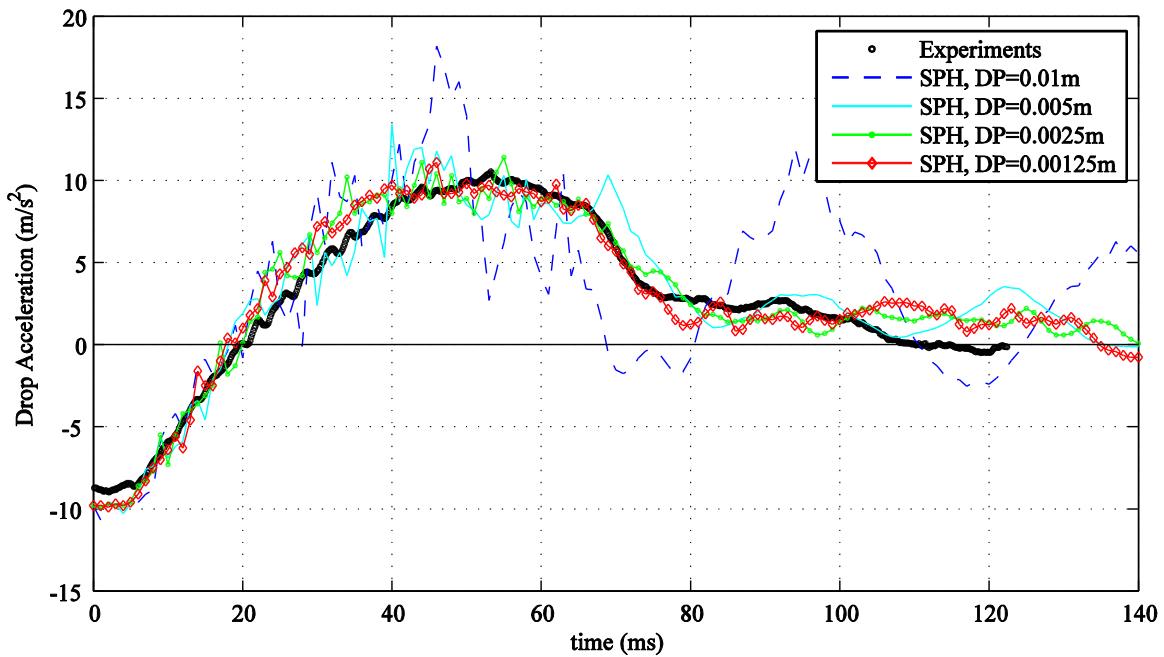


Figure 6.11: Comparison of drop acceleration for the 25 degree wedge with different particle spacing with mass number=0.29 and normalised drop height (NDH)=0.85

6.2.5. Damping in the fluid: spatial filter and artificial viscosity

Due to the Lagrangian nature of SPH, the fluid particles are free to move in any direction; however this advantage in SPH can sometimes become a source of instability. Application of XSPH formula (Equation (6-22)), artificial viscosity and spatial density filtering have been employed to apply enough damping in the system preventing adverse effects. In generating the results in Figure 6.11, the XSPH coefficient (ϵ) was taken as 0.5 and the artificial viscosity coefficient (α) used was 0.01.

Previously people have used $0.001 \leq \alpha \leq 0.1$ with $\alpha=0.01$ being more common [74-77, 88, 124-126, 129, 135, 152].

Because of the fast and transient nature of this problem, the viscous and turbulence effects around the drop section are minimal; increasing α unnecessarily increases the damping in the system which implies high decelerations to the drop section. Taking α too small is also not desired, since it leads to high pressure oscillations in the domain. Therefore, it was decided to use $\alpha=0.01$ which is sufficiently small and does not introduce unphysical behaviours in the fluid. However, to show the effects of applying various artificial viscosity values, a number of simulations were performed. Figure 6.12 shows a comparison of drop accelerations from the simulations (DP=0.00125 m) with various α values, and the experimental results. As seen, $\alpha=1$ caused high decelerations early which affected the drop velocity and immersion. Whereas the drop dynamics resulted from using $\alpha=0.1$, $\alpha=0.01$ and $\alpha=0.001$ are very close. Figure 6.13 shows a comparison of drop velocities for various α values, again showing that $\alpha=1$ deviates from the experiments, as a result of excessive damping on the system.

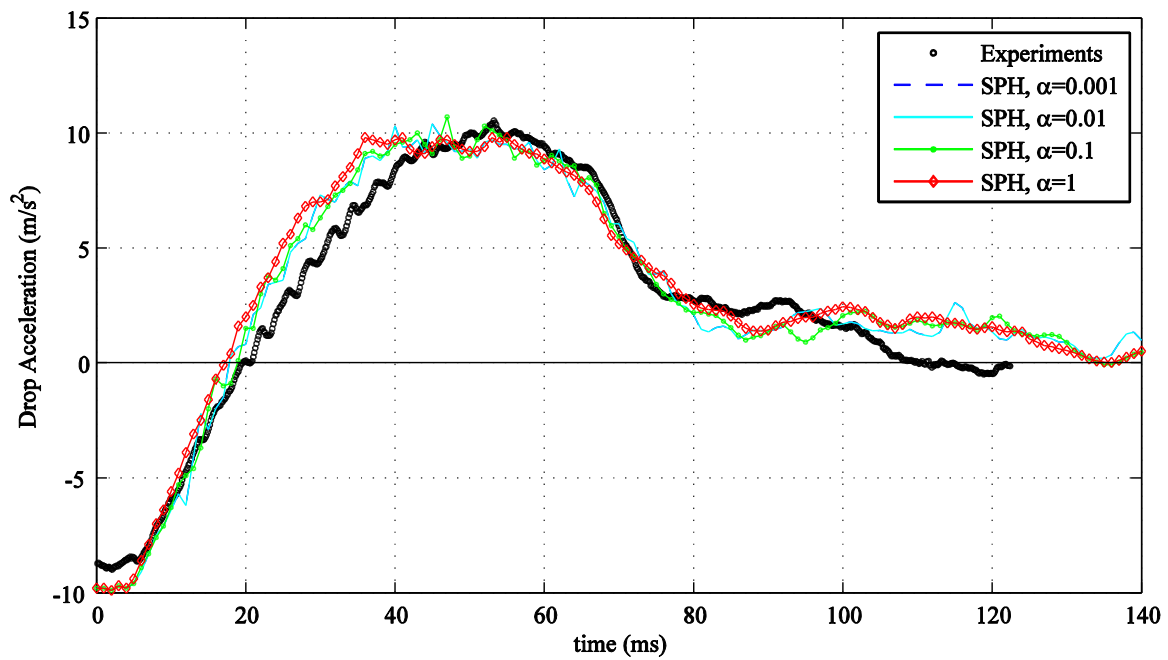


Figure 6.12: Comparison of drop acceleration for the 25 degree wedge with different artificial viscosity values with mass number=0.29 and normalised drop height (NDH)=0.85

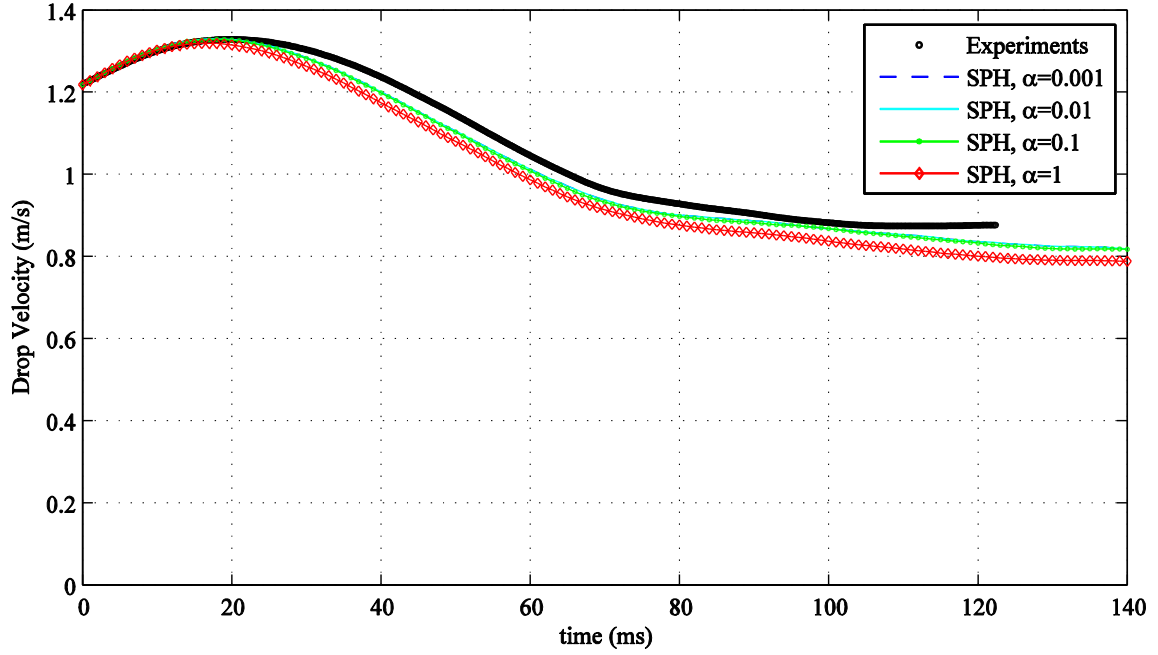


Figure 6.13: Comparison of drop acceleration for the 25 degree wedge with different artificial viscosity values with mass number=0.29 and normalised drop height (NDH)=0.85

The density filter used was a Shepard filter working every 5 time steps to damp the undesired pressure waves travelling in the tank. In some previous works, researchers have applied this filter every 30 time steps [75, 77, 123, 129, 135]. Gomez-Gesteria et al. [129] in modelling a dam breaking problem reported that changing the frequency of the Shepard filter application from 10 to 100 steps did not make any visible changes in the simulations. However, in the present work, the existence of pressure waves and their interactions with the drop section dynamics led to the application of the Shepard filter in smaller number of time steps in order to damp their effects.

The combination of damping from different sources was also tried with various particle spacing to ensure that these results are particle density independent. Figure 6.14 shows a comparison of the acceleration with the filter applied every 30 time steps and every 5 time steps against experimental results, with $DP=0.005$ m and $\alpha=0.01$. As seen, there exist much more oscillations when the Shepard filter is applied every 30 time steps compared to every 5 time step. Another example is shown in Figure 6.15 where with $DP=0.00125$ m and Shepard steps=30, the results of applying $\alpha=0.01$ and $\alpha=0.001$ are compared. As seen, having insufficient artificial viscosity may lead into instabilities which the pressure waves inside the fluid domain can build up and large acceleration oscillations occur. In such cases it is necessary to apply more frequent spatial filters.

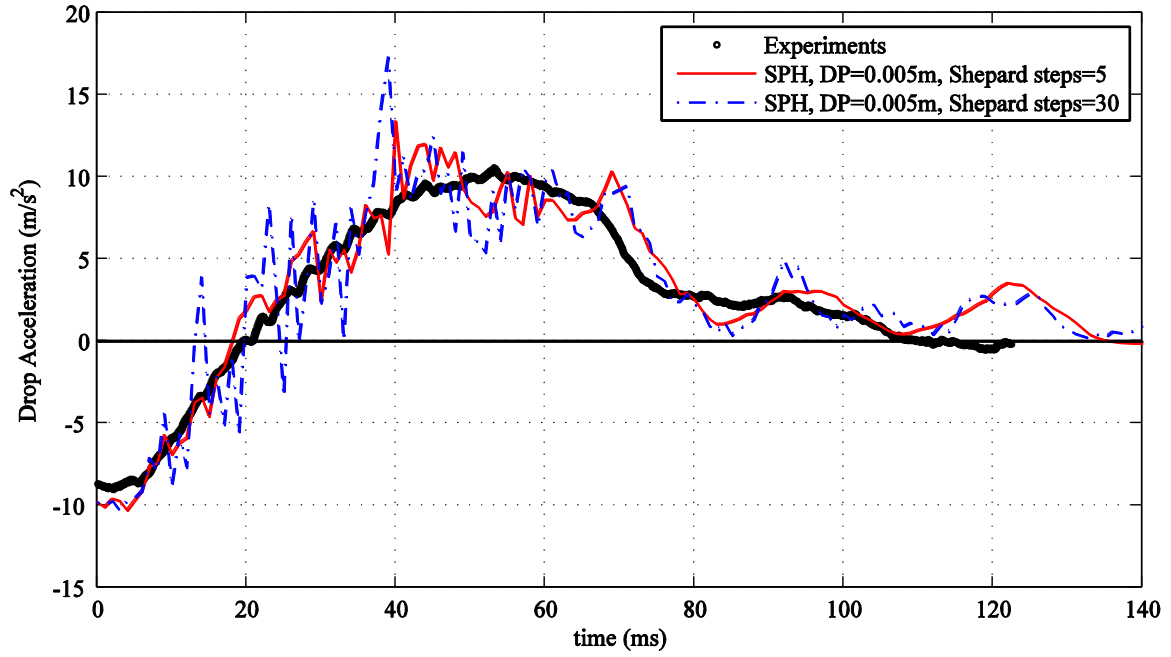


Figure 6.14: Drop acceleration of 25° wedge in SPH with DP=0.005 m with Shepard filter applied every (a) 5 and (b) 30 time steps compared to experiments (mass number=0.29 and normalised drop height (NDH)=0.85)

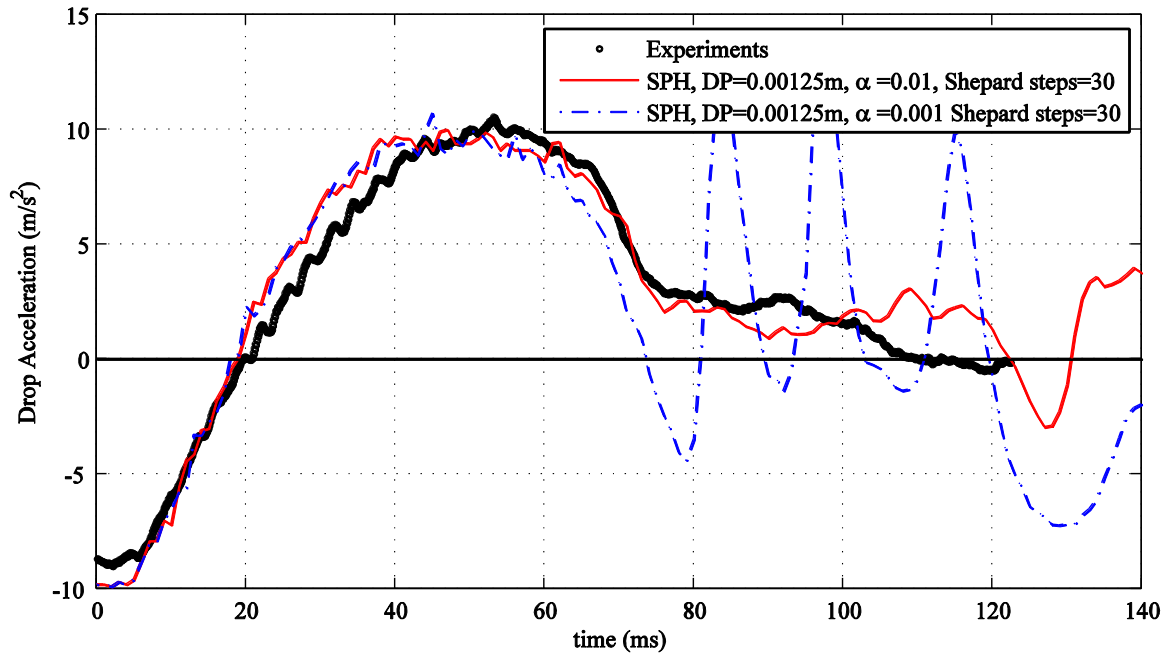


Figure 6.15: Drop acceleration of 25° wedge in SPH with DP=0.00125 m with Shepard filter applied every 30 time steps with artificial viscosity coefficient (α) of 0.01 and 0.001 compared to experiments (mass number=0.29 and normalised drop height (NDH)=0.85)

6.2.6. Visualisation of results

The simulation results were post processed using the tools of the Dual-SPHysics package which save targeted particle information as binary 'vtk' format. Open source ParaView software was then used for the visualisation. Figure 6.16 shows the pressure contour plots from the simulations compared with the experiments using mass number=0.29 and NDH=0.85. In this simulation, the initial velocity was 1.22 m/s and DP=0.00125 m and the other parameters were set according to Table 6.2. As seen, the water upwash is captured and the free surface deformation is close to the experiments. The high pressure regions are shown to be close to the spray root. Figure 6.17 shows a velocity contour plot of the particles 60 ms after the initial entry, in which high velocity regions are shown to be again under the spray root and.

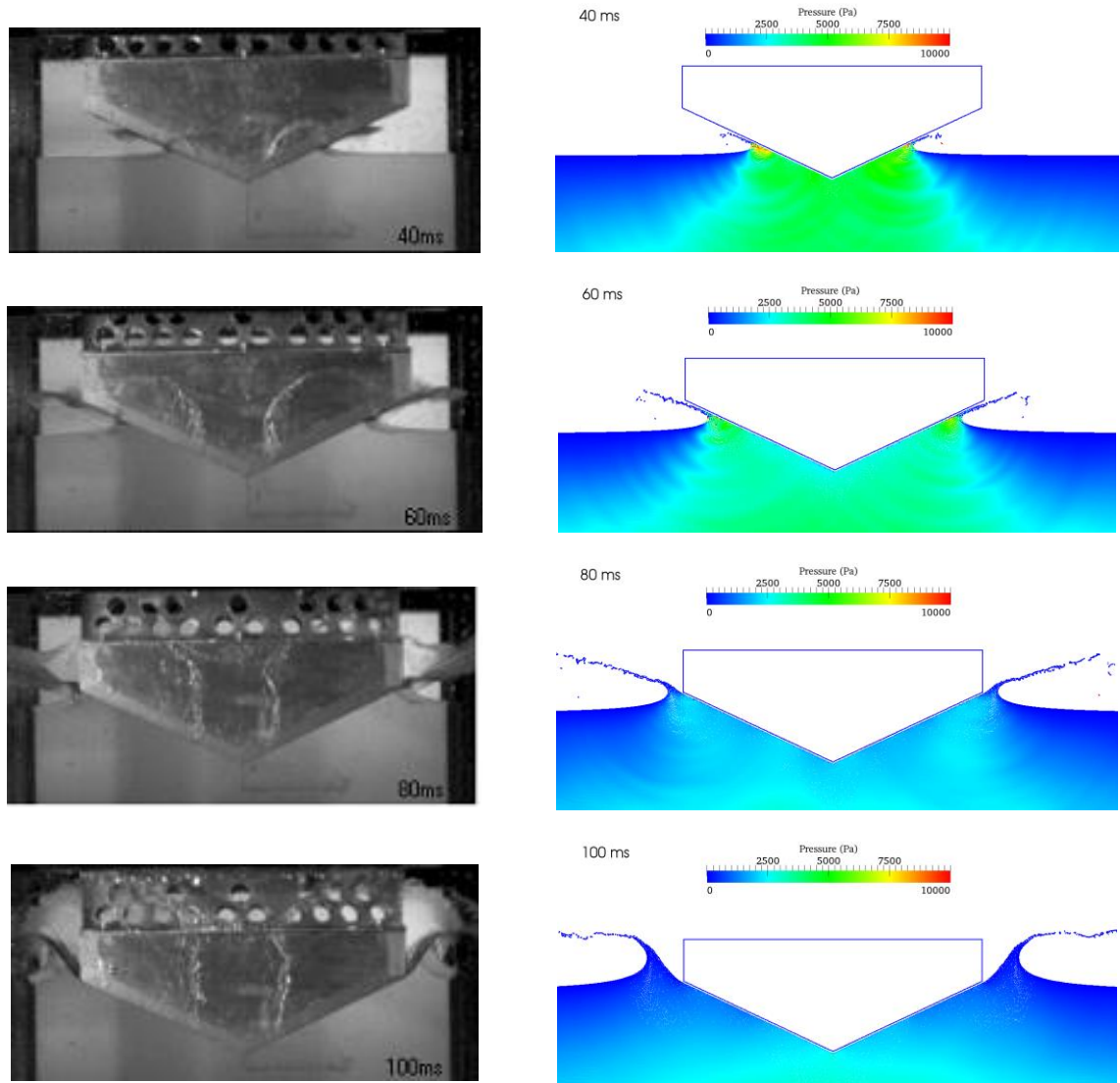


Figure 6.16: Comparison of 2-D SPH simulations of the 25° wedge drop section in various time steps with experiments of Whelan et al. [12, 33] (mass number=0.29 and normalised drop height (NDH)=0.85)

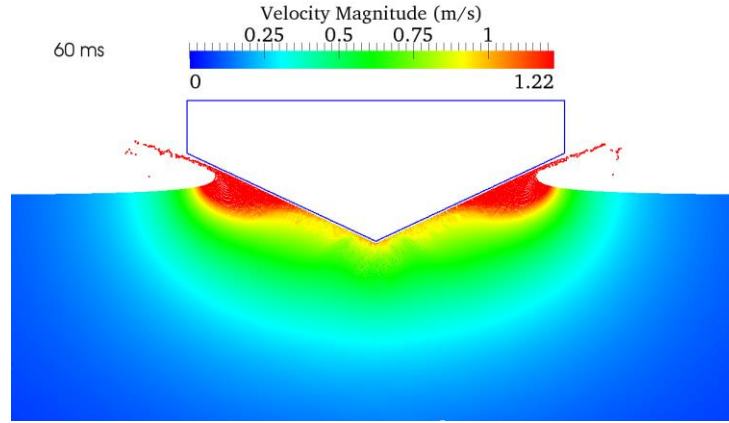


Figure 6.17: Velocity contours of 25° wedge simulations 60 milliseconds after drop (mass number=0.29 and normalised drop height (NDH)=0.85)

6.2.7. Drop kinematics

To verify of the SPH simulations, the accelerations, vertical velocity, submersion and pressures in time were extracted and compared to experimental results. These parameters are of importance as the general structure and seakeeping of the ship in waves is of interest. In slam events, if the amount of kinetic energy which the vessel needs to absorb is to be simulated, the vertical velocities and accelerations must be considered. The peak local pressure is also important if the local structure stiffening is of interest. Also, the progressive submersion relative to time is a good indicator for assessing the vessel motions predicted by the simulations.

Figure 6.18 shows the simulation results of vertical immersion of the 25° wedge compared to the experiments. As seen they both start from zero (where the wedge bottom hits the water surface) and follow in the negative region. The drop distance results match quite well with the experiments.

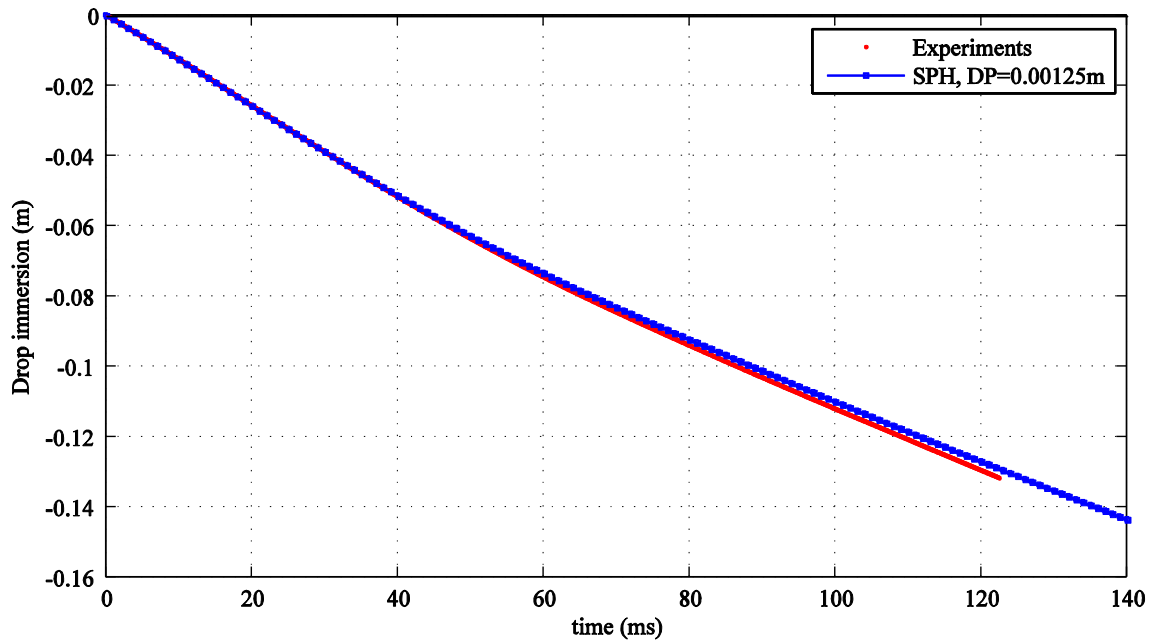


Figure 6.18: Immersion of 25° wedge simulations with mass number=0.29 and normalised drop height (NDH)=0.85

Figure 6.19 shows the vertical drop section velocity where both the simulations and experiments results start from initial velocity (V_{in}) of 1.22 m/s, increase for about 20 ms and then decrease to finally reach a constant water immersion velocity. The simulation drop velocity results follow the experimental results very well before 20 ms, deviate for about 3-4% between 20 ms and 80 ms where peak slam accelerations occur until the model slows down in final stages of the entry and reach the constant velocity region. At this stage, the velocity around the wedge becomes laminar and viscous forces dominate. Appropriate boundary layer and turbulence simulations are necessary if good correlation is expected. However, it is of interest in this study to look at initial stages of water entry where inertial loads are largest.

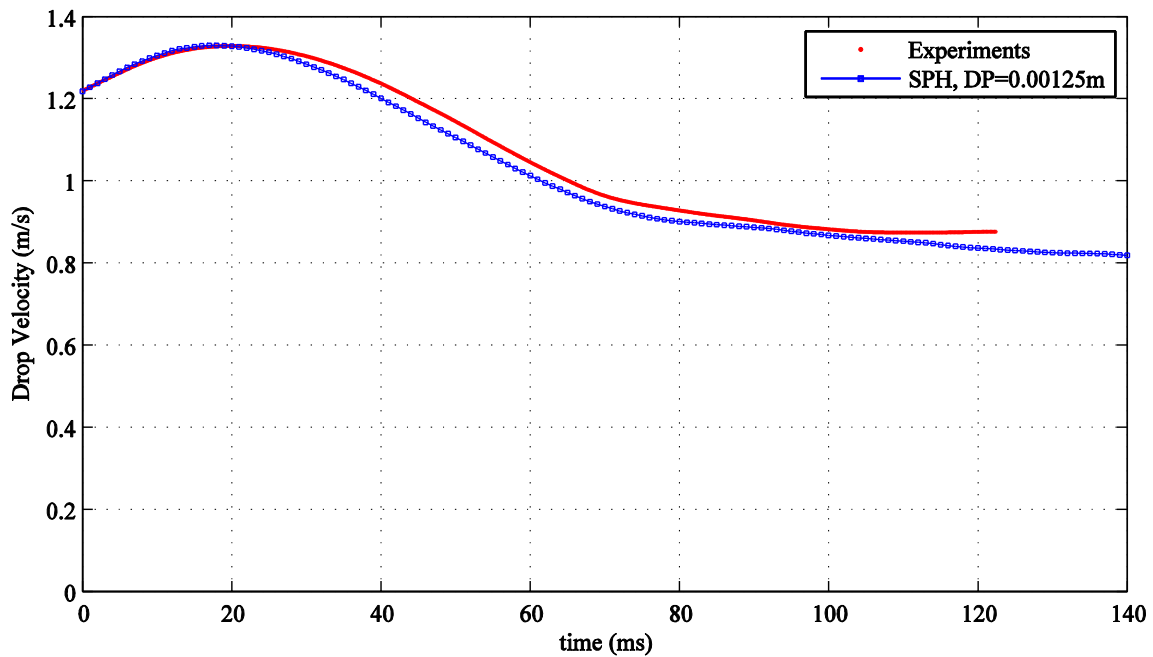


Figure 6.19: drop velocity with mass number=0.29 and normalised drop height (NDH)=0.85

Figure 6.20 shows the comparison of the drop acceleration results against the experimental results. As seen, the drop section has initial acceleration of -9.8 m/s^2 in simulations, the downward acceleration reduces until the direction alternates to positive and upward, it reaches a peak around 55 ms and reduces finally to zero where the velocity becomes constant. In the experiments, the initial acceleration is around 9.2 m/s^2 which could be due to the friction of the guide bar above or air drag.

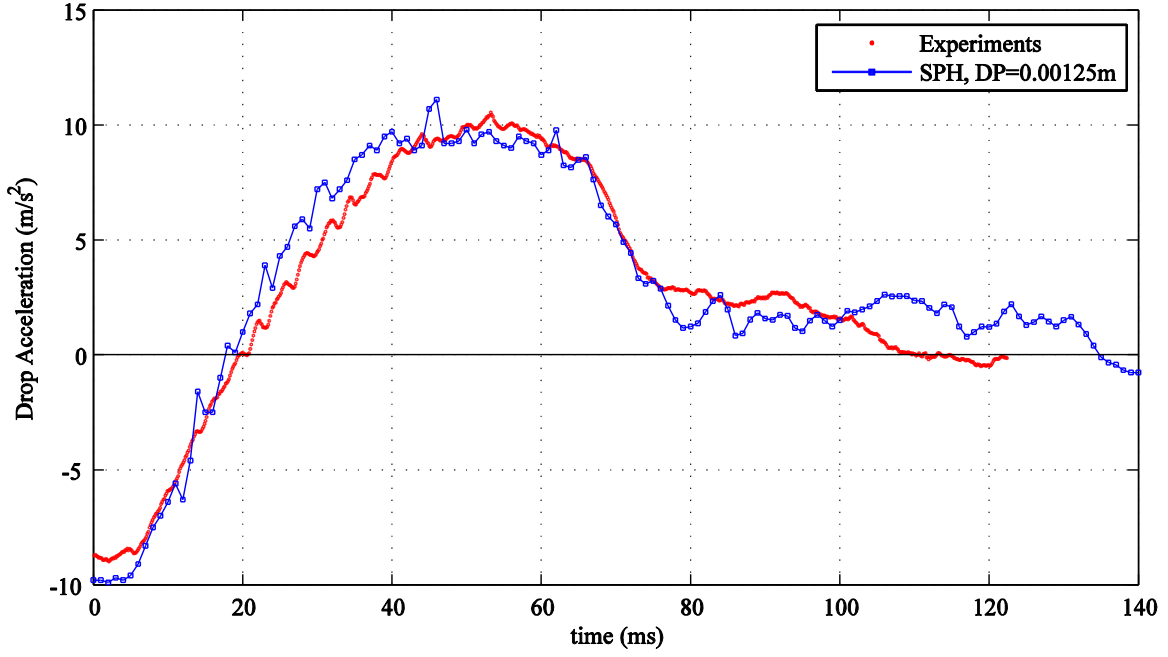


Figure 6.20: Drop acceleration of 25° wedge with mass number=0.29 and normalised drop height (NDH)=0.85

As also seen, there is a maximum at 15 ms (with a sharp rise from 13 ms) which is not seen in experimental results. This hump is caused by the pressure waves travelling with speed of sound ($c_0 = 62$ m/s) from the tank bottom upward; also seen in pressure contour plot of Figure 6.21. This wave hits the model at around 15 ms and creates a sudden high pressure region underneath the model. Throughout the drop event, the pressure waves from the tank bottom and the drop section itself reflect from the boundaries; e.g. resulting in local maximums in multiples of 15 ms (30 ms and 45 ms). Some techniques were used to mitigate these effects in the simulations including using finer particle spacing, removing solid boundaries from the side walls and instead using periodic open boundary condition and finally using an effective spatial filter.

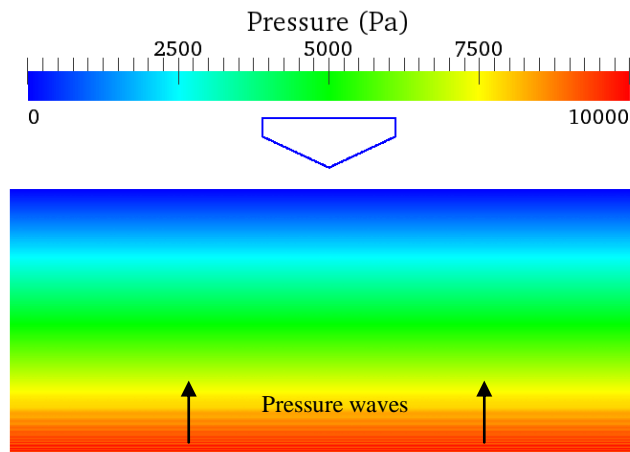


Figure 6.21: Pressure contour plot of the SPH fluid domain as it moves up from the bottom boundary

6.2.8. Wall pressures

Figure 6.22 shows the location of pressure transducers located on the side wall of the 25° wedge. As seen in Figure 6.23, the pressure on the wedge wall in the simulations were obtained by interpolating the fluid particle pressure in a circle of radius 4 times the smoothing length ($4h$ becomes 0.0077 m for $DP=0.00125$ m). The weighted interpolation was done based on Wendland kernel function and can be seen schematically in Figure 6.23. Figure 6.24 to Figure 6.27 show the wall pressures P1, P2, P3 and P4 respectively compared with the experiments. As seen, the pressures are small before P1 enters the water and then rises very sharply to a peak with magnitudes in the order of 12 to 4 kPa (from P1 to P4, reducing as moving upward along the wall) and then gradually reduces back to hydrostatic pressure. The results show good agreement with the experiments, following the same trend with around 10% error when comparing the peak value.

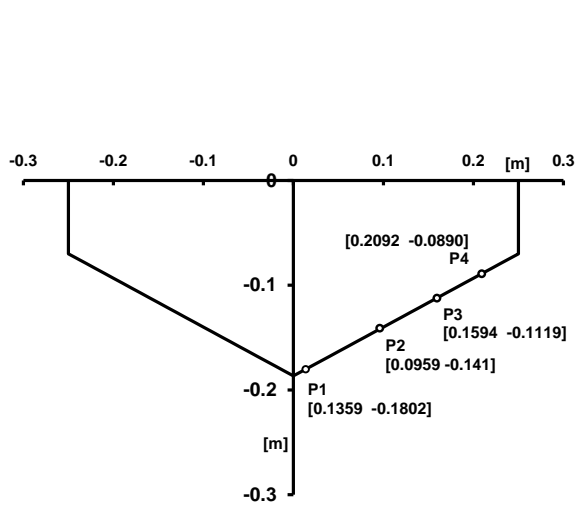


Figure 6.22: The location of pressure transducers on 25° wedge

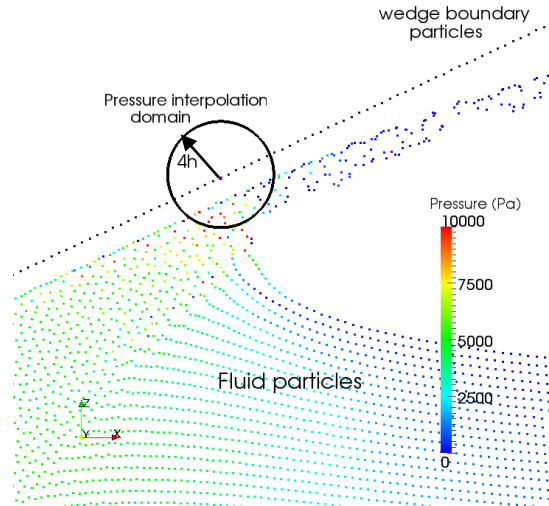


Figure 6.23: The close up of the jet flow in spray root and the wall pressure interpolation domain

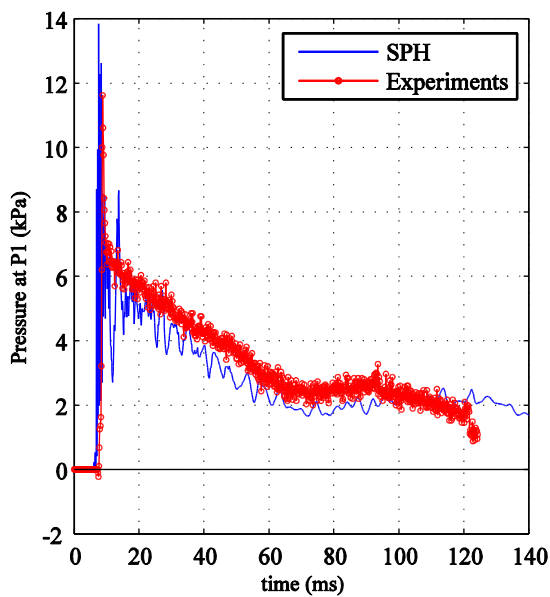


Figure 6.24: Drop pressures at P1 of the 25° wedge with mass number=0.29 and normalised drop height

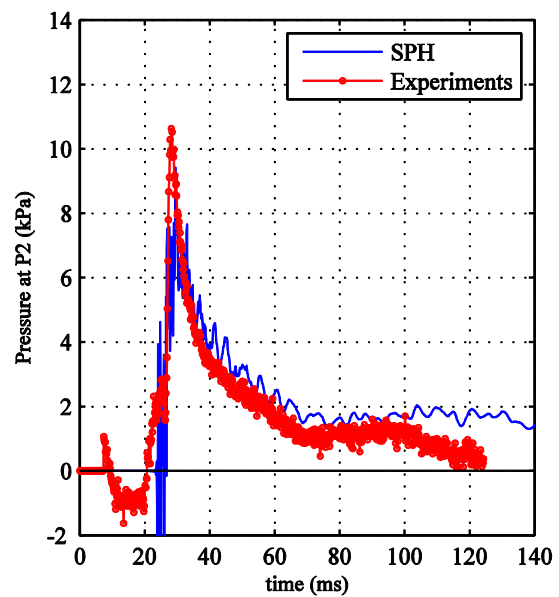


Figure 6.25: Drop pressures at P2 of the 25° wedge with mass number=0.29 and normalised drop height

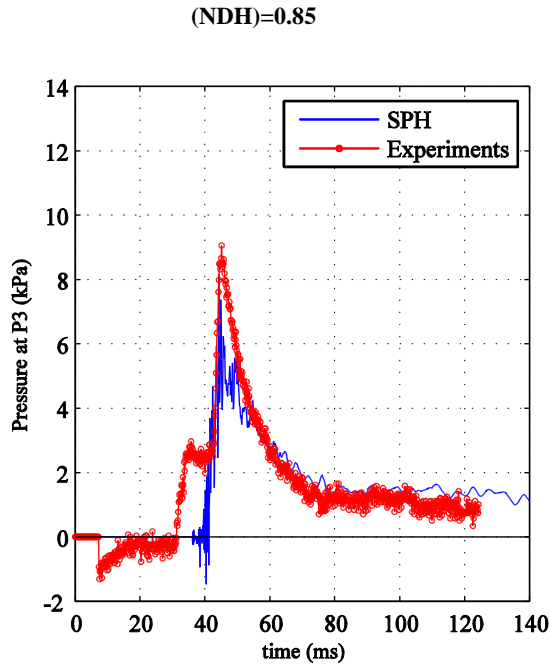


Figure 6.26: Drop pressures at P3 of the 25° wedge with mass number=0.29 and normalised drop height (NDH)=0.85

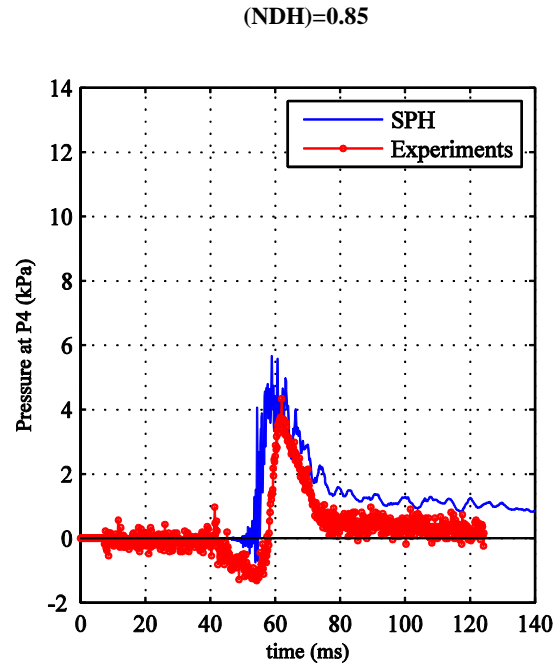


Figure 6.27: Drop pressures at P4 of the 25° wedge with mass number=0.29 and normalised drop height (NDH)=0.85

As seen in the simulation results, there are some fluctuations which can be attributed to the Lagrangian nature of SPH in which particles can accelerate more independently of the surrounding fluid particles. The fluid particles highly accelerate around the drop section approaching the wedge boundary particles causing individual high pressure peaks. Different dissipation techniques have been used here and by researchers to mitigate the pressure fluctuation effects such as using the XSPH formula, increasing particle density, density filtering, recently using dissipative terms in the continuity equation (delta-SPH) [149-151] and presenting the pressures on the wedge surface by averaging the pressures inside a domain close to the boundary [82-84].

6.2.9. Summary of configuration and parameter selection

Based on the study undertaken in the above section for the 25° wedge geometry, the optimal SPH parameters, particle configuration and domain setup are given in Table 6.3.

Table 6.3: The SPH Simulation Parameters for modelling slamming of various geometries

Features	Values
Fluid domain (tank) particle configuration	Straight line particle initial arrangement (not staggered)
Domain Bottom Boundary condition	Dynamic boundary condition Straight line particle arrangement
Domain side walls	Periodic open boundary
Drop section boundary condition	Dynamic boundary condition Straight line particle arrangement
Time stepping algorithm	Symplectic Variable time stepping
Speed of sound coefficient (C_{coef})	20
Speed of sound value (c_0)	62 m/s
Artificial viscosity coefficient (α)	0.01
Initial Distance between particles (DP)	$DP_x = DP_z = 0.00125$ m

Smoothing length	$h = 1.1 \sqrt{DP_x^2 + DP_z^2}$
Kernel function	Wendland (Quintic)
Spatial filter iteration (Shepard filter steps)	Every 5 time step
Wall pressure averaging domain	$4 \times h$ (h: smoothing length)

6.3. Drop tests results and comparison with experimental data

6.3.1. 25 degree wedge

Results for drop velocity, drop acceleration and wall pressures for NDH=0.89 and mass number=0.29 is presented in Section 6.2. Most of the drop geometries tested by Whelan [33] were dropped freely from different heights onto the water surface to examine the effects of various relative velocities in slamming. Now rather than modelling the geometries from a certain height, the initial velocity when touching the water surface was used to reduce simulation cost, since less time is required to complete the geometry drop. The 25° wedge was dropped with initial velocities of 0.9 m/s, 1.705 m/s and 2.075 m/s corresponding to NDH=0.8, 1.06 and 1.2. The velocity results of slam event simulations for these velocities with DP=0.00125 m is presented in Figure 6.28 to Figure 6.33. As seen the numerical and experiments velocity results agree quite well. However, as the initial velocity increases, the event becomes much quicker, more violent and more challenging to model, hence, the agreement with the experiments decreases. The simulations for NDH=1.2 were conducted using higher speed of sound ($C_{coef} = 30$) because of the increase in maximum fluid bulk velocity.

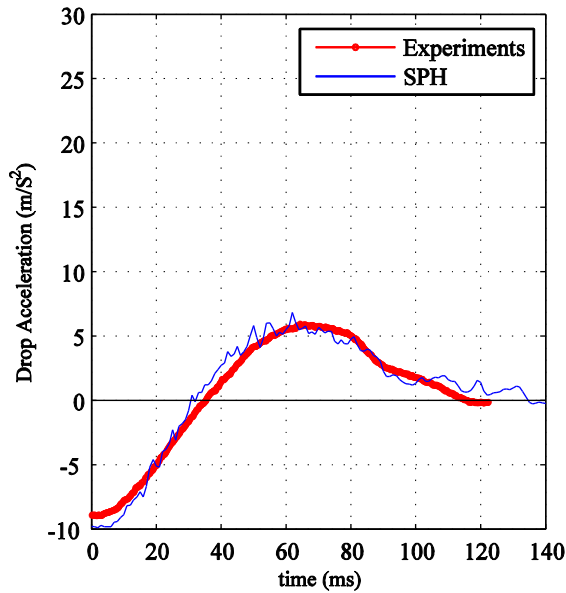


Figure 6.28: drop acceleration of 25° wedge with SPH for NDH=0.8 and mass number=0.29

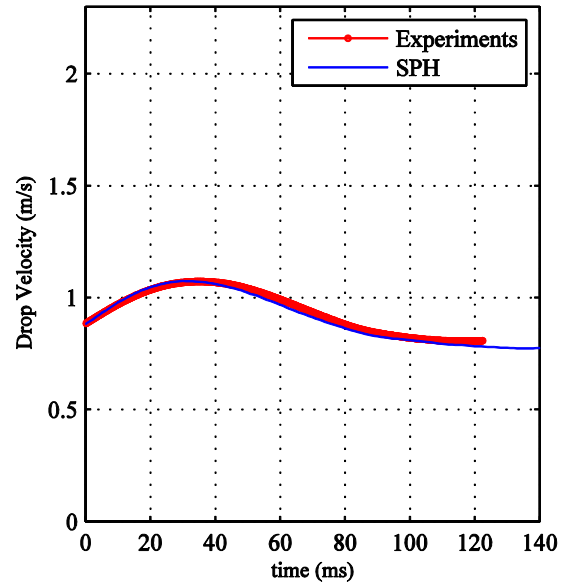


Figure 6.29: Drop velocity with SPH of 25° wedge with SPH for NDH=0.8 and mass number=0.29

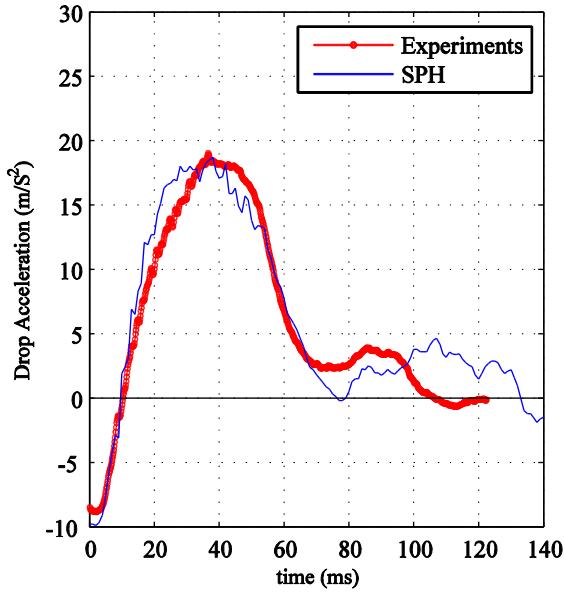


Figure 6.30: Drop acceleration with SPH of 25° wedge for NDH=1.06 and mass number=0.29

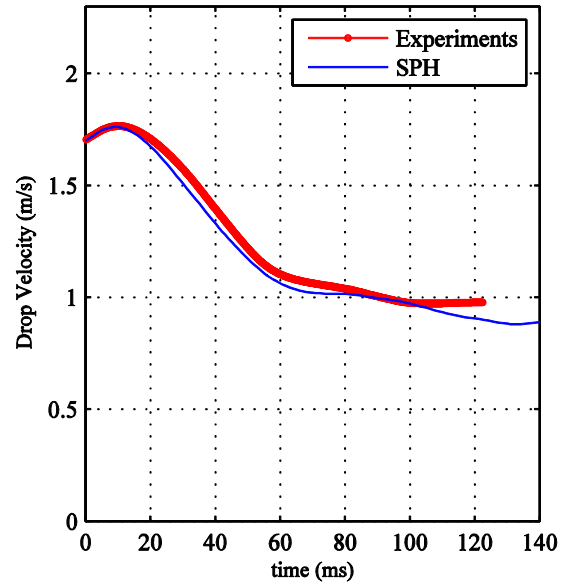


Figure 6.31: Drop velocity with SPH of 25° wedge for NDH=1.06 and mass number=0.29

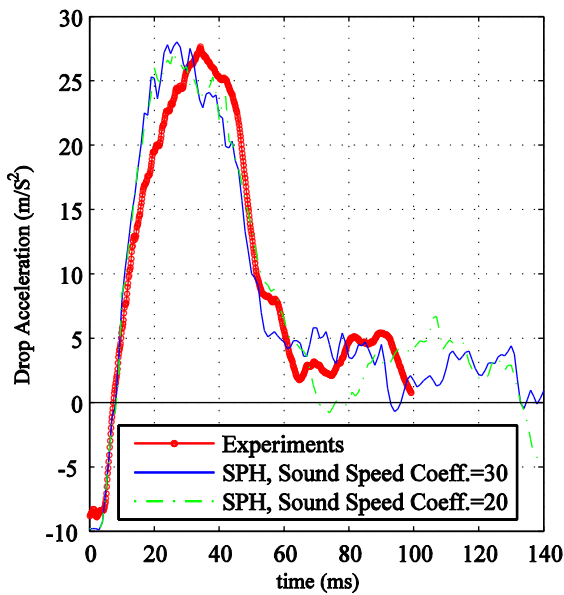


Figure 6.32: Drop acceleration with SPH of 25° wedge for NDH=1.2 and mass number=0.29

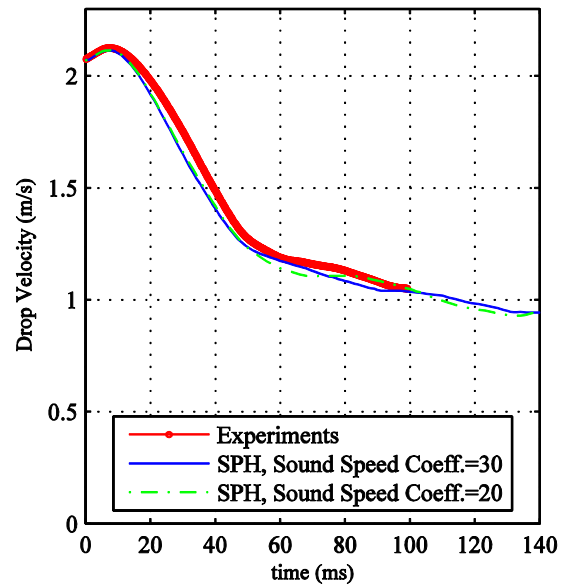


Figure 6.33: Drop velocity with SPH of 25° wedge for NDH=1.2 and mass number=0.29

25° wedge with various masses of drop geometry: Whelan [33] tested the drop geometries with two different model masses to investigate the effect of mass and inertia of the vessel bow sections on the slam event. Two non-dimensional values of mass number=0.29 and mass number=0.58 were used which corresponded to 72.5 kg/m and 145 kg/m. Figure 6.34 and Figure 6.35 show the acceleration and velocity results respectively for mass number=0.58 compared to the SPH results for NDH=0.89 and DP=0.00125 m. As seen, there is a good agreement between the SPH and experimental results.

Other initial velocities give similar correspondence with the experiments, raising the confidence on the simulations with this model mass.

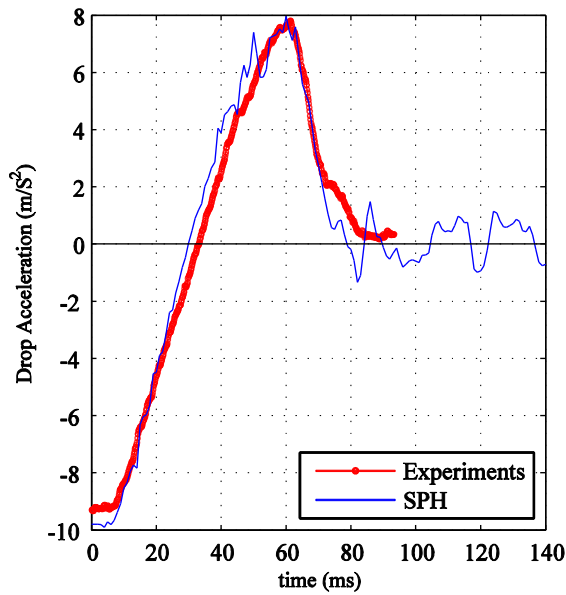


Figure 6.34: Drop acceleration with SPH of 25° wedge for NDH=0.89 and mass number=0.58

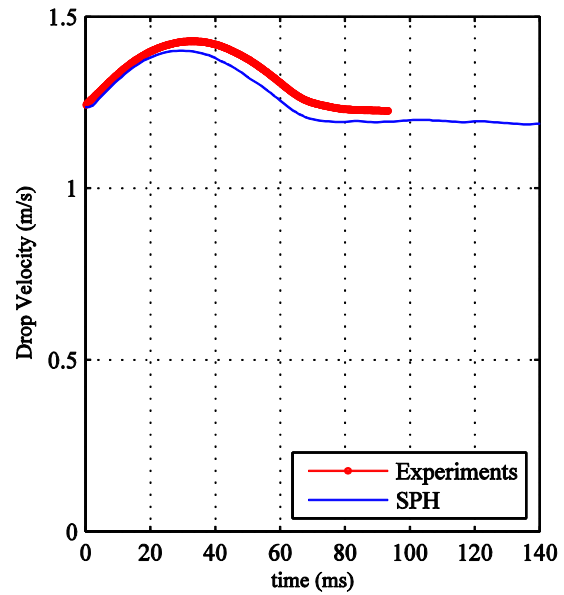


Figure 6.35: Drop velocity with SPH of 25° wedge for NDH=0.89 and mass number=0.58

Having performed these simulations successfully on 25° wedge with different initial velocities and model masses, provides a strong indication that the simulations results are so far independent of the particle density, model mass and initial velocity. Therefore, other tested geometries were also simulated using the same simulation parameters as Table 6.3.

6.3.2. 15 degree wedge

A wedge with 15° deadrise angle was tested in Whelan's experiments [33] where the section geometry can be seen in Figure 6.7. The 15° wedge was tested using various drop heights and masses. Generally because the small deadrise angle in 15° wedge, the impact was more rapidly transient with higher accelerations compared to the 25° wedge.

This section was modelled to investigate how lower deadrise angles will behave in SPH. The speed of sound had to be taken higher ($C_{coef}=30$) for 15° wedge since the maximum fluid bulk velocity is higher in the experiments. The 15° wedge was simulated for initial velocities of 1.27 m/s, 1.527 m/s and 1.928 m/s corresponding with NDH=0.8, 0.89 and 1.06. Figure 6.36 shows the pressure contour plot of 15° wedge water entry with NDH=0.89 and DP=0.00125 m compared to experiments. The high pressure region under the drop section is quite large in the early stages of the slam event (20 ms) which decelerate the section more rapidly compared to 25° wedge. The pressure pattern seen in 20 ms is a combination of drop generated pressure waves and the reflected waves from the tank bottom. This high pressure then moves outboard to be more concentrated around the spray roots (40 ms). The spray and upwash water were captured quite successfully through the simulations.

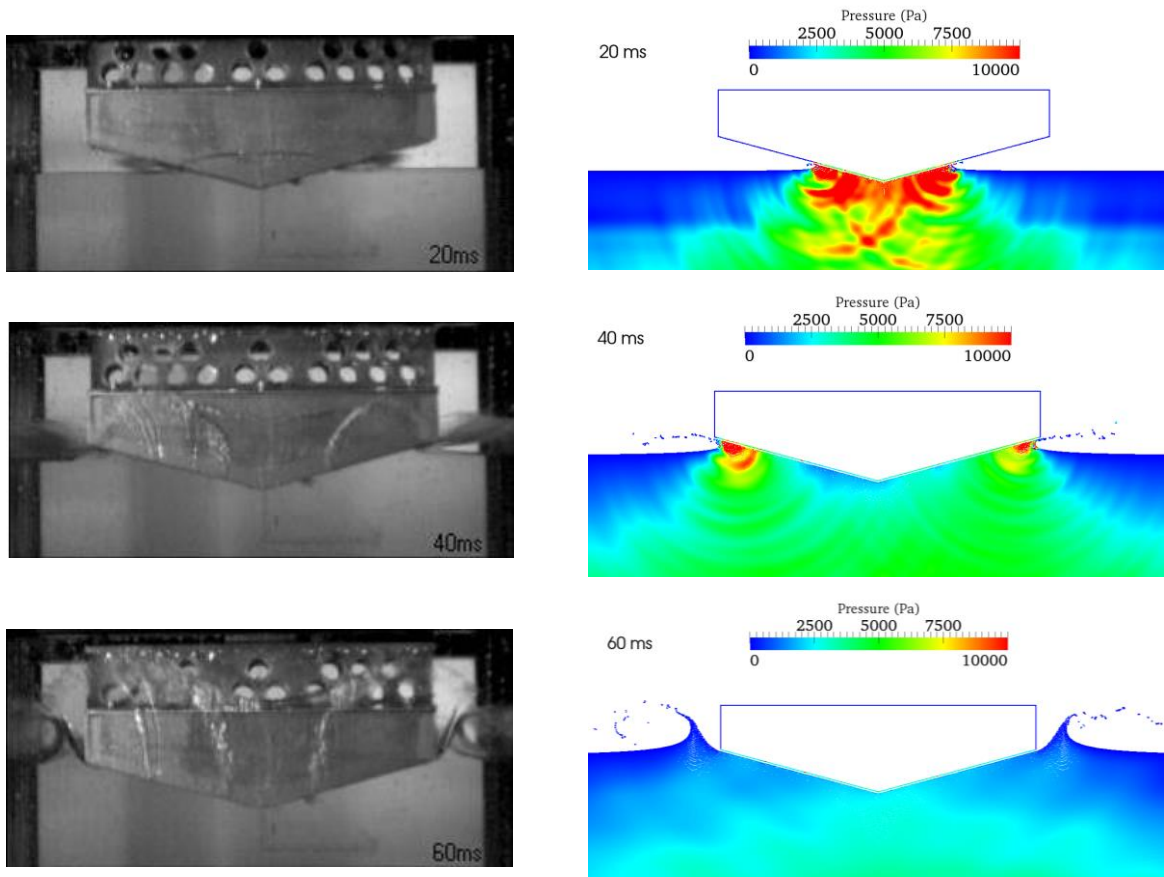


Figure 6.36: Comparison of 2-D SPH simulations of the 15° wedge drop section in various time steps (20,40 and 60 ms) with experiments of Whelan [33] (mass number=0.29 and normalised drop height (NDH)=0.89)

Figure 6.37 and Figure 6.38 shows the acceleration and velocity results respectively for NDH=0.8 and mass number=0.29 of the 15° wedge with DP=0.00125 m. As seen the SPH acceleration results follows the trend of experiments but less closely when compared to 25° wedge, especially in the region between 12 to 30 ms. The reasons could be the interaction of tank bottom pressure waves with pressure profile around the wedge bottom. The pressure waves rise from the tank bottom around 10 ms (due to higher speed of sound) to the surface increasing the pressure under the wedge causing high upward accelerations.

Figure 6.39 and Figure 6.40 show the acceleration and velocity results respectively for the 15° wedge with NDH=0.89 and mass number=0.29. Figure 6.41 and Figure 6.42 show the acceleration and velocity results respectively for NDH=1.06 and mass number=0.29. The SPH results show similar trends to the experiments with the peak accelerations deviating more as the drop velocity increases. For higher initial velocities as shown in Figure 6.47, possible creation of air pocket cushions under the 15° wedge section could be the reason of fairly flat maxima between 16 to 30 ms of the accelerations in the experiments.

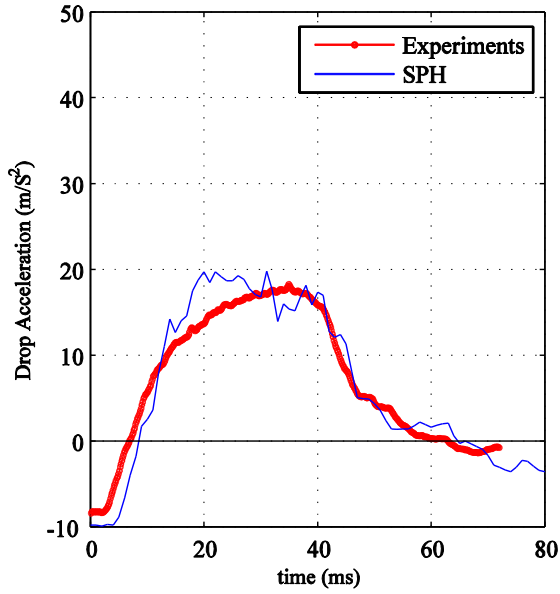


Figure 6.37: Drop acceleration with SPH of 15° wedge for NDH=0.8 and mass number=0.29

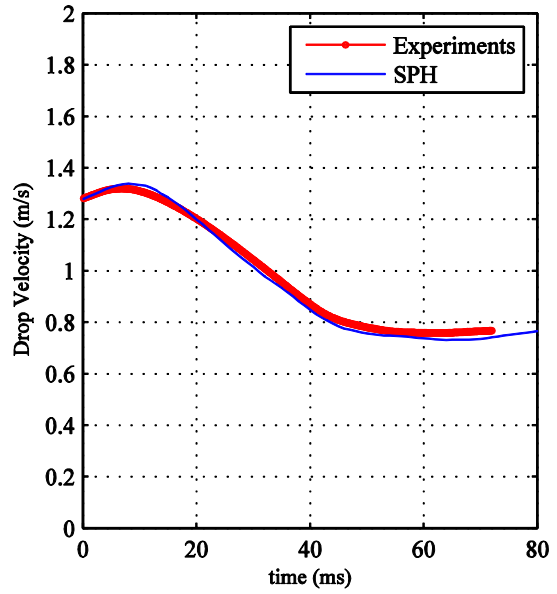


Figure 6.38: Drop velocity with SPH of 15° wedge for NDH=0.8 and mass number=0.29

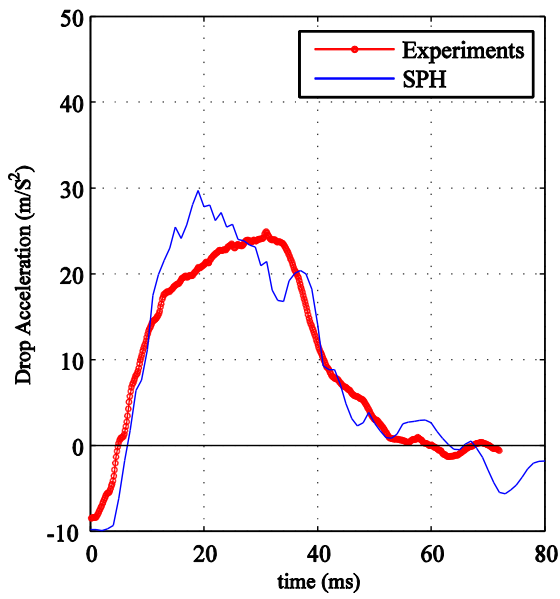


Figure 6.39: Drop acceleration with SPH of 15° wedge for NDH=0.89 and mass number=0.29

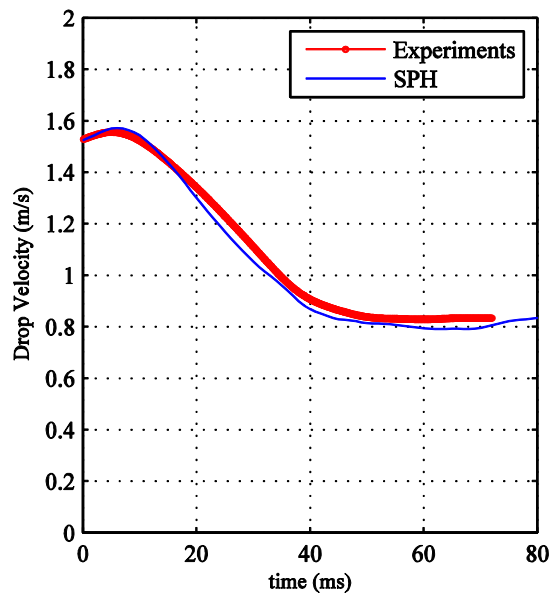


Figure 6.40: Drop velocity with SPH of 15° wedge for NDH=0.89 and mass number=0.29

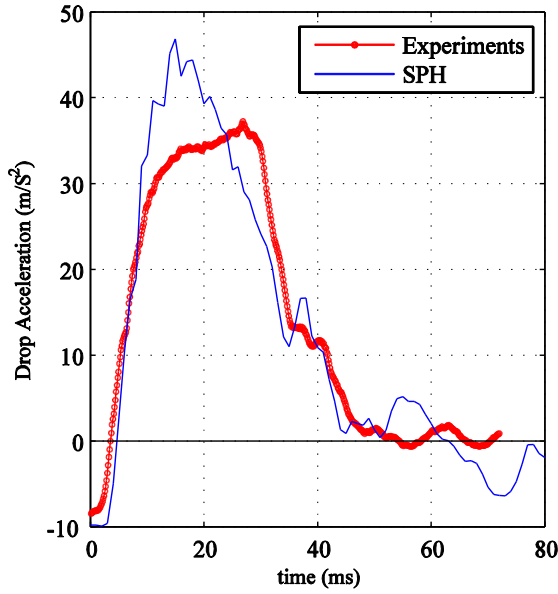


Figure 6.41: Drop acceleration with SPH of 15° wedge for NDH=1.06 and mass number=0.29

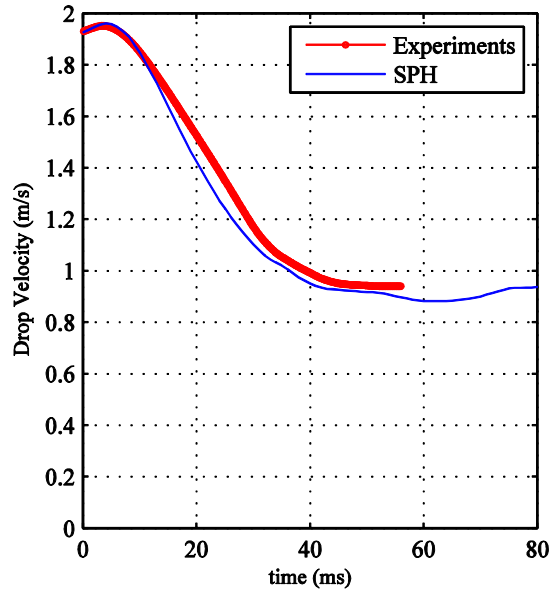


Figure 6.42: Drop velocity with SPH of 15° wedge for NDH=1.06 and mass number=0.29

Figure 6.43, Figure 6.44 and Figure 6.45 show the pressure results in P1, P2 and P3 compared with experiments for NDH=0.89 and mass number=0.29. The location of these pressure transducers is shown in Figure 6.46. As seen, the pressure signals are captured well (especially in P1 and P2), even though the peak pressures are a little different. Also it is seen that the pressure peak values are nearly 4 times higher than the 25° wedge which again illustrates the severity of slamming in smaller deadrise angles.

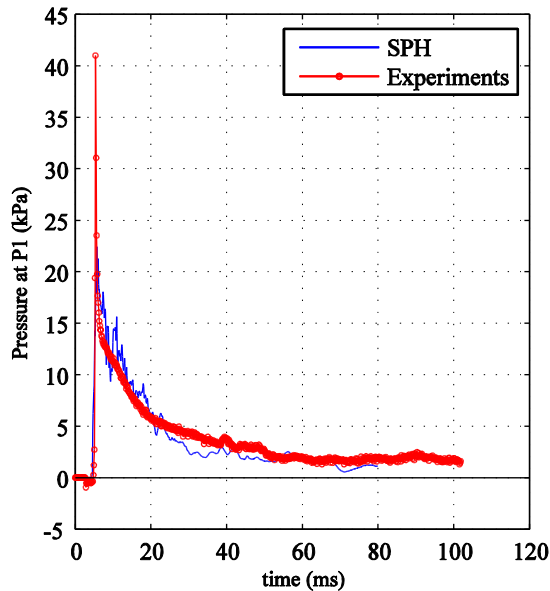


Figure 6.43: Pressure results of P1 with SPH of 15° wedge for NDH=0.89 and mass number=0.29

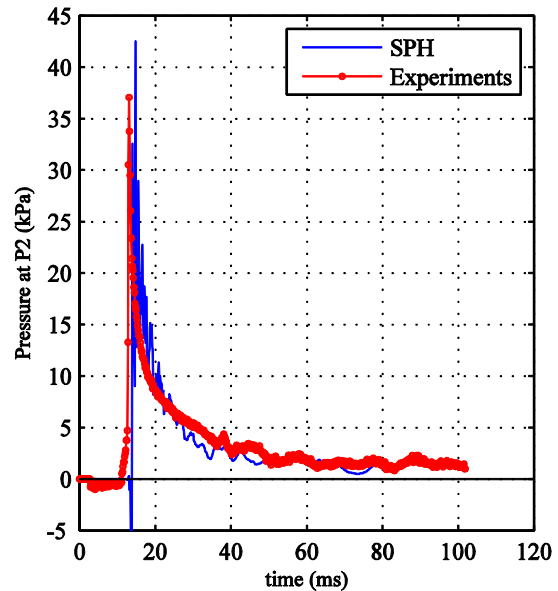


Figure 6.44: Pressure results of P2 with SPH of 15° wedge for NDH=0.89 and mass number=0.29

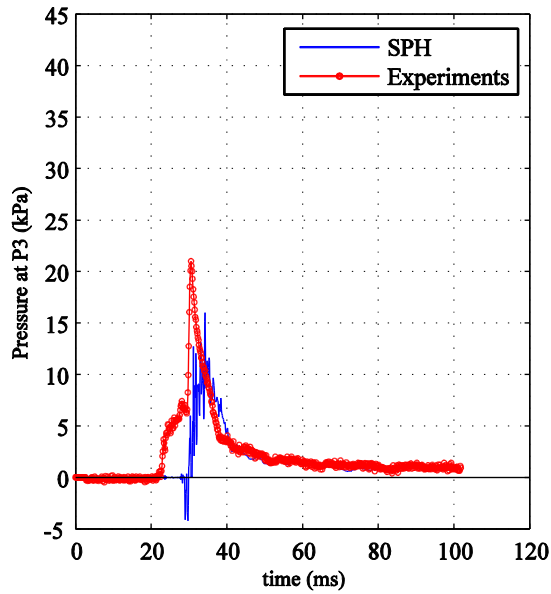


Figure 6.45: Pressure results of P3 with SPH of 15° wedge for NDH=0.89 and mass number=0.29

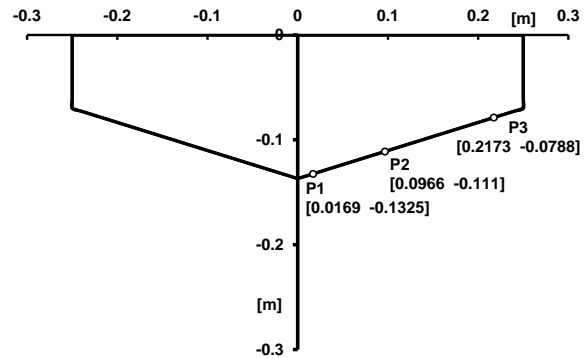


Figure 6.46: The location of pressure transducers on 15° wedge drop section

6.3.3. 25 degrees wedge with side plates

Whelan [33] transformed the 25° wedge into a simplified catamaran style hull form with a centrebow by fitting two 30 mm wide side plates with sharp ends for water entry corners, the section geometry can be seen in Figure 6.7. The discontinuity and blockage of the fluid upwash flow under the top knuckles of the wedge creates a severe slam in that corner; however having the air trapped underneath this section has a major effect on the drop dynamics. The sharp edges of the demihulls, the sudden high pressures and the air entrapment in top corners all make this a very challenging problem to simulate. Figure 6.47 shows the pressure contour plot of the 25° wedge with side plates geometry with initial velocity of 1.031 m/s (NDH=0.85) and DP=0.00125 m and mass number=0.29 (equivalent of 87.725 kg/m). As seen, the side plates pierce the surface creating an upwash on both sides. Then the wedge enters the water and appears to have the same flow features as for the 25° wedge alone. As seen in the 60 ms and 80 ms plots, the enclosed section fills up slightly quicker in SPH simulations compared to Whelan's experiments and the slam occurs earlier than in the physical tests. During the slam, a large area becomes pressurised causing high accelerations on the section. The likely reason for such behaviour is that the air is not simulated in the SPH simulations, whereas the entrapment of air under the section in the experiments reduces the section immersion rate significantly. This is exaggerated by the existence of only a small gap between the section side walls and the tank walls, allowing some venting of the air.

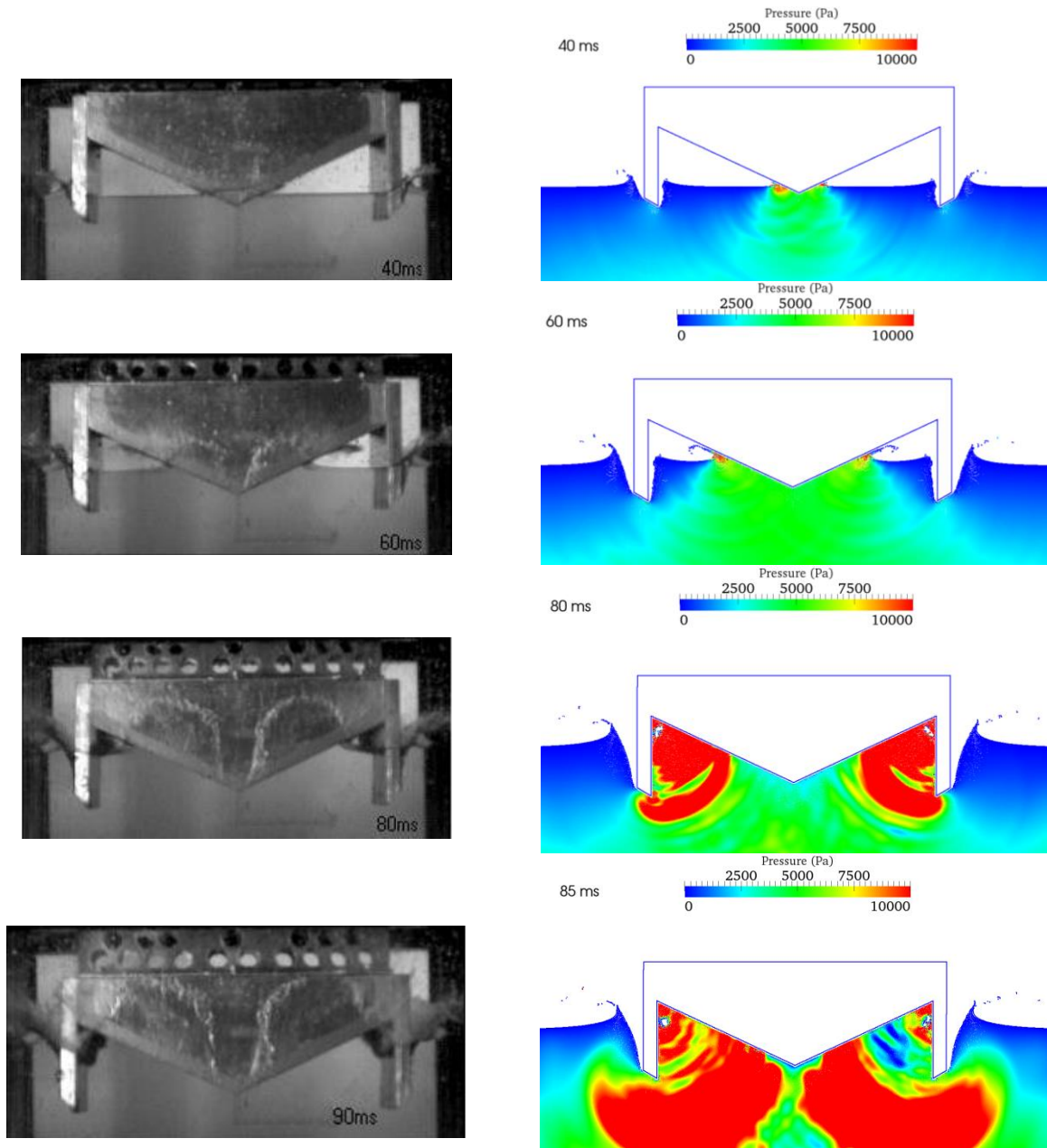


Figure 6.47: Comparison of 2-D SPH simulations of the 25° wedge with side plates drop section in various time steps (40, 60, 80 and 85 ms) with experiments of Whelan [12, 33] (mass number=0.29 and normalised drop height (NDH)=0.85)

Figure 6.48 shows the acceleration results for the 25° wedge with side plates simulations with 1.031 m/s initial velocity for NDH=0.85 and mass number=0.29. The simulation results have similar trends to the experiments before 65 ms after the entry; however, the peak acceleration in experiments occurs earlier and is much higher in the simulations. Figure 6.49 shows the drop velocity results of this event where the downward velocity has dropped significantly after the wetdeck slamming.

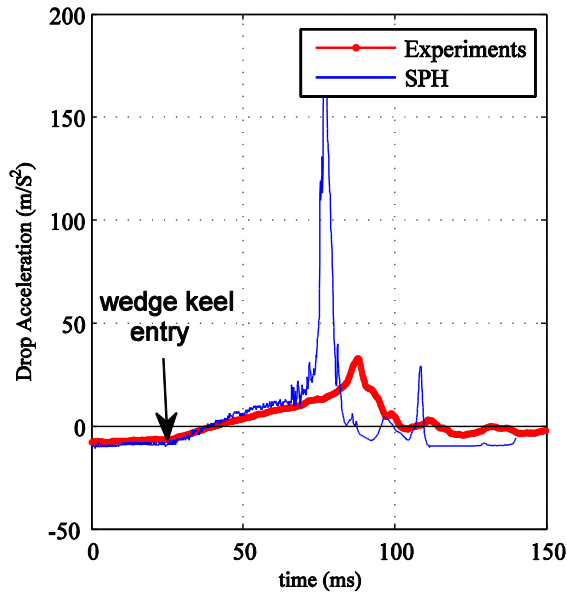


Figure 6.48: Drop acceleration with SPH of the 25° wedge with side plates section for NDH=0.85 and mass number=0.29

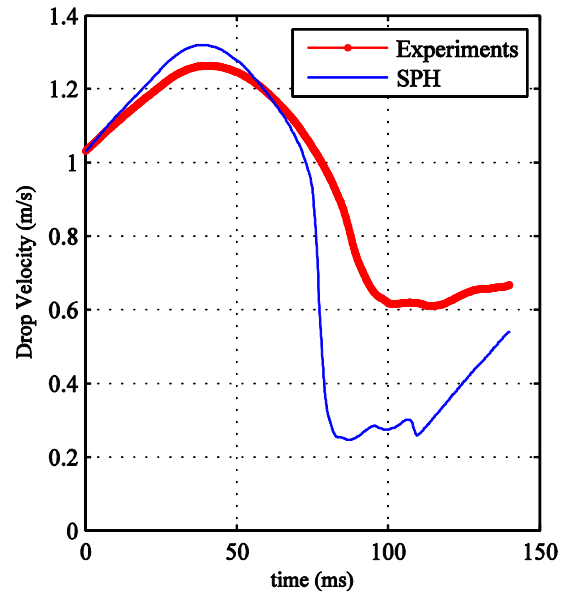


Figure 6.49: Drop velocity with SPH of the 25° wedge with side plates section for NDH=0.85 and mass number=0.29

There are two reasons for the high accelerations in the SPH simulations. Firstly the 2-D nature of the simulations means that there is no escape for the water particles that are trapped underneath the enclosed section, whereas in the experiments some water can escape due to the clearance between the section and tank walls – this water leakage can be seen in the photos in Figure 6.47. The second reason is the air entrapment in the archway region; in the experiments a mixture of air and water moves up to become trapped underneath the section and is an air cushion which alleviates the high pressures in the top corner and damps the high accelerations of the drop section. This effect cannot be simulated in SPH since there is not the ability to include both air and water in the simulation. Using a lower speed of sound can reduce the peak drop accelerations, which effectively makes the fluid more compressible. This however induces more than 1% compressibility to the system which is not physically acceptable.

Figure 6.50 shows the location of the pressure transducers under the enclosed 25° wedge with side plates section. They are in similar locations as in 25° wedge. Figure 6.51, Figure 6.52 and Figure 6.53 show the pressure results of the SPH simulations compared to the experiments. As seen, the pressures in both SPH and the experiments start at zero, have a sharp peak as the normal 25° wedge does and then reduces until about 90 ms. At this point in time, due to the top corner slamming, the pressures start to have large oscillations; these oscillations shows themselves as a very large peak in the SPH results but are much smaller in magnitude in the experiments.

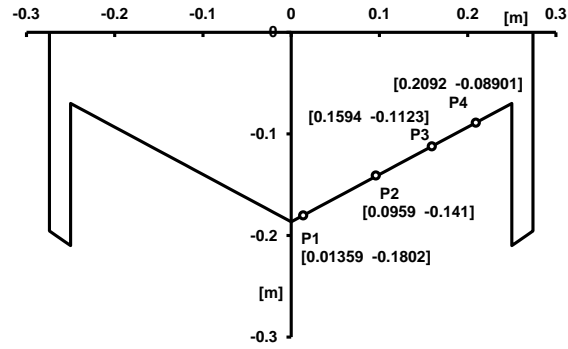


Figure 6.50: The location of pressure transducers on the 25° wedge with side plates

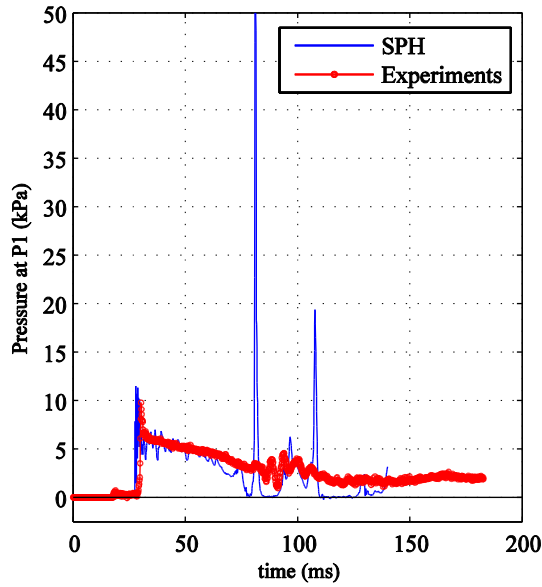


Figure 6.51: Pressure results at location P1 of the 25° wedge with side plates for NDH=0.85 and mass number=0.29

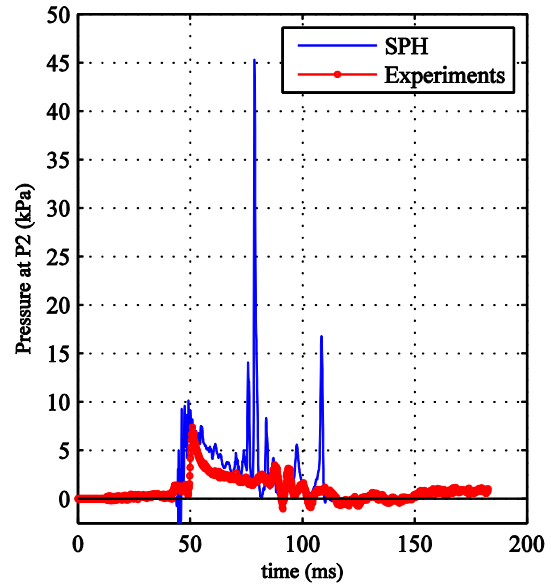


Figure 6.52: Pressure results at location P2 of the 25° wedge with side plates for NDH=0.85 and mass number=0.29

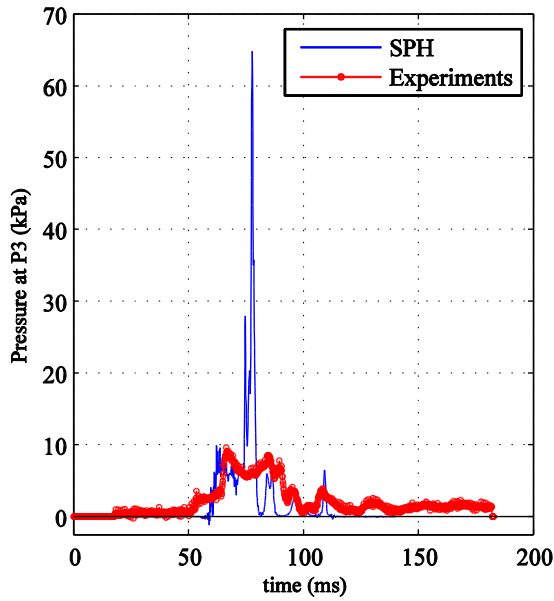


Figure 6.53: Pressure results at location P3 of the 25° wedge with side plates for NDH=0.85 and mass number=0.29

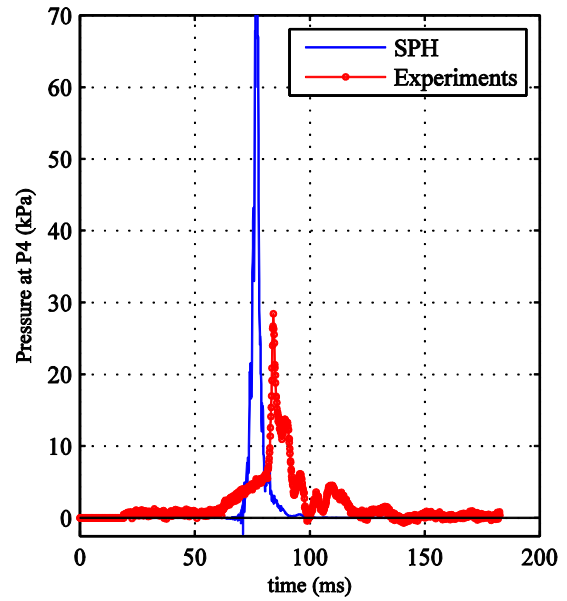


Figure 6.54: Pressure results at location P4 of the 25° wedge with side plates for NDH=0.85 and mass number=0.29

This large pressure peak also appears to at an earlier time in the simulations compared to the experiments. The larger magnitude SPH pressure results and its earlier occurrence when compared to the experiments, as previously explained, are due to not modelling the air, in addition to the 2-D geometry of the model which prevents any escapes from the sides in depth. The result for P4 shown in Figure 6.54 is somewhat different; there is only a single large peak in the pressure plot due to the proximity of the P4 location to the top corner of the section.

6.3.4. INCAT wave-piercing catamaran with centrebow (Incat1)

The Incat1 section tested by Whelan [12, 33] is an extrusion of a true bow section of an INCAT wave-piercing catamaran. The geometry can be seen in Figure 6.7 where the demihulls, centrebow and archways are shown. As this section enters the water, there are three important stages that occur as shown in Figure 6.55 with mass number=0.29 and NDH=0.86.

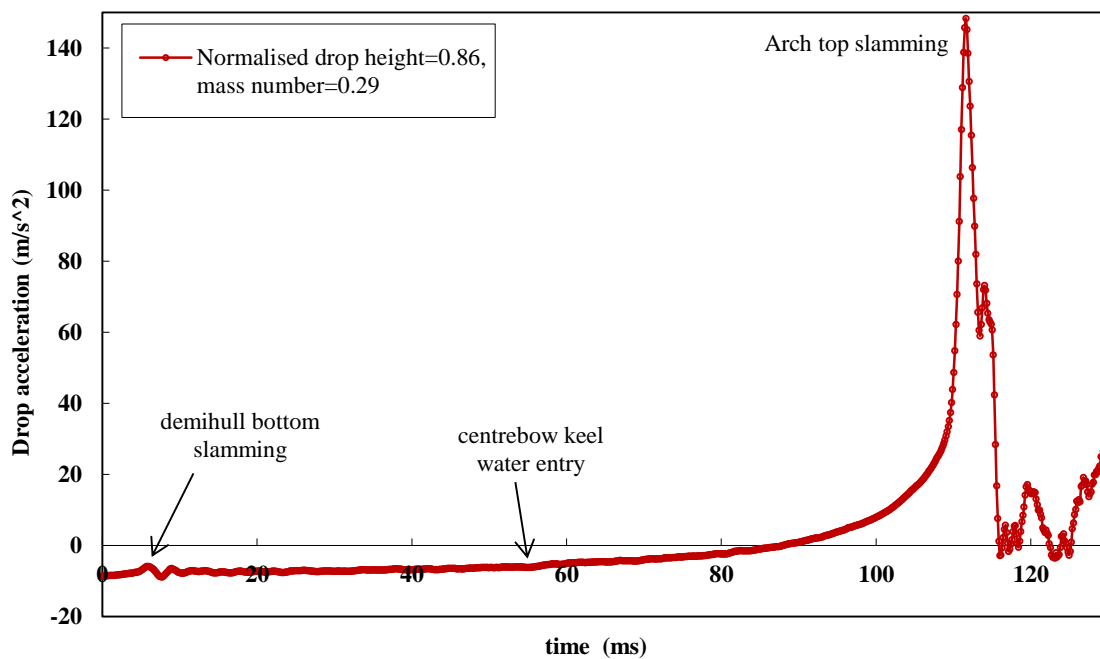
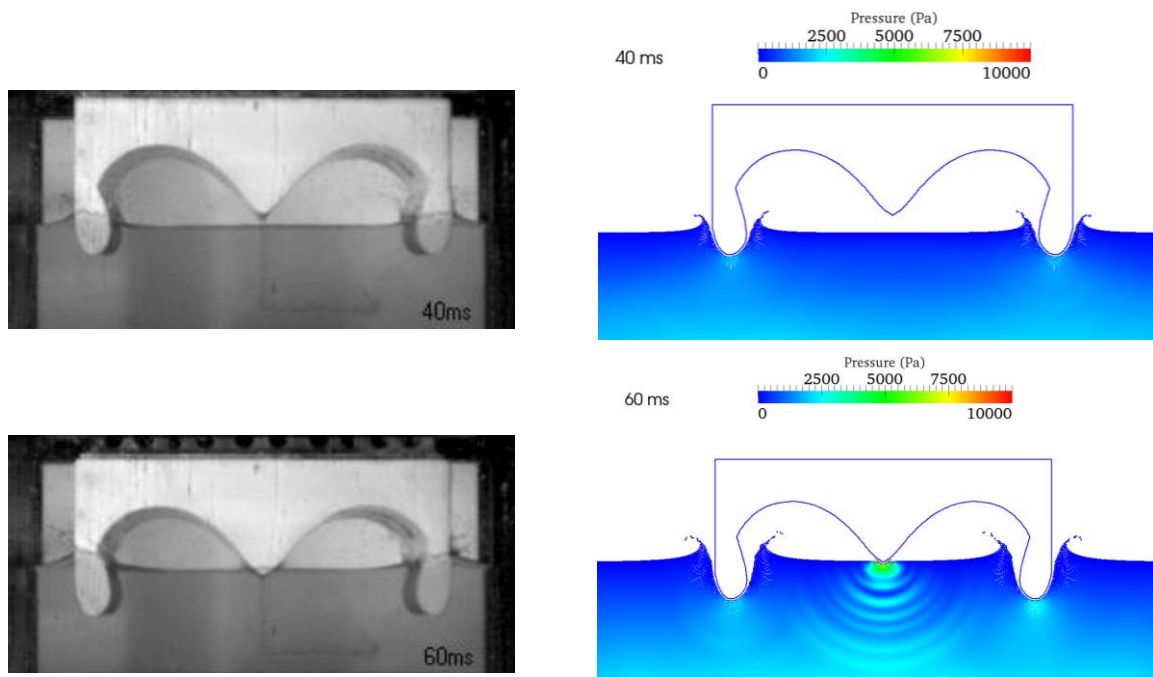


Figure 6.55: Drop accelerations of Incat1 section with normalised drop height (NDH)=0.86 and mass number=0.29 by Whelan [33]

The first stage is the demihull bottom entry slamming; it is relatively small and can be seen as small fluctuations in the acceleration plot in the first 10 milliseconds of the water entry. The second impact belongs to the centrebow keel water entry and shows itself as a mild deflection in the acceleration graph increasing the section deceleration (see Figure 6.56). The upwash water from the centrebow and demihulls moves upward, deflects around the archway curvature, entraps and forces the air out and creates a severe wetdeck slamming. This is seen as the large sharp acceleration peak (around 150 m/s^2). This is a very high acceleration, higher than values seen in any full-scale vessel measurements. The entrapped air finally escapes out and the upwash water of the centrebow and the demihulls meet

each other further outboard of the arch top; the high pressures are then alleviated by some water escaping as a planar jet flow from the clearance between the drop geometry and tank walls.

Figure 6.56 shows the pressure contour plot of the Incat1 geometry simulation results for mass number=0.29 and NDH=0.86 compared to the experimental results. At 40ms, the bottoms of the demihull are submerged and the centrebow keel enters the water after 60 ms. The enclosed water surface elevates between the demihulls and the centrebow in the simulations. As seen, at 80 and 90ms, the surface elevation is higher in the simulations compared to the experiments. The reason for this is the slight rise in air pressure underneath the section in the experiments before the water reaches the arch top (similar to the pressure profiles for the 25° wedge with side plates). The consequence of this fast immersion is the early wetdeck slamming at 100 ms in the simulation, 11ms earlier than in the experiments. The large high pressure region underneath the section causes a very high acceleration peak (see Figure 6.57). The enclosed section fills up outboard shortly after this wetdeck slam and creates another peak around 105 ms in the simulations, whereas the first wetdeck slam peak has not occurred yet in the experiments. Again this is predominantly due to the 2-D nature of the simulations thus giving no opportunity for the enclosed water to escape, causing severe containment and high pressures for a large fluid region propagating downward.



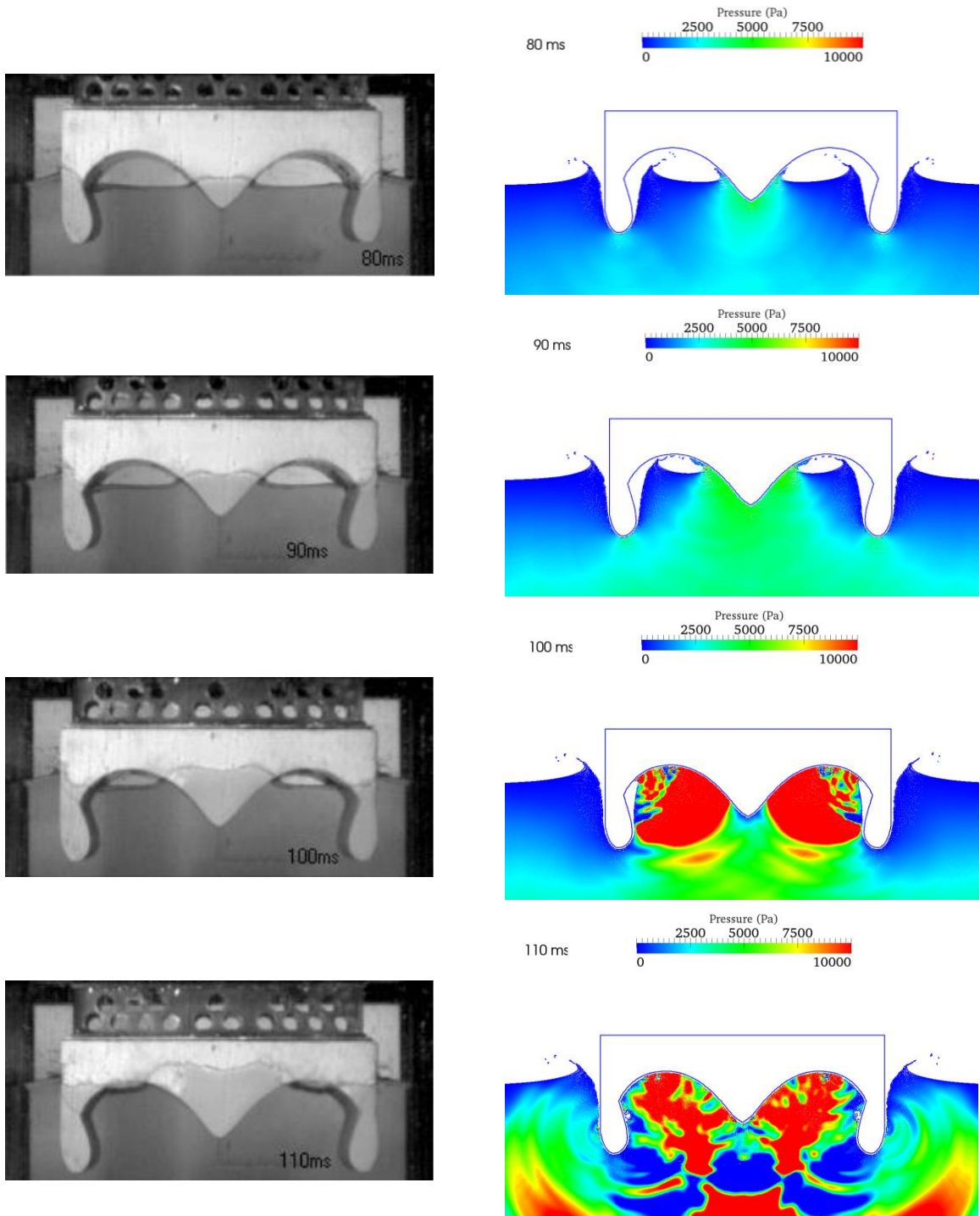


Figure 6.56: Comparison of 2-D SPH simulations of the Incat1 drop section in various time steps (40,60 80, 90,100 and 110 ms) with experiments of Whelan [12, 33] (mass number=0.29 and normalised drop height (NDH)=0.86)

Figure 6.57 and Figure 6.58 show the comparison of the drop acceleration and velocity of the dropped section for both the SPH and experimental results with mass number=0.29 and NDH=0.86. The results show that prior to wetdeck slamming the section gains a higher velocity, so water reaches the arch top sooner. The magnitude of the slam acceleration is also significantly larger in the simulations; this is due to the increased momentum (higher maximum drop velocity) in the simulations and also

the creation of air pockets in the experiments working as a cushion alleviating the severity of the slam event.

Figure 6.59 and Figure 6.60 show the drop acceleration and velocity results respectively for mass number=0.29 and NDH=0.77. Similarly the slams occur earlier in the simulations and include two slam acceleration peaks. Comparing this case with NDH=0.86 with a higher initial entry velocity, the first slam peak is lower due to lower momentum available in the drop section prior to the wetdeck slamming.

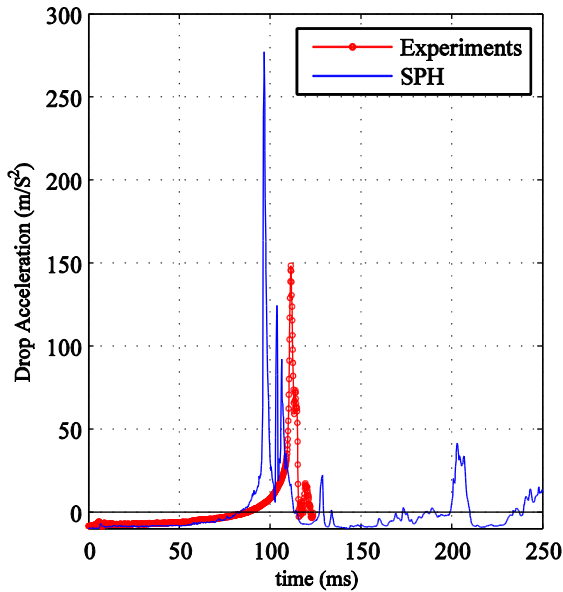


Figure 6.57: Drop acceleration with SPH of Incat1 section for NDH=0.86 and mass number=0.29

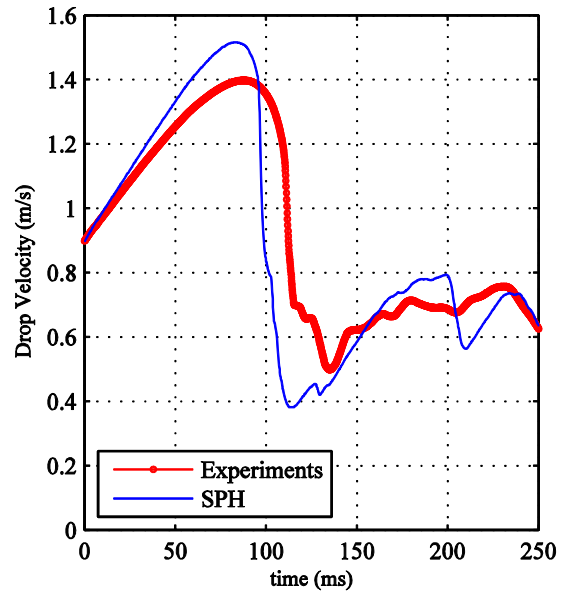


Figure 6.58: Drop velocity with SPH of Incat1 section for NDH=0.86 and mass number=0.29

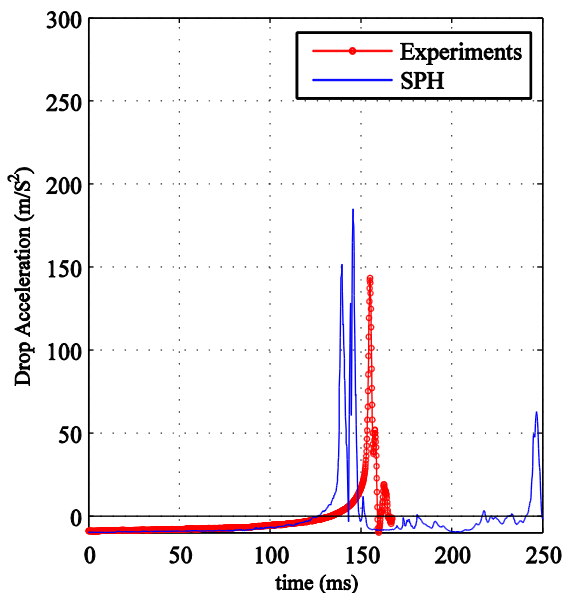


Figure 6.59: Drop acceleration with SPH of Incat1 section for NDH=0.77 and mass number=0.29

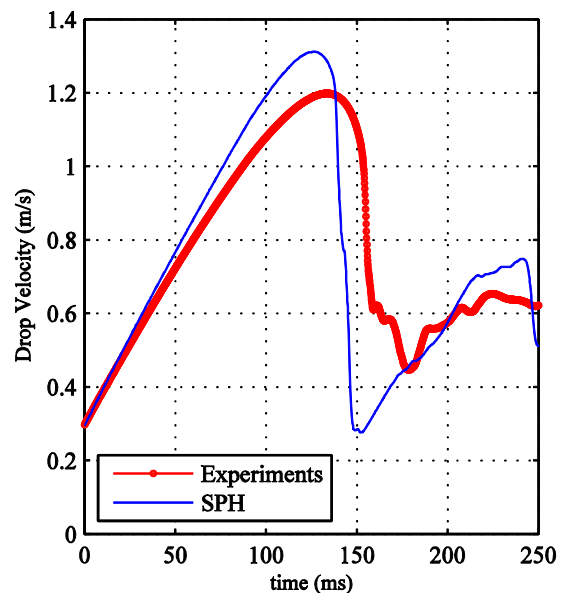


Figure 6.60: Drop velocity with SPH of Incat1 section for NDH=0.77 and mass number=0.29

Figure 6.61 shows the location of pressure transducers on the Incat1 geometry. P1 and P2 are on the centrebow, P3 is on top of the arch and P4 is located slightly outboard of the top of the archway. Figure 6.62 and Figure 6.63 show the SPH pressure results for P1 and P2 respectively compared to the experimental results. As seen in P1, before the wetdeck slamming, there is a 5 kPa pressure peak that has been captured by SPH but as it gets closer to archway slamming, the discrepancies emerge. In the experiments, the wetdeck slamming peak pressures at P1 and P2 are around 20 kPa whereas in the simulations, they are more than double this amount. In P3 and P4, which are on archtop and closely outboard of the archtop, the pressures are more than 68 kPa and 10 kPa respectively. For both these points, the SPH pressures are more than 100 kPa. The SPH peaks were also occurred earlier in time, for previously mentioned reasons.

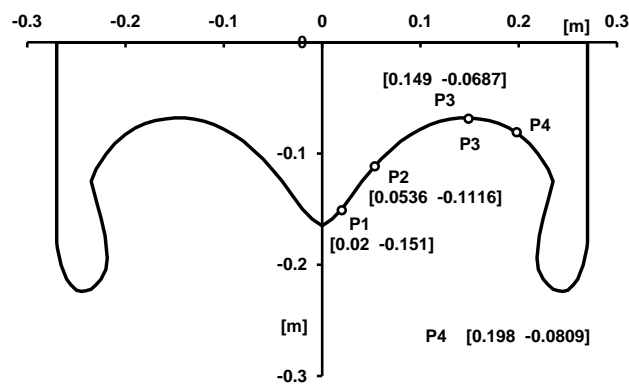


Figure 6.61: Incat1 drop section with pressure transducers location

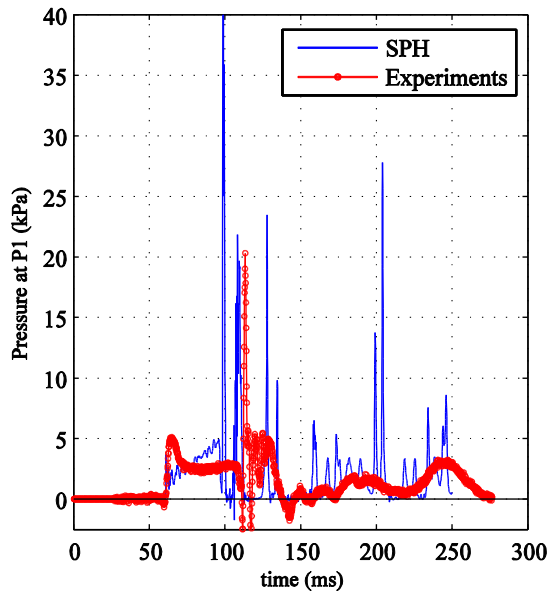


Figure 6.62: Pressure results at location P1 of the 25° wedge with side plates for NDH=0.86 and mass number=0.29

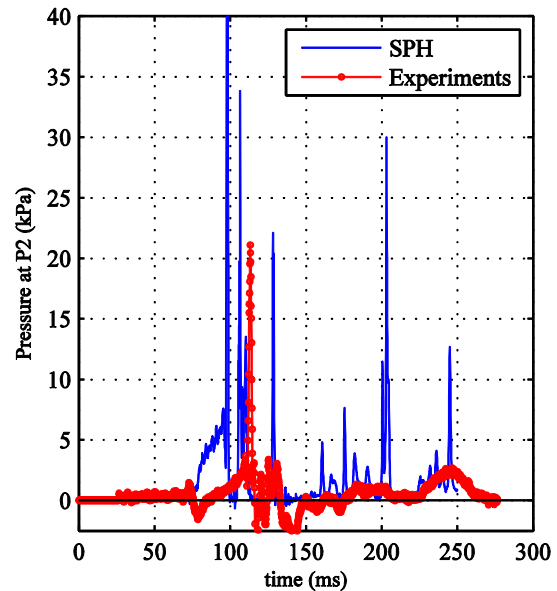


Figure 6.63: Pressure results at location P2 of the 25° wedge with side plates for NDH=0.86 and mass number=0.29

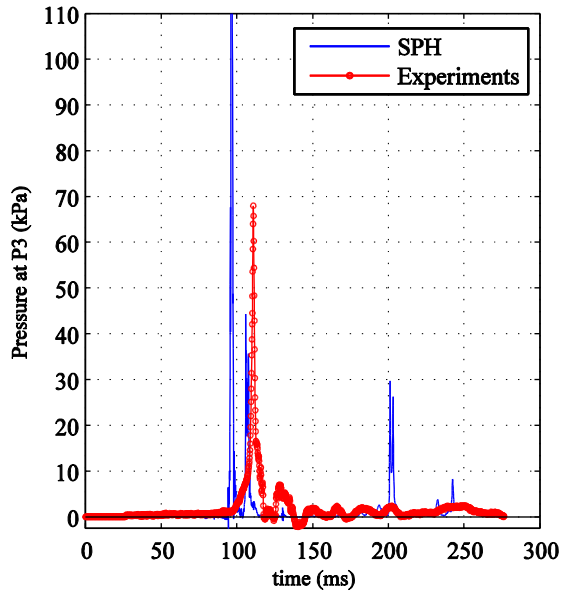


Figure 6.64: Pressure results at location P3 of the 25° wedge with side plates for NDH=0.86 and mass number=0.29

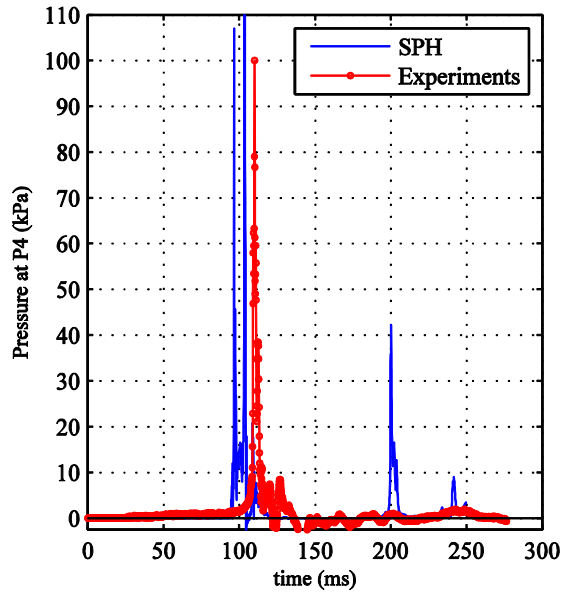


Figure 6.65: Pressure results at location P4 of the 25° wedge with side plates for NDH=0.86 and mass number=0.29

At this stage, from the 2-D SPH slamming simulation of 25° wedge with side plates and Incat1, it can be concluded that it is necessary to model air for the enclosed section drop simulation both for controlling the drop immersion velocity and also creating an air pocket under the archways at the point of wetdeck slamming. Including the effect of the air cushioning at the top of the archway would need a multi-phase solution to be developed. This is a non-trivial task, which would include significant development time since currently this SPH code is only single-phase fluid modelling. Such modelling has been done previously by Oger et. al. [157] for modelling free falling of a wedge to water surface. Modelling the 3-D effects are also important, as these effects were allowed in the experiments as the constrained water could escape from the wall clearance.

6.3.5. Effect of hull form on slamming of arched sections

Although differences were observed between the severity of 2-D SPH simulations and experiments in modelling enclosed geometries slamming, the SPH results may still be used for evaluating catamaran hull forms. In the experiments with NDH=0.86, the slamming acceleration peak for the wedge with side plates was around 35 m/s^2 and this value for the Incat1 section was significantly higher, around 148 m/s^2 . As also seen in Figure 6.66, in SPH results, the acceleration peak for the 25° wedge with side plates was around 170 m/s^2 and for Incat1 section this value was 275 m/s^2 , which is again higher than the wedge with side plates. The difference can be explained by the different submerged volume prior to slamming and the wetdeck dead rise angle. The 25° wedge with side plates has a significantly higher submerged volume prior to slamming compared to the Incat1 section; the drop momentum is absorbed by the hydrostatic forces, so less energy is left for slamming at the archtop. Also the wedge with side plates keeps its 25° deadrise angle until prior to slamming, whereas the deadrise angle in the Incat1 section decreases to zero in the archtop prior to wetdeck slamming. Lower deadrise angles lead

to more severe slamming. Comparing these two sections in slamming suggests that a larger centrebow volume and higher deadrise angle in the archtop is beneficial to avoid severe wetdeck slamming.

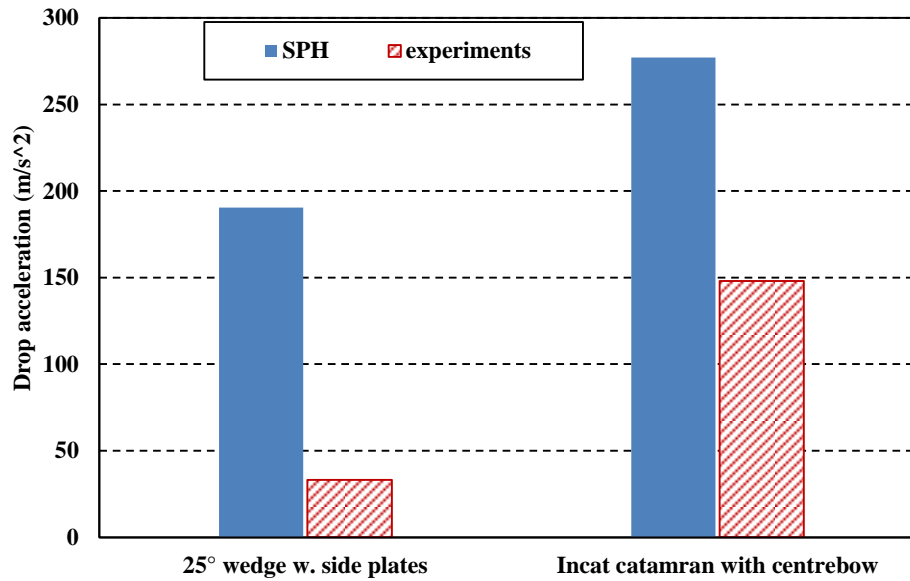


Figure 6.66: Drop acceleration of the 25° wedge with side plates and Incat1 for NDH=0.86 and mass number=0.29

Making this conclusion that to compare the impact of enclosed sections in water, even if air-entrapment is not accounted for, has to be treated very carefully as air-entrapment has such a large effect on the results. This method could be valid for sections that do not suffer from air-entrapment. Especially in full 3-D simulations, where there are more possibilities for pressure relief of the entrapped air this might be important without taking to account the effect of air inclusion.

6.4. Three-dimensional modelling of drop geometries

To achieve a three-dimensional simulation, the width of the domain should be increased to the width of the tank used by Whelan [33]. In the experiments, the wall clearance (the clearance between the tank wall and drop geometry wall) allows the entrapped air and pressurised water under the drop sections to escape like a planar jet and alleviate the high pressures. The depth of the model is 0.29 m and it is necessary in the SPH to model the tank slightly wider to stop interactions of the drop geometry with the tank walls. Effectively, the tank wall should be outside of the support domain of the drop geometry particles. As demonstrated in Figure 6.68, to model the planar jet of water in SPH, there should also be an additional wall clearance where fluid particles can escape. The tank walls are modelled with a periodic open boundary condition and the drop geometry and tank bottom are modelled with dynamic boundary particles. In open periodic boundary condition, the truncated support domain of the fluid particles will be virtually filled with the particles of opposite side tank wall.

As an example, for a particle spacing of $DP=0.004$ m, the support domain size will be $h = 1.1 \sqrt{DP_x^2 + DP_z^2 + DP_y^2} = 0.0076$; therefore, the wall clearance should be at least $3h = 0.0229$ m away to allow for at least one fluid particle escaping from the gap (one radius for geometry wall and one diameter for the fluid particle). This wall clearance is used for the following simulations; however, a full investigation into the effect of wall clearance on the drop dynamics is necessary in the future.

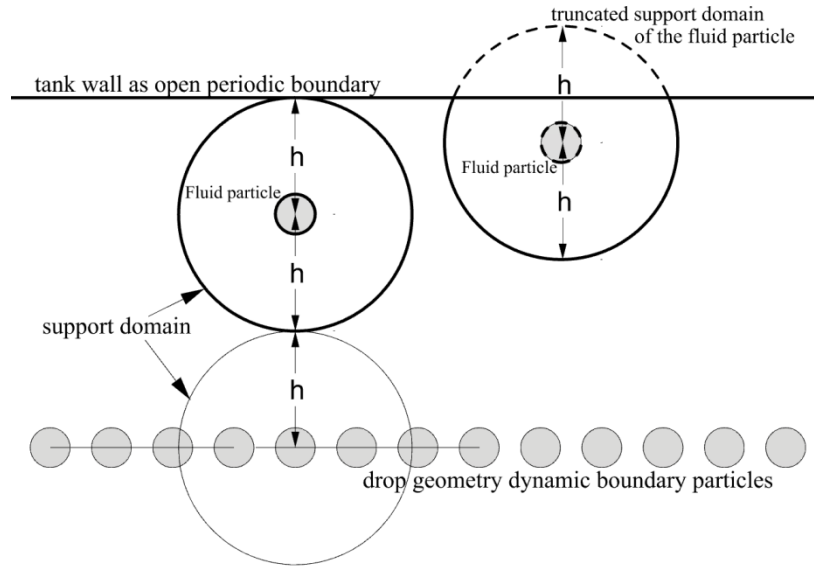


Figure 6.67: The clearance between the 3-D drop geometry particles and the tank open periodic boundary condition. The clearance should be sufficiently larger than the smoothing length (h) of the particles

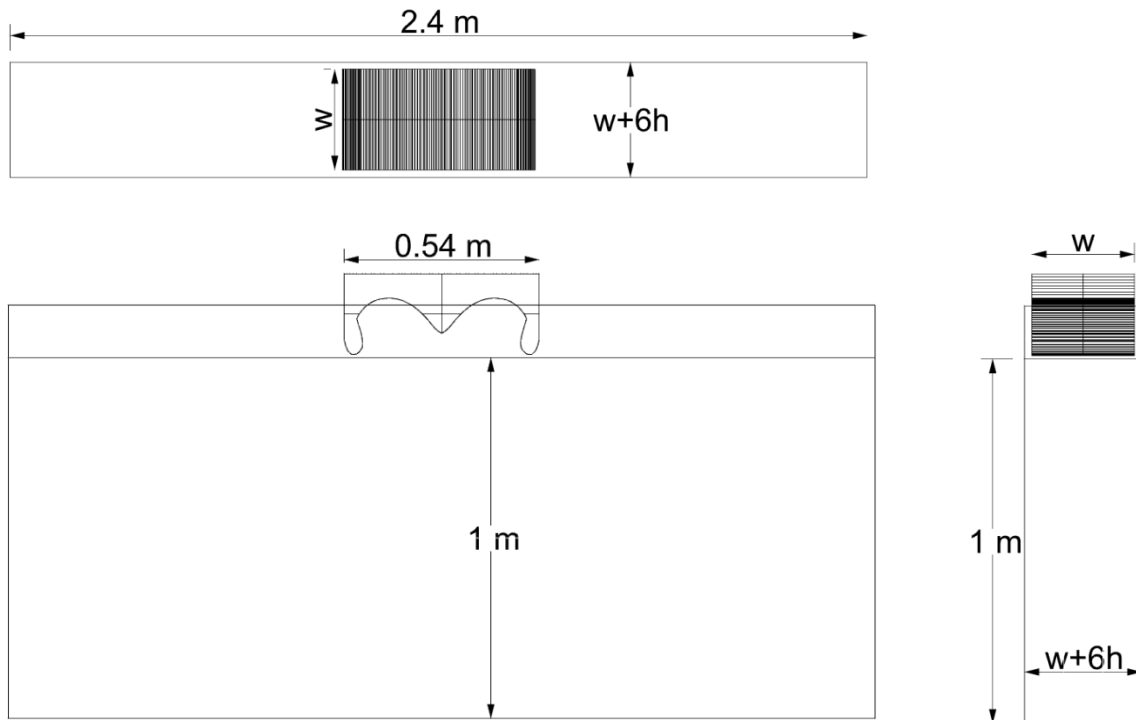


Figure 6.68: Three-dimensional geometry modelling in SPH for Incat1 drop geometry in a full size tank

Figure 6.69 shows the initial particle arrangement of the Incat1 geometry in the SPH with $DP=0.004$ m. In total more than 12 million particles were simulated and due to GPU memory limitations, it was not possible to model with higher particle density.

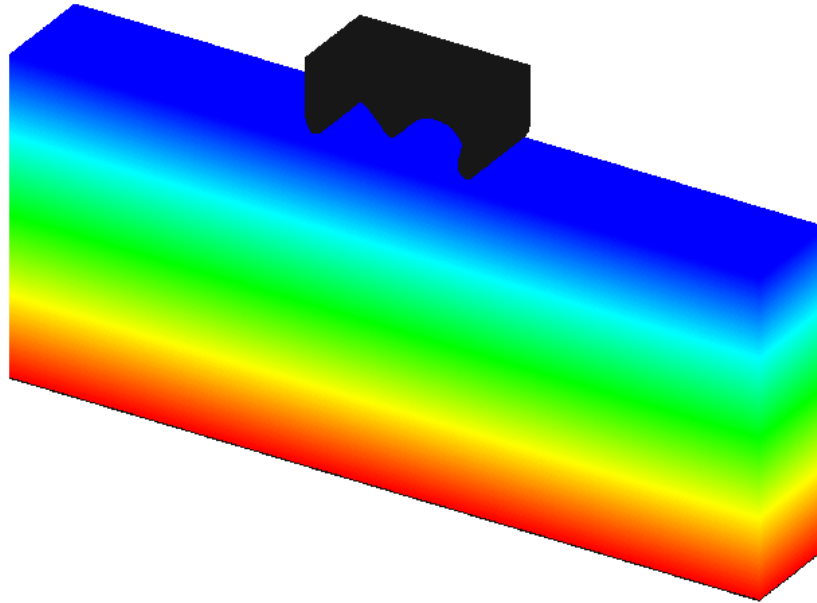


Figure 6.69: Three-dimensional geometry modelling in SPH for Incat1 drop geometry, the tank side walls are open periodic boundary condition, and the drop section and the tank bottom are dynamic boundary condition

Figure 6.70 shows Incat1 section, 105 ms after the drop with $NDH=0.86$ and mass number=0.29. As seen, similar to the experimental results of Whelan [33] there is a layer of water particles sliding up from the wall clearance.

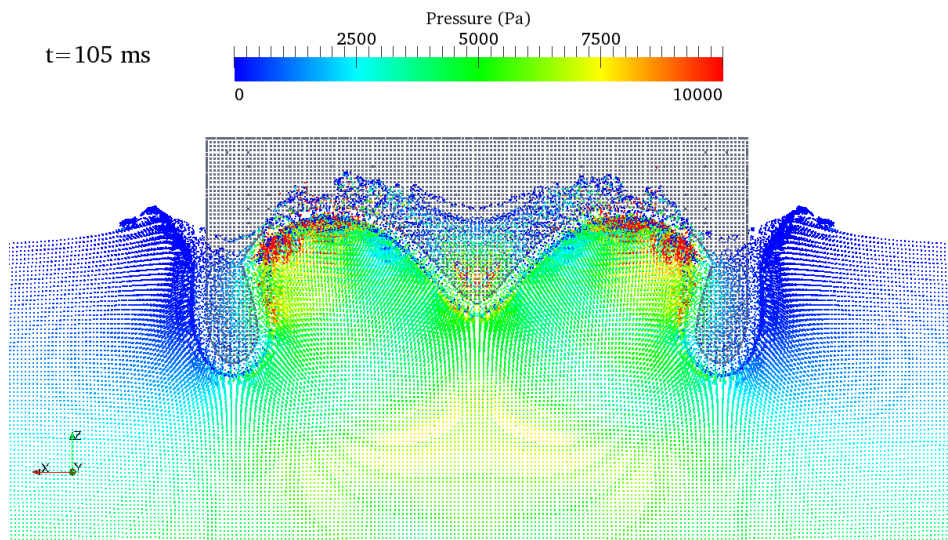


Figure 6.70: Three-dimensional SPH modelling of Incat1 drop geometry. Water particles can slide into the wall clearance and move upwards

Figure 6.71 shows a comparison of the drop acceleration modelled in both 2-D and 3-D for $DP=0.004$ m for $NDH=0.86$ and mass number=0.29. As seen, the 3-D acceleration peak value is lower than the 2-D value for the same particle density. Although higher resolution is necessary to achieve the correct dynamics of the drop test, these results clearly indicate the potential that 3-D modelling has to overcome the limitations of the 2-D modelling. However, the proposed future work of: conducting a separate 3-D particle independency study; investigating the effect of wall clearance and providing for an increase in the particle density, are all challenging assignments.

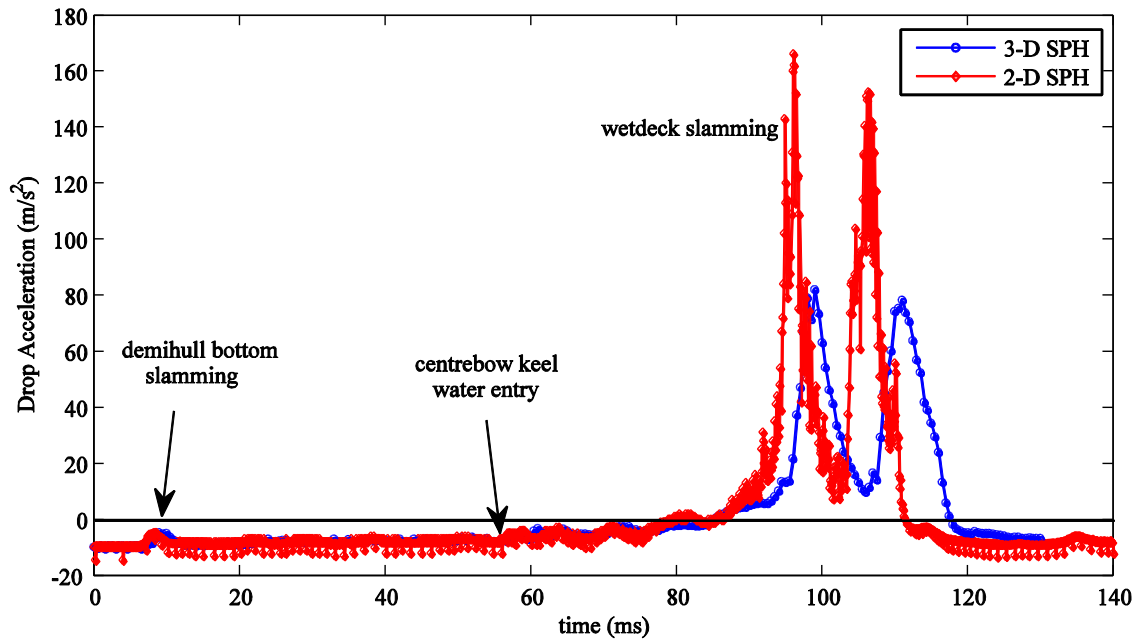


Figure 6.71: Comparison of the drop acceleration results of two and three-dimensional SPH modelling of INCAT catamaran with centrebow geometry (normalised drop height (NDH)=0.86 and mass number=0.29)

6.5. Summary

The SPH method was used to simulate the water entry of various drop geometries into the water. The simulation results of drop velocity, drop accelerations and section wall pressures were compared with the experiments of Whelan [33]. The effects of important simulation parameters, such as compressibility, artificial viscosity and spatial filtering were investigated. The 2-D simulations were proved to be independent of the particles resolution with the distance between particles of 0.00125 m being the most effective in accuracy and simulation time. The speed of sound coefficient was derived from the experiment's physics, not exceeding the compressibility criteria. Limitations were identified through the model setup such as pressure waves generated from the tank walls, propagating through the tank affecting drop kinematics. These effects were mitigated using periodic open boundary conditions in the tank side walls, using Shepard spatial filter every 5 time steps and refining the domain to a higher particle resolution. The results of simulations for the 25° wedge and 15° wedge were in good agreement with the experiments, independent of drop height and model mass (especially for 25° wedge).

The simulation of the enclosed sections, both the 25° wedge with side plates and catamaran with centrebow, followed the same general trend as the experiments. However, high drop accelerations (hence high pressures) were observed when compared to the experiments, representing unrealistically severe wetdeck slamming. This was due to the two-dimensional nature of the simulations where the pressurised fluid underneath the section could not escape, causing high deceleration of the section. Another limitation could be that the simulation was conducted using single-phase fluid and hence the air cushioning under the enclosed section prior to wetdeck slamming was not modelled. Having said that, the 2-D SPH simulation results could still somehow be used for comparing different geometries in slamming.

Three-dimensional modelling of an INCAT catamaran with centrebow was also performed with lower particle resolution. Visualisation of the results clearly showed the planar jet of water moving upward into the wall clearance. Comparing the results of 2-D and 3-D SPH simulation of INCAT geometry with the same particle resolution clearly showed the reduction in drop acceleration due to the 3-D effects.

Recommendations for future work include further 3-D simulation with a separate particle density study, examining the effect of wall clearance and simulating both air and water (multi-phase approach). Also testing new geometries rather than extended 2-D sections will help understanding of the behaviour of enclosed section in slamming. For example drop testing axially symmetric models, such models will allow air venting to be more controlled. Also drop testing the complete bow section of the catamaran into still water or at forward speed can help such enclosed sections to be understood.

7. Conclusions

As outlined in Chapter 1, the core research question of this work was “what are the effects of different hull shapes on the seakeeping and slamming behaviour of large high-speed catamarans at sea?” Various methodologies were undertaken which fall into three categories: 1) full-scale wave-piercing catamaran hull form exploratory study, 2) hydroelastic segmented model testing, and 3) numerical simulations with SPH. This chapter summarises the main work and findings of these studies, the implications of this research and recommendations for future research.

7.1. Results of the research methodologies

7.1.1. Exploratory study into existing large high-speed catamarans

An exploratory study identified the scope of large catamaran hull forms and the various approaches undertaken by designers in this field. Two main categories were compared: catamarans with high tunnel heights with the objective of reducing the incidence of slamming, and wave-piercing catamarans with a centrebow to reduce motions by increasing reserve buoyancy and counteract bow diving.

Whilst wave-piercing catamarans have some practical operational advantages over the high tunnel height catamarans, the question remains as to what tunnel height and centrebow shape is most effective in reducing slamming and promoting good seakeeping ability. To answer this question, hull form data from 15 INCAT Tasmania designed and constructed wave-piercing catamarans was examined. In particular, the tunnel heights, centrebow volumes, centrebow lengths, reserve buoyancies and unprotected areas of the centrebows were investigated. Whilst it was found that all of these parameters exhibited variation through the cohort of vessels, the following three had the most marked variations:

- The Centrebow Length Ratio (CLR) varies between 18% and 38% and generally decreases as the demihull length increases.
- The tunnel clearance to demihull length ratio (TCR) is between 2.8% and 5% and reduces as vessel size increases.
- The centrebow volume (strongly dependent on the centrebow length) to vessel displacement ratio varies between 2% to 5.2% and decreases for vessels of more than 80 m in length.

Since the variation in tunnel height and centrebow length were found to be most pronounced, and thus most likely to have an influence on the magnitude of motions and loads experienced by these vessels, these parameters were therefore chosen as the basis for the subsequent experimental investigation.

7.1.2. Hydroelastic model design, construction and experiments

To investigate the effect of hull design parameters on motion and loads in wave-piercing catamarans, a hydroelastic segmented model of a 112 m INCAT WPC was designed and constructed. Whilst a previous HSM model was used as a basis, the new design was a significant stepwise improvement with regards to its capabilities. In particular the following advances were achieved:

- The accurate measurement of centrebow slamming loads (both vertical and horizontal) and their location. This was accomplished by using two 6DOF force transducers attached to cross beams between the demihulls. The calibration of this new system showed highly accurate measurements for forces applied at different locations and angles.
- The ability to incorporate changes in hull parameters within the single model. For example: three centrebows with different lengths: 14.6%, 21% and 27.4% CLR and three centrebows and wet decks with varying heights: 2.2%, 2.8% and 4% TCR.
- The accurate measurement of vertical bending moments at all demihull cuts for all wave conditions by having integrated wet decks with their respective demihull segments.

The model was designed for a constricted weight budget and built using carbon-fibre sandwich panels with foam core. The rigidity of the demihull segments was increased using aluminium backbone beams. Elastic links were located between the model's three segments (for each demihull) to control the model's modal frequency and allow measurement of the vertical bending moments.

The wet modal whipping frequency of the model in zero speed and calm water was measured and found to be 14.7 Hz, equivalent to the required target value of 2.2 Hz for the full-scale vessel. This value was found to decrease in waves at speed to 12.82 Hz. Both the whipping frequency and damping factors replicate the full-scale behaviour of catamaran under slamming conditions of the strain gauge data from full-scale measurements.

Tests to determine the motions, slam loads and vertical bending moments were conducted for each of the three models with varying centrebow length. These tests were undertaken in regular waves of 60 mm height (2.68m full-scale) and 1.53 m/s speed (20 knots full-scale) in different wave frequencies. The following results and conclusion were determined:

- **Heave motions:** The length of centrebow was found to have a significant influence on the magnitude of the heave motion, in particular in the region of the resonant frequency. This resonant frequency remained constant for all the centrebows at approximately $\omega_e^* = 3.74$. As the centrebow length was increased the heave motions reduced. In the higher frequency region ($\omega_e^* \geq 3.74$) the heave response was similar for all three centrebows.
- **Pitch motions:** In contrast the centrebow length had a negligible effect on the pitch motions at the resonant frequency, but an increase in centrebow length increased the pitch motion for

wave frequencies with the most pronounced slamming ($3.7 \leq \omega_e^* \leq 5.5$). This clearly demonstrates the influence that slamming can have on the motions of a large catamaran, with the slam impacts increasing the motions due to the additional vertical force. The resonant peak frequency shifted slightly with a change in centrebow length, the shortest centrebow had the smallest resonant frequency, followed by the parent and long centrebow respectively. This showed the effect of the reduction in the model pitch stiffness in the short centrebow compared to the two other models.

- **Vertical slam force:** The slam events were characterised by a small peak in the vertical force as the keel of the centrebow first submerges into the water and then a rapid large peak as the archway impacts with the water surface and wetdeck slam occurs. This major wetdeck slamming peak has a duration of approximately 0.0075 s, and there are then two subsequent dynamic cycles in the vertical force due to added mass effects.

The length of centrebow had a very significant effect on the magnitude of the vertical slam forces, as the centrebow was increased the slam force also increased somewhat linearly. For example, for the peak slamming condition, the long centrebow had a slam force nearly double that of the short centrebow. This slam force difference was due to the increased volume of water being constrained in the archways as the centrebow length was increased. When a slam occurs some of the constrained water exits from the archway region via the top knuckles, but this volume of exiting water does not increase as the length of centrebow increases. For all centrebows the slam force showed a peak in the midrange frequency ($4 \leq \omega_e^* \leq 5$).

- **Horizontal slam force:** Measuring horizontal centrebow slam forces for the first time, the peak values were found to be higher than anticipated; between 24 to 70% of the corresponding vertical slam forces. The horizontal slam forces showed themselves as sharp aftward peaks in the time history during slamming. The longer centrebow experienced greater horizontal slam force compared to the shorter centrebows. An apparent linear relationship was observed between the horizontal forces magnitude and the tunnel blockage under the cross-deck. The more the tunnel is blocked by the centrebow, the greater the horizontal slam forces.
- **Slam resultant force location:** The location of the slam forces was found to vary significantly with the centrebow length and also the encountered wave frequency. The furthest forward slam location occurred in $\omega_e^* = 3.74$ where the motions were at maximum. The shortest centrebow had the most forward located slams due to constricting less water further aft. In fact for all three centrebow lengths, the slam occurred forward of the corresponding centrebow truncations.

- **Slam directions:** Having the synchronised body-fixed vertical and horizontal centrebow slam force, it enabled the slam direction variations between the three bows to be determined. The slam directions varied between 14 degrees and 35 degrees (from the vertical direction) with the long centrebow having the most vertical slam directions and the short centrebow experiencing the most inclined slams. The reason behind more inclined slams in shorter centrebow was the greater proportion of the horizontal force compared to its vertical slam forces. Therefore, parameters such as tunnel blockage which significantly affect the horizontal forces, can equally affect the slam direction.
- **Vertical Bending Moments (VBMs):** The vertical bending moment signals were characterised by large oscillations of whipping initiated by a slam, and then slowly dampening until the next slam. Similar full-scale behaviour has been seen in strain gauge data for catamarans under slamming conditions. The longer centrebow had significantly larger vertical bending moments compared to the other bows due to larger slam forces experienced by the model. The VBM magnitudes were found to be mainly dominated by the slam forces and their location.
- **Effects of centrebow on WPC motion and slamming:** It was clearly seen that the slams slow down the vessel relative bow motions. The slower motions then affect the slam mechanism for the subsequent encountered wave. This was best observed in the short centrebow with $\omega_e^* = 4.9$ where wetdeck slamming occurred for every second wave. The slam slowed down the vessel motion such that it did not meet the criteria for the next slam to occur; but the motion built up again for the subsequent slam. Having said that, it was observed that if the slam loads are very large, such as in the case of the long centrebow, the upward slam forces push the bow further upward, causing larger bow-up pitch angles. This again can excite the vessel to have another severe slam on the next encountered wave.
It was clearly evident that for the three centrebow lengths in the tested conditions, the shorter centrebow showed less slamming and less motion in the slamming conditions. However, in longer waves, the longer centrebows were more effective in reducing vessel motions.

7.1.3. Slam modelling with smoothed particle hydrodynamics (SPH)

The 2-D SPH simulation of water entry of vessel sections was successful, particularly for wedge sections. The open-source code Dual-SPHysics using GPU computations technology was used in order to increase the resolution and accelerate the simulations. Optimum simulation parameters, such as fluid compressibility and damping in the domain were found from the physics of the experiments and by performing parametric studies. Particle density independency study was also conducted resulting in particle spacing of 0.00125 m being the optimum. For the wedge sections, the drop accelerations, drop velocity, immersion and wall pressures were found to match well with the experimental results, independent of geometry mass and initial drop velocity. In the enclosed sections

such as a wedge with two vertical side plates and a realistic catamaran section, the 2-D results of drop kinematics showed much poorer agreement with the experimental results of Whelan [33]. The severity of wetdeck slamming was found to be larger than the experiments. The results however, could still be used in comparing the slam magnitudes of different drop geometries. The most likely reasons for higher accelerations in SPH were the inclusion of the air in the slamming mechanism and the 3-D effects that were not modelled. Since, developing a code to model multi-phase media is a non-trivial task; the inclusion of air is proposed as a subject for future work. Three-dimensional drop geometry of an INCAT catamaran section was simulated in SPH, modelling the 3-D effects and the planar water jet in the tank wall clearance. Comparison of the 2-D and 3-D results demonstrated the potential for more realistic slamming simulations with SPH.

7.2. Implication of the research

This work has clearly demonstrated that the new methodology used in the design and construction of this hydroelastic segmented model enables comparison of the behaviour of various hull forms in slamming conditions. The model-scale parametric study of hull forms in waves with reference to existing full-scale catamarans not only can help designers and classification societies to develop a deeper insight into wave-piercing catamarans but also can be used as a guide for improvements for other sea going vessels. The encouragement to extend this research to evaluate more hull form features especially the already built various wetdeck heights, reserve buoyancy and unprotected area of the centrebow are other implication of research.

The novel technique of accurately measuring slam characteristics using 6DOF force transducers, such as vertical and horizontal magnitudes, slam locations and slam directions has worked exceptionally well. It was shown that the horizontal slam loads can be significantly large, up to 70% of the vertical slam forces and this value can change depending on the wave condition and the geometry of centrebow. This significant force component has been almost neglected in previous designs. Measuring the slam force with good accuracy through model experiments such as these provides detailed loading information that can be used in Finite Element models during design process.

In addition to the innovations in the techniques, the experimental results are of significant value. From the experiments conducted on the three centrebow volumes in 20 knots speed and 2.69 m wave height, it can be concluded that in the slamming conditions, the shorter centrebows experience significantly less slam loads and less motions, whereas the longer centrebow was more effective in reducing motions in longer waves. The shorter centrebow increases the frequency gap between peak motions and peak loads in slamming conditions. Designers should note that a larger centrebow volume does not necessarily result in less motion in all conditions and it can have global structural consequences for the wave-piercing catamarans.

The use of computational fluid dynamics (CFD) in modelling sea going vessels is reaching a mature stage now. However, due to hull form complexity of certain vessels such as wave-piercing catamarans; these methods have to be constantly revised and improved. The use of SPH modelling for such vessels and inspecting its ability to capture slam dynamics can be interpreted in this scope. From the numerical simulations with SPH, it was shown that the 2-D simulations can replicate the slamming physics and therefore, behaviour of different hull forms in slamming can be evaluated using this method. However, for enclosed sections such as catamarans with centrebow, the three-dimensional effects and the entrapment of air and water during slamming needs to be simulated accurately.

7.3. Recommendations for future research

Successful evaluation of the effect of various centrebow lengths on slamming and seakeeping behaviour wave-piercing catamarans opens the way to a large field of possibilities in this area. Due to the complex geometry of these vessels and their non-linear motions with respect to environmental conditions; there are many opportunities not covered in this work which are recommended for future research:

- 1- Testing the various bow lengths in rougher environmental conditions e.g. higher speeds and larger waves. Testing for a single speed and wave height in headseas is acknowledged as being insufficient to make generalised conclusions about the effects of bow length.
- 2- As outlined in Chapter 2, the two chief design approaches for large catamarans were identified as being based on tunnel configuration differences. Testing the effect of changing the tunnel height for a catamaran with a centrebow needs to be completed in the future, especially since the model to enable this to be done has been designed and constructed as part of this project.
- 3- A range of other hull form features such as reserve buoyancy, unprotected area of the centrebow could be examined in the future. Testing a catamaran with a flat wetdeck also would give a good reference point for comparison of centrebow volumes. The effect of centrebow cross sections, particularly transverse location of the archtop point, can also be significant ; therefore designing and testing such sections is recommended
- 4- Based on the experimental results obtained for a change of centrebow length, it is recommended that a new centrebow be designed which will allow for the water that usually builds up in the archway, to be released easily thus reducing the slamming pressures. This will be achieved by truncating the centrebow close in the longitudinal direction to the aftmost jaw point.

- 5- To understand in some details the relationship between the slam forces and the resulting vertical bending moments, further work could be conducted to investigate the energy transfer in the vessel. To determine this, it is recommended to use more extensive instrumentation (such as accelerometers) on all the three model segments and use the structural dynamic equations for system identification.
- 6- The construction of centrebows with a transparent material to allow visual inspection and video recording of slam events, particularly in the archway region could provide designers with further valuable information on the mechanisms of slamming.
- 7- The SPH simulation of drop sections was performed successfully in 2-D with high spatial resolution employing GPU technology. However, limitations faced in 2-D single-phase modelling of enclosed vessel sections strongly suggests that air needs to be included in the simulations and that performing 3-D simulations could offer a satisfactory solution. This could be further extended to include full ship models in a variety of wave environment with SPH to benefit from its advantages to compare to other CFD models. The use of larger memories in GPU or the use of parallel GPU processing is recommended in order to increase the resolution of the domain and computational ability.

References:

- [1] G. Thomas, S. Winkler, M. Davis, D. Holloway, S. Matsubara, J. Lavroff, and B. French, "Slam events of high-speed catamarans in irregular waves," *Journal of Marine Science and Technology*, vol. 16, pp. 8-21, 2010.
- [2] G. Thomas, M. Davis, D. Holloway and T. Roberts, "Transient dynamic slam response of large high speed catamarans," in *Proceedings of FAST 2003, The 7th International Conference on Fast Sea Transportation*, Ischia (Italy), 2003, pp. B1-B8.
- [3] A. R. J. M. Lloyd, *Seakeeping: Ship Behaviour in Rough Weather*. Chichester: Ellis Horwood Limited, 1989.
- [4] R. Zhao and O. Faltinsen, "Water entry of two-dimensional bodies," *Journal of Fluid Mechanics*, vol. 246, pp. 593-612, 1993.
- [5] V. Bertram, *Practical Ship Hydrodynamics*: Butterworth Heinemann, 2000.
- [6] G. Thomas, M. Davis, D. Holloway, N. L. Watson, and T. Roberts, "Slamming response of a large high-speed wave-piercer catamaran," *Marine Technology*, vol. 40, pp. 126-140, 2003.
- [7] Newspaper Article;The China Post; Ferry accident could have been avoided: MOTC; T. C. P. n. staff; August 10, 2010
- [8] G. K. Kapsenberg, "Slamming of ships: where are we now?," *Philos Transact A Math Phys Eng Sci*, vol. 369, pp. 2892-919, Jul 28 2011.
- [9] S. E. Heggelund, T. Moan and S. Oma, "Determination of global design loads for large high-speed catamarans " *Proceedings of the Institution of Mechanical Engineers, Part M: Journal of Engineering for the Maritime Environment*, vol. 216, pp. 79-94, 2002.
- [10] G. Davidson, T. Roberts and G. Thomas, "Global and Slam Loads for a Large Wave piercing Catamaran Design," *Australian Journal of Mechanical Engineering*, vol. 3, pp. 155-164, 2006.
- [11] T. Roberts, N. L. Watson and M. Davis, "Evaluation of sea loads in high speed catamarans," presented at the Proceedings of Fast97 , 4th international conference on Fast Sea Transportation, Sydney, Australia, 1997.
- [12] M. R. Davis and J. R. Whelan, "Computation of wet deck bow slam loads for catamaran arched cross sections," *Ocean Engineering*, vol. 34, pp. 2265-2276, 2007.
- [13] G. Thomas, M. Davis, D. Holloway and T. Roberts, "The vibratory damping of large high-speed catamarans," *Marine Structures*, vol. 21, pp. 1-22, 2008.
- [14] W. Amin, M. R. Davis, G. A. Thomas and D. S. Holloway, "Slamming quasi-static Analysis of an 98m Incat high-speed wave piercing catamaran," presented at the International Conference for Innovation in High Speed Marine Vessels, Fremantle, Australia, 2009.
- [15] M. K. Ochi and L. E. Motter, "Prediction of slamming characteristics and hull responses for ship design," *SNAME Transactions*, 1973.
- [16] E. M. Haugen and O. M. Faltinsen, "Theoretical studies of wetdeck slamming and comparison with fullscale measurements," in *Proceedings FAST 99, 5th International Conference on Fast Sea Transportation*, , Seattle, 1999, pp. 577-591.
- [17] P. Steinmann, K. Fach and B. Menon, "Global and slamming sea loads acting on an 86m high speed catamaran ferry," in *5th International Conference in Fast Sea Transportation, FAST'99*, Seattle, Washington, USA, 1999.
- [18] M. R. Davis and D. S. Holloway, "The influence of hull form on the motions of high speed vessels in head seas," *Ocean Engineering*, vol. 30, pp. 2091-2115, 2003.
- [19] G. Thomas, M. Davis, J. Whelan, D. Holloway, and T. Roberts, "Slamming response of large high speed catamarans," presented at the 6th International conference on Fast Sea Transportation, Fast2001, Southampton, 2001.
- [20] W. Amin, " Non-linear unsteady wave loads on large high-speed wave piercing catamarans," PhD thesis, University of Tasmania, 2009.
- [21] W. Amin, M. R. Davis and G. A. Thomas, "Evaluation of finite element analysis as a tool to predict sea loads with the aid of trials data," presented at the 8th Symposium on High Speed Marine Vehicles (HSMV 2008), Naples, Italy, 21 - 23 May, 2008.

- [22] X.-j. Chen, Y.-s. Wu, W.-c. Cui and J. J. Jensen, "Review of hydroelasticity theories for global response of marine structures," *Ocean Engineering*, vol. 33, pp. 439-457, 2006.
- [23] O. M. Faltinsen, *Hydrodynamics of High-Speed Marine Vehicles*: Cambridge University Press, 2006.
- [24] O. M. Faltinsen, "Challenges in hydrodynamics of ships and ocean structures," *Brodogradnja*, vol. 58, 2007 2007.
- [25] M. K. Ochi and L. E. Motter, "A method to estimate slamming characteristics for ship design," *Marine Technology Society Journal*, vol. 8, 1971.
- [26] M. K. Ochi and L. E. Motter, "Prediction to extreme values of impact associated with ship slamming," *Journal of ship research*, vol. 13, 1969.
- [27] S. L. Chuang, "Slamming of rigid shaped bodies with various deadrise angles," David Taylor Model Basin, USA Report Number 0532346, 1966
- [28] R. Cointe, "Free-surface flows close to a surface-piercing body," *Mathematical Approaches in Hydrodynamics*, vol. SIAM, pp. 319-334, 1991.
- [29] S. G. Lewis, D. A. Hudson, S. R. Turnock and D. J. Taunton, "Impact of a free-falling wedge with water: synchronized visualization, pressure and acceleration measurements " *Fluid Dynamic Research*, vol. 42, 2010.
- [30] E. M. Haugen, O. M. Faltinsen and J. V. Aarsnes, "Application of theoretical and experimental studies of wave impact to wetdeck slamming," in *4th International Conference on Fast Sea Transportation*, Sydney, Australia, 1997.
- [31] J. Kvalsvold and O. M. Faltinsen, "Hydroelstic study of wetdeck slamming by Timoshenko beam model," in *The Ninth International Workshop on Water Waves and Floating Bodies*, Kuju, Oita, Japan, 1994, pp. 127-132, Research Institute for Applied Mechanics, Kyushu University, Kasuga, Fukuoka, Japan.
- [32] L. Zhu and D. Faulkner, "Design pressure for wetdeck structure of twin-hull ships," in *Third International Conference on Fast Sea transportation, FAST'95*, Lubeck-Travemunde, Germany, 1995, pp. 257-268, C. F. L. Kruppa, Schiffbautechnische Gessellschaft.
- [33] J. R. Whelan, "Wetdeck slamming of high-speed catamarans with a centrebow," PhD Thesis, University of Tasmania, 2004.
- [34] E. E. Zarnick, "Prediction of SWATH cross-structure slamming pressure," David Taylor Naval Ship Research and Development Centre, Bethesda, Maryland, USA1987
- [35] E. E. Zarnick and Y. S. Hong, "Relative bow motion and frequency of slamming of SWATH cross-structure," David W. Taylor Naval Ship Research and Development Centre, Bethesda, Maryland, USA1986
- [36] W.-M. Lin, S. Zhang, K. Weems, P. Jones, and M. Meinhold, "Numerical simulation and validation study of wetdeck slamming on high speed catamaran," presented at the 9th International Conference on Numerical Ship Hydrodynamics Ann Arbor, Michigan, USA, August 5-8, 2007.
- [37] W. M. Lin, M. Collete and D. Lavis, "Recent hydrodynamic tool development and validation for motions and slam loads on ocean-going high-speed vessels," presented at the 10th International Symposium on Practical Design of Ships and Other Floating Structures, 2007.
- [38] S. Zhu and T. Moan, "A comparative study of the influence of bow shape on hull girder vibrations through two backbone models," in *Hydroelasticity in Marine Technology*, Tokyo, Japan, 2012, K. Takagi and Y. Ogawa, The University of Tokyo.
- [39] J. Keuning, "The Nonlinear Behaviour of Fast Monohulls in Head Waves," PhD Thesis, Technische Universiteit Delft, 1994.
- [40] H. Kobayakawa, H. Kusumoto, T. Nagashima and I. Neki, "Hydroelastic response Analysis using unsteady time domain analysis of ship motions," in *Hydroelasticity in Marine Technology*, Tokyo, Japan, 2012, K. Takagi and Y. Ogawa, The University of Tokyo.
- [41] ISSC, "Dynamic Response," 16th International Ship and Offshore Structures Congress, Southampton, UK20-25 August 2006
- [42] J. Aarsnes, "Experimental techniques for loacal and global hydroelastic effect of ships," presented at the Seminar on Hydroelasticity in Marin Technology, Torendheim, Norway, 1996.

- [43] K. Iijima, O. A. Hermundstad, S. Zhub and T. Moan, "Symmetric and antisymmetric vibrations of a hydroelastically scaled model," in *5th International Conference on Hydroelasticity in Marine Technology*, Southampton, UK, 2009, Washington, DC, National Academic Press.
- [44] D. Dessi, "experimental analysis of the wave-induced response of a fast monohull via a segmented hull model," 2003.
- [45] D. Dessi, "Experimental identification of wet bending modes with segmented model tests," in *3rd International Conference of Fast Sea Transportation, FAST'95*, Lubeck-Travemunde, Germany, 1995, C. F. L. Kruppa, Schiffbautechnische Gesellschaft.
- [46] D. Dessi and D. D'Orazio, "Modal parameters of ship global modes: model-scale and full-scale estimations," in *Hydroelasticity in Marine Technology*, Tokyo, Japan, 2012, K. Takagi and Y. Ogawa, The University of Tokyo.
- [47] G. K. Kapsenberg and S. Brizzolara, "Hydro-elastic effects of bow flare slamming on fast monohull," presented at the 5th International Conference on Fast Sea Transportation, FAST'99, Seattle, Washington, USA, August 31- September 2 1999.
- [48] O. A. Hermundstad, J. V. Aarsnes and T. Moan, "Hydroelastic analysis of a flexible catamaran and comparison with experiments," presented at the Third International Conference of Fast Sea Transportation, FAST'95, Lübeck-Travemünde, Germany, September 25-27, 1995.
- [49] G. Ge, "Global hydroelastic response of catamarans due to wetdeck slamming," PhD Thesis, Department of Marine Technology, NTNU, Trondheim, Norway, 2002.
- [50] J. Lavroff, "The slamming and whipping vibratory response of a hydroelastic segmented catamaran model," PhD Thesis, University of Tasmania, Hobart, 2009.
- [51] S. Matsubara, "Ship motions and wave induced loads on high speed catamarans," PhD thesis, Australian Maritime College, University of Tasmania, Launceston, 2011.
- [52] G. Thomas, S. Matsubara, M. Davis, B. French, J. Lavroff, and W. Amin, "Lessons Learnt through design, construction and testing of hydroelastic model for determining motions, loads and slamming behaviour in severe sea states," presented at the Hydroelasticity in Marine Technology, Tokyo, Japan, 19-21 September, 2012.
- [53] V. Karman, "The impact on seaplane floats during landing," National Advisory Committee for Aeronautics, Washington 1929
- [54] H. Wagner, "The phenomena of impact and planning on water," *National Advisory Committee for Aeronautics, Translation 1366, Washington, D.C. ZAMM - Journal of Applied Mathematics and Mechanics* vol. 12, pp. 193-215, 1932.
- [55] R. L. Bisplinghoff and C. S. Doherty, "Some studies of the impact of vee wedges on a water surface," *Journal of the Franklin Institute*, vol. 253, pp. 547-561, 1952.
- [56] O. F. Hughes, "Solution of the wedge entry problem by numerical conformal mapping," *Journal of Fluid Mechanics*, vol. 56, pp. 173-192, 1972.
- [57] O. F. Hughes, "Some characteristics of the free surface in the wedge entry problem," *Journal of Engineering Mathematics*, vol. 7, 1973
- [58] O. F. Hughes, "Wedge Penetration of a free surface," in *Fourth Australian Conference on Hydrolics and Fluid Mechanics*, Monash University, Melbourne, Australia, 1971, pp. 307-320.
- [59] J. Kvalsvold and O. M. Faltinsen, "Hydroelastic modeling of wet deck slamming on multihull vessels," *journal of ship research*, vol. 39, pp. 225-239, 1995.
- [60] J. Kvalsvold and O. Faltinsen, "Hydroelastic modelling of slamming against the wetdeck of a catamaran," in *2nd International Conference of Fast Sea Transportation, FAST'93*, 1993, pp. 681-967.
- [61] O. M. Faltinsen, J. Kvalsvold and J. V. Aarsnes, "Wave impact on a horizontal elastic plate," *Journal of Marine Science and Technology*, vol. 2, pp. 87-100, 1997.
- [62] A. Korobkin, "Elastic response of catamaran wetdeck to liquid impact," *Ocean Engineering*, vol. 25, 1998.
- [63] J. Kvalsvold, O. Faltinsen and J. Aarsnes, "Effect of structural elasticity on slamming against wetdecks of multihull vessels," *Proc. PRADS'95, Korea, The Society of Naval Architects of Korea*, pp. 1.684-1699, 1995.

- [64] Z. N. Dobrovol'skaya, "On some problems of similarity flow of fluid with a free surface," *Journal of Fluid Mechanics*, vol. 36, pp. 805-829, 1969.
- [65] G. D. Xu, W. Y. Duan and G. X. Wu, "Numerical simulation of oblique water entry of an asymmetrical wedge," *Ocean Engineering*, vol. 35, pp. 1597-1603, 2008.
- [66] G. Xu, W. Duan and G. Wu, "Simulation of water entry of a wedge through free fall in three degrees of freedom," *Proceedings of the Royal Society A: Mathematical, Physical and Engineering Science*, vol. 466, pp. 2219-2239, 2010.
- [67] M. Arai, L.-Y. Cheng and Y. Inoue, "A computing method for analysis of water impact of arbitrary shaped bodies," *Journal of the Society of Naval Architects of Japan*, vol. 176, pp. 233-240, 1994.
- [68] O. M. Faltinsen, "Hydroelastic slamming," *Journal of Marine Science and Technology*, vol. 5, pp. 49-65, 2000.
- [69] R. Zhao and A. J. V, "Numerical and experimental studies of nonlinear motions and loads of a high speed catamaran," presented at the Third International Conference of Fast Sea Transportation, FAST'95,, 1995.
- [70] S. G. Lewis, D. A. Hudson, S. R. Turnock and D. J. Taunton, "Impact of a free-falling wedge with water: synchronized visualization, pressure and acceleration measurements," *Fluid Dynamics Research*, vol. 42, p. 035509, 2010.
- [71] D. A. Hudson, S. R. Turnock and S. G. Lewis, "Predicting motions of high-speed rigid inflatable boats: Improved wedge impact prediction," presented at the Ninth International Conference on Fast Sea Transportation, FAST2007, , Shanghai, China, September, 2007.
- [72] E.-M. Yettou, A. Desrochers and Y. Champoux, "Experimental study on the water impact of a symmetrical wedge," *Fluid Dynamics Research*, vol. 38, pp. 47-66, 2006.
- [73] G. R. Liu and M. B. Liu, *Smoothed Particle Hydrodynamics, a meshfree particle method*, First ed. vol. 1. Singapore: World Scientific Publishing Co. Pte. Ltd., 2003.
- [74] J. J. Monaghan, "An introduction to SPH," *Computer Physics Communications*, vol. 48, pp. 89-96, 1988.
- [75] J. J. Monaghan, "Simulating free surface flows with SPH," *Journal of Computational Physics*, vol. 110, pp. 399-406, 1994.
- [76] J. J. Monaghan, "Smoothed particle hydrodynamics," *Annual Review of Astronomy and Astrophysics*, vol. 30, pp. 543-574, 1992.
- [77] A. C. Crespo, J. M. Dominguez, A. Barreiro, M. Gómez-Gesteira, and B. D. Rogers, "GPUs, a New Tool of Acceleration in CFD: Efficiency and Reliability on Smoothed Particle Hydrodynamics Methods," *PLoS ONE*, vol. 6, p. e20685, 2011.
- [78] J. M. Domínguez, A. J. C. Crespo and M. Gómez-Gesteira, "Optimization strategies for CPU and GPU implementations of a smoothed particle hydrodynamics method," *Computer Physics Communications*.
- [79] J. M. Domínguez, A. J. C. Crespo, A. Barreiro and M. Gómez-Gesteira, "Implementación Multi-GPU del método Smoothed Particle Hydrodynamics."
- [80] T. Harada, S. Koshizuka and Y. Kawaguchi, "Smoothed Particle Hydrodynamics on GPUs," in *Computer Graphics International Conference*, Petropolis, Brazil, 2007, pp. 63-70.
- [81] A. Herault, G. Billotta and R. Dalrymple, "SPH on GPU with CUDA," *Journal of Hydraulic Research*, vol. 48, pp. 74-79, 2010.
- [82] G. Oger, M. Doring, B. Alessandrini and P. Ferrant, "Two-dimensional SPH simulations of wedge water entries," *Journal of Computational Physics*, vol. 213, pp. 803-822, 2006.
- [83] S. Brizzolara, N. Couty, O. Hermundstad, A. Ioan, T. Kukkanen, M. Viviani, and P. Temarel, "Comparison of experimental and numerical loads on an impacting bow section," *Ships and Offshore Structures*, vol. 3, pp. 305 - 324, 2008.
- [84] M. Viviani, S. Brizzolara and L. Savio, "Evaluation of slamming loads using smoothed particle hydrodynamics and Reynolds-averaged Navier–Stokes methods," *Proceedings of the Institution of Mechanical Engineers, Part M: Journal of Engineering for the Maritime Environment*, vol. 223, pp. 17-32, 2009.
- [85] D. J. Veen and T. P. Goulay, "An investigation of slam loads in two dimensions using smoothed particle hydrodynamics," in *10th international Conference on Fast Sea Transportation, Fast 2009*, Athens, Greece, 2009.

- [86] D. Veen and T. Gourlay, "A combined strip theory and Smoothed Particle Hydrodynamics approach for estimating slamming loads on a ship in head seas," *Ocean Engineering*, vol. 43, pp. 64-71, 2012.
- [87] M. Doring, G. Oger, B. Alessandrini and P. Ferrant, "SPH Simulations of Floating Bodies in Waves," in *ASME 2004 23rd International Conference on Offshore Mechanics and Arctic Engineering (OMAE2004)*, Vancouver, British Columbia, Canada 2004, pp. 741-747, ASME.
- [88] M. Gomez-Gesteira, B. Rogers, A. Crespo, R. Dalrymple, M. Narayanaswamy, and J. Dominguez, "SPHysics-development of a free-surface fluid solver-Part 1: Theory and Formulations," *Computers & Geosciences*, 2012.
- [89] M. Gomez-Gesteira, A. Crespo, B. Rogers, R. Dalrymple, J. Dominguez, and A. Barreiro, "SPHysics-development of a free-surface fluid solver-Part 2: Efficiency and test cases," *Computers & Geosciences*, 2012.
- [90] ANSYS AQWA User's Manual [Online]. Available: http://www1.ansys.com/customer/content/documentation/130/wb_aqwa.pdf
- [91] R. Marcer, C. Berhault, C. d. Jouette, N. Moiroud, and L. Shen, "Validation of CFD codes for slamming," presented at the V European Conference on Computational Fluid Dynamics, Lisbon, Portugal, 14-17 Jun 2010, 2010.
- [92] G. K. Kapsenberg and E. T. Thornhill, "A Practical Approach to Ship Slamming in Waves " presented at the 28th Symposium on Naval Hydrodynamics Pasadena, California, USA, 12-17 September, 2010.
- [93] P. C. Sames, G. K. Kapsenberg and P. Corrigan, "Prediction of bow door loads in extreme wave conditions," presented at the RINA Conference 'Design and Operation for Abnormal Condition II, London, 2001.
- [94] S. M. Mousaviraad, "CFD prediction of ship response to extreme winds and/or waves," PhD, University of Iowa, University of Iowa, Iowa, 2010.
- [95] M. D. Leffe, P.-M. Guicher, J. Candelier, D. LeTouze, G. Oger, and N. Grenier, "SPH for naval applications," in *2nd International Conference on Violent Flows*, Nantes, France, 2012, D. L. Touzé, *et al.*, Publibook.
- [96] [www.Austal.com](http://www.austal.com). (2012). <http://www.austal.com/Resources/PromotionSlides/4f0f31b7-eeed-4a8c-9e1a-bd11db612022/windfarm-brochure-web.pdf>.
- [97] Personal Communication, G. Davidson, Revolution Design Pty Ltd., 2012
- [98] L. R. o. Shipping. "Rules & Regulations for the Classification of Special Service Craft". 1999.
- [99] J. Lavroff, M. Davis, D. Holloway and G. Thomas, "The whipping vibratory response of a hydroelastic segmented catamaran model," presented at the 9th International Conference on Fast Sea Transportation, FAST2007, Shanghai China, 23-27 September, 2007.
- [100] J. Lavroff, M. R. Davis, D. Holloway and G. Thomas, "The vibratory response of a hydroelastic segmented catamaran model," presented at the FAST 2007, Shanghai, China, 2007.
- [101] S. Matsubara, G. Thomas, M. Davis, D. Holloway, and T. Roberts, "Influence of Centrebow on Motions and Loads of High-Speed Catamarans," presented at the 11th International Conference on Fast Sea Transportation (FAST 2011), Honolulu, Hawaii, 26-29 September 2011.
- [102] B. French, "Slamming of large high-speed catamarans in irregular waves," PhD thesis, Australian Maritime College, University of Tasmania, 2011.
- [103] S. Winkler, "Classification of high-speed catamaran slam events in irregular waves," Diploma of engineering, Australian Maritime college, University of Tasmania, Launceston, 2009.
- [104] S. Matsubara, G. Thomas, M. R. Davis, D. Holloway, and T. Roberts, "Influence of centrebow on motions and loads of high speed catamarans," presented at the 11th International Conference on Fast Sea Transportation, FAST 2011, Honolulu, Hawaii, USA, September, 2011.
- [105] O. A. Hermundstad and T. Moan, "Numerical and experimental analysis of bow flare slamming on a Ro-Ro vessel in regular oblique waves," *Journal of Marine Science and Technology*, vol. 10, pp. 105-122, 2005.

- [106] A. Bereznitski, "Slamming: The role of hydroelasticity," *International Shipbuilding Progress*, vol. 48, pp. 333-351, 2001.
- [107] N. Instruments, "Strain Gauge Measurement – A Tutorial", 1998, Available: <http://www.ni.com/white-paper/3642/en>
- [108] J. D. Fenton and W. D. McKee, "On calculating the lengths of water waves," *Coastal Engineering*, vol. 14, pp. 499-513, 1990.
- [109] J. Fenton, "Nonlinear wave theories," *The Sea*, vol. 9, pp. 3-25, 1990.
- [110] S. S. Rao, *Mechanical Vibrations*, 5th ed.: Pearson Education India, 2011.
- [111] Mathworks, 2010b MATLAB Help Documents, "Butterworth Filter" in Signal Processing Toolbox/ Functions/ Digital filters/ IIR Digital Filter Design/ Butter.
- [112] Alan V. Oppenheim and R. W. Schaffer, *Discrete-time signal processing*: Prentice-Hall, 2013.
- [113] NIST/SEMATECH. (2012). *e-Handbook of Statistical Methods*. Available: <http://www.itl.nist.gov/div898/handbook/>
- [114] J. Colwell, I. Datta and R. Rogers, "Head seas slamming tests on a fast surface ship hull form series," presented at the International Conference on Seakeeping and Weather, London, UK, 28 Feb & 1 March, 1995.
- [115] G. Thomas, "Wave slam response of large high speed catamarans," PhD Thesis, University of Tasmania, 2003.
- [116] A. Justel, D. Peña and R. Zamar, "A multivariate Kolmogorov-Smirnov test of goodness of fit," *Statistics & Probability Letters*, vol. 35, pp. 251-259, 1997.
- [117] D. N. Veritas, *Environmental conditions and environmental loads* vol. Recommended Practice, DNV-RP-C205: Norske Veritas, 2010.
- [118] J. A. Lund, "Water craft," United states Patent, Rhoda Stolk and Stolkraft Pty Ltd., Australia, Patent number: 5140930, August 25, 1992.
- [119] Personal Communication, S. Friezer, INCAT catamarans designer, 2013
- [120] S. Shao, "Incompressible SPH simulation of water entry of a free-falling object," *International Journal for Numerical Methods in Fluids*, vol. 59, pp. 91-115, 2009.
- [121] D. Veen and T. Gourlay, "SPH study of high speed ship slamming."
- [122] T. Belytschko, Y. Krongauz, D. Organ, M. Fleming, and P. Krysl, "Meshless methods: An overview and recent developments," *Computer Methods in Applied Mechanics and Engineering*, vol. 139, pp. 3-47, 1996.
- [123] R. A. Dalrymple and B. D. Rogers, "Numerical modeling of water waves with the SPH method," *Coastal Engineering*, vol. 53, pp. 141-147, 2006.
- [124] M. Gomez-Gesteira and R. A. Dalrymple, "Using a three-dimensional smoothed particle hydrodynamics method for wave impact on a tall structure," *Journal of Waterway, Port, Coastal, and Ocean Engineering*, vol. 130, pp. 63-69, 2004.
- [125] M. Gómez-Gesteira, D. Cerqueiro, C. Crespo and R. Dalrymple, "Green water overtopping analyzed with a SPH model," *Ocean Engineering*, vol. 32, pp. 223-238, 2005.
- [126] A. Crespo, M. Gomez-Gesteira and R. A. Dalrymple, "Modeling dam break behavior over a wet bed by a SPH technique," *Journal of Waterway, Port, Coastal, and Ocean Engineering*, vol. 134, pp. 313-320, 2008.
- [127] A. Souto-Iglesias, R. Zamora-Rodríguez, D. Fernández-Gutiérrez and L. Pérez-Rojas, "Analysis of the wave system of a catamaran for CFD validation," *Experiments in Fluids*, vol. 42, pp. 321-332, 2006.
- [128] H. Wendland, "Piecewise polynomial, positive definite and compactly supported radial functions of minimal degree," *Advances in Computational Mathematics*, vol. 4, pp. 389-396, 1995/12/01 1995.
- [129] M. Gomez-Gesteira, B. D. Rogers, R. A. Dalrymple and A. J. C. Crespo, "State-of-the-art of classical SPH for free-surface flows," *Journal of Hydraulic Research*, vol. 48, pp. 6-27, 2010/01/01 2010.
- [130] T. Capone, A. Panizzo, C. Cecioni and R. A. Dalrymple, "Accuracy and stability of numerical schemes in SPH," presented at the Second International Workshop- SPHERIC – Smoothed Particle Hydrodynamics European Research Interest Community, Escuela Técnica Superior de Ingenieros Navales, Universidad Politécnica de Madrid. Madrid, May 23rd-25th, 2007.

- [131] J. Bonet and T.-S. Lok, "Variational and momentum preservation aspects of smooth particle hydrodynamic formulations," *Computer Methods in Applied Mechanics and Engineering*, vol. 180, pp. 97-115, 1999.
- [132] W. K. Liu, S. F. Li and T. Belytschko, "Moving least squares Galerkin methods (I) methodology and convergence," *Computer Methods in Applied Mechanics and Engineering*, vol. 143, pp. 113-154, 1997.
- [133] A. Colagrossi and M. Landrini, "Numerical simulation of interfacial flows by smoothed particle hydrodynamics," *Journal of Computational Physics*, vol. 191, pp. 448-475, 2003.
- [134] T. Belytschko, Y. Krongauz, J. Dolbow and C. Gerlach, "On the completeness of meshfree particle methods," *International Journal for Numerical Methods in Engineering*, vol. 43, pp. 785-819, 1998.
- [135] J. J. Monaghan, "Smoothed particle hydrodynamics," *Reports on progress in physics*, vol. 68, p. 1703, 2005.
- [136] J. J. Monaghan and R. A. Gingold, "Shock simulation by the particle method SPH," *Journal of Computational Physics*, vol. 52, pp. 374-389, 1983.
- [137] H. Gotoh, S. Shao and T. Memita, "SPH-LES model for numerical investigation of wave interaction with partially immersed breakwater," *Coastal Engineering Journal*, vol. 46, pp. 39-63, 2004.
- [138] E. Y.M. Lo and S. Shao, "Simulation of near-shore solitary wave mechanics by an incompressible SPH method," *Applied Ocean Research*, vol. 24, pp. 275-286, 2002.
- [139] J. J. Monaghan, "On the Problem of Penetration in Particle Methods," 1-15, vol. 82, 1989.
- [140] Y. H. Li, "Equation of state of water and sea water," *Journal of Geophysical Research*, vol. 72, pp. 2665-2678, 1967.
- [141] M. G. Gesteria, B. D. Rogers, R. A. Dalrymple, A. J. C. Crespo, and M. Narayanaswamy, "User guid for the SPHysics code," 2010. <http://www.sphysics.org>
- [142] B. J. Leimkuhler, S. Reich and R. D. Skeel, "Integration methods for molecular dynamics," in *Mathematical Approaches to biomolecular structure and dynamics*, ed: Springer, 1996, pp. 161-185.
- [143] L. Verlet, "Computer "Experiments" on Classical Fluids. I. Thermodynamical Properties of Lennard-Jones Molecules," *Physical Review*, vol. 159, pp. 98-103, 1967.
- [144] R. Courant, K. Friedrichs and H. Lewy, "On the partial difference equations of mathematical physics," *IBM journal of Research and Development*, vol. 11, pp. 215-234, 1967.
- [145] J. J. Monaghan, "On the problem of penetration in particle methods," *Journal of Computational Physics*, vol. 82, pp. 1-15, 1989.
- [146] J. J. Monaghan and A. Kos, "Solitary waves on a Cretan beach," *Journal of Waterway, Port, Coastal and Ocean Engineering*, vol. 125, pp. 145-154, 1999.
- [147] J. Monaghan, A. Kos and N. Issa, "Fluid motion generated by impact," *Journal of Waterway, Port, Coastal, and Ocean Engineering*, vol. 129, pp. 250-259, 2003.
- [148] M. Liu, G. Liu and K. Lam, "Investigations into water mitigation using a meshless particle method," *Shock Waves*, vol. 12, pp. 181-195, 2002.
- [149] S. Marrone, M. Antuono, A. Colagrossi, G. Colicchio, and G. Graziani, "Enhanced boundary treatment in 2D smoothed particle hydrodynamics models," in *Proc. XIX Congress AIMETA*, 2009.
- [150] S. Marrone, "Enhanced SPH modeling of free-surface flows with large deformations," PhD Thesis, Università di ` Roma "Sapienza", 2012.
- [151] I. Federico, S. Marrone, A. Colagrossi, F. Aristodemo, and P. Veltri, "Simulation of hydraulic jump through sph model," in *IDRA XXXII Italian Conference of Hydraulics and Hydraulic Construction*, 2010.
- [152] A. Crespo, M. Gómez-Gesteira and R. A. Dalrymple, "Boundary conditions generated by dynamic particles in SPH methods," *CMC-TECH SCIENCE PRESS*, vol. 5, p. 173, 2007.
- [153] A. J. C. Crespo, J. M. Dominguez, M. Gomez-Gesteira, A. Barreiro, and B. D. rogers, "User Guide for Dual-SPHysics," 2011
- [154] J. M. Domínguez, A. J. C. Crespo and M. Gómez-Gesteira, "Optimization strategies for CPU and GPU implementations of a smoothed particle hydrodynamics method," *Computer Physics Communications*, vol. 184, pp. 617-627, 2013.

- [155] A. J. C. Crespo, J. M. Dominguez, M. Gomez-Gesteira, A. Barreiro, and B. D. rogers, "User Guide for Dual-SPHysics, V02," 2012
- [156] R. A. Dalrymple and O. Knio, "SPH modelling of water waves," in *Coastal dynamics '01*, Lund, Sweden, 2001, pp. 779-787, H. Hanson and M. Larson, American Society of Civil Engineers.
- [157] G. Oger, P. Ferrant and B. Alessandrini, "Free Surface Impact in a Biphase SPH Simulation."

Appendices

Appendix 1: Specifications of ATI MINI45 Force transducer

Product Advantages

One of the Smallest 6-axis Sensors in the World:

The Mini45 has a compact, low-profile design with a through-hole to allow passage of linkages or cables.

Extremely High Strength:

- EDM wire-cut from high yield-strength stainless steel.
- Maximum allowable single-axis overload values are 5.7 to 25.3 times rated capacities.

High Signal-to-Noise Ratio: Silicon strain gages provide a signal 75 times stronger than conventional foil gages. This signal is amplified, resulting in near-zero noise distortion.

Typical Applications

- Telerobotics
- Robotic surgery
- Robotic hand research
- Finger-force research



The Mini45 F/T transducer

The transducer is made of hardened stainless steel with integral interface plates made from high-strength aircraft aluminum.

ENGLISH CALIBRATIONS	SENSING RANGES	Calibrations					
	Axes	US-30-40		US-60-80		US-120-160	
	Fx, Fy (±lbf)	30		60		120	
	Fz (±lbf)	60		120		240	
	Tx, Ty (±lbf-in)	40		80		160	
	Tz (±lbf-in)	40		80		160	
	RESOLUTION	System Type*					
	Axes	CTL	Net/DAQ	CTL	Net/DAQ	CTL	Net/DAQ
	Fx, Fy (lbf)	1/40	1/80	1/20	1/40	1/10	1/20
	Fz (lbf)	1/40	1/80	1/20	1/40	1/10	1/20
Tx, Ty (lbf-in)	1/44	1/88	1/22	1/44	1/22	1/44	
Tz (lbf-in)	1/88	1/176	1/44	1/88	1/22	1/44	

METRIC CALIBRATIONS	SENSING RANGES	Calibrations					
	Axes	SI-145-5		SI-290-10		SI-580-20	
	Fx, Fy (±N)	145		290		580	
	Fz (±N)	290		580		1160	
	Tx, Ty (±Nm)	5		10		20	
	Tz (±Nm)	5		10		20	
	RESOLUTION	System Type*					
	Axes	CTL	Net/DAQ	CTL	Net/DAQ	CTL	Net/DAQ
	Fx, Fy (N)	1/8	1/16	1/4	1/8	1/2	1/4
	Fz (N)	1/8	1/16	1/4	1/8	1/2	1/4
Tx, Ty (Nm)	1/376	1/752	1/188	1/376	1/94	1/188	
Tz (Nm)	1/752	1/1504	1/376	1/752	1/188	1/376	

*CTL: Controller F/T System; Net: Net F/T System; DAQ: 16-bit DAQ F/T System. The resolution is typical for most applications and can be improved with filtering. Resolutions quoted are the effective resolution after dropping four counts of noise (Net/DAQ) or eight counts of noise (CTL). All sensors calibrated by ATI.

Applied loads must be within range in each of the six axes for the F/T sensor to measure correctly (refer to the transducer manual for complex loading information).

Appendix 2: Feasibility study of using two 6DOF Force transducers

To investigate the system response against centrebow asymmetric forces, an extreme uneven force on the centrebow is applied and the deflection of the centrebow side edges is measured. If it was less than a deflection threshold, it will have been assumed safe (see **Error! Reference source not found.**). By assuming rigid mounting frames, the deflection of the centrebow side edge would be due to the flexibility of the centrebow structure plus the flexibility of the sensors themselves. The two deflection sources were determined as follows:

Deflection due to transducer flexibility: For this case, the centrebow structure is assumed rigid; therefore, the deflection of the centrebow edges was only due to the transducer flexibility. The transducer rotational stiffness could be found in ATI MINI45 product manual as given in Table 0.1 and Appendix 1.

Table 0.1: Stiffness Values of MINI45 Force Transducer

Stiffness (Calculated)	Metric
X-axis & Y-axis force (K_x, K_y)	7.4×10^7 N/m
Z-axis force (K_z)	9.8×10^7 N/m
X-axis & Y-axis torque (K_{tx}, K_{ty})	1.7×10^4 Nm/rad
Z-axis torque (K_{tz})	3.5×10^4 Nm/rad

Based on this table the rotational stiffness of the transducer is 1.7×10^4 Nm/rad. The deflection angle of the transducer (θ) were calculated from the rotational stiffness (k) and the applied moment as in Equation (0-1),

$$k = \frac{M}{\theta} \quad (0-1)$$

The moment was derived by multiplying the asymmetric force to the load arm (lateral distance to centrebow centreline) as seen in Equation (0-2) and Figure 0.1,

$$M = \text{asymmetric Force} \times \text{Load Arm} \quad (0-2)$$

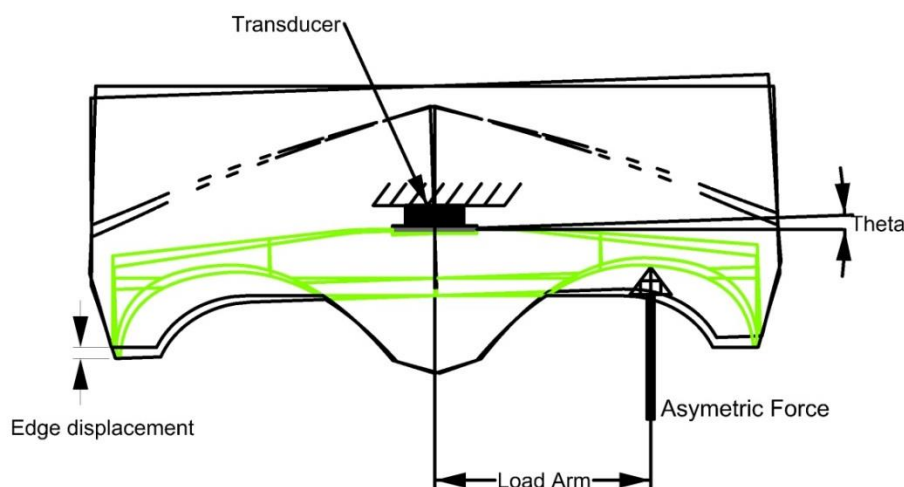


Figure 0.1: Deflection of the centrebow because of flexibility of the transducer where the centrebow structure is assumed rigid

The rapid transient nature of slamming and the uncertainties in the colliding angle of the waves, even in a controlled environment like the towing tank, led to the assumption of a maximum 20% of asymmetry in the slam loads. It was decided to apply these forces at the top of the archways, where the peak pressures normally occur. If according to previous results of HSM01, the maximum slam loads on the model were assumed to be 300 N, then the applied load would be 60 N. If we take average load arm at 0.29 m, then it would result in 0.092 mm maximum edge displacement. The displacement of the centrebow edge can be calculated by Equation (0-3),

$$\text{Edge Displacement} = \theta \times \text{Load Arm} \quad (0-3)$$

Deflection due to centrebow structure flexibility: Here, the transducer is assumed rigid and the deflection is only due to the centrebow structure and joints. To investigate this case a mock up configuration of the load measuring system with an existing centrebow model was designed. Two dummy transducers with relatively high rigidity were built out of solid aluminium cylinder. As seen in Figure 0.2, the block was machined and the bolt connections were manufactured similar to the ATI MINI45. The stiffness of the each solid cylinder was calculated to be 897516 Nm/rad using $k = EI/L$ formula where E is the young modulus of aluminium, I is the second moment of inertia of the cylinder base with 45 mm diameter and L is the height of the cylinder block being 15.7 mm. Thus, the dummy transducer stiffness is more than 52 times the actual ATI MINI45 transducer.

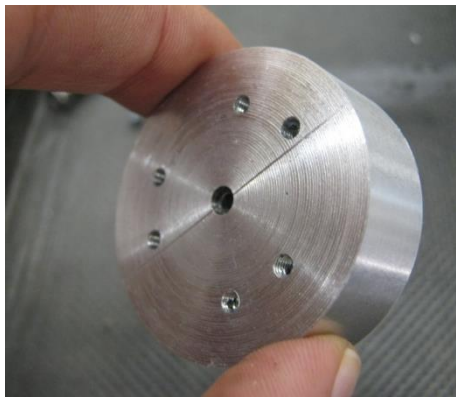


Figure 0.2: Aluminium block with threaded holes as dummy transducer.

Since HSM01 centrebow had two connections points in each frame, aluminium square hollow sections of 50×30×3 mm were used to attach the transducer to the centrebow. The same section beams were used to make a rigid frame on top of the centrebow and the dummy load cell (see Figure 0.3 and Figure 0.4).

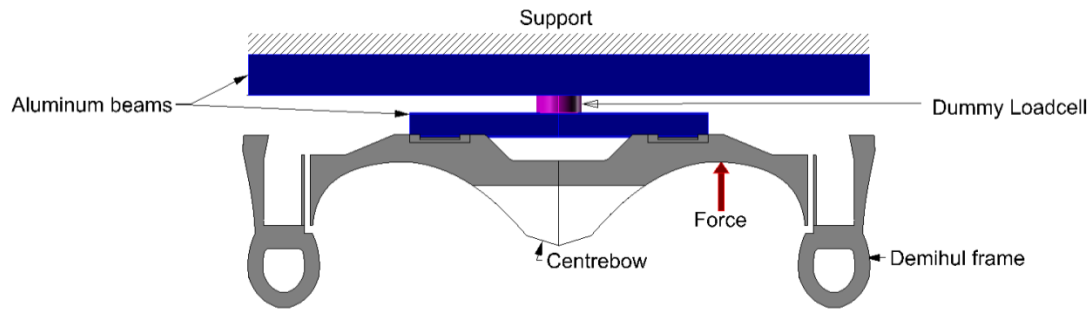


Figure 0.3: The configuration of the asymmetric force, the dummy sensor and holding frames on HSM01 centrebow

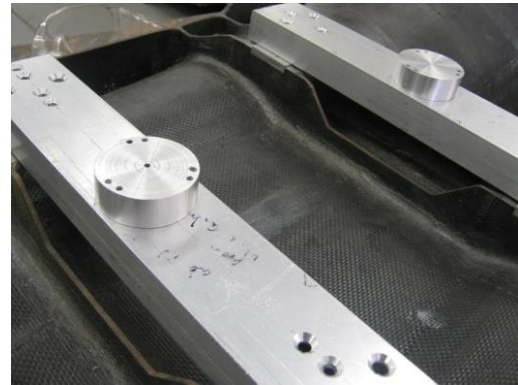


Figure 0.4: Aluminium blocks and the holding frames of the mock up centrebow load measuring system

The centrebow and the frames were placed upside down on a surface table and the aluminium bars were fixed to the table by applying heavy loads on each side. Weights were placed on the centrebow archway as shown in Figure 0.5, a measuring gauge was used at the edge of the centrebow to measure the displacement of the edge due to the loading.

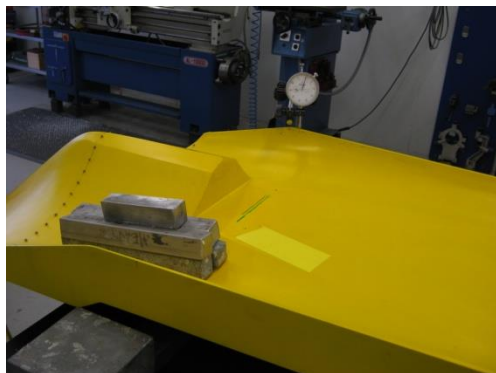


Figure 0.5: Measuring the deflection of the centrebow edge under asymmetric loading with a dial gauge. The centrebow was fixed upside down on aluminium frames.

As illustrated in Figure 0.6 loading and displacement measurements were performed at several locations on the centrebow. Loadings from 0.5 kg and to 6 kg were applied; all loading conditions are shown in Table 0.2.

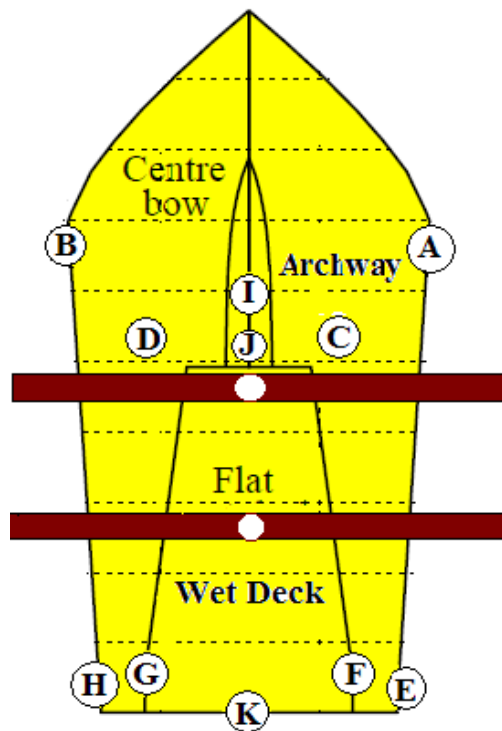


Figure 0.6: Asymmetric load application and measuring locations on the centrebow.

Table 0.2: Loading Conditions and Measuring Locations on The Centrebow. The Locations Are Shown in Figure 0.6

Condition No.	Load point	Deflection measuring point
Condition 1	D	A
Condition 2	C	A
Condition 3	G	A
Condition 4	G	E
Condition 5	F	E
Condition 6	D	E
Condition 7	J*	K
Condition 8	I*	K
Condition 9	C	B
Condition 10	D	B

*This load is a distributed load applied by a foam mould on the centrebow.

Figure 3.31 shows the measured displacement of the centrebow edges in each loading condition. Condition 5 has been disregarded as it is far from the expected of slam locations. The results show a displacement of less than 0.4 mm at the centrebow edges when an extreme asymmetric load of 61 N is applied on the archway.

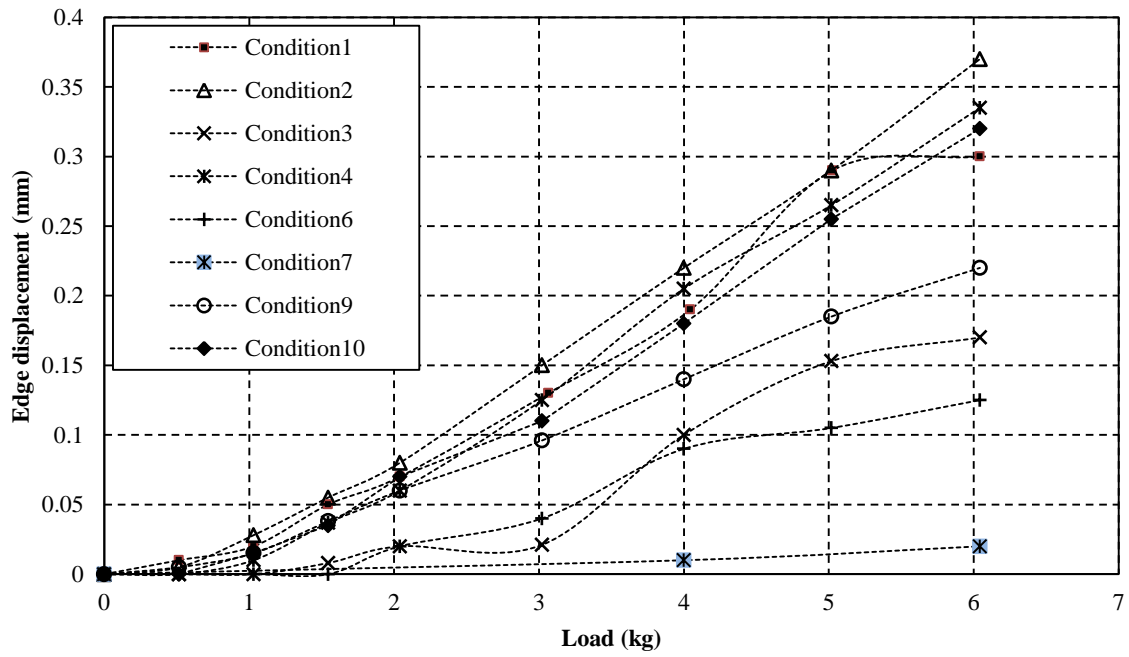


Figure 0.7: Displacement of centrebow edge in asymmetric loading conditions

By adding the two maximum edge displacements from the transducer and centrebow structure resulted in a maximum edge displacement of 0.5 mm which is considered very small. Visual and manual inspections also showed that the system is sufficiently rigid and safe.

Appendix 3: Pressure measurement instruments

(a) ENDEVCO Piezoresistive pressure transducer model 8510C-50



MEGGITT
smart engineering for
extreme environments

8510C -15, -50, -100 Piezoresistive pressure transducer

Features

- 15, 50 and 100 psig ranges
- 225 mV full scale output
- Rugged, miniature
- Gage reference



Description

The Endevco® model 8510C is a rugged, miniature, high sensitivity piezoresistive pressure transducer. Its high sensitivity combined with high resonance makes it ideal for measuring dynamic pressure. It has a 10-32 mounting thread, 0.15 inch (3.8 mm) face diameter and is available in ranges from 15 psi to 100 psi. The model 8510B is available for lower and higher pressure ranges.

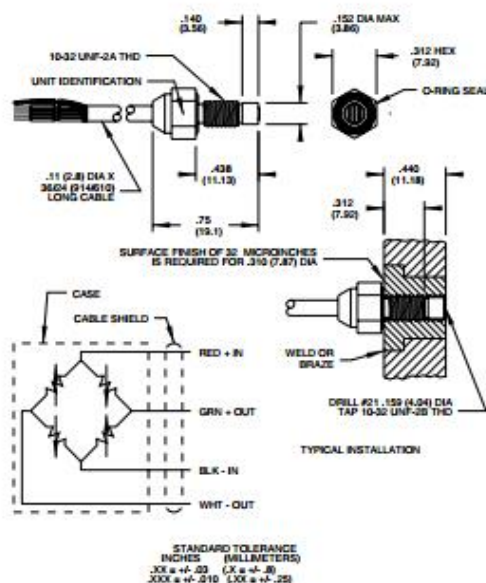
Endevco pressure transducers feature a four arm strain gage bridge ion implanted into a unique sculptured silicon diaphragm for maximum sensitivity and wideband frequency response. Self-contained hybrid temperature compensation provides stable performance over the temperature range of 0°F to 200°F (-18°C to +93°C).

Endevco transducers also feature excellent linearity (even to 3X range), high shock resistance, and high stability during temperature transients.

The model 8510C is designed for a wide variety of aerospace, automotive and industrial measurements which require a combination of small size, high sensitivity, and wideband frequency response. Typical applications include process control, jet engine inlet pressure measurements and wind tunnel flow measurements. Its vent tube may be connected to a standard reference manifold or used for differential pressure measurements.

The model 8510C is available with metric M5X0.8 mounting thread as 8510C-XXM5 on special order.

Recommended electronics for signal conditioning and power supply are the Endevco model 126 and 136 general purpose three channel conditioners, ultra low noise 4430A conditioner, or the 4990A-X (Oasis) multi-channel rack mount system.



8510C -15, -50, -100 Piezoresistive pressure transducer

MEGGITT
smart engineering for
extreme environments

Specifications

Certified performance: All specifications assume +75°F (+24°C) and 10 Vdc excitation unless otherwise stated. The following parameters are 100% tested. Calibration data, traceable to the National Institute of Standards and Technology (NIST), is supplied.

Dynamic characteristics	Units	8510C-15	-50	-100
Range [1]	psig	0-15	0-50	0-100
Positive sensitivity [2]	mV/psi typ [min]	15.0 [9.3]	4.5 [2.8]	2.25 [1.4]
Combined: non-linearity, non-repeatability, pressure hysteresis	% FSO RSS max	0.50	0.40	0.40
Non-linearity, independent	% FSO typ	0.15	0.1	0.1
Non-repeatability	% FSO typ	0.1	0.1	0.1
Pressure hysteresis	% FSO typ	0.1	0.1	0.1
Zero measurand output [3]	mV max	±20	±20	±20
Zero shift after 3X range	±% 3X FSO max (typ)	0.2 [0.02]	0.2 [0.02]	0.2 [0.02]
Thermal zero shift				
from 0°F to +200°F (-18°C to +93°C)	±% FSO max	3	3	3
Thermal sensitivity shift				
from 0°F and +200°F (-18°C to +93°C)	±% max	3	3	3
Resonance frequency	Hz	180 000	320 000	500 000
Non-linearity at 3X range	% 3X FSO	1.0	1.0	1.0
Thermal transient response per ISA-S37.10, para. 6.7, procedure I [4]	psi/°F	0.003	0.003	0.01
	psi/°C	0.005	0.005	0.02
Photoflash response [5]	Equiv. psi	0.1	0.3	0.6
Warm-up time [6]	ms	1	1	1
Acceleration sensitivity	Equiv. psi/g	0.00015	0.00015	0.00015
Burst pressure (diaphragm/reference side) [7]	psi min	75/300	250/300	400/300
Electrical				
Full scale output	225 mV typical [140 mV minimum] at 10.0 Vdc			
Supply voltage [8]	10.0 Vdc recommended, 15 Vdc maximum			
Electrical configuration	Active four-arm piezoresistive bridge			
Polarity	Positive output for increasing pressure into (+) port [end with screen on it]			
Resistance				
Input	2600 ohms typical, 1700 ohms minimum			
Output	1500 ohms typical, 2200 ohms maximum			
Isolation	100 megohms minimum at 50 volts; leads to case, leads to shield, shield to case			
Noise	5 microvolts rms typical, dc to 50 000 Hz; 50 microvolts rms maximum, dc to 50 000 Hz			
Mechanical				
Case material	Stainless steel [17-4 PH CRES]			
Cable, integral	4 conductor No. 32 AWG Teflon® insulated leads, braided shield, silicone jacket			
Dead volume (+) port	0.0003 cubic inches (0.005 cc)			
Mounting torque	10-32 UNF-2A threaded case 0.438 inch [11.12 mm] long/15 ±5 lbf-in [1.7 ±0.6 Nm]			
Weight	2.3 grams [cable weighs 9 grams/meter]			
Environmental characteristics				
Media [9]				
Temperature [10] [11]	-65°F to +250°F [-54°C to +121°C]			
Vibration	1000 g pk			
Acceleration	1000 g			
Shock	20 000 g, 100 microsecond haversine pulse			
Humidity	Isolation resistance greater than 100 megohms at 50 volts when tested per MIL-STD-202E, method 103B, test condition B			

(b) ENDEVCO DC Amplifier model 136



Endevco

Model 136 DC amplifier

Features

- Three-channel DC differential voltage amplifier
- 200 kHz bandwidth (-3dB corner)
- Auto-zero and shunt calibration
- Gain range 0 to 1000
- Four selectable excitation voltage levels
- RS-232 serial interface
- 12 VDC power option
- Built-in 4-pole Butterworth lowpass filter

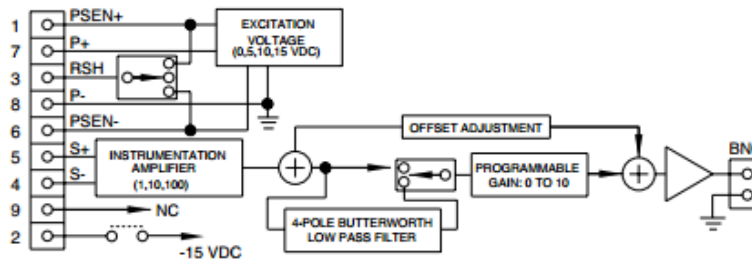


Description

The Endevco® model 136 is a three-channel, DC amplifier that is manually or computer programmable. Manual control is accomplished at the front panel by means of a "select channel" push-button, three (3) "channel LEDs", one "select function" push-button, five "function LEDs", a four character LED display, showing the state of each function/channel, and four "edit" push-buttons to change the entries in the LED display. There are three LEDs used as fault status indicators for the auto zero function. Computer control is accomplished using the standard RS-232 port and optional application software.

There are two modes of operation, Normal and Programming/Setup. Both modes of operation utilize the front panel LED display. In the Normal mode, there are two states, Monitoring mode and No-Monitoring. In the Monitoring mode the LED display indicates the RMS reading of the signal present at the output of the selected channel. The Non-Monitoring mode turns off the LED display for lower noise applications and to minimize power consumption. In the Programming mode, the unit is ready for manual programming or editing of existing channel setups. The unit will automatically return to the Normal mode of operation after 20 seconds of inactivity of the front panel or after pressing the "select function" push-button while the "monitoring state" function LED is flashing.

The rear panel contains (on a per-channel basis) a BNC output connector, a 9-pin "D" input connector, the RS-232 connector, and the input power connector. Three model 136 units may be configured in a 19-inch rack mount adapter. The standard unit is powered by 90-264 VAC, 50/60 Hz. The -1 option is powered by 9 to 18 VDC, making it ideal for portable use or for automobile test applications.



Technical Illustration

MEGGITT

Model 136 DC amplifier

Endevco

Specifications

Inputs

Input impedance	1 Meg Ohm minimum
Input range: differential	0 to ± 10 VDC or peak VAC, 9 pin "D" connector for each bridge sensor
Common mode	± 10 VDC or pk VAC, inclusive of signal 50 Vpk without damage
Common mode rejection	70 dB minimum, 2000 or less input imbalance, DC to 60 kHz
Input imbalance adjustment	± 100 mVDC, $100 \leq \text{gain} \leq 1000$ ± 1 VDC, $10 \leq \text{gain} \leq 100$ ± 10 VDC, $0 \leq \text{gain} \leq 10$

Outputs

AC/DC voltage	Single-ended, short circuit protected
Output impedance	0.2 ohm maximum
Linear output	10 V pk
Current output	10 mA, minimum
Output DC bias stability temp	$\pm 5 \mu\text{V}/^\circ\text{C}$ RTI or $\pm 0.1 \text{ mV}/^\circ\text{C}$ RTO
Output DC bias stability time	$\pm 20 \mu\text{V}$ RTI or $\pm 5 \text{ mV}$ RTO, whichever is greater, for 24 hours, after a 1 hour warmup
Excitation voltage	0, 5.0, 10.0, or 15.0 VDC, front panel or computer selected; 1 selection for all 3 channels
Excitation voltage accuracy	$\pm 1\%$
Excitation current	30 mA maximum, short circuit protected
Noise and ripple	1 mV rms maximum, 10 Hz to 50 kHz, with 1 kOhm load

Transfer characteristics

Gain	
Range	Programmable from 0 to 1000
Resolution	0.0025, $0 \leq \text{gain} \leq 10$ 0.025, $10 \leq \text{gain} \leq 100$ 0.25, $100 \leq \text{gain} \leq 1000$
Accuracy	$\pm 0.5\%$ of full scale maximum, DC to 1 kHz, filters disabled
Linearity	0.1% of full scale, best fit straight line at 1 kHz reference
Stability	$\pm 0.2\%$ of full scale, 0°C to $+50^\circ\text{C}$
Noise	20 μV rms RTI plus 1 mV rms RTO, whichever is greater, DC to 50 kHz, with a 1 kOhm source resistance unit in Non-monitoring state, 10 kHz internal lowpass filter enabled
Broadband frequency response	DC to 200 kHz -3dB referenced to 1 kHz
Filter characteristics/type	4-pole Butterworth
Corner frequency (-3 dB)	10 kHz $\pm 12\%$ (other corners available by changing internal module 31875: 10 Hz to 80 kHz)
Crosstalk between channels	80 dB RTI

Power requirements

Voltage	Standard unit: 90-264 VAC 50 to 60 Hz; -1 option: 9-18 VDC
Power dissipation	10 Watts typical
Isolation	No isolation channel to channel or signal ground to caseground

Physical characteristics

Dimensions	5.57" x 2.52" x 12"
Weight	4 lbs typical
Case	Black aluminum cover, medium grey plastic bezel

Accessories

IM136	Instruction manual
EW599	Power cord
31875-1000	10 kHz, 4-pole, Butterworth lowpass filter module

Optional accessories

35933	Application software
EJ847	RJ11 (6X4) straight wired inline coupler
EW1077	RJ11 4 conductor modular flat cable, straight wired, 2 feet long
EW1027	RJ11 4 conductor modular flat cable, straight wired, 7 feet long
EJ807	Serial DB9F/RJ11 adapter

Optional accessories continued

EJ822	Modular splitter adapter-1 (6x4) male to 3 (6x4) female
136-1	9 - 18 VDC input power option
31875-XXXX	Lowpass filter modules (see 31875 data sheet)
31979	Rack mount kit
EHM1471	Blank panel
EHM1413	Desktop DC power supply
EHM1409	Automotive power plug
29719-2	DB9M connector kit

Warning! Use of RJ11 cable other than that specified herein will cause catastrophic failure of the unit.

Notes:

1. Maintain high levels of precision and accuracy using Endevco's factory calibration services. Call Endevco's inside sales force at 800-982-6732 for recommended intervals, pricing and turn-around time for these services as well as for quotations on our standard products.

Continued product improvement necessitates that Endevco reserve the right to modify these specifications without notice. Endevco maintains a program of constant surveillance over all products to ensure a high level of reliability. This program includes attention to reliability factors during product design, the support of stringent Quality Control requirements, and compulsory corrective action procedures. These measures, together with conservative specifications have made the name Endevco synonymous with reliability.

© ENDEVCO CORPORATION. ALL RIGHTS RESERVED 36700 RANCHO VIEJO ROAD, SAN JUAN CAPISTRANO, CA 92675 USA
(800) 982-6732 • (714) 472-8181 fax (714) 441-7231 • www.endevco.com • Email: applications@endevco.com

011909

MEGGITT
smart engineering for
extreme environments

Appendix 4: Acceleration measurement instruments

(a) B&K 4370 accelerometer specifications

Piezoelectric Accelerometer Charge Accelerometer — Type 4370, 4370 S and 4370 V

FEATURES

- General purpose
- High sensitivity
- Low-level, low-frequency measurements



Description

Type 4370 is a piezoelectric, DeltaShear[®], Unigain[®] accelerometer with top connector. Type 4370 features 10–32 UNF receptacle for output connection and can be mounted on the object by means of a 10–32 UNF threaded steel stud.

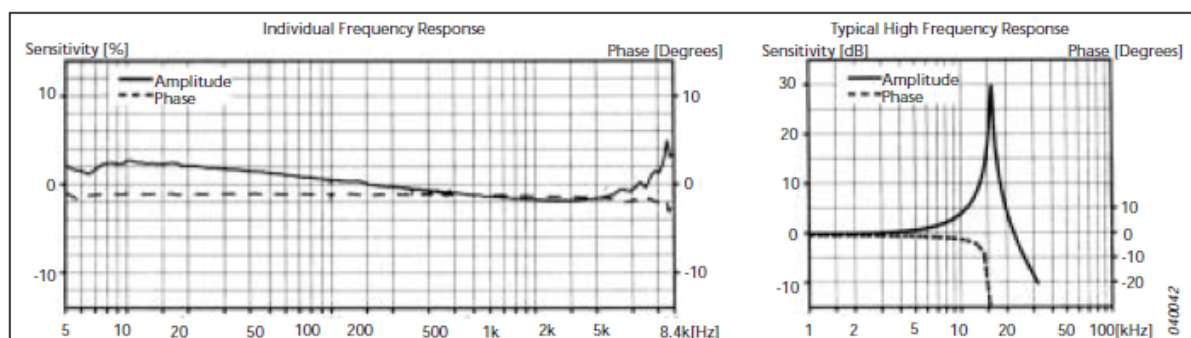
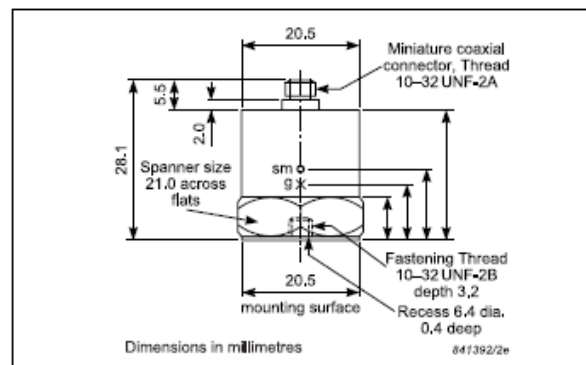
Characteristics

This piezoelectric accelerometer may be treated as a charge source. Its sensitivity is expressed in terms of charge per unit acceleration (pC/g).

The DeltaShear design involves three piezoelectric elements and three masses arranged in a triangular configuration around a triangular centre post. The ring prestresses the piezoelectric elements to give a high degree of linearity. The charge is collected between the housing and the clamping ring. The piezoelectric element used is a PZ 23 lead zirconate titanate element. The housing material is stainless steel.

Calibration

The sensitivity given in the calibration chart has been measured at 159.2 Hz and an acceleration of 10 g. For 99.9% confidence level, the accuracy of the factory calibration is $\pm 2\%$.



Specifications – Charge Accelerometer Type 4370, 4370 S and 4370 V

	Units	4370/4370 S	4370 V
Dynamic Characteristics			
Charge Sensitivity (@ 159.2 Hz)	pC/g	98 ± 2%	98 ± 15%
Frequency Response		See typical Amplitude Response	
Mounted Resonance Frequency	kHz	16	
Amplitude Response ±10% [1]	Hz	0.1 to 4800	
Transverse Sensitivity	%	<4	
Transverse Resonance Frequency	kHz	10	
Electrical Characteristics			
Min. Leakage Resistance @ 20°C	GΩ	≥20	
Capacitance	pF	1200	
Grounding		Signal ground connected to case	
Environmental Characteristics			
Temperature Range	°C (°F)	-74 to 250 (-101 to 482)	
Humidity		Welded	
Max. Operational Sinusoidal Vibration (peak)	g pk	2000	
Max. Operational Shock (± peak)	g pk	2000	
Base Strain Sensitivity	Equiv. g/μ strain	0.003	
Thermal Transient Sensitivity	Equiv. g/°C (g/°F)	0.002 (0.011)	
Magnetic Sensitivity (50 Hz–0.03 Tesla)	g/T	0.1	
Physical Characteristics			
Dimensions		See outline drawing	
Weight	gram (oz.)	54 (1.89)	
Case Material		Stainless steel	
Connector		10–32 UNF	
Mounting		10–32 UNF × 5 mm threaded hole	

[1] Low-end response of the transducer is a function of its associated electronics

Ordering Information

Type 4370 includes the following accessories:

- Carrying box
- Calibration chart
- AO 0038: Low noise cable fitted with 10–32 connectors, 1.2 m
- 10–32 UNF threaded steel stud. Length 12.7 mm

Type 4370 S includes the following accessories:

- Carrying box
- Calibration chart
- AO 0038: Low noise cable fitted with 10–32 connectors, 1.2 m
- 10–32 UNF threaded steel stud. Length 12.7 mm
- UA 0078: Accessory box including:
 - Cementing stud, 10–32 UNF
 - EP610 input adaptor, TNC to 10–32 UNF microdot
 - Mounting magnet, 10–32 UNF thread
 - Case of beeswax
 - Insulating disk

- Insulating stud
- Steel stud 10–32 UNF × ½"
- Tools

Type 4370V includes the following accessories:

- Carrying box
- Calibration chart
- 10–32 UNF threaded steel stud. Length 12.7 mm

OPTIONAL ACCESSORIES

- AO 0038: 260°C Teflon® low-noise cable, 10–32 UNF, length 1.2 m (4 ft)
- AO 0122: 250°C, reinforced super low noise cable, 10–32, 3 m (10 ft)
- AO 0231: 260°C Teflon low-noise cable, 10–32 UNF/TNC, length 3 m (10 ft)
- AO 1382: Teflon low noise cable, double screened 10–32, 1.2 m (4 ft)
- DB 0544: 10–32 UNF Round tip
- JJ 0207: 2-pin TNC/10–32 UNF plug adaptor
- JP 0162: 10–32 UNF to TNC connector adaptor

- QA 0013: Hexagonal key for 10–32 UNF studs
- QA 0029: Tap for 10–32 UNF thread
- UA 0559: Mechanical filter for Accelerometer
- UA 0641: Extension Connector, 10–32 UNF/TNC (only top connector accelerometer)
- UA 0642: Mounting magnet and 2 insulating discs
- UA 0866: Cement stud 10–32 UNF 0.14 mm (set of 25)
- YG 0150: Steel stud 10–32/10–32 with flange
- YJ 0216: Beeswax for mounting
- YP 0080: Probe with sharp tip
- YP 0150: 10–32 UNF insulated stud. Length 12.7 mm
- YQ 2960: 0–32 UNF threaded steel stud. Length 12.7 mm
- YQ 2962: 0–32 UNF threaded steel stud. Length 7.62 mm

(b) Conditioning Amplifier 2626 to amplify the B&K accelerometer signal

With compliments

Helmut Singer Elektronik

www.helmut-singer.de info@helmut-singer.de
fon +49 241 155 315 fax +49 241 152 066
Feldchen 16-24 D-52070 Aachen Germany

Conditioning Amplifier Type 2626

SPECIFIC FEATURES:

- Direct indication of system sensitivity in V/g
- High sensitivity up to 1 V/pC
- Signal level indicator lamps
- Output direct coupled with negligible DC off-set, or transformer coupled floating
- Fast recovery
- Low noise

USES:

- Vibration measurements with long cables between transducer and preamplifier
- General purpose vibration measurement
- Signal conditioning in vibration test servo loops

The Conditioning Amplifier Type 2626 is a charge preamplifier offering comprehensive signal conditioning facilities together with a very high signal to noise ratio which make it an ideal general purpose vibration preamplifier for use with pi-

ezoelectric transducers. The amplifier features a 3 digit sensitivity adjustment network which enables the amplifier sensitivity to be conditioned to suit transducer sensitivities between 1 and 1100 pC/g. This feature greatly simplifies the calibration and reading of a measuring system, especially when using transducers which have "odd" sensitivity values, i. e. non Uni-Gain® types.

The amplifier has a rated output switchable in decades between 1 mV/g and 10 V/g depending on

the sensitivity of the transducer. The maximum gain is 60 dB with a source capacitance of 1 nF. Adjustable High-pass and Low-pass filters are provided to enable the pass band of the instrument to be limited to the frequency range of interest, thus reducing the influence of noise and spurious signals outside this band. The filter switch positions marked on the front panel give the 5% as well as the 3 dB frequency limits.

Fig. 7 shows the block diagram of the 2626. The signal from the trans-

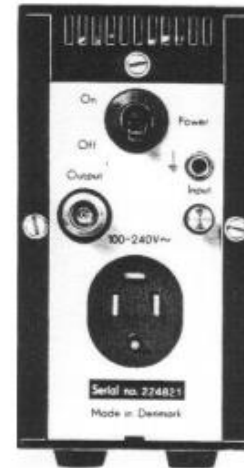
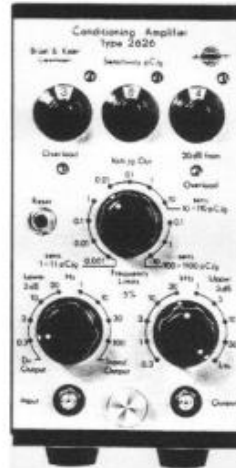


Fig.6. Rear panel of Type 2626

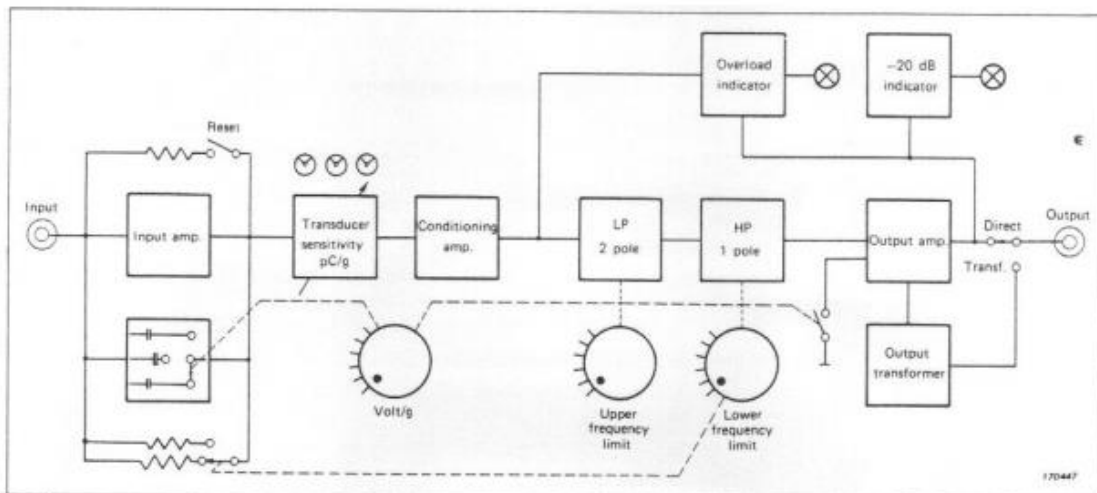


Fig.7. Block diagram of Type 2626

ducer is fed to the input section which contains an amplifier stage with capacitive feedback forming a charge amplifier. The signal goes on to the conditioning section where the sensitivity is adjusted to match the transducer and further to a Low-pass filter (2 pole Butterworth) and a High-pass filter (single pole) where the upper and lower frequency limits of the amplifier can be set.

From the filters the signal is fed to an output amplifier and further to the output. The signal is available either directly coupled or through a transformer; the transformer output will be used where ground loop problems exist and will be found ideal for use in the feedback loop of vibration exciter systems. Two neon signal level indicators are connected to the output, one acts as an overload indicator, the other lights when the signal level is within

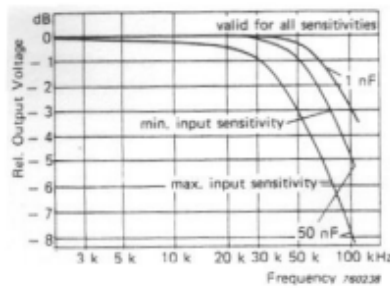


Fig. 8. High frequency response of Type 2626 with different capacitive input loads for maximum and minimum amplifier sensitivity. A 50 nF load is equivalent to cable length of 550 m (1800 ft)

20 dB of full output thus indicating the best working area to obtain minimum noise.

Both input and output sockets on the front panel suit B & K standard

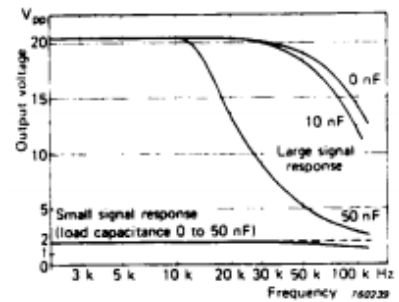


Fig. 9. High frequency response of Type 2626 for a large signal and a small signal with different capacitive output loads (Distortion %). 50 nF = 550 m (1800 ft) output cable

miniature plugs. Duplicate input and output sockets of the BNC type are provided on the rear panel. A power supply is built into the instrument so that operation is direct from AC mains.